Dynamics and nonlinear thermo-acoustic stability analysis of premixed conical flames

Alexis Cuquel

École Centrale Paris

THÈSE

présentée par

Alexis Cuquel

pour l'obtention du

GRADE de DOCTEUR

Formation doctorale : Énergétique

Laboratoire d'accueil : Laboratoire d'Énergétique Moléculaire et Macroscopique, Combustion (EM2C) du CNRS et de l'ECP

Dynamics and nonlinear thermo-acoustic stability analysis of premixed conical flames

Soutenue le 11 Juin 2013

Jury :	MM	Baillot	F.	Rapporteur
		Polifke	W.	Rapporteur
		Quinard	J.	
		Selle	L.	
		Roux	S.	
		Schuller	T.	Directeur de thèse
		Durox	D.	Co-Directeur de thèse

École Centrale des Arts et Manufactures
Grand Établissement sous tutelle
du Ministère de l'Éducation Nationale
Grande Voie des Vignes
92295 Châtenay-Malabry Cedex
Tél : 33 (1) 41 13 10 00
Télex : 634 991 F EC PARIS

Laboratoire d'Énergétique Moléculaire et Macroscopique, Combustion (E.M2.C.)
UPR 288, CNRS et École Centrale Paris
Tél : 33 (1) 41 13 10 31
Fax : 33 (1) 47 02 80 35

XXXX - XX

Abstract

Thermo-acoustic instabilities in combustion chambers are generated by the interactions between a flame and the combustor acoustics, leading to a resonant coupling. These self-sustained oscillations may be observed in many practical systems such as domestic boilers, industrial furnaces, gas turbines or rocket engines. Although this phenomenon has already been the topic of many investigations, there is yet no generalized robust framework to predict the onset of these self-sustained oscillations and to determine the evolution of the flow variables within the combustor during unstable operation. This work builds on previous models and experiments to improve the description of the response of laminar conical flames to flow perturbations and the prediction of thermo-acoustic instability in burners operating with conical flames.

In the first part of the manuscript, an extensive review of conical flame dynamics modeling is undertaken and a general framework for the modeling of their Flame Transfer Function (FTF) is presented. The experimental setup and the diagnostics used to characterize their response to flow disturbances are then described. They are used to measure the FTF when the flames are submitted to harmonic flow perturbations. A novel experimental technique is also proposed to control the flow perturbation level at the burner outlet. It enables to modulate the flow with random white noise perturbations and to measure the FTF with a better frequency resolution. Results with this alternative technique compare well with results from the classical method using harmonic signals for small disturbances. Limits of this technique are also highlighted when the perturbation level increases.

Different analytical expressions for the FTF of conical flames are derived in the second part of the thesis by progressively introducing more physics into the models. Models based on convected flow disturbances are extended by taking into account the incompressible nature of the perturbed velocity field. It is shown that the prediction of the FTF phase lag of a conical flame is greatly improved and collapses well with measurements. Then, a thorough investigation of the flame base dynamics interacting with the anchoring device is conducted by considering unsteady heat loss from the flame to the burner. This mechanism is shown to drive the motion of the flame base and the flame dynamics at high frequencies. It is also shown that this contribution to the FTF rules the high frequency behavior of the FTF as well as the nonlinear

evolution of the FTF when the perturbation level increases. Finally, an analysis is conducted on the dynamics of a single conical flame placed into cylindrical flame tubes featuring different diameters. It is shown that confinement effects need to be taken into account when the burnt gases cannot fully expand. Large differences are observed between FTF measured for different confinement tube diameters. A new dimensionless number is derived to take these effects into account and make all the FTF collapse on a single curve. These different models are then used to model the response of a collection of small conical flames stabilized on a perforated plate. It is shown that by sorting out the different contributing mechanisms to the FTF, the expressions proposed in this work may be combined to capture the main behavior and correct phase lag evolution of these flames in the frequency range of interest for thermo-acoustic instability prediction.

Finally, methods for thermo-acoustic instability prediction are considered in the last part of this manuscript. A nonlinear stability analysis relying on the Flame Describing Function (FDF) is coupled to a numerical Helmholtz solver (AVSP) to analyze the different limit cycles observed in a configuration featuring a multipoint injection system with small laminar conical flames. This type of acoustic solver enables the prediction of thermo-acoustic instabilities over 3D complex combustor geometries and the analysis of the unstable system evolution to limit cycle. It is shown that this combination enables to predict linearly unstable modes that reach a limit cycle as the perturbation level increases. The amplitude and the frequency of limit cycles observed in the experiments are fairly well retrieved by the simulations. It is also shown that some typical nonlinear phenomena such as mode triggering or mode switching can be also anticipated with the method developed. These different tools and models enable to improve the prediction of thermo-acoustic instabilities.

Résumé

Les instabilités thermo-acoustiques présentes dans les chambres de combustion sont générées par des interactions entre une flamme et l'acoustique du foyer. Ces oscillations auto-entretenues peuvent être observées dans de nombreux systèmes industriels tels que des chaudières domestiques, des fours industriels, des turbines à gaz ou des moteurs fusée. Bien que ce phénomène ait fait l'objet de nombreux travaux, il n'existe toujours pas de cadre d'étude assez général et robuste pour prédire le déclenchement de ces oscillations auto-entretenues et pour déterminer l'évolution des variables de l'écoulement à l'intérieur de la chambre de combustion. Ce travail s'appuie à la fois sur des modèles et des expériences. L'objectif est d'améliorer la description de la réponse de flammes coniques laminaires prémélangées à des perturbations de l'écoulement et les prédictions d'instabilités thermo-acoustiques dans des foyers alimentés par des flammes coniques.
Dans la première partie du manuscrit, une revue des modèles décrivant la dynamique de flammes coniques est entreprise et un cadre général d'étude pour la modélisation de la Fonction de Transfert de Flamme (FTF) est présenté. Le dispositif expérimental ainsi que les diagnostics utilisés sont ensuite décrits. Ces systèmes sont utilisés pour mesurer la FTF de flammes coniques laminaires prémélangées soumises à des perturbations harmoniques de l'écoulement. Une nouvelle technique expérimentale est proposée pour contrôler les perturbations de l'écoulement à la sortie du brûleur. Elle est utilisée pour moduler l'écoulement avec un bruit blanc aléatoire et déterminer la FTF avec une résolution fréquentielle bien meilleure. Pour de faibles niveaux d'excitation, les résultats obtenus avec cette technique sont en accord avec ceux obtenus par la méthode classique utilisant des perturbations harmoniques. Les limites de cette technique sont décrites lorsque le niveau de perturbation augmente.
Plusieurs expressions analytiques de la FTF de flammes coniques sont établies dans la seconde partie de cette thèse en introduisant progressivement plus de phénomènes physiques dans le modèle. Les modèles basés sur des perturbations convectées par l'écoulement sont étendus en tenant compte de la nature incompressible du champ de perturbation de vitesse. La prévision de la phase de la FTF de flamme conique est améliorée et présente un bon accord avec les mesures. Ensuite, une étude détaillée des interactions de la base de la flamme avec le bord du brûleur est conduite en tenant compte des pertes thermiques

instationnaires de la flamme vers le brûleur. Ce mécanisme contrôle le mouvement de la base de la flamme et la dynamique de flamme à haute fréquence. Cette contribution à la FTF détermine le comportement haute fréquence de la FTF ainsi que l'évolution non-linéaire de la FTF lorsque le niveau de perturbation augmente. Enfin, une analyse de la dynamique des flammes coniques est entreprise pour des flammes placées dans des tubes de différents diamètres. Il est montré que les effets de confinement doivent être pris en compte lorsque les gaz brûlés ne peuvent se dilater complètement. Des différences importantes sont observées entre des FTF mesurées pour des tubes de confinement de diamètres différents. Un nouveau nombre sans dimension est établi pour prendre en compte ces effets. Ces différents modèles sont ensuite utilisés pour modéliser la réponse d'une collection de petites flammes coniques stabilisées sur une plaque perforée. Il est montré qu'une combinaison de ces modèles permet de capturer le comportement de ces flammes ainsi que l'évolution de la phase de la FTF couvrant le spectre fréquentiel pertinent pour la prédiction d'instabilités thermo-acoustiques.

Finalement, la dernière partie de ce manuscrit traite des méthodes de prévision d'instabilités thermo-acoustiques. Une analyse de stabilité non-linéaire basée sur la méthode de l'équivalent harmonique (FDF) est couplée à un solveur numérique de l'équation de Helmholtz dans le but d'analyser les différents cycles limites observés dans une configuration présentant un système d'injection multipoint avec de petites flammes coniques et laminaires. Ce type de solveur acoustique permet la prévision d'instabilités thermo-acoustiques dans des géométries 3D complexes de foyers et l'analyse de l'évolution d'un système instable jusqu'au cycle limite. Cette combinaison permet de prévoir le déclenchement de modes linéairement instables qui atteignent un cycle limite lorsque le niveau de perturbation augmente. L'amplitude et la fréquence de ces cycles limites sont correctement retrouvées par les simulations. Il est montré que certains phénomènes non-linéaires peuvent être également prédits grâce à cette méthode, tels que des déclenchements à partir d'un seuil ou une commutation de modes. Ces différents outils et modèles permettent d'améliorer la prévision d'instabilités thermo-acoustiques.

Contents

Introduction

Over the last two centuries, combustion became the most widely used and the most affordable technology to generate thermal energy. It represented in 2010 more than 80 % of the worldwide primary energy consumption including energy generated from fossil fuels (oil, natural gas and coal), waste and biofuels (see Fig. 1-left), and its use is still growing (International Energy Agency, www.iea.org). Combustion technology prevails in the power generation industry (fossil fuel power plants, gas turbines), in the transport industry (automotive, aeronautical and aerospace propulsion), for industrial material processing (glass furnaces, steel furnaces, radiant burners), for industrial boilers and for household devices (domestic boilers, gas stoves). This predominant position for thermal energy generation is mainly due to the high energy density of the fuels used as well as their easy storage and transport. These fuels can also be burnt quickly on demand, a feature which is especially important for power generation during load peaks.

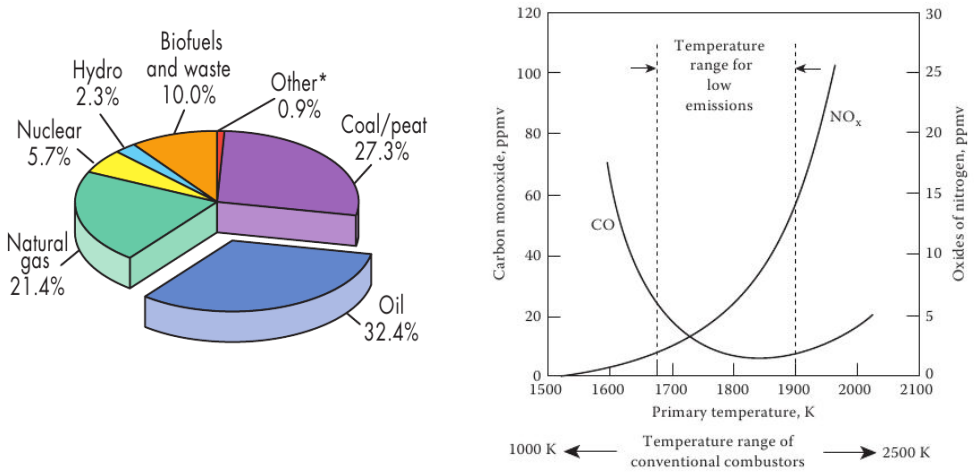

Figure 1: (left) *World total primary energy supply in 2010 from the International Energy Agency. "Other*" includes geothermal, solar and wind.* **(right)** *CO and* NO_x *concentrations as a function of the combustion zone temperature, from Lefebvre and Ballal (2010).*

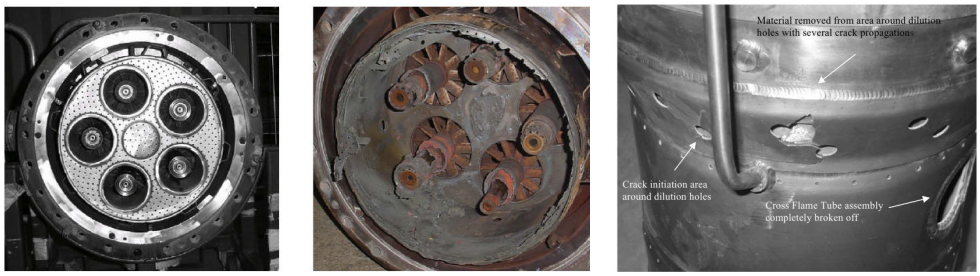

Figure 2: (left) *Multiple swirled injector combustor. Reproduced from Goy et al. (2006).* **(middle)** *Damaged system. Perforates in the back plane chamber have melted. Reproduced from Goy et al. (2006).* **(right)** *Photograph of combustor damage caused by high frequency thermo-acoustic instabilities. Material was removed from the area around the dilution holes with several crack propagations. Reproduced from Sewell and Sobieski (2006).*

During the past two decades, concerns about the impact of combustion on the environment and global climate change have raised. It lead to more restrictive regulations on the emission of green house gases such as CO_2 and the emission of pollutants like nitrogen oxides NO_x and carbon monoxide CO [Lefebvre and Ballal (2010)]. In order to decrease CO_2 emission, the efficiency of the combustion process has to be improved. In the case of CO and NO_x emissions, the problem is more complex. NO_x are generated by high temperatures in the combustor and CO are created by dissociation of the CO_2 at high temperatures or by incomplete combustion. These two constraints define an optimum temperature range that minimizes pollutant emissions, as shown in Fig. 1-right. One of the technological solutions that has been developed is based on lean premixed prevaporized (LPP) burners. In these burners, the reactants are premixed ahead of the combustion zone to obtain a more uniform temperature field compared to non-premixed flames. The use of an excess of air compared to stoichiometric conditions enables to decrease the adiabatic flame temperature. When liquid fuel is injected, the fuel is prevaporized before combustion. These burners ultimately lead to significantly lower temperatures in the combustor and enabled to drastically reduce NO_x pollutant emissions [Correa (1998)].

However, it is known that this technology makes the combustors more prone to unsteadiness, reducing the operating range of industrial facilities. Flame stabilization is greatly deteriorated and this is accompanied by several undesired phenomena such as global or local flame extinctions, flame blow-off, flashback and thermo-acoustic instabilities (see the collection of articles edited by Lieuwen and Yang (2005)). Combustion dynamics coupled to the combustor acoustics cause recurrent serious problems in many installations such as flame extinction, increased heat fluxes at the wall and large pressure oscillations leading to structural vibrations. These undesirable phenomena induce possible damages or even the destruction of the combustor as exemplified in Fig. 2.

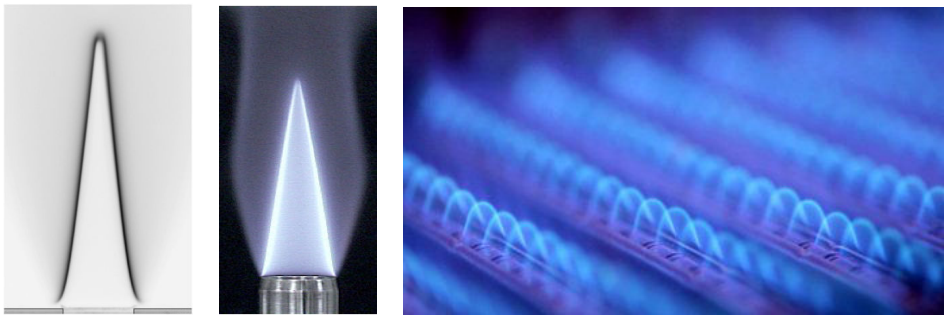

Figure 3: (left) *2D premixed laminar conical flame. Reproduced from Selle* et al. *(2011).* **(center)** *Axisymmetric laminar premixed conical flame. Reproduced from Durox* et al. *(2004).* **(right)** *Premixed laminar conical flames of a burner placed inside a domestic boiler. Reproduced from www.lovekin.co.uk.*

Thermo-acoustic instabilities are one of the research topic at EM2C. Over the last two decades, a systematic investigation of these phenomena was conducted by considering well-controlled experiments and simplified configurations to study fundamental mechanisms. Work was initiated with laminar premixed flames in order to isolate the different mechanisms triggering thermo-acoustic instabilities and to understand their coupling. The present work is in direct line with these previous Ph.D. theses. One of the main objectives is to improve the flame dynamics modeling. A generic inclined flame configuration is considered here. The work is focused on the response of laminar conical flames to flow perturbations and their coupling with the combustor acoustics. This type of flame is of fundamental and of technological interests (see Figs. 3-left and -center for examples on academic burners). It is also used in some industrial burners such as radiant burners for paper drying. Many burners in domestic boilers or in preheaters feature a series of regularly spaced holes to stabilize small conical flames as shown in Fig. 3-right. The thesis objective is two folds:

- The first objective is to improve the description of the fundamental physical mechanisms controlling the response of an inclined conical flame when submitted to flow perturbations. This work builds on previous analyses at EM2C by Ducruix (1999), Schuller (2003) and Birbaud (2006). The present work extends these analyses by taking into account a better representation of velocity perturbations in the fresh reactant stream, by including effects of unsteady heat loss taking place at the burner rim and those associated with confinement of the burnt gases. Effects of the perturbation level are considered as well. This has led to a unified representation of the dynamics of conical flames perturbed by velocity disturbances.

- The second objective concerns the prediction of thermo-acoustic insta-

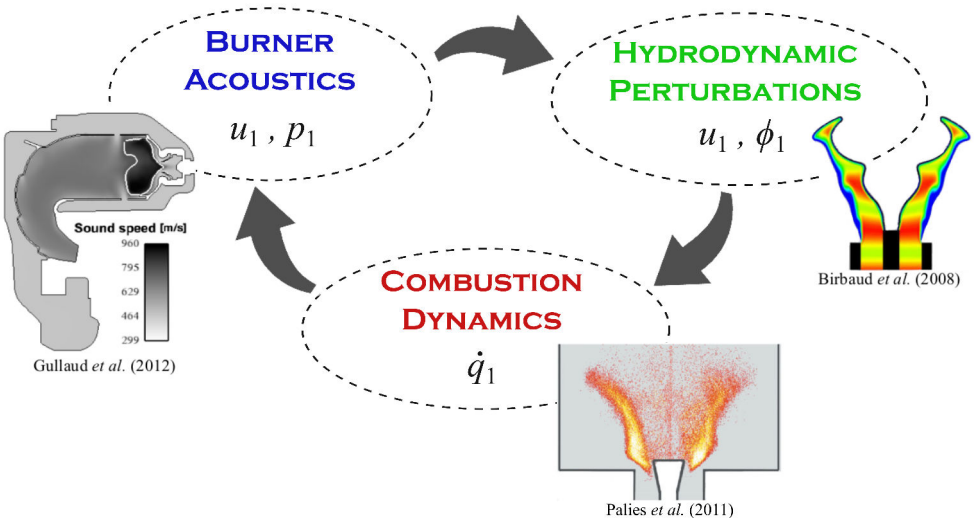

Figure 4: *Representation of the resonant coupling leading to thermo-acoustic instabilities. The acoustic waves are characterized by their velocity and pressure perturbations u_1, p_1 that satisfy the wave equation. Acoustic perturbations produce hydrodynamic perturbations u_1, ϕ_1. The unsteady combustion leads to delayed heat release rate perturbations $\dot{q}_1$ that act as a source term in the wave equation.*

bilities by taking into account the nonlinear response of these flames. This work builds on previous works by LeHelley (1994), Schuller (2003), Noiray (2007) and Boudy (2012). It extends a nonlinear stability analysis methodology recently developed to practical and complex 3D combustor geometries by using a numerical Helmholtz solver. This method is validated on a multipoint injection generic combustor featuring a collection of conical flames. The nonlinear dynamics of this configuration was thoroughly characterized by [Boudy (2012)]. The different linearly and nonlinearly unstable modes observed provide reference solutions to validate the numerical solver.

General background on thermo-acoustic instabilities

Thermo-acoustic instabilities have been identified in early investigations of sound produced by flames [Rayleigh (1878)]. Extensive reviews of this problem can be found in the monographs from Crocco and Cheng (1956), Putnam (1970) and Culick (2006), in more recent publications by Candel (1992), Candel (2002) and de Goey *et al.* (2011), in the books by Williams (1985) and Poinsot and Veynante (2012), or in a recent collection of articles edited by Lieuwen and Yang (2005). Early investigations on thermo-acoustic instabilities concerned liquid propellant rocket engines due to several spectacular failures [Crocco (1951); Tsien (1952); Crocco and Cheng (1956); Culick (2006)] but

the focus recently moved also towards gas turbines due to recurrent problems in LPP systems [Lieuwen and Yang (2005)]. These instabilities are the most damaging in confined combustion systems and are characterized by a resonant coupling between the combustor acoustics and the unsteady combustion (see Fig. 4). Acoustic waves that are propagating in the combustion chamber interact with the system boundaries and the shear layers, generating hydrodynamic perturbations in the flow. These perturbations can be either velocity, vortical or mixture composition disturbances [Ducruix *et al.* (2003)]. Together, these acoustic and hydrodynamic perturbations combine leading to flame unsteadiness, resulting in heat release rate perturbations that act as sound sources. If properly synchronized, these disturbances can couple and turn into resonance. A thermo-acoustic instability is often characterized by oscillations of the flow variables at a well-defined frequency that can range from a few Hertz to several thousands Hertz, depending on the size of the combustor and the type of coupling.

Rayleigh (1878) first looked into this phenomenon. He found that this resonant coupling occurs only when the flame is feeding energy back into the acoustic field, i.e. when pressure and heat release rate perturbations are in phase. This necessary condition reduces in a mathematical form to [Putnam (1970)]:

$$\int_{V_f} \int_0^T \dot{q}_1(t) p_1(t)\ dt dV > 0 \tag{1}$$

where $\dot{q}_1(t)$ stands for volumetric heat release rate perturbations, $p_1(t)$ for pressure perturbations, V_f for the flame volume and $T = 1/f$ for the period of the acoustic oscillations. A modern version may be derived from an acoustic energy budget that also takes into account acoustic losses at the boundaries due to sound radiation and non-ideal reflection [Candel (1992); Poinsot and Veynante (2012)]:

$$\frac{dE_1}{dt} = \int_0^T \left[\frac{\gamma - 1}{\gamma p_0} \int_{V_f} \dot{q}_1(t) p_1(t)\ dV - \int_{A_b} p_1(t) \mathbf{v_1}(t) \cdot \mathbf{n_b}\ dA \right] dt > 0 \tag{2}$$

where E_1 is the period-averaged acoustic energy in the combustor, A_b is the surface area of the system boundaries and $\mathbf{v_1}(t) \cdot \mathbf{n_b}$ is the normal acoustic velocity flux at the boundaries. Equations (1) and (2) give a necessary condition to trigger a thermo-acoustic instability, but these expressions do not provide any information on the coupling between combustion dynamics and acoustics, i.e. between $\dot{q}_1(t)$ and $p_1(t)$ (see Fig. 4). Modern analyses rely on a more detailed description of the system dynamics. They also aim at developing a better understanding of the flame dynamics and its coupling with the combustor acoustics, at designing new prediction methods for thermo-acoustic instabilities

and at developing passive or active control solutions to hinder these instabilities [Docquier and Candel (2002); Candel (2002); Richards *et al.* (2003); Dowling and Morgans (2005)] .

Prediction of thermo-acoustic instabilities

The prediction of thermo-acoustic instabilities is an active field of research [Candel (2002)]. Combustion chamber design methods still mainly rely on experimental tests. They are however costly and numerical methods become more affordable and more accurate. Recently, progress in numerical methods [Poinsot and Veynante (2012); Gicquel *et al.* (2012)] and computational resources lead to the generalization of the use of Large Eddy Simulations (LES) to simulate thermo-acoustic instabilities. LES codes solve the Navier-Stokes equations in reactive flows within complex combustor geometries. Only the large turbulent scales are simulated and the smaller ones are modeled using sub-grid models [Poinsot and Veynante (2012)]. These large scales are essential to reproduce the unsteady motions executed by the flame. Solver based on Reynolds Averaged Navier-Stokes (RANS) equations are not well adapted to reproduce flame unsteadiness. Direct Numerical Simulations (DNS) that solve all the scales can also be used in simple geometrical configurations, but they still require much too large computational resources to envisage calculations of practical configurations. LES simulations were successfully used to determine the flame response to flow perturbations in generic laminar configurations [Birbaud *et al.* (2008); Duchaine *et al.* (2011)]. Recent works also demonstrate that this type of simulation may be used to determine the flame response for a few forcing frequencies on practical configurations such as in a combustion chamber equipped with a single swirler [Giauque *et al.* (2005)] or in a full annular combustion chamber of an helicopter [Wolf *et al.* (2012)]. Using specific forcing signals, LES was recently shown to be able to capture the flame response over the whole frequency range of interest in a generic combustor equipped with a swirler [Tay-Wo-Chong *et al.* (2012)]. Simulations were also conducted to determine the stability of practical combustors with respect to thermo-acoustic oscillations [Roux *et al.* (2005); Selle *et al.* (2006)]. However, these calculations only yield information on a relatively limited set of flow and geometrical configurations due to the resources needed for each calculation. Therefore, the computational cost of the simulations still prohibits combustor design based on these numerical tools, even if progress is rapid.

For this purpose, low-order models and associated numerical tools were developed. These methods are generally based on the linearized Euler equations that allow to determine the acoustic eigenmodes of the combustor. Acoustics in reacting flows is ruled by a heterogeneous wave equation for the pressure perturbations p_1. Under the assumptions of low Mach number mean flow, non viscous flow and linear acoustics, this equation writes [Crighton *et al.* (1992);

Poinsot and Veynante (2012)]:

$$\nabla \cdot \left(\frac{1}{\rho_0} \nabla p_1 \right) - \frac{1}{\gamma p_0} \frac{\partial^2 p_1}{\partial t^2} = - \frac{\gamma - 1}{\gamma p_0} \frac{\partial \dot{q}_1}{\partial t} \tag{3}$$

where ρ_0 is the mean flow density that depends on the flow temperature and the gas composition, p_0 denote the mean flow pressure, p_1 is the pressure perturbations and $\dot{q}_1$ denote local heat release rate disturbances. Solutions of Eq. (3) may be determined using different numerical methods. They can be divided into two groups: time domain methods and frequency domain methods.

Low-order time domain simulations have been used for a long time to analyze the stability of liquid propellant rocket engines [Culick (2006)]. They rely on a Galerkin projection of the acoustic pressure perturbations on an orthogonal basis that is related to the system acoustic eigenmodes. Many early analyses used this description to examine nonlinear gas dynamics phenomena that are significant in the case of rocket engines [Culick (2006)]. The flame response to flow perturbation appearing in the right hand side of Eq. (3) is generally represented by a sensitive time lag model introduced by Crocco and Cheng (1956). Time domain methods were also examined to analyze thermo-acoustic instabilities in gas turbines. Nonlinear stability analyses in the time domain are carried out in order to fully take into account flame nonlinearities and interactions between unstable modes [Stow and Dowling (2009); Kashinath *et al.* (2012); Noiray and Schuermans (2012)], a feature that is difficult to describe with frequency domain methods. However, stability analyses in the frequency domain remain the most widely used approach.

Frequency domain methods generally rely on a separation of the different physical phenomena involved in thermo-acoustic instabilities (see Fig. 4). One may distinguish the burner acoustics from combustion dynamics and from acoustic-induced hydrodynamic perturbations. This separation is done by discriminating spatial zones following the characteristic wavelength of the dominant physical phenomenon present in that zone. The first region regroups the combustor ducts where only acoustic waves are propagating. Sound waves have a wavelength $\lambda_a = 2\pi c_0/\omega$ where ω is the angular frequency and c_0 is the speed of sound. In these regions of the flow, there is no flame, thus $\dot{q}_1(t) = 0$ and Eq. (3) reduces to the homogeneous wave equation. The second region of interest is the region of the flow where unsteady combustion and hydrodynamic perturbations take place. In this region, flow perturbations feature a much smaller length scale than λ_a and are related to hydrodynamic or chemistry length scales. Low-order models for thermo-acoustic instabilities have been developed in order to draw stability maps and design stable combustors [Sattelmayer and Polifke (2003)]. They are all based on a stability analysis that discriminates stable from unstable eigenmodes of the combustor. The three

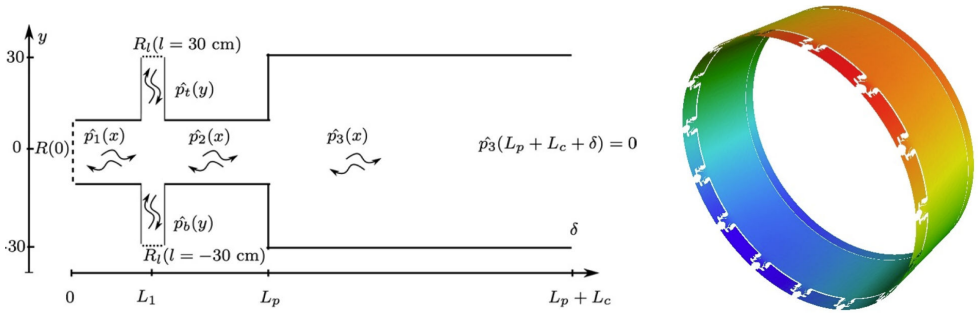

Figure 5: **(left)** *Acoustic network method applied to a two-cavity combustor with the feeding lines. Reproduced from Richecoeur* et al. *(2013).* **(right)** *First azimuthal mode in an annular chamber simulated with the Helmholtz solver AVSP. Reproduced from Sensiau (2008).*

different physical phenomena that need to be taken into account are described in the following sections.

Burner acoustics

In the frequency domain, the heterogeneous wave equation reduces to the Helmholtz equation:

$$\nabla \cdot \left(\frac{1}{\rho_0} \nabla \tilde{p}_1 \right) + \frac{\omega^2}{\gamma p_0} \tilde{p}_1 = i\omega \frac{\gamma - 1}{\gamma p_0} \tilde{q}_1 \tag{4}$$

where $\tilde{a}$ indicates the Fourier transform of a flow variable $a = \tilde{a} \exp(-i\omega t)$ at the angular frequency ω. This equation has to be coupled with relevant boundary conditions described by specific impedances:

$$Z(\omega) = \frac{\zeta(\omega)}{\zeta_0} = \frac{\widetilde{p_1}}{\rho_0 c_0 \widetilde{\mathbf{v}_1} \cdot \mathbf{n}} \tag{5}$$

where ω is the angular frequency, ρ_0 is the density and $\mathbf{n}$ is the unit vector normal to the boundary. These boundary conditions may be fixed by analytical expressions in a few cases. They may also be measured or determined numerically in more complex configurations [Lamarque and Poinsot (2008); Tran *et al.* (2009)].

Acoustic analysis in the frequency domain may be conducted analytically or numerically. Numerical integration of the Helmholtz equation Eq. (4) is now possible with solvers for 3D complex geometries. This integration is performed with either a finite element or a finite volume numerical method. These numerical tools can be used to determine the acoustic eigenmodes of the combustor

[Roux *et al.* (2005); Selle *et al.* (2006)] or more recently to perform linear stability analyses of the combustor [Nicoud *et al.* (2007); Camporeale *et al.* (2011)] (see Fig. 5-right). It was also recently used to perform a nonlinear stability analysis on a swirling flame combustor [Silva *et al.* (2013)] by including in the solver a nonlinear description of the flame response to flow perturbations. These numerical tools enable to take into account the spatial distribution of the heat release rate and thus to consider non-compact flames [Wolf *et al.* (2012)], to consider simulations with realistic speed of sound fields determined from LES or RANS simulations [Roux *et al.* (2005); Selle *et al.* (2006); Martin *et al.* (2006)] and more importantly, to perform stability analysis on practical configurations featuring complex 3D geometries [Wolf *et al.* (2012); Gullaud and Nicoud (2012)]. Linear stability analyses yield the eigenfrequency f and the growth rate ω_i for each mode investigated. Ultimately, the system stability may be determined by looking at the sign of the growth rate for each mode. This method is described in details in Chapter 7 of the present work.

The second type of method is based on a low-order representation of the combustor acoustics by using a network of compact elements which are interconnected [LeHelley (1994); Keller (1995); Hubbard and Dowling (1998); Lawn *et al.* (2004); Poinsot and Veynante (2012)]. The system is divided in a set of cavities including the plenum and the combustion chamber (see Fig. 5-left). The feeding lines can eventually be included in that description [Richecoeur *et al.* (2013)]. Acoustic waves are assumed to be propagating in each cavity at a constant speed of sound that depends on the cavity flow temperature. Volume flow rate and pressure continuity at the interface between cavities link the acoustic variables of each cavity. Inlet and outlet impedances are also necessary to obtain a closed system of equations. Unsteady combustion may also be included in this description. Unsteady heat release rate $\tilde{\dot{Q}}_1$ produces an acoustic volume source at the interface between the i^{th} and the $(i+1)^{\text{th}}$ cavities where compact combustion takes place:

$$S_{i+1}\tilde{v}_1(x_{i+1}) - S_i\tilde{v}_1(x_i) = \frac{\gamma - 1}{\rho_i c_i^2}\tilde{\dot{Q}}_1 \tag{6}$$

where S_i, ρ_i and c_i are the cross section area, density and speed of sound of the i^{th} cavity, and $\tilde{\dot{Q}}_1$ is the global heat release rate perturbation. The flame is thus considered compact with respect to the acoustic wavelength in this representation of the combustor acoustics. The resolution of this system of equations usually leads to an eigenvalue problem or to a dispersion relation $\mathcal{D}(\omega) = 0$ where $\mathcal{D}$ is the determinant of the system which is a function of the complex angular frequency $\omega = 2\pi f + i\omega_i$. Results of that dispersion relation give the eigenfrequencies f and the growth rates ω_i of the different eigenmodes of the system. This method was successfully applied to gas turbine combustors to retrieve the main frequencies of unstable modes and to determine

the combustor stability regions [Krebs *et al.* (2002); Schuermans *et al.* (2010)].

Combustion dynamics modeling

For both direct numerical integration of the Helmholtz equation and low-order representation of the combustor acoustics, heat release rate perturbations need to be prescribed in Eqs. (4) or (6). These perturbations constitute the driving source of instabilities. One objective of combustion dynamics studies is to characterize the flame response when submitted to flow perturbations in order to determine the delayed heat release rate fluctuation with respect to the input disturbances. Numerous experiments, numerical simulations and theoretical developments in simplified configurations have allowed to understand and to characterize the different physical mechanisms controlling the dynamics of laminar flames [Baillot *et al.* (1992); Baillot *et al.* (1996); Durox *et al.* (2005); Birbaud *et al.* (2006)] and swirled flames [Kulsheimer and Buchner (2002); Bellows *et al.* (2007); Kim *et al.* (2010); Palies *et al.* (2010)]. The flame frequency response to flow perturbations may be characterized by its Flame Transfer Function (FTF) that links the incoming perturbations to the resulting heat release rate perturbations. In the case of a perturbation of a field a, it is defined as:

$$\frac{\widetilde{\dot{Q}}_1}{\dot{Q}_0} = \mathcal{F}_a(\omega)\frac{\widetilde{a}_1}{a_0} \tag{7}$$

where a can be the velocity $a = v$ or the equivalence ratio $a = \phi$ for example. The flame response to equivalence ratio perturbations are difficult to characterize experimentally [Zimmer and Tachibana (2007); Schwarz *et al.* (2010); Kim *et al.* (2011)] but they can be studied numerically [Birbaud *et al.* (2008); Graham and Dowling (2011); Hemchandra (2012); Hermeth *et al.* (2013)] or theoretically [Hubbard and Dowling (2001); Cho and Lieuwen (2005); Shreekrishna *et al.* (2010)]. Regarding velocity perturbations, the FTF can be derived theoretically as revisited in Chapter 1. Semi-analytical models calibrated on experiments may be used as well. FTF can also be determined numerically based on unsteady RANS simulations [Armitage *et al.* (2006)], LES simulations [Giauque *et al.* (2005); Tay-Wo-Chong *et al.* (2012)] or level-set tracker simulations [Schuller *et al.* (2002); Preetham *et al.* (2007)]. For perfectly premixed flames, the FTF can be determined experimentally by measuring the heat release rate with the chemiluminescence emitted by the flame [Hurle *et al.* (1968)], and measuring the velocity perturbations by hot-wire or laser doppler anemometry [Ducruix *et al.* (2000); Hirsch *et al.* (2005); Kim *et al.* (2010)]. Due to the limited optical access on many combustor, this experimental determination is however more difficult in practical configurations. Alternatively, purely acoustic methods can be applied to determine the flame

frequency response. The Transfer Matrix (TM) is defined by [Polifke *et al.* (2001); Paschereit *et al.* (2002); Schreel *et al.* (2002)]:

$$\begin{pmatrix} \tilde{p}_{1d} \\ \tilde{u}_{1d} \end{pmatrix} = T \begin{pmatrix} \tilde{p}_{1u} \\ \tilde{u}_{1u} \end{pmatrix} = \begin{pmatrix} T_{11} & T_{12} \\ T_{21} & T_{22} \end{pmatrix} \begin{pmatrix} \tilde{p}_{1u} \\ \tilde{u}_{1u} \end{pmatrix} \tag{8}$$

where $\tilde{p}_{1d}$ and $\tilde{u}_{1d}$ (resp. $\tilde{p}_{1u}$ and $\tilde{u}_{1u}$) are the acoustic pressure and velocity perturbations at a location downstream of the flame (resp. upstream of the flame). For a compact flame and under the assumption of a low Mach number flow in the fresh and hot gas streams, the matrix elements reduce to: $T_{11} = 1$, $T_{12} = T_{21} = 0$ and $T_{22} = 1 + (T_2/T_1 - 1)\mathcal{F}(\omega)$ where T_2 is the burnt gas temperature, T_1 is the fresh gas temperature and $\mathcal{F}(\omega)$ is the FTF. In this case, the determination of the TM reduces to the determination of the link between upstream and downstream velocity perturbations. Both TM and FTF determination methods have advantages and drawbacks. On one hand, the FTF is difficult to determine for non-perfectly premixed flames because the heat release rate is no longer directly proportional to some chemiluminescent radical emitted by the flame in these cases. The TM solely relies on acoustic measurements and may in principle be used to determine the flame response in non-premixed combustion regimes. The TM method requires however that the microphones are set close to the flame region [Truffin and Poinsot (2005)] and that the flame is not too sensitive to a modification of the combustor acoustics on upstream and downstream sides of the combustor. For non-compact flames, it is easier to handle the FTF that can take into account the spatial distribution of the flame response [Kim *et al.* (2010)].

The FTF represents the flame frequency response to vanishingly small acoustic perturbations. Methods based on the FTF allow to predict linearly unstable modes but they fail to describe the evolution of the system up to the limit cycle in the nonlinear regime. In the case of gas turbines, the relative pressure perturbation oscillation level $|p_1/p_0|$ is usually less than 10%. Propagation of acoustic waves thus remain largely linear while the combustion dynamics constitutes the main source of nonlinearity in the system [Dowling (1997); Bourehla and Baillot (1998); Lieuwen and Neumeier (2002); Balachandran *et al.* (2005); Bellows *et al.* (2007); Durox *et al.* (2009)]. To overcome that issue, the FTF concept has been extended to take into account nonlinearities and lead to the concept of Flame Describing Function (FDF) [Dowling (1997); Noiray *et al.* (2008); Palies *et al.* (2011); Boudy *et al.* (2011); Schimek *et al.* (2011)]. When considering velocity perturbations, the FDF is defined as a set of flame frequency response gathered for different perturbation levels $|v_1/v_0|$. The FDF is thus a function of the frequency and the perturbation amplitude:

$$\mathcal{F}(\omega, |v_1/v_0|) = G(\omega, |v_1/v_0|)e^{i\varphi(\omega,|v_1/v_0|)} = \frac{\widetilde{\dot{Q}}_1/\dot{Q}_0}{\widetilde{v}_1/v_0} \tag{9}$$

This nonlinear description of the flame response was used to conduct stability analyses with analytical [Noiray *et al.* (2008); Boudy *et al.* (2011); Palies *et al.* (2011)] or numerical [Silva *et al.* (2013)] tools. They can be used to investigate the system evolution up to the limit cycle and to predict both the limit cycle amplitude and frequency. They were also shown to retrieve some nonlinear phenomena such as mode switching, mode triggering and hysteresis phenomena [Noiray *et al.* (2008)].

Acoustic-induced hydrodynamic perturbations

FTF and FDF are used to link heat release rate perturbations to acoustic velocity modulations. However, the link between these quantities is generally not direct. Heat release rate disturbances produced by acoustic fluctuations often involve numerous physical mechanisms, especially in complex turbulent flows. In order to understand the mechanisms that drive the flame dynamics, it is important to look into some hydrodynamic and heat transfer unsteady phenomena that are triggered by the acoustic waves and that modify greatly the flame dynamics. Figure 6 shows four examples where a mode conversion is taking place and where acoustic waves are generating hydrodynamic perturbations, i.e. perturbations that are transported by the mean flow:

(a) In the case of V-shaped flames, acoustic waves can excite the shear layers behind the injection unit [Birbaud *et al.* (2007b)] and thus trigger the shedding of vortices that roll up the flame front [Schuller (2003); Durox *et al.* (2005); Bellows *et al.* (2007)]. Vortical structures are convected in the fresh gas zone from the burner lip to the flame front. These perturbations generate strong flame front deformations and heat release rate perturbations that can drive thermo-acoustic instabilities [Poinsot *et al.* (1987)].

(b) In the case of swirled flames, the interaction between incoming acoustic waves and the swirler yields an azimuthal vorticity wave that is convected at the mean flow speed towards the flame and modifies its dynamics [Hirsch *et al.* (2005); Komarek and Polifke (2010); Palies *et al.* (2010); Palies *et al.* (2011)].

(c) Unsteady heat loss can drive unsteady flame-wall interactions when the flame anchoring regions lies close to solid components of the burner or when the flame tail is stabilized close to the combustion chamber walls. These interactions produce enthalpy perturbations that are convected by the mean flow and generate heat release rate disturbances [Joulin (1982); McIntosh and Clarke (1984); Rook *et al.* (2002); de Goey *et al.* (2011)].

(d) In combustion systems where the reactants are not premixed far ahead of the combustion chamber, acoustic waves can interact with the air or fuel

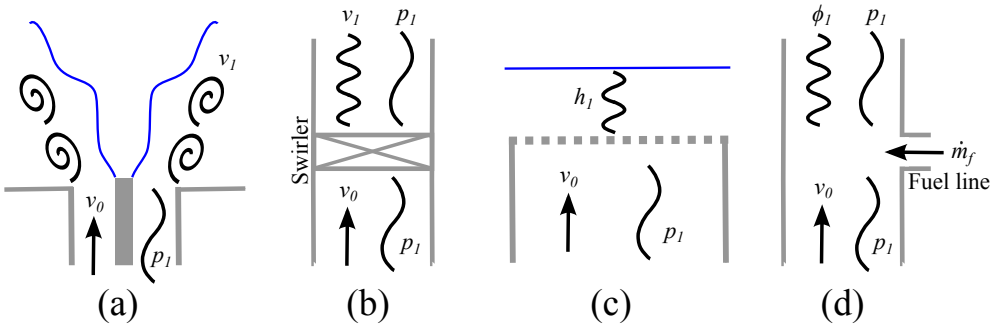

Figure 6: *(a) Vortices are generated in the shear layer above the burner exit by the acoustic perturbations (b) Transverse hydrodynamic velocity perturbations v_1 are generated at a swirler submitted to acoustic perturbations. (c) Enthalpy perturbations h_1 are generated when acoustic perturbations induce a motion of a planar flame stabilized above a porous burner. (d) Equivalence ratio perturbations ϕ_1 are generated when a fuel line (with a fuel mass flow rate $\dot{m}_f$) is submitted to acoustic perturbations.*

feeding lines and produce fluctuations of the mixture composition. Equivalence ratio fluctuations are convected at the mean flow speed towards the flame front. They have a significant impact on thermo-acoustic instabilities [Baade (1978); Keller (1995); Lieuwen and Zinn (1998)] by modifying the flame burning rate and the flame surface area. These perturbations may produce large heat release rate perturbations [Hubbard and Dowling (2001)].

These phenomena were identified in numerous experiments and are known to induce strong flame disturbances that may alter greatly the thermo-acoustic coupling. From a practical point of view, these hydrodynamic perturbations are generally taken into account in the system modeling by including them in the flame frequency response. This is usually done by determining the FTF with a velocity signal measured at a location ahead of any hydrodynamic perturbation, where only acoustic perturbations are present.

Although considerable work has already been conducted on thermo-acoustic instabilities, much remains to be investigated in order to design better predictive tools. This thesis aims at tackling some of the remaining problems, as described in the next section.

Thesis objectives and contents

This Ph.D. thesis was funded by the European Community Seventh Framework Programme (FP7/2007-2013) via the KIAI project.

The objectives of KIAI (Knowledge for Ignition, Acoustics and Instabilities, see www.kiai-project.eu/ for further details) consist in providing reliable low NO_x methodologies for combustors to predict their stability and their ignition process from spark to annular combustor. When used at an early stage in the conception cycle of low NO_x combustors, KIAI CFD methodologies will play a key role and considerably accelerate the delivery process of lean combustion technology. The objective of KIAI is to reach the 80% NO_x emissions reduction required for introduction into service before 2020 with a proven capability and the necessary reliability, safety and economical viability.

KIAI focuses on a better understanding and prediction of unsteady phenomena caused by low NO_x technologies which are not yet fully controlled or predictable. Therefore, the scientific objectives of this Ph.D. in the Work Packages 2.1 and 2.3 in the KIAI project are to:

- Develop the determination and the modeling of the FTF.

- Validate the FDF methodology on a generic confined configuration.

KIAI is a European funded research programme involving 18 partner organizations from major European engine manufactures, universities, research institutes and companies from the combustion area. KIAI was launched in May 2009 for duration of 4 years under the leadership of Snecma.

Flame dynamics (Parts I)

An extensive review on laminar flame dynamics and FTF modeling is first carried out in Chapter 1. Early FTF models and modern analytical techniques based on level-set descriptions of the flame motion (G-equation) are revisited. The work then focuses on premixed inclined flames submitted to acoustic perturbations. A general expression of the FTF is derived as a function of the velocity perturbations in the fresh stream and the flame base motion. Different physical mechanisms are then reviewed including kinematic effects, flame base motion, heat loss to the burner rim, stretch effects, collective flame effects and nonlinearities of the flame response to flow perturbations. A discussion is carried out to highlight the remaining challenges concerning flame dynamics modeling.

In Chapter 2, the experimental setup used in this work is presented. This description includes the burner geometry, the actuation system and the diag-

nostics used to measure the velocity and the heat release rate. The system used to record flame images is also described.

Finally, two experimental methods for FTF determination are examined in Chapter 3. FTF are first determined using harmonic velocity perturbations. Then, a method is presented to create random velocity perturbations with a nearly white noise spectrum at the burner outlet. Cross-correlation and system identification methods are described and used to determine the FTF with random velocity perturbations. Comparisons between harmonic and random perturbation techniques are carried out for different perturbation levels. The influence of the number of coefficients used to determine the FTF with the system identification technique is also studied in the last section of the chapter.

Flame Transfer Function modeling (Parts II)

The next three chapters constitute the second part of this manuscript. They deal with premixed conical flame dynamics and the developments made to obtain an improved description of their FTF. Chapter 4 concerns the velocity perturbation field that needs to be modeled to solve the G-equation. A model featuring incompressible convected perturbations is used to derive a new expression for the flame front perturbations and the FTF. It is compared with previously derived models and experimental data. This improved FTF model yields a better match with measurements, especially concerning the FTF phase lag in the low and intermediate frequency ranges. An axially decaying velocity perturbation model is also considered and shows great improvements on the FTF gain prediction. Finally, the same study is carried out in the time domain to derive the unit impulse response of a conical premixed flame.

A second contribution to the FTF, related to the flame base motion, is derived in Chapter 5. Flame front disturbances at the flame base are convected along the steady flame front and produce additionnal heat release rate perturbations. It is shown that the flame base motion results from the incoming acoustic velocity perturbations. Heat loss to the burner rim is modeled to retrieve the flame base displacement frequency response. This model relies on enthalpy perturbations that propagate from the burner rim to the flame front. Predictions are compared to measurements in terms of flame base motion frequency response and FTF. This contribution controls the high frequency behavior of the FTF. By combining this contribution to that of velocity disturbances, it is possible to explain the nonlinear behavior of the FTF of a premixed conical flame submitted to acoustic perturbations. The nonlinear response is controlled by a modification in the relative magnitude of the two contributions (from velocity disturbances and from flame base oscillations) to the FTF.

Finally, the case of a confined conical flame is considered in Chapter 6. An experimental investigation shows that the FTF of these flames is stretched to higher frequencies when the burnt gases cannot fully expand. The flame

response features in these cases large differences compared to unconfined flames. These differences are explained by a change in the mean time lag between heat release rate and velocity disturbances due to changes taking place in the fresh reactant steady velocity field. These modifications are modeled and are used to explain the changes observed on the steady flame shape when the flame is confined. It is then shown how to take this phenomenon into account to characterize the FTF of flames that are confined by different flame tubes, using a new dimensionless reduced frequency. These different models are then combined to explore the response of small premixed conical flames stabilized on a perforated plate. It is shown that this frequency response to acoustic disturbances may be fairly well captured.

Thermo-acoustic instability predictions (Part III)

This last part deals with the prediction of thermo-acoustic instabilities by performing a nonlinear stability analysis. A combination of the Flame Describing Function (FDF) methodology and the numerical Helmholtz solver AVSP developed by CERFACS and Université Montpellier II is used to determine the nonlinear dynamics of the combustor studied by Boudy (2012). In Chapter 7, the nonlinear stability analysis method based on the FDF methodology is first described. The method considers a FDF that is a set of FTF determined for different perturbation levels. Successive stability analyses are carried out for each FTF, i.e. for each perturbation level. These calculations yield the eigenfrequencies and the growth rates associated to the eigenmodes of the system as a function of the perturbation level. This method is coupled to the Helmholtz solver AVSP which is briefly described. This numerical tool allows to solve the Helmholtz equation over 3D combustor geometries with relevant complex boundary conditions and unsteady combustion effects.

The coupled FDF/AVSP methodology is carried out in Chapter 8 on a generic configuration featuring two cavities and a flame anchored on a perforated plate. The experimental configuration is first presented. The numerical setup is then introduced along with the boundary conditions and the FDF used for the stability analysis. The acoustic eigenmodes are computed and predictions are compared to measurements. A nonlinear stability analysis is then carried out for different cases depending on the length of the feeding manifold. First cases feature linearly unstable modes that reach limit cycle as the perturbation level is increased. Other cases considered feature linearly and nonlinearly unstable modes that interact and lead to a mode switching phenomena. It is shown that the numerical solver may be use to reproduce this phenomena.

Part I

Conical flame dynamics

Chapter 1

Combustion dynamics modeling

The dynamics of premixed flames submitted to acoustic perturbations is a central issue for the prediction of thermo-acoustic instabilities. As such, the case of premixed laminar flames and their Flame Transfer Function (FTF) have been extensively studied both theoretically and experimentally, and only recently numerically. This chapter aims at providing an overview of the different models describing the response of conical premixed flames to flow perturbations. Some remaining issues are identified and are tackled later in the following chapters.

1.1 Introduction

The flame response to flow perturbations is often characterized by its Flame Transfer Function (FTF). For perfectly premixed flames kept at constant equivalence ratio, the FTF is defined as the linear relationship between dimensionless harmonic heat release rate perturbations and dimensionless incoming velocity modulations at some location upstream of the flame front [Blackshear (1953); Merk (1957); Matsui (1981); Ducruix *et al.* (2003); Truffin and Poinsot (2005)]. At this point, it is necessary to define the notations in order to clarify this review. The following notation convention will be used all over the manuscript. Harmonic time varying quantities are considered in the form $a(\mathbf{x},t) = a_0 + \tilde{a}_1(\mathbf{x})\exp(-i\omega t)$, where a is a flow quantity and ω the angular frequency. All FTF analytical expressions presented in this chapter are written with this convention even though some expressions were originally derived by considering harmonic perturbations of the form $\exp(i\omega t)$. Subscripts 0 and 1 respectively refer to the steady state and to first-order perturbations. The Fourier transform of the perturbation $a_1(\mathbf{x},t)$ examined at the angular frequency ω is noted $\tilde{a}_1(\mathbf{x})$. Using these conventions the FTF can be written as:

$$\frac{\tilde{\dot{Q}}_1}{\dot{Q}_0} = F(\omega)\frac{\tilde{v}_1}{v_0}(\mathbf{x}_{\text{ref}}) \tag{1.1}$$

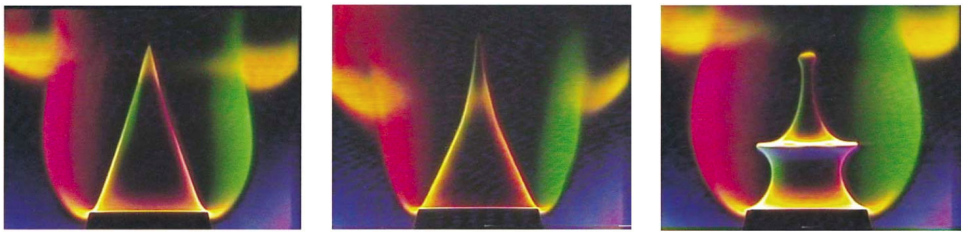

Figure 1.1: *Three color Schlieren images of CH_4/air conical flames.* **(left)** *Steady flame for $v_0 = 0.96\ m.s^{-1}$ and $\phi = 0.95$.* **(center)** *Perturbed flame at $f = 25\ Hz$.* **(right)** *Perturbed flame at $f = 75\ Hz$. Reproduced from Ducruix et al. (2000).*

where $\widetilde{\dot{Q}_1/\dot{Q}_0}$ is the delayed relative heat release rate perturbation and $\tilde{v}_1/v_0$ denotes the relative velocity fluctuation at a reference point $\mathbf{x}_{\text{ref}}$ that is usually taken at the injection outlet. The FTF is a complex function $F(\omega) = G(\omega)\exp(i\varphi(\omega))$ where the gain $G(\omega)$ and the phase lag $\varphi(\omega)$ depend on frequency, mean flow properties [Mehta *et al.* (2005); Durox *et al.* (2009)], combustor geometry [Duchaine *et al.* (2011); Tay-Wo-Chong and Polifke (2012)], heat fluxes at the walls [Rook and de Goey (2003); Duchaine *et al.* (2011); Tay-Wo-Chong and Polifke (2012)] and flame shape [Durox *et al.* (2009)]. This expression is also generally a function of the modulation level [Dowling (1997); Noiray *et al.* (2008); Durox *et al.* (2009)].

Early work in rocket engine instabilities established a link between pressure and heat release rate fluctuations using a time lag model. Based on causality arguments, Crocco (1951) proposed to link these two quantities by an interaction index n and a time lag τ. The same type of model may be used to link heat release rate and velocity disturbances. A velocity perturbation v_1 produces a perturbation of the heat release rate $\dot{Q}_1$ after a certain time lag τ and the coefficient n characterizes the strength of this coupling. In the time domain, it leads to the following phenomenological relation:

$$\frac{\tilde{\dot{Q}}_1(t)}{\dot{Q}_0} = n\frac{\tilde{v}_1(\mathbf{x}_{\text{ref}}, t-\tau)}{v_0} \tag{1.2}$$

The corresponding FTF in the frequency domain writes:

$$F(\omega) = ne^{i\omega\tau} \tag{1.3}$$

Expressions for the parameters n and τ are often based on semi-empirical formulations using a wide range of parameters [Tsien (1952); Crocco and Cheng (1956)]. The quality of the model predictions depends strongly on the guess of the main physical mechanisms controlling the flame response to incoming disturbances.

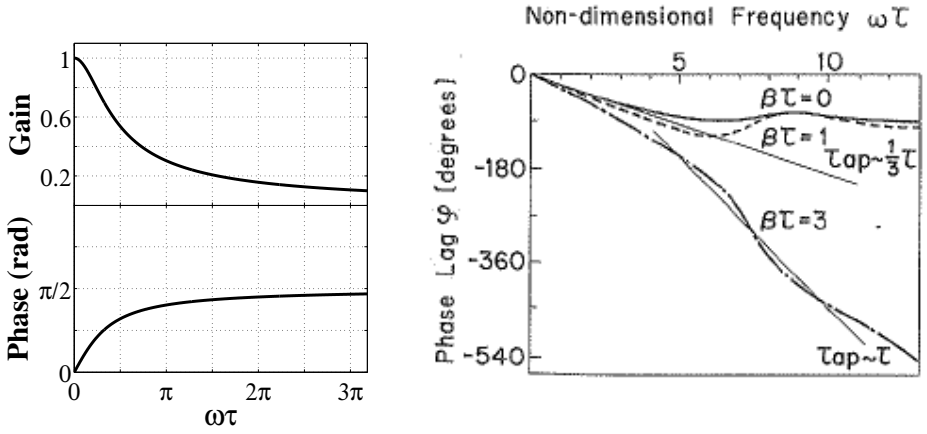

Figure 1.2: (left) *FTF gain and phase lag from Eq. (1.4) as a function of the dimensionless frequency $\omega\tau$.* **(right)** *Phase of the FTF as a function of the dimensionless frequency $\omega\tau$, plotted for different values of $\beta\tau$ (see Eq. (1.7)) [Sugimoto and Matsui (1982)]. The FTF phase lag decreases because the "$\exp(i\omega t)$" convention was adopted in this article.*

The response of conical flames to flow perturbations was thoroughly investigated. Figure 1.1 shows the shape taken by the flame when submitted to acoustic excitation. It is interesting to start by examining early descriptions of the corresponding FTF. First theoretical attempts to derive exact expressions for the n-τ parameters were conducted by Blackshear (1953) and Merk (1957) for laminar premixed conical flames. These authors obtained the following FTF for an axisymmetric conical flame:

$$F(\omega) = \frac{1 + i\omega\tau}{1 + (\omega\tau)^2} \tag{1.4}$$

where:

$$\tau = \frac{R}{3S_L}\left[1 - \left(\frac{S_L}{v_0}\right)^2\right]^{-\frac{1}{2}} = \frac{1}{3}\frac{R}{S_L \cos\alpha} \tag{1.5}$$

In these expressions, R is the injection tube radius, $\alpha = \arcsin(S_L/v_0)$ is the flame tip half-angle and S_L is the laminar burning velocity. The gain and phase lag of this FTF model are plotted in Fig. 1.2-left. The gain is a low-pass filter and the phase increases up to $\omega\tau = \pi/2$ before saturating around $\varphi = \pi/2$. Experiments show however that the validity of this model is limited to very low frequencies and does not cover the entire useful frequency range for instability purpose [Ducruix *et al.* (2000)]. It is however worth noting that the time lag τ in Eq. (1.5) is a function of the burner outlet radius, laminar burning velocity

and the flame aspect ratio.

Later, an experimental and theoretical investigation of the conical flame dynamics was performed by Matsui (1981) and Sugimoto and Matsui (1982). These authors measured the FTF of a conical flame and found that the FTF phase lag features a regular increase with frequency at low and intermediate frequencies before a phase saturation estimated around $\varphi \simeq \pi/2$. The gain curve was shown to behave like a low-pass filter with values above unity at low frequencies and a jagged behavior at higher frequencies. Thanks to LDV measurements, these authors found that velocity disturbances in the fresh reactant stream are convected at a speed close to the mean flow velocity. A model for the FTF was proposed assuming that the fluctuations of the CH^* emission per unit area $i_1(y,t)$ are convected at a constant velocity U_i and grow exponentially along the steady flame front with a growth rate σ:

$$i_1(y,t) = i_1^0 \; e^{\sigma y} \; e^{-i\omega(t-y/U_i)} \tag{1.6}$$

Sugimoto and Matsui (1982) derived the following expression for the FTF:

$$F(\omega) = \frac{2}{(i\omega+\beta)^2\tau_1^2}\left[-1-(i\omega+\beta)\tau_1 + e^{(i\omega+\beta)\tau_1}\right] \tag{1.7}$$

where $\beta = \sigma U_i$ and $\tau_1 = H/U_i$ is a time lag with $H = R/\tan\alpha$ being the steady flame height. This model was shown to match their experimental data when τ_1 was taken equal to 13 ms and when the quantity $\beta = \sigma U_i$ was modified by assuming linearly increasing values for $f < 50$ Hz and constant values for $f \geq 50$ Hz. In particular, the authors showed that the FTF phase slope scaled with $H/(3v_0)$ in the low frequency range (where $\beta\tau_1 = \sigma U_i \tau_1 \simeq 0$) and with H/v_0 for higher frequencies (where $\beta\tau_1 = \sigma U_i \tau_1 \simeq 3$) as indicated by Fig 1.2-right.

In this early description, the flame front wrinkles were prescribed from experimental observations. To overcome that issue, modern theoretical developments use a level-set description to model the flame front kinematic response to flow perturbations.

1.2 Level-set description of flame wrinkling

1.2.1 Transport equation for flame wrinkles

The following theoretical developments will make use of the G-equation to estimate flame front disturbances and resulting flame surface area perturbations. The flame front is here considered as an infinitely thin interface separating

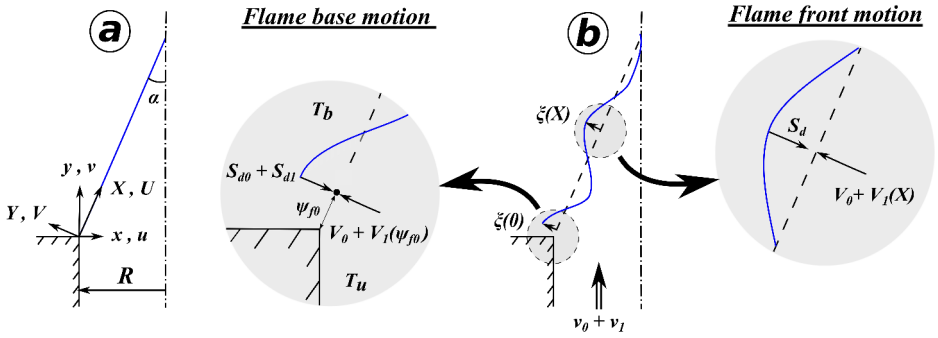

Figure 1.3: *Schematic of the configuration investigated. (a) Steady conical flame along with the different frames used in this chapter. (b) Acoustically perturbed conical flame, with a focus on the flame base region and the flame front displacement far from the burner lip.*

fresh and burnt gases. This interface is modeled by a scalar function G so that $G(\mathbf{x}, t) = 0$ at the interface. Considering a constant flame speed S_d, the G-equation is expressed as [Markstein *et al.* (1964); Williams (1985)]:

$$\frac{\partial G}{\partial t} + \mathbf{v}.\nabla G = S_d|\nabla G| \tag{1.8}$$

The steady flow field is here assumed to be axial and uniform. The flow velocity is equal to a constant value v_0. Changes in the mean flow properties will be tackled later in Chap. 6. We will further assume vanishingly velocity perturbations compared to the mean flow velocity. The perturbed flow field in the burner frame writes:

$$\mathbf{v}(\mathbf{x}, t) = u_1(\mathbf{x}, t)\mathbf{e_x} + (v_0 + v_1(\mathbf{x}, t))\mathbf{e_y} \tag{1.9}$$

In the frame attached to the steady flame front, this perturbed flow field has two components (see Fig. 1.3-a):

$$\mathbf{V}(\mathbf{X}, t) = [U_0 + U_1(\mathbf{X}, t)]\,\mathbf{e_X} + [V_0 + V_1(\mathbf{X}, t)]\,\mathbf{e_Y} \tag{1.10}$$

where $U_0 = v_0 \cos\alpha$ is the mean flow velocity component tangential to the flame front, $V_0 = v_0 \sin\alpha$ is the mean flow velocity component normal to the flame front and α is the flame tip half-angle.
In this case, the G-equation expressed in the frame attached to the steady conical flame position reduces to [Boyer and Quinard (1990); Schuller *et al.* (2003a)]:

$$\frac{\partial \xi}{\partial t} + U_0 \frac{\partial \xi}{\partial X} = V_1(X, t) \tag{1.11}$$

where $\xi(X,t) = \tilde{\xi}(X)e^{-i\omega t}$ is the harmonic perturbation of the flame front position in the normal direction with respect to its steady position and $V_1(X,t)$ is the velocity perturbation component normal to the steady flame front and taken at the flame front i.e. along the axis $Y = 0$ in Fig. 1.3. The solution of this partial derivative equation can be found with the characteristics method [Baillot *et al.* (1992); Baillot *et al.* (1996)] or can be given by the following telegraph integral [Boyer and Quinard (1990); Schuller *et al.* (2003a); Preetham and Lieuwen (2004)]:

$$\xi(X,t) = \frac{1}{U_0}\int_0^X V_1\left(X', t - \frac{X - X'}{U_0}\right)dX' + \xi\left(0, t - \frac{X}{U_0}\right) \tag{1.12}$$

In the frequency domain, it leads to:

$$\tilde{\xi}(X) = \frac{e^{iKX}}{U_0}\int_0^X \tilde{V}_1(X')e^{-iKX'}dX' + \tilde{\xi}(0)e^{iKX} \tag{1.13}$$

where $K = \omega/U_0$ is the wave number associated to the convection of the flame wrinkles along the steady flame front and $\tilde{\xi}(0)$ is the flame front displacement amplitude at the flame base, i.e. at $X = 0$ (see Fig. 1.3).
Equation (1.13) exhibits two main contributions to flame wrinkling. The first contribution results from the velocity perturbation component that is normal to the steady flame front in the fresh stream, which is acting as a forcing term in Eq. (1.11). The second contribution results from the flame base motion at $X = 0$ that produces perturbations convected along the steady flame front.

1.2.2 Flame surface area perturbations

Flame wrinkles must be integrated over the flame surface area to determine the corresponding heat release rate perturbations. This integration is carried out in the frame associated to the steady flame front:

$$A = A_0 + \tilde{A}_1 e^{-i\omega t} = \int_0^L dA = \int_0^L 2\pi r(X)dl \tag{1.14}$$

where dA is an infinitesimal flame surface area ring, dl is the infinetisimal flame front length, $L = R/\sin\alpha$ is the steady flame front length and $r(X)$ is the unsteady local flame front radius.
The steady axisymmetric flame surface area is given by:

$$A_0 = \int_0^L 2\pi(R - X\sin\alpha)dX = \frac{\pi R^2}{\sin\alpha} \tag{1.15}$$

Perturbations in both the local flame front radius and infinitesimal flame element need to be taken into account up to the first order:

$$r(X) = r_0(X) + \tilde{r}_1(X)e^{-i\omega t} = (R - X\sin\alpha) + \tilde{\xi}(X)\cos\alpha e^{-i\omega t} \tag{1.16}$$

$$dl = \left[dX^2 + d\xi^2\right]^{1/2} = \left[1 + \left(\frac{d\xi}{dX}\right)^2\right]^{1/2} dX \simeq dX \tag{1.17}$$

The perturbed flame surface area contribution to Eq. 1.14 then reduces to

$$\tilde{A}_1 = \int_0^L 2\pi\cos\alpha\tilde{\xi}(X)dX \tag{1.18}$$

The corresponding dimensionless flame surface area perturbations may be deduced:

$$\frac{\tilde{A}_1}{A_0} = \frac{2\cos\alpha\sin\alpha}{R^2}\int_0^L \tilde{\xi}(X)dX \tag{1.19}$$

It is well known that, in the case of premixed flames and in the absence of mixture composition inhomogeneities, the flame surface area is proportional to the heat release rate [Hurle *et al.* (1968)]. One may thus write:

$$\frac{\tilde{A}_1}{A_0} = \frac{\tilde{\dot{Q}}_1}{\dot{Q}_0} \tag{1.20}$$

The two contributions to flame wrinkling identified in Eq. (1.12) may also be separated when examining flame surface area perturbations. It is thus interesting to expand the FTF as the sum of these two contributions:

$$F(\omega) = \frac{\tilde{\dot{Q}}_1/\dot{Q}_0}{\tilde{v}_1/v_0} = F_A(\omega) + F_B(\omega) \tag{1.21}$$

where $\dot{Q} = \dot{Q}_0 + \dot{Q}_1$ is the heat release rate. The first component F_A stands for the velocity contribution to the FTF and the second component F_B stands for the contribution from the flame base motion.
This last equation shows that both the perturbed velocity field and the anchoring point dynamics need to be determined to capture the FTF of conical premixed flames submitted to acoustic perturbations. Several studies over the years have looked into these mechanisms. The main conclusions are synthesized in the next section.

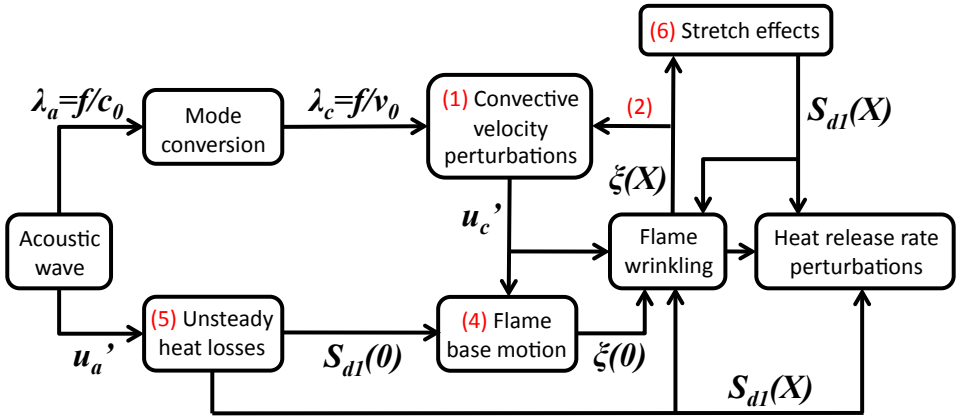

Figure 1.4: *Mechanisms contributing to the conical flame dynamics when submitted to acoustic perturbations.* u'_a*: acoustic velocity perturbations of wavelength* λ_a*.* u'_c*: convective velocity perturbations of wavelength* λ_c*.* $S_{d1}(X)$*: flame speed disturbances.* $\xi(X)$*: flame front wrinkle.* $X = 0$*: flame base location. Red numbers in between parentheses refer to the mechanisms listed in Section 1.3 below.*

1.3 FTF modeling related to acoustic perturbations

The level-set description of flame front motion has motivated rapid developments to fill the gap between theory and experiments. Numerous phenomena were experimentally explored and analytical models were developed. The main ones are listed below:

(1) Effects of the type of velocity perturbation impinging the flame [Baillot *et al.* (1992); Baillot *et al.* (1996); Schuller *et al.* (2002); Schuller *et al.* (2003a); Preetham and Lieuwen (2004)],
(2) The flame feedback upon the perturbed flow field [Birbaud *et al.* (2006)],
(3) Effects induced by exothermicity and confinement of the burnt gases [Mehta *et al.* (2005); Birbaud *et al.* (2007a)],
(4) The dynamics of the anchoring point [Kornilov *et al.* (2007); Karimi *et al.* (2009); Shin and Lieuwen (2012)]
(5) Unsteady heat loss to the burner rim [Rook *et al.* (2002); Schreel *et al.* (2002); Rook and de Goey (2003); Altay *et al.* (2009); Kedia *et al.* (2011)],
(6) Stretch effects [Wang *et al.* (2009); Preetham *et al.* (2010); Shin and Lieuwen (2012)],
(7) Time domain representation of the flame response [Blumenthal *et al.* (2013)],
(8) Multiple flame effects [Kornilov *et al.* (2009); Duchaine *et al.* (2011)],
(9) Nonlinear effects [Schuller *et al.* (2002); Lieuwen (2005); Preetham *et al.* (2008)].

Each of these mechanisms is examined in the following sections. Figure 1.4 gives a block diagram highlighting the main interactions for an unconfined premixed conical flame submitted to small amplitude disturbances.

(1) Flow perturbations

Depending on the type of flow perturbation imposed in the fresh stream, the flame executes a different motion. Fleifil *et al.* (1996) used a kinematic description of the perturbed flame front motion to determine the FTF of conical flames submitted to axial and uniform disturbances in the fresh reactants:

$$\widetilde{u}_1 = 0 \tag{1.22}$$
$$\widetilde{v}_1 = v_1 \tag{1.23}$$

These authors derived an expression for the FTF for elongated conical flames stabilized in a Poiseuille flow. They found that the FTF may be expressed in terms of a single dimensionless number corresponding to a reduced frequency or a Strouhal number $\mathrm{St} = \omega R/S_L$, where S_L is the laminar burning velocity and R the burner radius. The generalization of this model to a flame stabilized in a uniform steady flow featuring an arbitrary flame angle with respect to the flow direction was conducted by Ducruix *et al.* (2000). In this case, the FTF depends only on the reduced frequency $\omega_* = \omega R/(S_L \cos\alpha)$, where α is the flame tip half-angle:

$$F_A(\omega_*) = \frac{2}{\omega_*^2}(1 - \exp(i\omega_*) + i\omega_*) \tag{1.24}$$

It is interesting to notice that this model corresponds to the model by Sugimoto and Matsui (1982) if one takes $\sigma = 0$ and $U_i = v_0 \cos^2\alpha$ in Eq. (1.7). In this case, U_i is the steady velocity component tangential to the flame front, projected on the burner axis. Experiments from Ducruix *et al.* (2000) conducted with large and small tip half-angle conical flames show a good collapse of data with predictions for the gain of the FTF, but the model rapidly fails in predicting the FTF phase lag for increasing frequencies (see Fig. 1.5-left). A FTF model that retrieves a regular phase increase was proposed by Schuller *et al.* (2003a). It is based on experimental observations that velocity perturbations in the fresh reactant stream are not uniform, but are convected by the mean flow [Sugimoto and Matsui (1982); Baillot *et al.* (1992); Baillot *et al.* (1996)] with a wavenumber $k = \omega/v_0$:

$$\widetilde{u}_1 = 0 \tag{1.25}$$
$$\widetilde{v}_1 = v_1 \exp(iky) \tag{1.26}$$

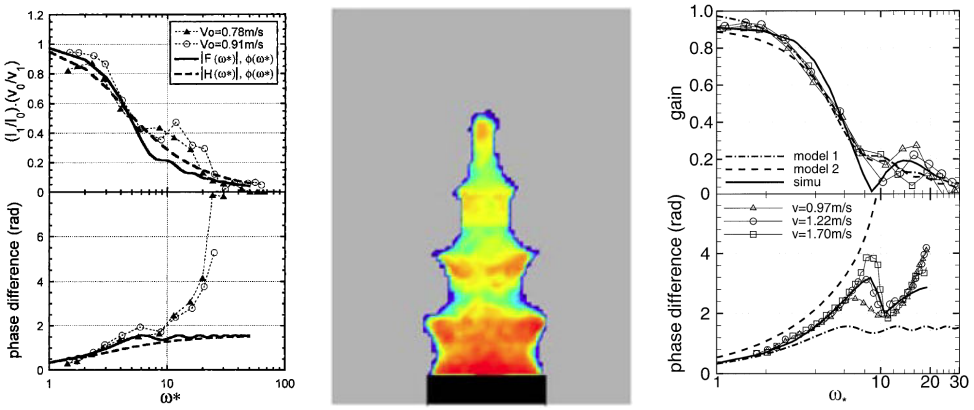

Figure 1.5: (center) *PIV measurements of an acoustically perturbed conical flame, from Birbaud* et al. *(2006). The fresh gas zone is colored with the axial velocity field.* **(left and right)** *Comparisons between experimentally determined FTF and the FTF component F_A gain (top) and phase (bottom) from the models derived by Ducruix* et al. *(2000) (left) and by Schuller* et al. *(2003a) (right). The FTF gain and phase lag are plotted as a function of the reduced frequency ω_*.*

By prescribing such a convective pattern to the perturbed flow, it was possible to derive a new expression for the FTF of conical flames [Schuller *et al.* (2003a)]:

$$F_A(\omega_*, \alpha) = \frac{2}{\omega_*^2(1-\cos^2\alpha)}\left[1 - \exp(i\omega_*) + \frac{\exp(i\omega_*\cos^2\alpha) - 1}{\cos^2\alpha}\right] \quad (1.27)$$

This new model captures correctly the gain of the FTF and a regularly increasing behavior for the phase lag (see model 2 in Fig.1.5-right). However, a gap between the model and the experimental data is still observable. In particular, it was shown that phase lag measurements lie between predictions with the uniform model (model 1 in Fig.1.5-right) that saturates at $\pi/2$ and the convective model that features a regular increase of the phase lag with the frequency (see model 2 in Fig.1.5-right). In this new description, the flame transfer function depends on two dimensionless numbers ω_* and the steady flame front angle with respect to the flow direction α.

It is interesting to compare the different models by examining their behaviors at low and high frequencies. By examining the FTF phase lag evolution from different experiments, the best approximation is given by a constant time lag $\tau = (1/3)H/(v_0\cos^2\alpha)$ in the low frequency limit that is well captured by the uniform model Eq. (1.24). The convective model Eq. (1.27) gives a time lag $\tau = (1/3)H(1+1/\cos^2\alpha)/v_0$ in the low frequency approximation that is twice as large as the right one for elongated flames. However, at higher frequencies the phase evolves with a different time lag [Sugimoto and Matsui (1982); Schuller *et al.* (2003a)] that is well captured by the convective model and which

is equal to $\tau = H/(v_0 \cos^2 \alpha)$ for elongated conical flames. The time lag τ thus triples in the high frequency limit. However, reproducing these asymptotic behaviors does not enable to fully reproduce the FTF because the phase is poorly predicted over most of the frequency band of interest for combustion instabilities. Moreover, the convective origin of the velocity perturbations in the fresh reactant flow field remains unclear. Some studies have conjectured vortices at the origin of the convective waves observed in the fresh reactant flow field of conical flames, but large coherent structures are however absent as shown by PIV measurements [Schuller *et al.* (2002); Noiray *et al.* (2006a)] or more recently by smoke visualizations [Kornilov *et al.* (2007)]. These observations were confirmed by many experiments for different flame angles, equivalence ratios, flames of different sizes and for different perturbation levels [Ducruix *et al.* (2000); Durox *et al.* (2009); Karimi *et al.* (2009)].

(2) Flame feedback

Convective waves observed even at very low frequencies [Baillot *et al.* (1992); Birbaud *et al.* (2006)] are in appearance in contradiction with acoustic laws. When submitting a burner to a low frequency flow modulation, one intuitively expects a perturbation with a wavelength λ_c based on the sound celerity $\lambda_c = c/f$. For the low frequencies of interest, conical flames are compact with respect to these acoustic wavelengths. However experiments have shown that the associated perturbed flow field cannot be considered uniform even for very small conical flames modulated at relatively low frequencies [Noiray *et al.* (2006a); Kornilov *et al.* (2009)]. The flow in the reactant stream of perturbed conical flames is dominated by a convective wave and the uniform perturbation approximation is only valid for compact flames with respect to these convective wavelengths $\lambda_c = v_0/f$: $\lambda_c/H \ll 1$, where H is the flame height. This drastically reduces the validity of the uniform flow perturbation model Eq. (1.24) to the very low frequency band. The origin of the flow dominated convective wave pattern at low frequencies was partly elucidated by Birbaud *et al.* (2006) using detailed particle image velocimetry and laser doppler velocimetry measurements in the fresh reactants and spectral analysis (see Fig. 1.5-center). Their conclusion is that undulations along the flame generate a feedback onto the fresh reactant flow field over a distance of the order of the undulation wavelength. It was also found that the region of influence obeys to a velocity potential. Three regimes are identified. The first regime at low frequencies corresponds to a purely convective wave because the undulation wavelength is large and thus the feedback influence zone covers the entire fresh reactant region. The last regime at high frequencies is dominated by an acoustic wave because the wavelength of the undulations along the flame front is short. The hydrodynamic zone of influence of flame undulations is thus reduced and flow perturbations are essentially uniform in the fresh flow field. The intermedi-

ate regime is dominated by an acoustic wave near the burner outlet and by a convective wave near the flame tip region. This mechanism is confirmed by velocity measurements [Baillot *et al.* (1992); Baillot *et al.* (1996)] and by the smoke visualization from Kornilov *et al.* (2007), where undulations along the flame are shown to deform fresh reactant streamlines in the neighborhood of the flame front.

These observations may be used to introduce a new velocity perturbation model. As shown by Boyer and Quinard (1990), Baillot *et al.* (1992) and later by others [Schuller *et al.* (2002); Kornilov *et al.* (2007)], harmonic flow oscillations at the burner outlet produces flame wrinkles of wavelength $\lambda \simeq v_0/f$. This purely kinematic mechanism is well predicted by using the telegraph equation Eq. (1.12) [Boyer and Quinard (1990)]. The feedback flow perturbations resulting from flame front undulations obey to a velocity potential and correspond thus to an incompressible velocity field. The perturbed velocity field in the neighborhood of the flame front should thus be (1) divergence free and (2) of convective type. The simplest harmonic perturbed flow field satisfying these conditions was proposed by Baillot *et al.* (1992) and was later confirmed by Schuller *et al.* (2002) with PIV measurements on an axisymmetric burner:

$$\widetilde{u}_1 = ik\frac{(R-x)}{2}v_1\exp(iky) \tag{1.28}$$

$$\widetilde{v}_1 = v_1\exp(iky) \tag{1.29}$$

where R denotes the burner radius. The mean flow field is assumed to be uniform and axial ($u_0 = 0, v_0 =$Cte) and $k = \omega/v_0$ corresponds to the convective wavenumber based on the mean flow velocity. Numerical integration of the G-equation Eq. (1.8) was carried out by Schuller *et al.* (2002) to determine the FTF corresponding to this new perturbed field. Simulations showed a good agreement for the phase of the FTF with experimental data obtained for a large modulation level. This perturbed flow model was later used to derive an analytical expression for the FTF [Preetham *et al.* (2008)] but these authors found no clear differences with the FTF obtained by only considering an axially convected disturbances Eqs. (1.25) and (1.26). This model is revisited in Chap. 4 to obtain an analytical expression of the FTF for vanishingly small velocity perturbations. It will be shown that it features several important differences with a purely convected disturbances that may be use to reduce the gap between predicitions and experiments.

(3) Exothermicity and confinement effects

The level-set description of the flame sheet response to flow disturbances presented in the previous section does not consider effects of the burnt gas ex-

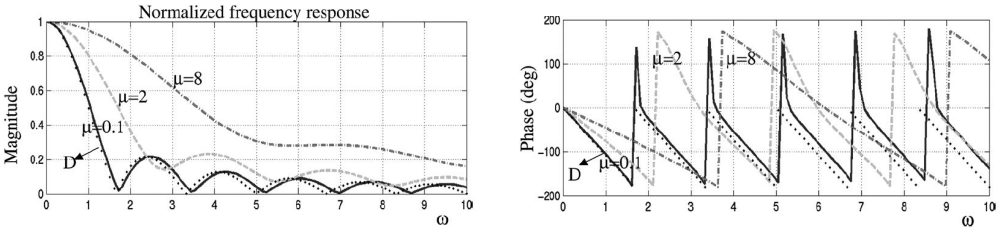

Figure 1.6: *Exothermicity effects on the FTF gain (left) and phase lag (right) of a ducted V-flame. The different curves are a function of the parameter* $\mu = \rho_u/\rho_b - 1$. *Reproduced from Mehta* et al. *(2005). The FTF phase decreases at low frequencies because the "*$\exp(i\omega t)$*" convention was adopted in this article.*

pansion on the flame dynamics. When the burnt gases cannot fully expand, they exert an overpressure on the stream of the fresh reactants that modifies the shape of the steady flame. Effects of exothermicity were mainly studied for V-flames stabilized in a flame tube in the wake of a bluff-body. This phenomenon was for example described by Poinsot and Candel (1988). Mehta *et al.* (2005) found a strong dependence of the FTF on the ratio of burnt to unburnt gas density ρ_b/ρ_u. They first studied the mean flow field around a confined rod-stabilized V-flame and found both analytically and numerically that the spatial variations of the mean velocity field has a significant impact on the flame dynamics. By assuming a uniform velocity perturbation, they derived an analytical expression of the FTF of a ducted V-flame featuring strong variations with the parameter $\mu = \rho_u/\rho_b - 1$:

$$F(\omega) = \frac{\left[1 + \mu_{\text{eff}}\left(1 - \frac{a}{b}\right)\right]^{1+i\omega\tau_e/2} - 1}{\mu_{\text{eff}}\left(1 - \frac{a}{b}\right)\left(1 + \frac{i\omega\tau_e}{2}\right)} \tag{1.30}$$

where $\mu_{\text{eff}} = \mu/(1+\mu)^{\frac{1}{2}}$, a is the bluff-body radius, b is the flame tube radius, $\tau_e = b/(\mu_{\text{eff}} S_T)$ and S_T is the turbulent flame speed. This expression shows that the flame frequency response is stretched out to higher frequencies when μ is increased as shown in Fig. 1.6. In particular, the FTF phase lag features deviation up to π when μ is varied compared to predictions obtained for $\mu = 0$. Birbaud *et al.* (2007a) conducted an experimental study on effects of confinement on the response of a ducted V-flame. By changing the flame tube radius, they observed strong modifications of the FTF. These differences were mainly due to modifications of the vortex shedding at the burner lip.

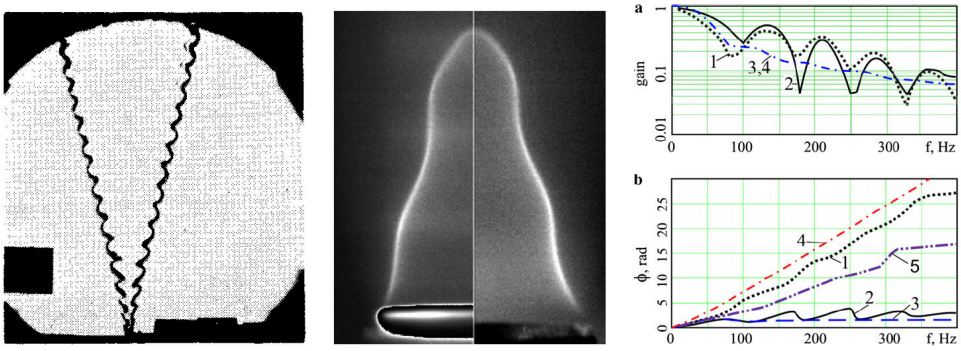

Figure 1.7: (left) *Image of a V-flame which rim is undergoing a transverse motion. Reproduced from Petersen and Emmons (1961).* **(center)** *Comparison between shapes taken by conical flames with a longitudinal rim perturbation and an acoustic flow modulation. Reproduced from Kornilov* et al. *(2007).* **(right)** *Comparison of different FTFs: 1-Experimental FTF of an acoustically perturbed flame. 2-Experimental FTF of a flame with a longitudinal rim excitation. 3-Theoretical FTF from Ducruix* et al. *(2000). 4-Theoretical FTF from Schuller* et al. *(2003a). 5-Experimental FTF of a flame with a transverse rim excitation. Reproduced from Kornilov* et al. *(2007).*

(4) Dynamics of the anchoring point

The flame response to flow perturbations is very sensitive to the anchoring point dynamics as it is a source of wrinkling (see Eq. 1.13). It was shown by Petersen and Emmons (1961) (see Fig. 1.7-left) and then analyzed theoretically by Boyer and Quinard (1990) that by imposing an oscillatory motion of the anchoring point of an inclined premixed flame, a convective undulation develops along the flame front even in a steady uniform flow field. This wave convected along the flame front was also observed for a conical flame attached to a vibrating rim [Kornilov *et al.* (2007)]. In this study, the authors have compared the response of conical flames anchored to a fixed rim and submitted to flow oscillations and the response of the same flames to a vibration of the anchoring rim in a uniform flow field. It is striking that the same kind of undulations develop along the flame front (see Fig. 1.7-center), but different phase behaviors were observed for the corresponding FTFs. In Fig. 1.7-right, one can observe that the phase lag of the rim excited flames rapidly reaches an asymptotic value and oscillates between $\varphi = \pi/2$ and $\varphi = \pi$ (see the black curve #2 in Fig. 1.7-right). Further experimental investigation using TiO_2 smoke visualizations indicated that flame wrinkles generated by the rim oscillation are inducing in turn perturbations in the fresh gas flow, where the streamlines are deviated. This mechanism was described in the previous section.

A theoretical analysis conducted by Lee and Lieuwen (2003) shows indeed that the flame base motion is a source of flame wrinkling. To study the impact of the flame base motion on the FTF, the link between the flame base motion

and velocity perturbations must be considered. An attempt was made by Lee and Lieuwen (2003) but their flame base motion model is not realistic as it features a singularity at low frequencies. Thus, no use of that formulation is used in their work. Shin and Lieuwen (2012) recently conducted a theoretical study of stretch effects on a V-flame which base was harmonically perturbed. A recent experimental analysis conducted on a ducted conical flame submitted to acoustic forcing of increasing level [Karimi *et al.* (2009)] has demonstrated the existence of a flame base motion up to the order of 1 mm for a flame anchored on a rim of 25 mm diameter. These authors also found that the mean value of the flame base diameter is found equal to its steady value for perturbation amplitudes up to $|v_1/v_0| = 1$ and that the dimensionless flame base diameter perturbations scales linearly with $|v_1/v_0|$. This means that the flame base responds linearly to flow perturbations, even for strong forcing levels. Kornilov *et al.* (2007) and de Goey *et al.* (2011) assumed, without a clear justification, that this flame base motion induces an offset component in the FTF that causes the FTF phase lag to saturate at high frequencies. The physical mechanism associated to the flame base motion is assumed to be linked to unsteady heat transfer between the flame and the burner rim. Several theories have looked into that phenomenon and they are synthesized in the next section.

(5) Unsteady heat loss to the burner rim

Unsteady heat loss is one important element for the FTF determination in certain configurations. This is the case when examining the response to acoustic perturbations of a planar flame sheet stabilized close to a porous burner. This configuration has been studied experimentally [Schreel *et al.* (2002); Schreel *et al.* (2005)], numerically [Rook and de Goey (2003); Schreel *et al.* (2005)] and analytically [McIntosh and Clarke (1984); Rook *et al.* (2002); Schreel *et al.* (2002)]. It was shown that a planar flame close to a solid boundary can be perturbed in two ways. Firstly, acoustic velocity perturbations produce regular oscillations of the flame front stand-off distance with respect to the burner outlet. Secondly, these perturbations in the flame position may lead to a resonant coupling in certain circumstances [Rook *et al.* (2002)]. Heat transfer from the flame to the burner lip is here of significant importance. This problem may be tackled by examining the transport of enthalpy $h = \Delta h_f^0\, Y_f + c_p T$ between the flame front and the burner lip, where Δh_f^0 is the heat value per unit mass of fuel, Y_f is the fuel mass fraction in the mixture, c_p is the mixture specific heat at constant pressure and T is the mixture temperature. This mechanism identified by making use of asymptotic analysis [Margolis (1980); Joulin (1982)] has been thoroughly investigated by McIntosh and co-workers in a series of articles (see for examples [McIntosh and Clarke (1984); McIntosh (1990)]) yielding a complete theoretical framework to analyze the dynamics of planar premixed flames stabilized in the vicinity of solid boundaries. This configuration was

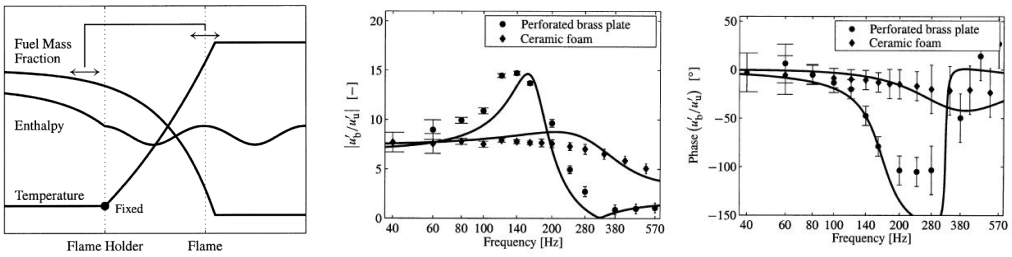

Figure 1.8: (left) *Scheme of the resonant coupling that can occur between the flame holder and the flame front involving enthalpy fluctuation and flame front motion.* **(center and right)** *Velocity Transfer Function gain and phase for two different burner materials. Experimental data are plotted with circles while the theoretical model is plotted with lines. All the figures are reproduced from [Schreel* et al. *(2002)]. A* $\exp(i\omega t)$*-convention was adopted in this article.*

recently examined in the review by de Goey *et al.* (2011).

The physical mechanism is the following [Rook *et al.* (2002)] (see Fig.1.8-left). In this simplified description, it is assumed that the temperature of the burner is fixed and the fuel mass fraction consumed by the flame is fixed as well. A perturbation in the flame front location, where the fuel mass fraction is fixed $Y_{f1} = 0$, induces a perturbation of the thermal flame zone location and thus a perturbation in the fuel mass fraction at the burner rim. As the temperature is assumed to be fixed at the burner rim $T_s = \text{Cte}$, enthalpy disturbances are generated at the burner rim and are further transported by convection and diffusion processes towards the flame front where they induce temperature fluctuations (as the fuel mass fraction is constant there). When these disturbances reach the flame front, they induce in turn perturbations in flame speed, leading to perturbations of the flame front position. These phenomena can couple and lead to resonance when the enthalpy disturbance wavelength is of the order of $4\psi_{f_0}$ [Rook *et al.* (2002); Rook and de Goey (2003)], where ψ_{f_0} is the flame stand-off distance with respect to the burner outlet.

It is possible to model the transfer function linking flame speed perturbations S_{d1} and incoming acoustic velocity disturbances in the unburnt gases u_{u_1} at the flame base [Rook *et al.* (2002)]. A planar flame stablized over a porous burner is considered here. One-step chemistry with all species having a unit Lewis number and constant and equal specific heat are considered here. The mass fraction Y_f and enthaly $h = \Delta h_f^0\ Y_f + c_p T$ balance equations then reduce to:

$$\frac{\partial \rho Y_f}{\partial t} + \frac{\partial \rho u Y_f}{\partial y} - \frac{\partial}{\partial y}\left(\frac{\lambda}{c_p}\frac{\partial Y_f}{\partial y}\right) = \dot{\omega}_f \tag{1.31}$$

$$\frac{\partial \rho h}{\partial t} + \frac{\partial \rho u h}{\partial y} - \frac{\partial}{\partial y}\left(\frac{\lambda}{c_p}\frac{\partial h}{\partial y}\right) = 0 \tag{1.32}$$

where ρ is the density, λ is the heat conductivity of the mixture, $\dot{\omega}_f$ is the consumption rate of methane and c_p is the mixture specific heat at constant pressure. These equations are solved along with the following boundary conditions: $T = T_u = \text{Cte}$ inside the burner, $Y_f = Y_u$ for $y \to -\infty$, $Y_f = 0$ and $\partial T/\partial y = 0$ at the flame front. Rook *et al.* (2002) found an expression for the transfer function betwen velocity perturbations in the fresh stream and in the burnt gases:

$$\begin{aligned}\frac{\tilde{u}_{b_1}}{\tilde{u}_{u_1}} &= 1 + \frac{T_b - T_u}{T_u}\mathcal{A}(\hat{\omega}) \\ &- \frac{1}{2}\frac{T_{ad} - T_u}{T_u}\exp\left(-\frac{\psi_{f_0}}{\delta_f}\right)\left(1 + (1 - 4i\hat{\omega})^{\frac{1}{2}}\right)\frac{1 - \mathcal{A}(\hat{\omega})}{i\hat{\omega}}\end{aligned} \tag{1.33}$$

where $\hat{\omega} = \omega\delta_f/S_{d0}$ is the acoustic frequency made dimensionless by a thermal diffusion time scale. In this expression, $\delta_f = \lambda/(\rho_u S_{d0} c_p)$ is the thermal flame thickness, c_p is the mixture specific heat at constant pressure, λ is the heat conductivity of the mixture, T_u is the fresh gas temperature, T_b is the burnt gas temperature, T_{ad} is the adiabatic flame temperature and $\mathcal{A}(\hat{\omega})$ is the frequency response between flame speed and acoustic velocity perturbations:

$$\begin{aligned}\mathcal{A}(\hat{\omega}) &= \frac{\tilde{S}_{d_1}}{\tilde{u}_{u_1}} \\ &= \left[1 - \frac{2i\hat{\omega}}{\text{Ze}}\frac{T_b - T_u}{T_{ad} - T_b}\exp\left(-\frac{\psi_{f_0}}{2\delta_f}\left(1 - (1 - 4i\hat{\omega})^{\frac{1}{2}}\right)\right)\right]^{-1}\end{aligned} \tag{1.34}$$

where Ze is the Zeldovich number and ψ_{f_0} is the stand-off distance defined by:

$$\psi_{f_0} = \delta_f \log\left(\frac{T_{ad} - T_u}{T_{ad} - T_b}\right) \tag{1.35}$$

An extension of this model was proposed by Schreel *et al.* (2002) and Schreel *et al.* (2005) in order to take into account the temperature of the porous burner surface. Heat transfer mechanisms such as heat conduction and radiation were considered to determine this surface temperature as a function of the thickness, the heat capacity, the heat conductivity and the emissivity of the flame holder. Predictions from Eq. (1.34) are reproduced from Schreel *et al.* (2002) in Fig. 1.8 in terms of gain (center figure) and phase (right figure), along with experimental data obtained for flames stabilized above two burners made of different burner materials. The model shows a good agreement with measurements, especially

concerning the resonant peak location. This problem will be further considered in the present work in Chapter 5.

(6) Stretch effect modeling

Besides physical mechanisms producing flame wrinkles, other mechanisms modify existing wrinkles on the flame front. One of them is the stretch exerted on a wrinkled flame front. It was shown that stretch, including curvature and hydrodynamic strain, may have an important influence on laminar flame dynamics and on FTF for conical and wedge flames stabilized in a uniform mean flow [LeHelley (1994); Wang *et al.* (2009); Preetham *et al.* (2010)] or a Poiseuille mean flow [Wee *et al.* (2012)]. It is also known that flame front curvature and hydrodynamic strain may alter the fuel consumption rate. These phenomena have a direct effect on the laminar flame speed [Chung and Law (1988); Law and Sung (2000)]:

$$S_{d1} = S_{d0}\left[1 - \delta_f \nabla \cdot \mathbf{n}\right] + \frac{Ze}{2}\left(\frac{1}{Le} - 1\right)\delta_f \kappa \tag{1.36}$$

where Ze stands for the Zeldovich number, δ_f is the thermal flame thickness, Le denotes the Lewis number and κ stands for the flame stretch rate [Markstein *et al.* (1964); Matalon and Matkowsky (1982); Chung and Law (1984)].

Stretch effects may be included in the level-set description of the flame motion. Wang *et al.* (2009) and Preetham *et al.* (2010) proposed the following transport equation for flame wrinkles:

$$\Sigma_C \frac{\partial^2 \xi_1}{\partial x^2} + \frac{\partial \xi_1}{\partial x} + i\omega_* \xi_1 = f(v_1/v_0) \tag{1.37}$$

where

$$\Sigma_C = \left[1 - \frac{\mathrm{Ze}}{2}\left(\mathrm{Le}^{-1} - 1\right)\right] \frac{\delta_f \cos\alpha}{R} \tan^2\alpha \tag{1.38}$$

The right hand side $f(v_1/v_0)$ of Eq. (1.37) depends on the velocity perturbation model considered. The G-equation is now a second-order equation in space requiring the use of two boundary conditions. In the case of a wedge flame, its base is here assumed to be steadily anchored at the burner rim and the flame tail is set free to move:

$$\xi(r = 0, t) = 0 \tag{1.39}$$

$$\frac{\partial^2 \xi}{\partial y^2}(r = R, t) = 0 \tag{1.40}$$

The stretch-modified G-equation was solved by assuming uniform [Wang *et al.* (2009)] or convected [Preetham *et al.* (2010)] velocity perturbations. The FTF of stretched flames features two contributions. The first is due to mass burning rate fluctuations $\rho_u \tilde{S}_{d1}$. The second is associated to flame surface area perturbations $\tilde{A}_1$:

$$\frac{\tilde{\dot{Q}}_1}{\dot{Q}_0} = \frac{\int_{A_0} \tilde{S}_{d1} dA}{S_{d0} A_0} + \frac{\tilde{A}_1}{A_0} \tag{1.41}$$

These authors found that flame wrinkles are damped along the steady flame front and this effect increases as the Markstein length $\sigma_c = (1 - Ze(Le^{-1} - 1)/2)(\delta_f/R)$ increases. They also found that the FTF is essentially unsensitive to stretch up to $\omega_* = 2\pi$. For higher frequencies, stretch effects are more significant. The gain of the FTF now features humps which are smoothened compared to the FTF derived without taking into account stretch effects. The phase lag is however barely modified. No comparison to experiments has been carried out yet to validate these models. However, a numerical integration of the stretch-dependent G-equation was performed by LeHelley (1994) for a conical flame stabilized in a uniform flow and submitted to both uniform and incompressible convective velocity perturbations. Results in terms of flame wrinkles and FTF were compared to DNS simulation results and a good agreement was found.

(7) Time domain representation

The expressions derived for the FTF contribution $F_A(\omega_*, \alpha)$ in the frequency domain by Ducruix *et al.* (2000) and by Schuller *et al.* (2003a) have been recently extended to the time domain by Blumenthal *et al.* (2013). The time domain representation provides interesting insight on the different time lags controlling the flame response to flow perturbations. Starting from the G-equation Eq. (1.11), the impulse response (IR) may be derived by considering two types of perturbations. The first is a uniform impulse perturbation in the direction of the flow: $v_1(t) = \epsilon\delta(t)$. The second corresponds to a convective impulse perturbation travelling along the axial direction at the mean flow velocity: $v_1(t) = \epsilon\delta(t - y/v_0)$. Blumenthal *et al.* (2013) found two different expressions for the impulse response of a conical axisymmetric flame:

$$h_U(t) = \begin{cases} \dfrac{2}{\tau_r}\left(1 - \dfrac{t}{\tau_r}\right) & \text{for } t \in [0; \tau_r] \\ 0 & \text{for } t \geq \tau_r \end{cases} \tag{1.42}$$

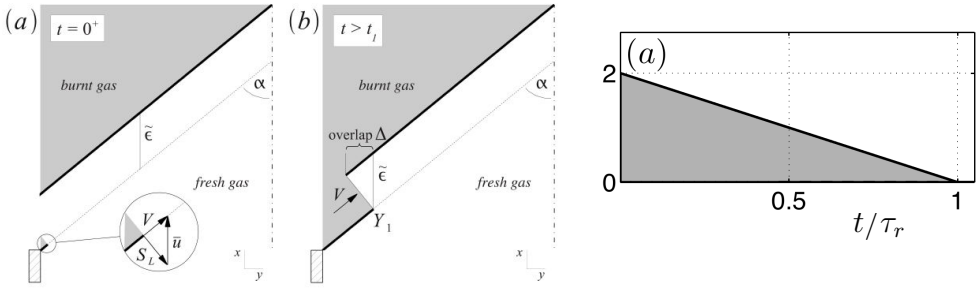

Figure 1.9: *Flame response (left) and dimensionless impulse response of a conical flame $h_U(t)\tau_r$ (right) in the case of a uniform velocity perturbation. Reproduced from [Blumenthal et al. (2013)].*

$$h_C(t) = \begin{cases} \dfrac{2t}{\tau_r \tau_c} & \text{for } t \in [0; \tau_c] \\ \dfrac{2}{\tau_r} \dfrac{\tau_r - t}{\tau_r - \tau_c} & \text{for } t \in [\tau_c; \tau_r] \\ 0 & \text{for } t \geq \tau_r \end{cases} \tag{1.43}$$

where the time scales τ_r and τ_c are defined below.

The impulse response obtained in Eq. (1.42) for a uniform velocity perturbation $h_U(t)$ is a function of time t and the characteristic time scale $\tau_r = L/(v_0 \cos\alpha)$ which may be associated to the reduced frequency ω_* in the frequency domain. This time scale is called the "restoration" time scale. This response is obtained by assuming that, at the initial instant, the flame front is uniformly displaced from its steady position and comes back to its steady position after a restoration time τ_r (see Fig. 1.9-left). The impulse response exhibits a jump at initial time before decreasing linearly towards zero up to $t = \tau_r$ (see Fig. 1.9-right).
The impulse response obtained for a convective velocity perturbation $h_C(t)$ in Eq. (1.43) depends on two characteristic time scales. The first is the restoration time scale identified previously and the second is a "convection" time scale $\tau_c = H/v_0 = \tau_r \cos^2\alpha$ that may be associated to the reduced frequency $k_* = \omega_* \cos^2\alpha$ in the frequency domain that is defined in Chapter 4. This impulse response exhibits a linear increase from $t = 0$ and $t = \tau_c$ before linearly decreasing between $t = \tau_c$ and $t = \tau_r$. This impulse response is further studied in Chapter 4.

(8) Extension to a collection of conical flames with multiple flame effects

The previous models were derived for the response of single conical or planar flames. A collection of conical flames is often used in practical and industrial burners, such as those used in domestic boilers, burners for material processing like paper drying or for glass heating, and these combustion systems are prone to thermo-acoustic instabilities. Different investigations have considered over the past few years the FTF of a collection of small conical flames stabilized on burners featuring circular injection holes [Noiray *et al.* (2006b); Durox *et al.* (2009); Altay *et al.* (2009); Boudy *et al.* (2011); Kedia *et al.* (2011); Duchaine *et al.* (2011)] or 2D rectangular slits [Kornilov *et al.* (2009); Kornilov *et al.* (2009); Coats *et al.* (2010); Coats *et al.* (2011); Duchaine *et al.* (2011)].

The configuration studied at MIT [Altay *et al.* (2009); Kedia *et al.* (2011); Kedia and Ghoniem (2013)] corresponds to a collection of conical flames featuring planar and inclined flame fronts (see the diagram in Fig. 1.10-top-left). The flame height is significantly smaller than the acoustic and hydrodynamic perturbation wavelengths. The flame response was modeled by discriminating the planar part of the flame from its inclined part. First, the planar flame contribution to the FTF was modeled by considering velocity perturbations and the unsteady heat loss from the flame to the perforated plate using the model Eq. (1.34) from Rook *et al.* (2002). The conical flame contribution to the FTF was also modeled by considering a uniform velocity perturbations in the fresh stream and flame speed perturbations that are generated by unsteady heat loss. The heat release rate mean value and perturbations were divided into two components, one related to the combustion generated power $\dot{Q}^{\rm gen}$ and the other to the heat loss to the burner $\dot{Q}^{\rm loss}$:

$$\dot{Q}_0^{\rm rel} = \dot{Q}_0^{\rm gen} - \dot{Q}_0^{\rm loss} \tag{1.44}$$

$$\tilde{\dot{Q}}_1^{\rm rel}(\omega) = \tilde{\dot{Q}}_1^{\rm gen}(\omega) - \tilde{\dot{Q}}_1^{\rm loss}(\omega) \tag{1.45}$$

These different components were modeled as:

$$\dot{Q}_0^{\rm gen} = \rho_u S_{d0} \Delta H (A_{c0} + A_p) \tag{1.46}$$

$$\tilde{\dot{Q}}_1^{\rm gen}(\omega) = \rho_u \Delta H \left[(A_{c0} + A_p)\tilde{S}_{d1}(\omega) + S_{d0}\tilde{A}_{c1}(\omega) \right] \tag{1.47}$$

where ρ_u stands for the unburnt gas density, ΔH for the heat value per unit mass of fuel, S_d for the flame speed, A_c for the flame surface area of the conical part, A_p for the flame surface area of the planar reaction layer. These authors found:

$$\frac{\dot{Q}_0^{\text{loss}}}{\rho_u S_{d0} \Delta H A_p} = \exp\left(-\frac{\psi_{f0}}{\delta_f}\right) \tag{1.48}$$

$$\frac{\tilde{\dot{Q}}_1^{\text{loss}}(\omega)}{\rho_u S_{d0} \Delta H A_p} = -\exp\left(-\frac{\psi_{f0}}{\delta_f}\right) \frac{1+\left(1-\dfrac{4i\omega\delta_f}{S_{d0}}\right)^{\frac{1}{2}}}{\dfrac{2\delta_f i\omega}{S_{d0}}} \left[\frac{\tilde{S}_{d1}(\omega)}{S_{d0}} - \frac{\tilde{u}_{u1}(\omega)}{u_{u0}}\right] \tag{1.49}$$

where

$$\tilde{A}_{c1}(\omega) = \frac{2\pi N S_{d0}\beta^2}{(i\omega)^2} (u_{c0} - S_{d0}) \left[\frac{\tilde{u}_{u1}(\omega)}{u_{u0}} - \frac{\tilde{S}_{d1}(\omega)}{S_{d0}}\right] \left[\exp\left(\frac{i\omega R}{S_{d0}\beta}\right) - \frac{i\omega R}{S_{d0}\beta} - 1\right] \tag{1.50}$$

The function $\tilde{S}_{d1}(\omega)$ is defined by the model derived by Rook *et al.* (2002) corresponding to Eq. (1.34). In the previous expressions, ψ_{f0} represents the flame stand-off distance with respect to the solid burner outlet, δ the thermal flame thickness, u_u the unburnt gas velocity, u_c the fresh gas velocity in the conical flame, N the number of holes of the perforated plate, R the hole radius and $\beta = \cos\alpha$ is a parameter related to the flame tip half-angle α. The total FTF is finally defined by:

$$F(\omega) = \frac{\tilde{\dot{Q}}_1^{\text{rel}}(\omega)/\dot{Q}_0^{\text{rel}}}{\tilde{u}_{u1}(\omega)/u_{u0}} \tag{1.51}$$

Predictions were compared to experimental data (see Fig. 1.10-bottom-left). An overall reasonable match was found. The model retrieves the frequency location of the FTF gain peak [Rook *et al.* (2002); Schreel *et al.* (2002); Rook and de Goey (2003)]. The FTF phase is also captured by the model. This model is thus adapted to configurations where the conical flames are compact with respect to the hydrodynamic wavelength. Further studies have looked into effects of heat loss with numerical tools [Kedia *et al.* (2011)]. An investigation of the conical flame base stabilization mechanism has lead to an improvement of the FTF model [Altay *et al.* (2010); Kedia and Ghoniem (2012)]. The model proposed by Altay *et al.* (2009) relies on values of different parameters such as the burner plate temperature and the flame stand-off distance. To obtain these informations, Kedia and Ghoniem (2013) derived a heat transfer model for the perforated plate. Their results are then used as inputs to the FTF model. This methodology enables to take into account the steady heat transfer coupling between the burner plate and the flame.

Flame visualization of the response to flow perturbations of small conical flames

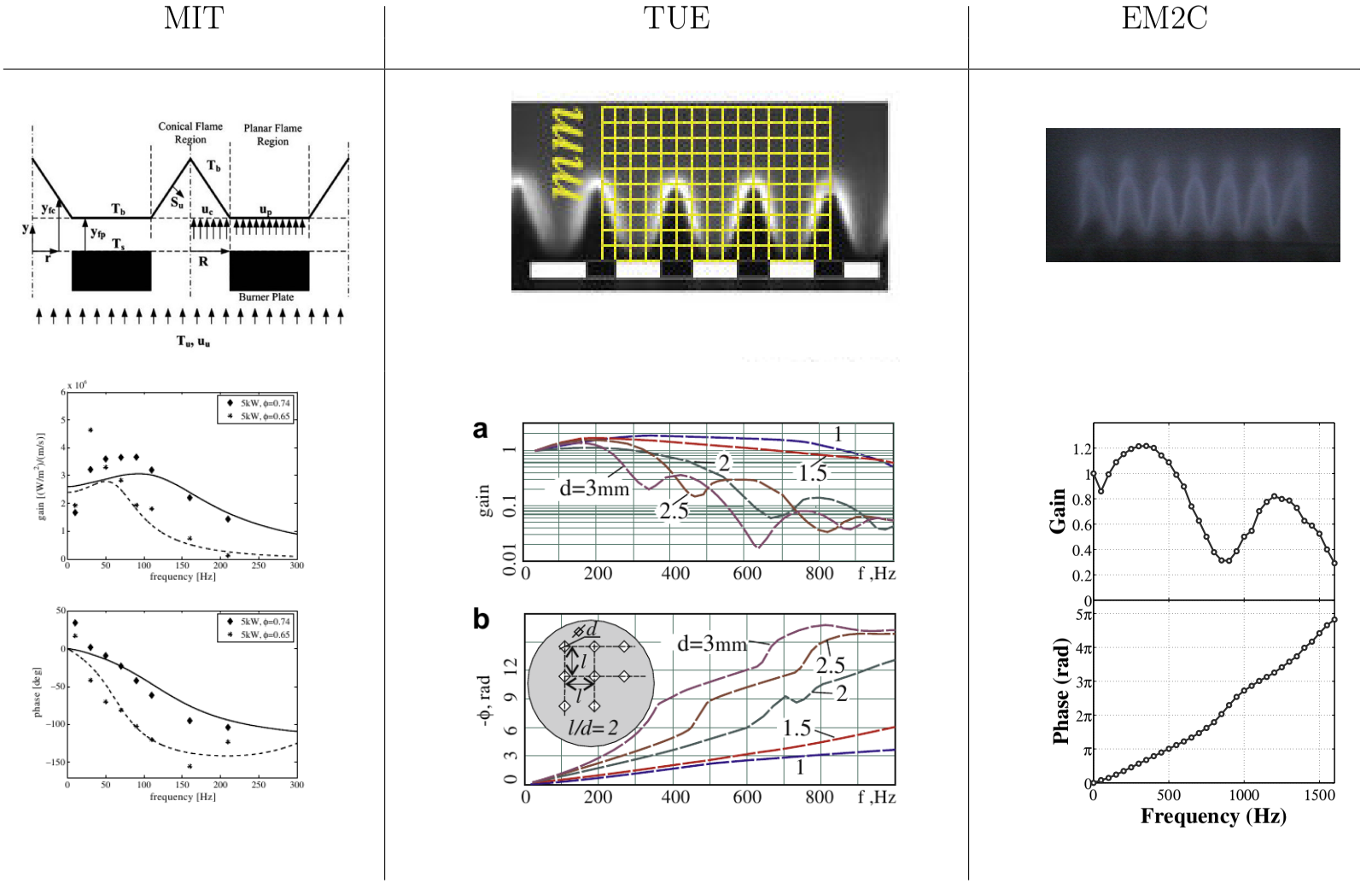

Figure 1.10: (left) *Configuration modeled by Altay* et al. *(2009) (top) and comparison between predictions and measurements (bottom). A* $\exp(i\omega t)$*-convention was adopted in this article. -* **(center)** *Image of a collection of conical flames anchored above of a perforated plate from Kornilov* et al. *(2009) (top) and experimentally determined FTF plotted as a function of frequency for different hole diameters from Kornilov* et al. *(2009) (bottom) -* **(right)** *Image of acoustically perturbed conical flames anchored on a perforated plate (top) and the corresponding measured FTF from Boudy (2012) (bottom)*

anchored on a perforated plate reveal however that the flames may not be compact with respect to the hydrodynamic wavelength and this phenomenon needs to be considered to model the FTF. PIV measurements of such a configuration were carried out by Noiray *et al.* (2006a) and have revealed that convective velocity perturbations are present in the fresh gases. This has a significant impact on both the FTF gain and phase. One can observe that the FTF measured for small flames stabilized on rectangular slits (see Fig. 1.10-center) [Kornilov *et al.* (2009); Kornilov *et al.* (2009)] or on circular holes (see Fig. 1.10-right) [Noiray *et al.* (2006b); Boudy *et al.* (2011)] has a behavior quite similar to the one measured for single conical flames. The gain features several humps and the phase lag exhibits a convective behavior associated to the convection of perturbations at the mean flow velocity over a distance of the order of the flame height. This behavior differs from the one calculated for a "quasi-planar" configuration where the time lag is only related to the flame stand-off distance. It is also worth noting that the FTF gain might exceed unity in the low frequency range.

Recently, this configuration was calculated by direct numerical simulations (DNS) and a sensitivity analysis was conducted to determine the sensitivity of the FTF to different physical parameters [Duchaine *et al.* (2011)]. The authors investigated the configurations from Boudy *et al.* (2011) and Kornilov *et al.* (2009) by simulating only one conical flame with lateral periodic boundary conditions to take into account the influence of surrounding flames. They showed that DNS simulations retrieve with a good accuracy both the FTF gain and phase if a relevant confinement angle of the numerical domain is taken into account in the simulations. In particular, the almost constant slope of the FTF phase observed in the experiments is reproduced by the simulations. However, a sensitivity analysis revealed that the FTF is very sensible to some of the parameters of the problem, such as the laminar burning velocity S_L, the confinement angle as well as upstream flow and perforated plate temperatures.

Kornilov *et al.* (2009) investigated experimentally the impact of the hole diameter and the hole pitch on the FTF. They found that both have a strong influence on the FTF gain and phase as shown in Fig. 1.10-center-bottom. The authors found that the frequency response is shifted to higher frequencies as the hole pitch is decreased. The slope of the FTF phase lag also reduces when the hole pitch is decreased. An expression was also proposed to determine the FTF of a multi-injection plate configuration featuring holes of different sizes,

by linking the global FTF to the FTF of each single conical flame taken alone:

$$F(\omega) = \frac{\sum_{i=1}^{N} F_i(\omega) A_i v_{0_i}}{\sum_{i=1}^{N} A_i v_{0_i}} \tag{1.52}$$

where N is the number of hole in the perforated plate, $F_i(\omega)$ stands for the FTF of a single conical flame anchored over a hole of cross-section area A_i where the mean velocity at the hole exit is equal to v_{0_i}. It will be shown in Chapter 6 that an additional phenomenon has to be considerd when the hole pitch is decreased to describe collective effects.

(9) Nonlinear effects on the Flame Transfer Function

In order to predict the amplitude and frequency reached by thermo-acoustic instabilities at limit cycle, several studies looked into the effect of the perturbation level on the flame frequency response. Dowling (1997) introduced the Describing Function concept to take into account the effects of the perturbation level on the gain of the FTF. Later, it was extended to the Flame Describing Function (FDF) to take also into account modifications of the FTF phase lag with the modulation level [Noiray *et al.* (2008)]. The FDF is defined by introducing the perturbation level in the flame frequency response description:

$$\frac{\tilde{\dot{Q}}_1}{\dot{Q}_0} = F(\omega, |v_1/v_0|) \frac{\tilde{v}_1}{v_0}(\mathbf{x}_{\text{ref}}) \tag{1.53}$$

Numerous experimental studies [Lieuwen and Neumeier (2002); Balachandran *et al.* (2005); Bellows *et al.* (2007)] have highlighted the effects of the perturbation level on flame dynamics. In many configurations, both the FTF gain and phase are function of the input level [Durox *et al.* (2009); Boudy *et al.* (2011); Schimek *et al.* (2011); Kim and Hochgreb (2011)]. In the case of a single conical flame, the FTF gain decreases for increasing perturbation levels. The phase lag regularly increases at low frequency but the saturation appearing at high frequency is triggered at lower frequency as the perturbation level is increased. The saturation frequency, defined as the frequency where the phase lag stops increasing regularly, decreases as the perturbation level is increased. In the case of a collection of conical flames [Noiray *et al.* (2008); Boudy *et al.* (2011)], the FDF gain decreases rapidly to zero when the perturbation amplitude increases. The FDF phase lag is also impacted but on a limited frequency range. No saturation of the FDF phase lag were observed in these cases.

Theoretical studies on perturbation level effects are more seldom. Lieuwen (2005) listed different cases where nonlinearities need to be considered for the

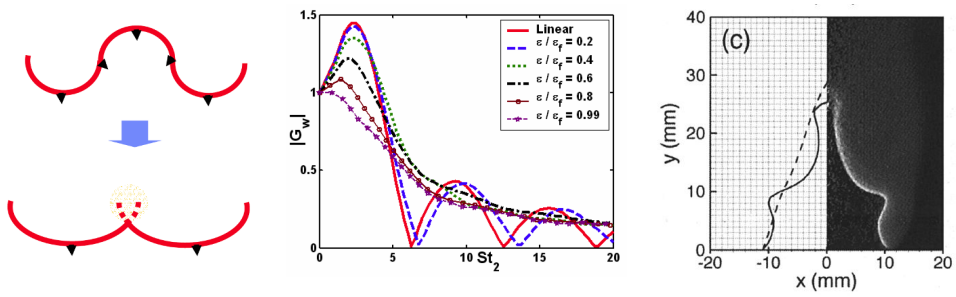

Figure 1.11: (left) *Nonlinear kinematic restoration process induced by the flame front propagation normal to itself. Reproduced from Preetham and Lieuwen (2004).* **(center)** *FTF gain as a function of the Strouhal number and the velocity perturbation level ϵ, in the case of a wedge flame. Reproduced from Preetham and Lieuwen (2004).* **(right)** *Comparison between an experimental image of an acoustically perturbed flame (left-half) and the result from a G-equation solver (right-half). Reproduced from Schuller* et al. *(2002).*

response of acoustically perturbed flames. Nonlinearities appear to be stronger at high Strouhal number, i.e. in the high frequency range. Nonlinear effects on flame front perturbations are more important for small flames compared to elongated flames. Wedge flames have a stronger nonlinear behavior than conical flames. This last point results from the "kinematic restoration“ process [Lieuwen (2005); Hemchandra *et al.* (2011)]. The flame front propagates in a direction normal to itself. Cusps and nonlinearities develop along the flame front (see Fig. 1.11-left and Baillot *et al.* (1996)). This phenomenon is more pronounced for axisymmetric wedge flames than for axisymmetric conical flames. The reason is that most of the flame surface area is located near the flame tail for wedge flames. A large fraction of the flame surface area is located near the flame base for conical flames. This mechanism was also observed with numerical simulations based on level-set trackers [Schuller *et al.* (2003a)]. These numerical solvers were designed to solve the G-equation while releasing the small perturbation assumption. Inputs in terms of fresh gas velocity field and flame front displacement speed are needed. For a specific forcing frequency, they allow to simulate the evolution of the flame front position. Post-processing is then used to determine the flame surface area perturbation and the resulting FTF. Schuller *et al.* (2002), Schuller *et al.* (2003a) studied the influence of the velocity perturbation model on the resulting FTF in the cases of a conical and a wedge flame. For the conical flame, an incompressible convective perturbation model that linearly decays along the axial direction allowed to retrieve the flame front deformations observed experimentally (cf Fig. 1.11-right). The correct evolution of the FTF gain and phase also compared well with measurements. Nonlinear effects on the FTF were more explicitly studied by Preetham and Lieuwen (2004), Preetham *et al.* (2008). Analytical expressions for a perturbation-level-dependent FTF were given. Similar results were

found concerning the FTF gain and phase (see Fig. 1.11-center for the FTF gain of a wedge flame) that are shown to be coherent with measurements from Durox *et al.* (2009) in the case of wedge flames. Later, G-equation solvers were extended to turbulent flows. The case of turbulent conical flames was treated by Preetham *et al.* (2007). FTF of turbulent flames were compared to FTF of laminar flames. Turbulent wedge flames were also considered by Hemchandra and Lieuwen (2010).

1.4 Discussion

Theoretical modeling of FTF has progressed rapidly in the last few years, but several issues remain to be investigated. The present section aims at providing some new leads in the conical flame dynamic modeling that will be considered in the next chapters.

The mode conversion from acoustic to hydrodynamic perturbation taking place in the fresh stream of conical flames remains unclear. Despite the recent experimental investigations highlighting the incompressible nature of the velocity perturbations in this region (this topic is adressed in Chapter 4) as well as the feedback from flame front perturbations onto the fresh reactant stream, this problem is generally not considered to describe the response of inclined flames. In cases where flames are perturbed by an acoustic field, this issue maybe overcome by considering that the convective velocity perturbation amplitude is equal to the acoustic velocity perturbation amplitude at the burner exit. However, in cases where the flame is only submitted to equivalence ratio perturbations or to a flame base oscillation, this substitution can no longer be used. Convective velocity perturbations are still present and partly rules the flame dynamics [Kornilov *et al.* (2007); Hemchandra (2012)]. Convected velocity disturbances need thus to be included in the modeling of the flame front wrinkles.

Secondly, the interaction between the unsteady flame and solid elements from the burner needs further modeling to be fully understood. Because the model by Altay *et al.* (2009) takes only into account uniform velocity perturbations in the conical flame fresh gases, it is only valid for conical flames that are close to the planar flame configuration. An extension towards elongated conical flames that are not compact with respect to the hydrodynamic wavelength has to be adressed to understand the competition between thermal and kinematic mechanisms. This issue is considered in Chapter 5.

Progress in the study of strech effects on FTF has shown that it can have a substantial impact in the high frequency range and for high perturbation levels. However, none of these FTF models have been backed-up by any experiments.

A careful experimental validation of these models is thus to be designed and performed. This problem will not be treated in this work.

To extend models for the response of single conical flames to treat the response of collections of conical flames, the interaction between neighbouring flames has to be taken into account. Different type of interactions can be present in the system. First, direct interactions between flame fronts can take place and thus have an impact on the flame dynamics and the FTF [Worth and Dawson (2012)]. Secondly, undirect interactions can take place when the burnt gases cannot fully expand. The burnt gas expansion acts as a confinement to neighbouring flames. This problem is studied here in Chapter 6.

Finally, a complete description of the conical flame dynamics should also include the influence of the perturbation level on the conical flame frequency response. Previous experiments showed that the FTF phase lag saturates at high frequency when the perturbation level is increased [Durox *et al.* (2009)]. This particular observation is considered in Chapter 5 by considering the competition between thermal and kinematic mechanisms in the nonlinear regime. From a numerical point of view, G-equation solvers could also be used to tackle this problem.

1.5 Conclusion

A current state of art concerning conical flame dynamics has been established in this chapter. This topic received a lot of attention over the past 20 years. The use of the G-equation enabled great progresses in the theoretical flame dynamics modeling while a considerable amount of experimental data have been used for mechanism identification and validation. Lately, accurate numerical simulations allowed to investigate new phenomena that are difficult to study with experiments. However, some discrepancies remain between theory and experiments. The problems raised in this chapter are studied in the next chapters of the present thesis.

Chapter 2

Experimental setup

The experimental setup used to analyze the conical flame dynamics is introduced in this chapter. The burner geometry is first described, detailing the different geometrical configurations investigated in the next chapters. The diagnostics are then presented, with a focus on the measurements of velocity and heat release rate time-resolved signals that are used to determine the Flame Transfer Function. Finally, the flame front imaging setup is described as well as the post-processing used to detect the flame front and the flame base positions.

2.1 Burner description

The configuration studied in this work is presented in Fig. 2.1. The methane/air mixture is realized upstream of the burner. The flow is perfectly premixed before entering the manifold. Two mass flow controllers set the methane and air mass flow rates injected in the burner as well as the mixture equivalence ratio. The burner is composed of different pieces:

- The bottom of the burner is closed air-tightly by a loudspeaker and the methane/air mixture is injected in the plenum above the loudspeaker through two pipes.
- It then features a cylindrical feeding manifold equipped with a laminarization grid and a honeycomb to break the coherent structures and reduce remaining turbulent fluctuations.
- A convergent nozzle is then used to get a nearly uniform top-hat velocity profile at the burner exit. A cooling system with water circulation is installed around the nozzle to keep the flow temperature constant.
- A flame anchoring piece is installed above the convergent nozzle. The burner exit is a cylinder of inner radius $R_0 = 11$ mm. Three burner exit configurations may be used. The first one (noted "a" in Fig. 2.1) features a 1 mm-wide beveled edge. The second one (noted "b" in Fig. 2.1) is equipped with an external plateau of outer radius $R_p = 18$ mm. In

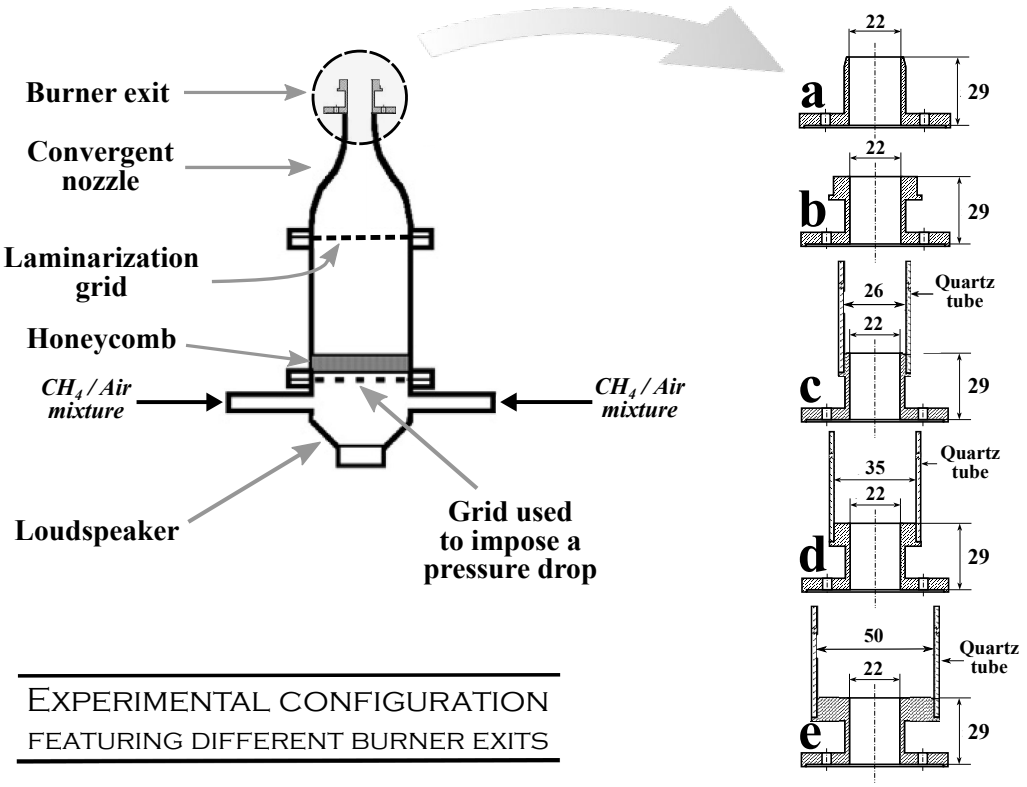

Figure 2.1: *Burner geometry used for the experimental investigation. The reactive mixture is injected at the bottom and outflows the burner through a cylindrical exit. Three burner exit configurations were used: (a) a cylindrical piece with a beveled edge, (b) a cylindrical piece with a plateau and (c,d,e) a cylindrical piece with a plateau supporting a quartz tube.*

the third configuration (noted "c","d" and "e" in Fig. 2.1), the external plateau supports a confinement quartz tube. Three quartz tubes of length $L = 0.3$ m and of radius $R_1 = 13.55$ mm (case "c"), $R_1 = 18.55$ mm (case "d") and $R_1 = 25$ mm (case "e") were used to confine the flame.

2.2 Equipments and Diagnostics

The different diagnostics used to study the flame dynamics are sketched in Fig. 2.2 and are described in the following paragraphs.

Flow modulation

The bottom of the burner is equipped with a loudspeaker to impose acoustic velocity perturbations in the feeding manifold that are propagating towards the burner exit and the base of the flame. A home-made LabVIEW@ program

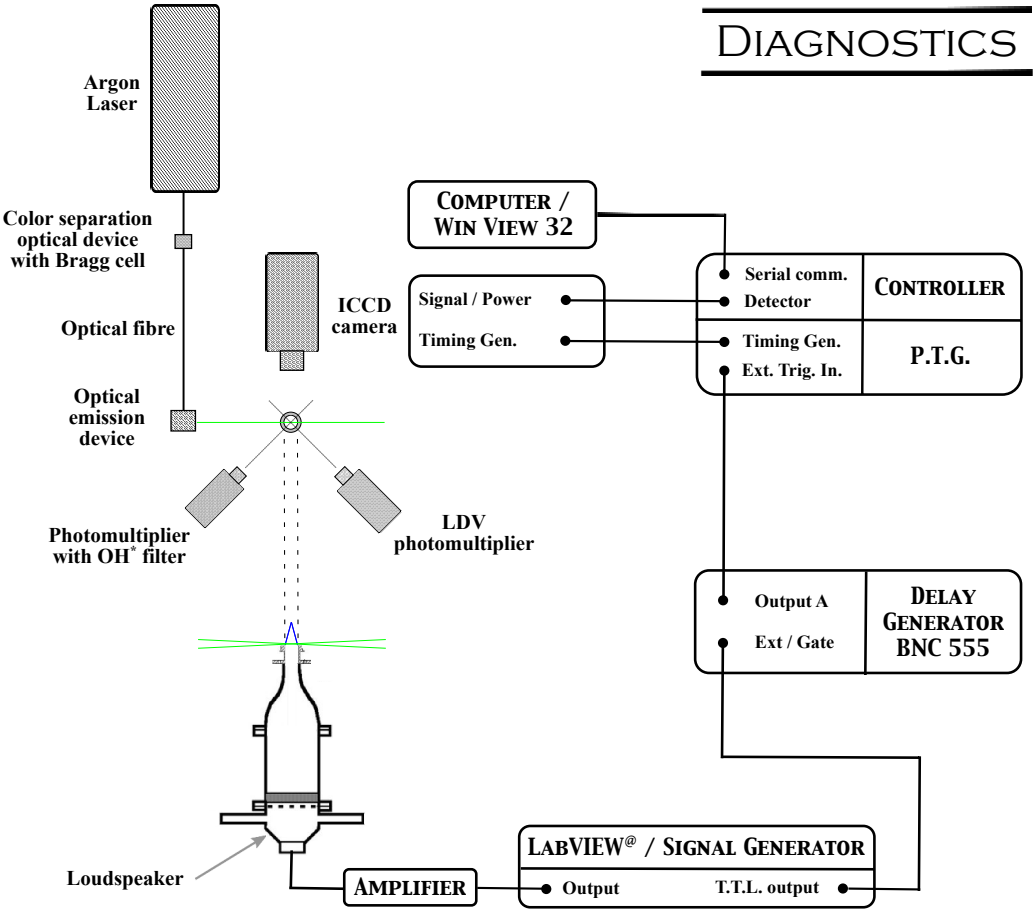

Figure 2.2: *Setup with diagnostics. A signal is generated to trigger the ICCD camera and to drive the loudspeaker. The loudspeaker generates acoustic velocity perturbations measured with a LDV system at the burner outlet. These perturbations produce flame front wrinkles that are captured by the camera and heat release rate perturbations that are recorded by a photomultiplier equipped with an OH* filter.*

was designed to modulate the flow and to easily sweep the perturbation frequency and amplitude. The program generates a harmonic or random signal, sampled at 4096 Hz, that is sent to an amplifier and to the loudspeaker thanks to a National Instrument analog-to-digital converter board. The program is also acquiring the velocity signal measured from a Laser Doppler Velocimeter described in the next section. A real-time control algorithm was implemented into the LabVIEW@ program to control the dimensionless velocity perturbation amplitude v_1^{rms}/v_0 and keep it at a chosen value (with an error of less than 5%) during the duration of experiments.

The loudspeaker input, velocity and heat release rate signals are all recorded

with the LabVIEW@ software at a sampling frequency of 4096 Hz. Further post-processing techniques are explained in the next chapter for the determination of the FTF by different methods.

Laser Doppler Velocimetry

A Laser Doppler Velocimeter (LDV) is used in this setup to measure the local axial velocity and provides a time-resolved signal. The system is briefly described in the following. The laser beam first exits the Argon laser system with a power of 4 W before entering a Bragg cell. In this optical device, the beam is divided into two beams by diffraction. The zeroth order and the first order beams are gathered to eventually obtain two beams including one that is shifted in frequency by 40 MHz. Then, the beams enter a color separation device where they are split into different colors. One can thus recover the 514-nm green beam (with a power of about 300 mW). A blue beam is also available to measure another velocity component but it was not used in this work. At the exit of the color separation device, the beams enter an optical fibre and propagate into it until they reach the optical emission device. Then, the beams are crossed in the region of interest thanks to an achromatic converging lens. The flow is seeded with oil particles (~ 2 μm in diameter) by means of a perfume atomizer [Durox *et al.* (1999)]. A photomultiplier (PM) located in the forward direction receives the light diffused by the droplets that are crossing the interference fringes, with an inter-fringe distance of 3.704 μm. The particle velocity is then computed by a counter from the frequency of the signal received by the PM. The counting rate is kept above $17,000$ data per second to ensure that the signal is well sampled in time.

The axial flow velocity is measured for two purposes. First, the axial velocity is measured at the base of the flame, about 2 mm above the burner exit on the burner axis. This was done to determine the FTF when the flow is submitted to harmonic (see Section 3.2.1) or random (see Section 3.2.2) velocity disturbances. The axial velocity component is also measured along the burner axis to investigate the evolution of the mean and rms velocity in the fresh gases when the flow is submitted to harmonic acoustic excitations.

Examples of time-resolved measurements when the loudspeaker is driven by harmonic excitations are presented in Fig. 2.3, for different forcing frequencies $f = 20, 100$ and 200 Hz and for different dimensionless perturbation amplitudes $|v_1/v_0| = 0.1$ and 0.3. The curves exhibit a periodic time-dependence that is sinusoidal with a clear influence of background noise, especially at low perturbation levels (see Fig. 2.3-top). This phenomenon can also be observed in Figs. 2.4 and 2.5 where the power spectral density (PSD) of two signals are shown, for forcing frequencies of $f = 20$ and 100 Hz, respectively, and for two perturbation levels. An energy transfer from the base forcing tone to its harmonics (at 40 and 200 Hz) is observed when the perturbation level is increased. However, a gap larger than 20 dB is still observed between the main peak and

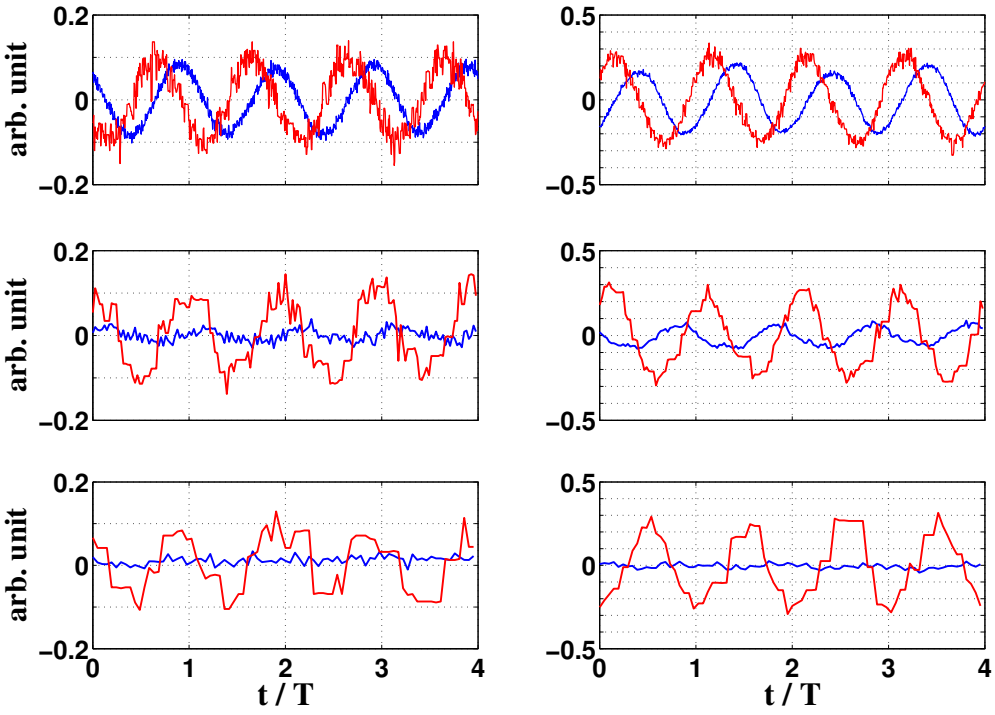

Figure 2.3: *Dimensionless heat release rate perturbations* $\dot{Q}_1/Q_0$ *(blue line) and velocity modulations* v_1/v_0 *(red line) are plotted as a function of the time that is made dimensionless by the period* $T = 1/f$ *associated to the forcing frequency. Upper row:* $f = 20$ Hz. *Middle row:* $f = 100$ Hz. *Lower row:* $f = 200$ Hz. *Left column:* $|v_1/v_0| = 0.1$. *Right column:* $|v_1/v_0| = 0.3$.

the different harmonics. The harmonics can thus be considered as filtered out by the system and the response can be considered as harmonic for all forcing frequencies investigated.
A small peak around 10 Hz is also observed on the PSD presented in Figs. 2.4 and 2.5. It corresponds to the phenomenon of flame flickering [Durox *et al.* (1990); Yuan *et al.* (1994); Kostiuk and Cheng (1994); Bédat and Cheng (1996)], resulting from the unsteady motion of the flame tip due to a buoyancy-induced instability taking place between burnt gases and ambient air.

Heat release rate measurements

The heat release rate ca be estimated using spontaneous OH*, CH* or C_2* radical emission measurements. In the case of premixed flames, with a fixed equivalence ratio, it was shown that the emission intensity of these radicals is proportional to the flame surface area [Hurle *et al.* (1968); Schuller (2003)].

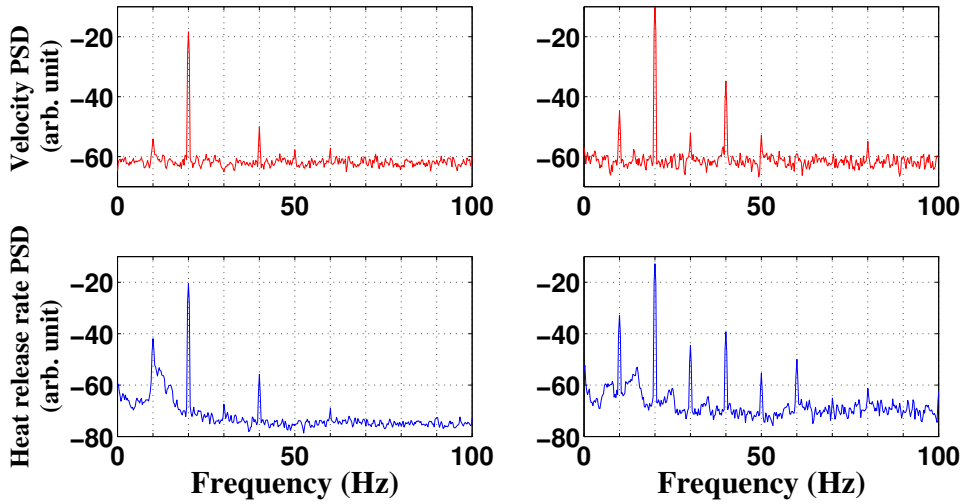

Figure 2.4: *Power spectral density of the velocity signal (red line) and the heat release rate signal (bue line) for a forcing frequency* $f = 20$ Hz *and perturbation levels of* $|v_1/v_0| = 0.1$ *(left) and* 0.3 *(right).*

This is well verified for lean and stoichiometric conical flames where all the reactive mixture is consumed.
A photomultiplier (PM) equipped with an OH* filter is used to collect the chemiluminescence emission from the flame. It is located about 50 cm away from the flame, so that the sensor captures the light emitted by the whole flame. The current delivered by the PM is proportional to the photon flux collected by the detector and emitted from the flame. This signal is converted in a voltage which is acquired through LabVIEW@ for further processing.
Time-resolved signals of the heat release rate are shown in Fig. 2.3 in solid blue lines, for different forcing frequencies $f = 20, 100$ and 200 Hz and for different dimensionless perturbation amplitudes $|v_1/v_0| = 0.1$ and 0.3. The amplitude of the signal decreases as the forcing frequency is increased, highlighting the low-pass filter behavior of the flame. The ratio between the dimensionless amplitudes of the heat release rate and velocity harmonic disturbances defines the FTF gain. It also can be seen that the heat release rate signal is out of phase compared to the velocity signal. This phase difference defines the FTF phase lag.
The heat release rate signals are further studied by determining their PSD. Spectra are shown in Fig. 2.4 for $f = 20$ Hz and in Fig. 2.5 for $f = 100$ Hz, for two different perturbation levels. They exhibit a strong component at the forcing frequency, with some harmonics as the perturbation level is increased. The nonlinearity appears to be stronger in the heat release rate signal than in the velocity signal with contributions up to the fourth harmonic of the forcing frequency. This emphasizes the fact that the flame can be considered as the

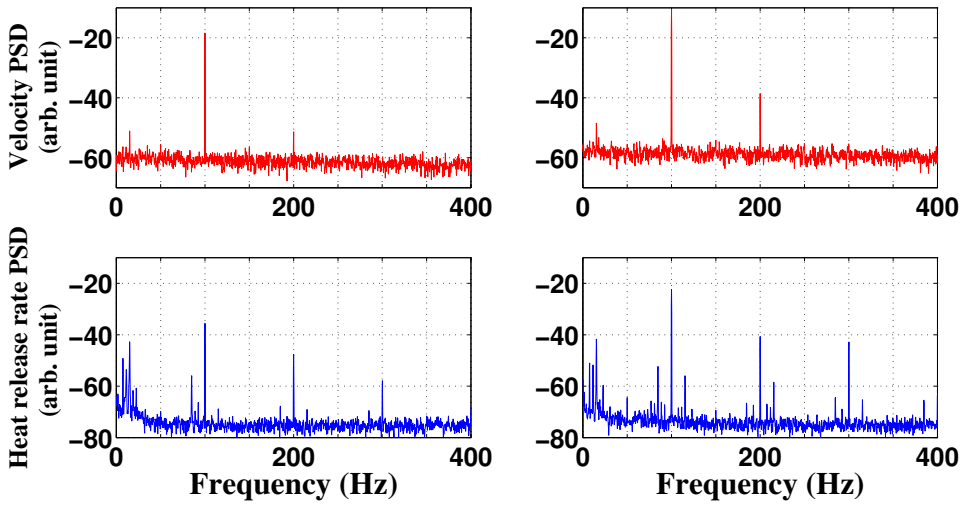

Figure 2.5: *Power spectral density of the velocity signal (red line) and the heat release rate signal (bue line) for a forcing frequency* $f = 100$ Hz *and perturbation levels of* $|v_1/v_0| = 0.1$ *(left) and* 0.3 *(right).*

main nonlinearity in many thermo-acoustic processes [Dowling (1997); Dowling (1999)].
It has to be noted that the contribution around 10 Hz, coming from the buoyancy instability, is more important here than in the velocity signal. This phenomenon can even couple with the acoustic perturbations to create harmonic components at 30 and 50 Hz in Fig. 2.4-right and several peaks around 100 Hz and its harmonics in Fig. 2.5-right.

Flame front visualization

In addition to measurements of velocity and heat release rate signals, flame visualization is used to examine the motion executed by the flame when it is perturbed. An intensified charge-coupled device (ICCD) camera is equipped with a 60 mm Nikkon objective and placed at a distance of 50 cm away from the burner. This camera represented in Fig. 2.2 is used to take 512-by-512 pixel images of both steady and acoustically perturbed flames. The ICCD camera is controlled with a programmable timing generator that is coupled to the WinView 32 software in order to tune the settings and to externally trigger the camera. The camera is used under a repetitive (continuous) gating mode. The following parameters were set for the experiments conducted in this work:

- Gate width: 25 μs.
- Gate delay: 25 ns.
- Exposure time: 50 μs.
- Gain: 100.

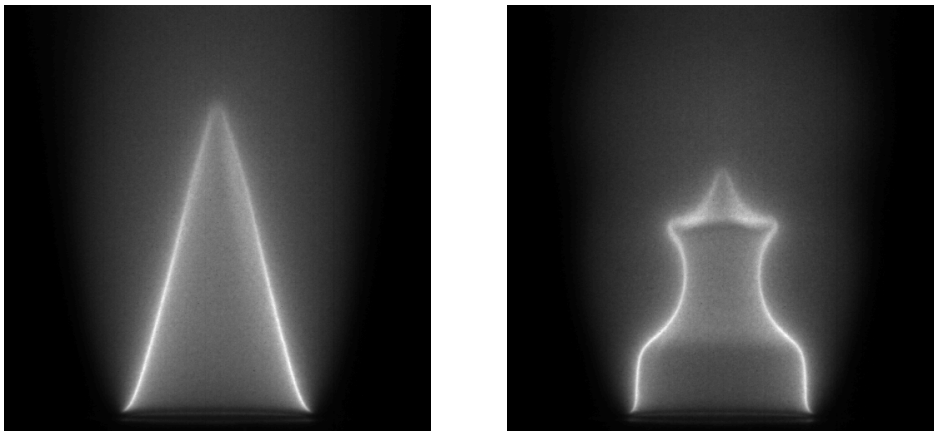

Figure 2.6: *Images of a steady (left) and acoustically perturbed (right) conical flame.* $\phi = 1.03$. $v_0 = 1.56$ m.s^{-1}. *Right figure:* $f = 100$ Hz.

A signal generator or the LabVIEW@ software that is used to drive the Hi-Fi amplifier and the loudspeaker at the bottom of the burner, generates a TTL signal synchronized with the forcing signal. This TTL signal is sent to a delay generator BNC 555 from Berkeley Nucleonics Corporation (BNC). The delayed signal is then used to externally trigger the camera to obtain phase-conditioned images of the flame motion during the modulation cycle. The delay is calculated to obtain equally-spaced phase conditioned images:

$$\Delta t = \frac{n}{Nf} \tag{2.1}$$

where Δt is the time delay with respect to the beginning of the modulation cycle, N the number of images and $n \in [0 : N-1]$. The images are averaged over more than a hundred snapshots per phase to improve the signal-to-noise ratio.
Typical images of steady and perturbed flames are shown in Fig. 2.6. The left figure shows a perfectly conical steady flame and the right figure shows an acoustically perturbed flame that features regular wrinkles along its front. These measurements are used to investigate the dynamics of confined and unconfined flames in Chapters 4 and 6. An extensive set of images are also taken by zooming on the flame base to investigate and characterize the flame base motion in Chapter 5.

Different post-processing of these images can be realized. The images of the steady flames are the first treated. Knowing the burner exit mean velocity v_0,

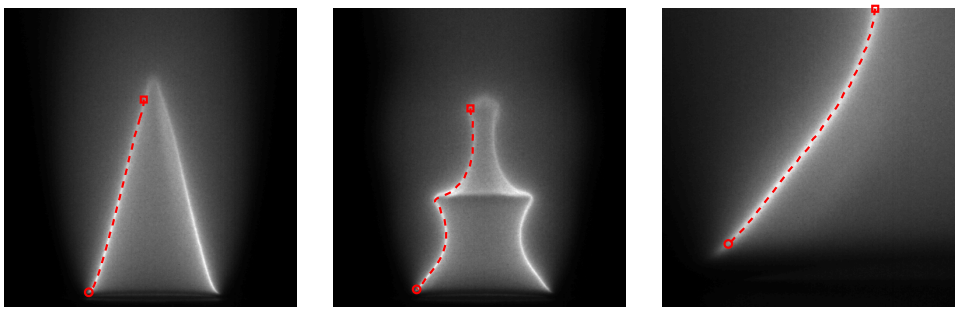

Figure 2.7: *Images of a steady (left) and acoustically perturbed (center) conical flames. A zoomed image of the perturbed flame base is also shown (right). On each image, a dashed red line shows the result of the flame front detection algorithm, with a flame base and tip detection threshold of 60 % of the maximum value.* $\phi = 1.03$. $v_0 = 1.56$ m.s^{-1}.

measurement of the flame front slope enables to determine the flame speed, defined as $S_d = v_0 \sin\alpha$ where α stands for the flame tip half-angle. A flame front detection algorithm was designed to this purpose. It finds the maximum pixel value on each row of the image, and discard every points which value is lower than 60% of the maximum pixel value over the whole image. This threshold level is chosen to determine the flame base location. An example of result of that detection algorithm is shown in Fig. 2.7 for a steady (left figure) and perturbed (center figure) flames. These figures indicate that the flame front is well detected, even when the flame is wrinkled by acoustic perturbations. The only difficulty lies in the determination of the flame tip location, where the luminosity emitted by the flame is not high enough to be properly detected.
This algorithm is also applied on the zoomed images of the flame base, as shown in Fig. 2.7-right. It enables a more accurate identification of the flame base location. The use of that algorithm on phase-conditioned zoomed images allows to obtain the location of the flame base as a function of the phase of the periodic excitation, i.e. as a function of time. This time-resolved signal is thus sampled at a rate of $1/(Nf)$, where f is the acoustic forcing frequency and N is the number of phase-conditioned images per acoustic period. This signal is further used in Chapter 5 to determine experimentally the transfer function relating the incoming velocity perturbation to the induced flame base motion.

2.3 Conclusion

The different burner configurations that are investigated in this work and the diagnostics used were briefly presented in this chapter. This instrumented setup enables to gather data on conical flame dynamics with the possibility of char-

acterizing the unsteady velocity field in the fresh gases and the heat release rate generated by the flame (from which the FTF may be deduced) as well as images of both steady and perturbed flames. In the next chapters, measurements are systematically compared to predictions from analytical models or from numerical simulations to improve our understanding of the response of laminar premixed conical flames to flow perturbations.

Chapter 3

Experimental FTF determination

This chapter focuses on the experimental determination of the Flame Transfer Function (FTF). In the present work, both harmonic and random non-harmonic velocity perturbations are generated to modulate the flame. The first method based on harmonic signals is widely used. The use of random disturbances enables to rapidly determine the FTF compared to the former technique and improves the frequency resolution. A system identification (SI) technique is used to model the frequency response of the different components of the test bench. This model is then used to impose a white noise velocity signal at the burner exit, with a tunable perturbation level. Random flow disturbances combined with SI tools and spectral analysis are used to reconstruct the FTF of laminar conical flames. Experiments are conducted for different operating conditions and forcing levels. Results obtained with the two excitation techniques are compared. Differences are finally examined when the modulation amplitude is increased.

3.1 Introduction

The FTF is generally determined by imposing harmonic velocity modulations. The velocity fluctuations may be determined by Laser Doppler Velocimetry [Durox *et al.* (2009)] or with a hot wire probe [Palies *et al.* (2010)]. A photodiode or a photomultiplier equipped with a CH* or OH* filter is generally used to determine the resulting heat release rate fluctuations [Hurle *et al.* (1968); Ducruix *et al.* (2000); Paschereit *et al.* (2002); Balachandran *et al.* (2005); Kim *et al.* (2010)]. These signals are gathered and post processed by calculating the cross- and auto-power spectra to obtain the FTF. The FTF may also be deduced from a multiple microphone techniques. The same type of procedure can be used to determine the Flame Describing Function (FDF) when the perturbation level needs to be considered. In this case, the velocity perturbation

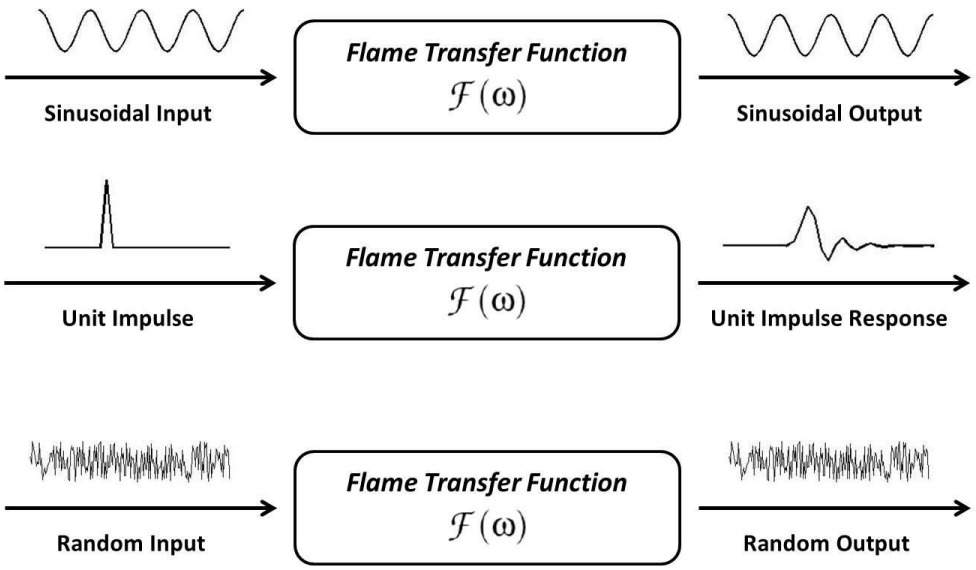

Figure 3.1: *Different input signals can be used to determine the FTF, such as harmonic signals, unit impulse or random signals.*

level is first fixed to a small value and kept constant over the forcing frequency range investigated. Measurements are then repeated to obtain a set of FTF at different forcing levels [Noiray *et al.* (2008); Durox *et al.* (2009); Palies *et al.* (2010); Schimek *et al.* (2011)].

Recently, alternatives to determine transfer functions in aeroacoustics have been tested to reconstruct this frequency response with numerical simulations. Following the theory of system identification (see [Ljung (1999)] for example), these methods require the use of broadband frequency signals or unit impulse signals to perturb the system as shown in Fig. 3.1. The resulting velocity and heat release rate signals recorded by the sensors are used to retrieve the coefficients of a filter approximating the FTF. In the simulations from Polifke *et al.* (2001), the auto- and cross-correlation matrices between velocity and heat release rate signals were numerically computed and an inversion of the Wiener-Hopf equation was performed:

$$\Gamma h = c \tag{3.1}$$

where Γ is the auto-correlation matrix of the velocity signal and c is the cross-correlation matrix of the heat release rate and velocity perturbation signals. Equation 3.1 was used to determine the unit impulse response h, which z-transform is the acoustic transfer function that can be approximated as a Finite Impulse Response (FIR) filter. The same type of tool were used, but coupled to several broadband noisy signals to modulate a swirling flame and retrieve

the FTF with a good accuracy [Huber and Polifke (2009a); Huber and Polifke (2009b)]. A space-dependent FTF was numerically approximated by Zhu *et al.* (2005) using a sum of random-phase sinusoids to modulate the flow and an auto-regressive exogeneous model to compute the filter coefficients of the flame Infinite Impulse Response (IIR).
Recently, these techniques have been put to work in several numerical investigations of the response of swirl stabilized flames to flow perturbations. These methods were validated by comparisons with FTF obtained experimentally [Tay-Wo-Chong *et al.* (2010)]. They were then used to examine the influence of several parameters on the FTF, such as the width of the combustion chamber confining the flame and effects of heat loss [Tay-Wo-Chong and Polifke (2012)]. Differences between results obtained with LES and URANS simulations were also analyzed [Tay-Wo-Chong *et al.* (2012)].

In the present work, these alternative methods of flow perturbations and analysis of flame response are tested experimentally. They are used to determine the FTF of a conical flame. It is shown that random velocity perturbations can be used instead of harmonic signals to obtain results with a better frequency resolution in a shorter time. The theoretical framework for FTF determination with harmonic or non-harmonic signals is first presented. The procedure developed in this work to control the velocity forcing signal at the burner nozzle outlet is then presented. This method enables to generate a nearly white noise velocity perturbation signal at the burner outlet. Spectral analysis is then used to compare results for the FTF obtained with harmonic and random velocity perturbations. Effects of the input level are examined at the end of the chapter. A sensitivity analysis is also conducted to determine the influence of the number of coefficients used to built the IIR filter that models the flame response.

3.2 Flame Transfer Function determination

The FTF relates velocity perturbations at the burner outlet to heat release rate perturbations. The type of forcing signal used to determine this response is an important aspect of the methodology and can take different forms as shown in Fig. 3.1. Two kinds of forcing signal are tested here: harmonic and random signals.

3.2.1 Harmonic perturbation technique

To analyze the flame response in the Fourier space, a set of harmonic velocity perturbations $v_1(t)$ may be produced at different forcing frequencies as described in Chapter 2. These signals are defined by an amplitude $|v_1|$ and a real angular frequency ω so that $v_1(t) = \Re\{|v_1|e^{-i\omega t}\}$ where $\Re$, $|v_1|$ and ω respectively stands for the real part of a complex number, the amplitude and the angular frequency of the velocity perturbation. The flame response to this har-

monic perturbation is not necessarily a harmonic signal [Schuller *et al.* (2003b)] (see also Chapter 2). The heat release rate is thus filtered around the forcing frequency and one obtains a harmonic signal that is delayed compared to the velocity signal: $\dot{Q}_1(t) = \Re\{|\dot{Q}_1|e^{-i\omega(t-\varphi)}\}$ where $|\dot{Q}_1|$ is the amplitude of the heat release rate signal and φ is the phase difference between velocity and heat release rate signals examined at the forcing frequency. The FTF may then be determined at the forcing frequency. It corresponds to the ratio of the complex heat release rate disturbance divided by the complex velocity perturbation. This complex numbers are generally expressed in terms of a gain G and a phase difference φ between heat release rate and velocity fluctuations. To improve the signal to noise ratio, one possibility is to determine the FTF by calculating the cross-spectral density $S_{v_1,\dot{Q}_1}$ of heat release rate and velocity perturbations and the power spectral density S_{v_1,v_1} of the velocity perturbations. This operation is repeated for a set of discrete forcing frequencies covering the range of frequency where the FTF gain differs from zero. One obtains:

$$\mathcal{F}(\omega) = \frac{S_{v_1,\dot{Q}_1}(\omega)}{S_{v_1,v_1}(\omega)} = G(\omega)e^{i\varphi(\omega)} \tag{3.2}$$

Long windowed time series can be used along with averaging techniques in order to reach statistical convergence:

$$\mathcal{F}(\omega) = \frac{1}{N}\sum_{k=1}^{N}\frac{S^k_{v_1,\dot{Q}_1}(\omega)}{S^k_{v_1,v_1}(\omega)} \tag{3.3}$$

where $S^k_{v_1,\dot{Q}_1}(\omega)/S^k_{v_1,v_1}(\omega)$ is the FTF determined over the k^{th} window and N is the number of windows used to average the flame frequency response.

Examples of FTF determined with this method are shown in Figs. 3.2 and 3.3. These FTF were measured by acquiring velocity and chemiluminescence signals with a sampling frequency $f_s = 16384$ Hz during an acquisition time equal to 2 s. The corresponding number of samples is equal to 32768. No averaging methods were used here. The FTF presented in Fig. 3.2 were determined with the beveled burner shown in Fig. 2.1. Results in Fig. 3.2-left are compared for two different flow velocities, all other parameters being kept constant. The FTF gain features a low-pass filtering behavior while the FTF phase lag features a regular increase with the forcing frequency associated to a hydrodynamic convective process before reaching an almost constant value at high frequencies. Figure 3.2 shows that the inlet flow velocity has a weak influence on the FTF at low frequencies in the cases investigated. The reason is that the FTF only depends on $\omega_* = \omega R/(S_d \cos\alpha)$ for elongated flame (when $\alpha \ll 1$). One can also assume that $\cos\alpha \simeq 1$ and thus ω_* weakly depends on the inlet flow velocity. Only small differences appear for frequencies higher than 100 Hz, where the

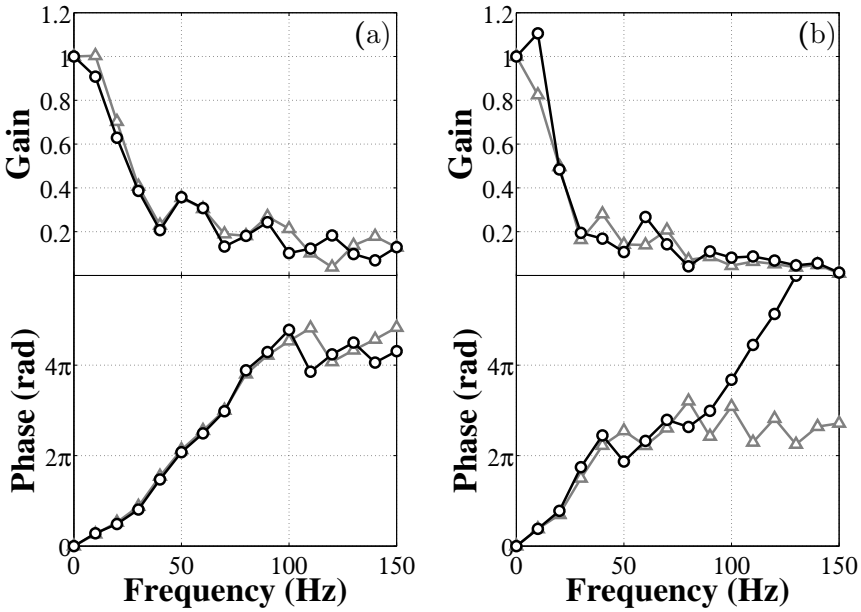

Figure 3.2: *Flame Transfer Function gain (top) and phase (bottom) as a function of the acoustic perturbation frequency. (a) FTF measured on the 22 mm-diameter beveled burner exit. $\phi = 1.1$. Black line: $v_0 = 1.3$ $m.s^{-1}$ Grey line: $v_0 = 2.5$ $m.s^{-1}$ (b) FTF measured on the 30 mm-diameter beveled burner exit. Black line: $v_0 = 1.27$ $m.s^{-1}$. $\phi = 0.8$ Grey line: $v_0 = 1.3$ $m.s^{-1}$. $\phi = 1.1$.*

FTF gain extrema and the FTF phase oscillations slightly differ between the two cases explored in Fig. 3.2-left.
The same behaviors are observed on the 30 mm-diameter beveled burner where the equivalence ratio is used as a varying parameter (see Fig. 3.2-right). A small difference in the FTF phase slope is observed, due to the difference in the equivalence ratio ϕ and thus on the flame speed S_d. This observation results from the dependence of ω_* on S_d. The reduced frequency ω_* is proportional to the inverse of the flame speed S_d. FTFs measured with a plateau-shaped burner are plotted in Fig. 3.3-left. Measurements obtained with a plateau show no major differences compared to those obtained with the beveled edge burner, except for the FTF phase lag at high frequencies. In Fig. 3.3-right, FTF measured with a confinement tube are plotted. This figure shows that a difference in phase slope appears between the FTFs determined with different inlet flow velocities. A significant phase difference of about 0.4π is observed around 100 Hz between the two cases. This problem is treated in Chapter 6.

3.2.2 Random perturbation techniques

Measurements of the FTF with harmonic signals are fairly long. One difficulty is that experiments must be repeated for each forcing frequency investigated.

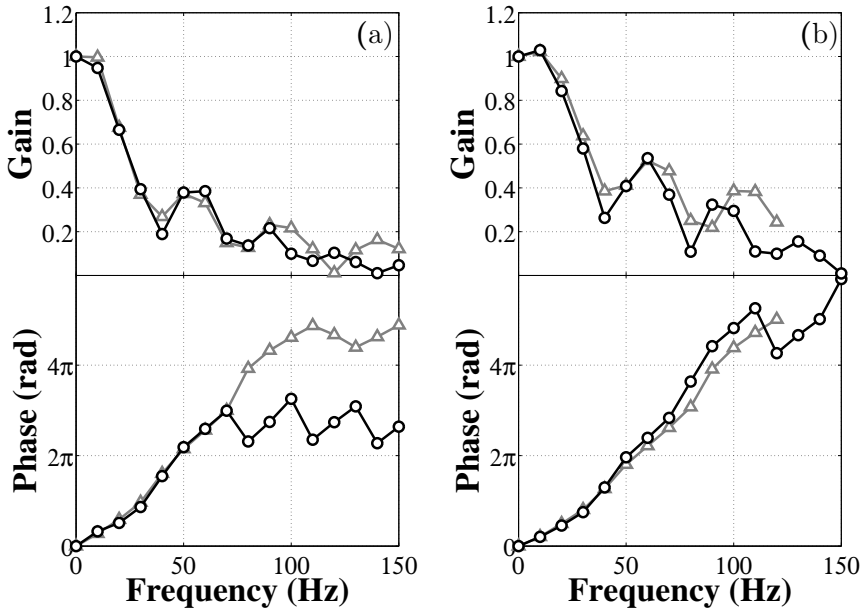

Figure 3.3: *Flame Transfer Function gain (top) and phase (bottom) as a function of the acoustic perturbation frequency. (a) FTF measured on the 22mm-diameter burner exit with a 35 mm-diameter plateau. $\phi = 1.1$. Black line: $v_0 = 1.3\ m.s^{-1}$ Grey line: $v_0 = 2.5\ m.s^{-1}$ (b) FTF measured on the 22 mm-diameter burner exit with a 35mm-diameter confinement tube. $\phi = 1.1$. Black line: $v_0 = 1.34\ m.s^{-1}$ Grey line: $v_0 = 2.27\ m.s^{-1}$*

Multi-tone signals have been proposed as an alternative technique to excite the flame. Imposing random multi-tone velocity perturbations enables to modulate the flame over a large frequency range. This can be used to obtain the whole FTF at once, but also to increase the frequency resolution of the FTF determination. In the following, a white noise signal is used as a random multi-tone excitation signal to determine the flame response. This excitation signal is defined by:

$$v_1(t) = |v_1|\ \mathrm{rand}_{[-1,1]} \tag{3.4}$$

where $|v_1|$ is the velocity perturbation amplitude and $\mathrm{rand}_{[-1,1]}$ stands for a random number generator which results are statistically uniformly distributed over the interval [-1,1]. With such a white noise signal, it is possible to excite the flame with an equally distributed power over a large range of frequencies. This synthetic signal may be easily generated and was already used in numerical simulations [Huber and Polifke (2009b)]. Its generation raises some experimental difficulties which must be overcome as further described in this study.

Adapted post-processing techniques were developed to compute the FTF from random velocity modulations. Cross-power spectral density analysis is a natural first choice to examine the flame response. The use of a random input signal enables to determine the FTF over a wide frequency range. The auto and cross-power spectral densities of the input v_1 and output $\dot{Q}_1$ signals can easily be computed by making use of Eq. (3.3).
When only a limited number of time samples are available (as for the results of LES simulations for example), System Identification (SI) methods can also be used to compute the linear FTF from time series of the input (incoming velocity perturbations) and output (heat release rate perturbations) signals. A SI method based on the reconstruction of an IIR model of the flame is used in the following to determine the system impulse response. This impulse response $h(t)$ completely defines a linear process:

$$\dot{Q}_1(t) = \int_{-\infty}^{+\infty} h(\tau) v_1(t-\tau) d\tau \tag{3.5}$$

where $v_1(t)$ and $\dot{Q}_1(t)$ are the input and output signals of the process. This equation can be approximated in a discrete form by an IIR discrete filter:

$$\begin{aligned} &\dot{Q}_1^{(n)} + a_1 \dot{Q}_1^{(n-1)} + ... + a_{n_a} \dot{Q}_1^{(n-n_a)} \\ &\qquad = b_0 v_1^{(n)} + b_1 v_1^{(n-1)} + ... + b_{n_b} v_1^{(n-n_b)} + e(t) \end{aligned} \tag{3.6}$$

where $v_1^{(i)}$ and $\dot{Q}_1^{(i)}$ are the sampled input and output signals, a_i and b_i stand for the reverse and forward coefficients of the IIR filter, n_a and n_b define the order of the model and $e(t)$ denotes the background noise disturbance. A sufficient number of coefficients n_a and n_b have to be chosen to take into account the largest time lag involved in the system. This point will be further examined for the FTF determination in Section 3.5. By taking the z-transform of Eq. (3.6), one obtains an approximation of the FTF as an IIR filter of the form:

$$\mathcal{F}(\omega) = \frac{\sum_{k=0}^{n_b} b_k z^{-k}}{\sum_{k=0}^{n_a} a_k z^{-k}} \tag{3.7}$$

where $z = \exp(i\omega)$, ω being the angular frequency.

3.3 Loudspeaker, amplifier and burner transfer function

Random velocity disturbances with a white noise spectrum must be generated at the burner outlet to keep the velocity modulation level constant over the frequency range investigated. The white noise electrical signal can be generated with the LabVIEW@ software. This signal is sent to the amplifier followed by the loudspeaker to modulate the flow in the burner cavity as represented in Fig. 3.4-left. It is interesting to first characterize the resulting velocity perturbation signal at the burner exit. When the flow is acoustically forced with a harmonic signal, it was shown in Chapter 2 that the flow is also responding harmonically. In this case, the amplitude of the velocity modulation can be measured by LDV and tuned to keep the same forcing level for each frequency investigated. When random broadband velocity fluctuations are synthesized, the situation is different. The response can be first examined by plotting the power spectral density of the velocity signal measured at the burner outlet and can be compared with the power spectral density of the random signal generated by the signal synthesizer.
Figure 3.5-top shows large differences between the perturbation level reached by the resulting velocity modulations over the frequency range of interest. This signal does not correspond to a white noise signal, but features a colored spectrum. This is due to the combined responses of the loudspeaker, amplifier and burner which filter the perturbations. This response can be characterized by the transfer function $\mathcal{H}(\omega)$ represented in Fig. 3.4 that must be determined.
A system identification is conducted to characterize the transfer function $\mathcal{H}(\omega)$ of the elements formed by the amplifier, the loudspeaker and the burner. By using the white noise signal $L_1(t)$ generated with LabVIEW@ and gathering the velocity disturbances produced at the burner exit, it is possible to determine the transfer function $\mathcal{H}(\omega)$ defined as follows :

$$\mathcal{H}(\omega) = \frac{\tilde{v}_1/v_0}{\tilde{L}_1} \tag{3.8}$$

where L_1 stands for the LabVIEW@-generated white noise signal used as an input to drive the amplifier. This signal was measured with a sampling frequency of 4096 Hz. A total of $n_a = 50$ and $n_b = 50$ filter coefficients were used to reach a good estimation of $\mathcal{H}(\omega)$. As shown in Fig. 3.5-top, this frequency response corresponds to a pass band filter where frequencies lower than 80 Hz and higher than 200 Hz are greatly damped. A correction needs to be applied to compensate the effects of the amplifier and the loudspeaker and flatten this frequency response.

To generate a white noise velocity signal at the burner outlet, the inverse transfer function $\mathcal{H}^{-1}(\omega)$ was first applied to the LabVIEW@ white noise electrical

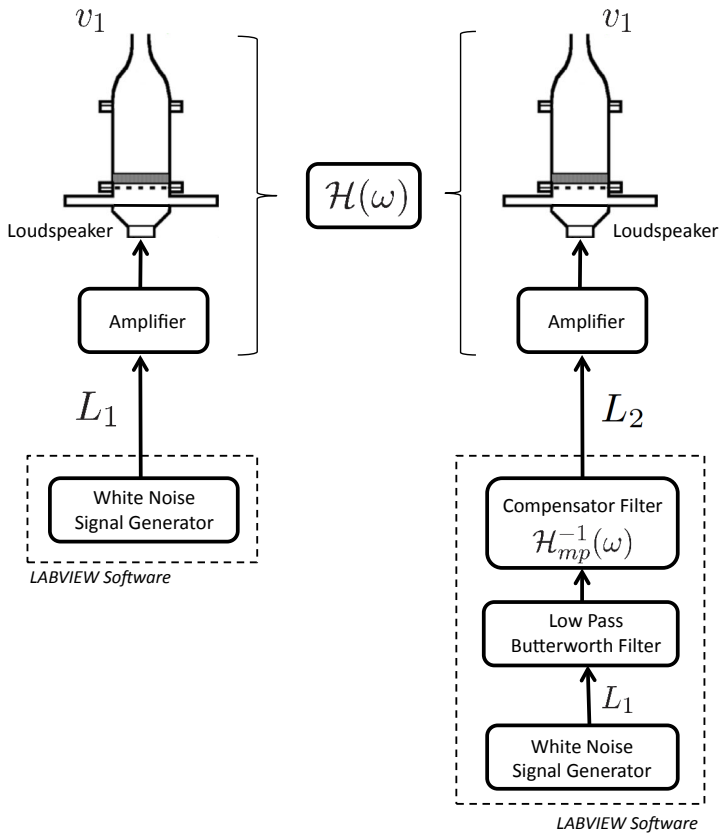

Figure 3.4: *Diagram of the setup used to obtain uncontrolled (left side) and controlled (right side) flow modulations v_1 at the burner exit.*

signal. The resulting signal, not shown here, clearly exhibited that $\mathcal{H}^{-1}(\omega)$ was unstable. Some of the zeros of the function $\mathcal{H}(\omega)$ were out of the unit circle. To cope with that issue, we choose to compute the minimum-phase inverse transfer function $\mathcal{H}_{mp}^{-1}(\omega)$, which is a stable transfer function that has the same exact gain as $\mathcal{H}^{-1}(\omega)$, but has a different phase [Oppenheim *et al.* (1998)]. As we are here dealing with random phase signals, inverting the magnitude of $\mathcal{H}(\omega)$ to obtain a nearly-white-noise velocity disturbance signal at the burner outlet is essential whereas the phase of the resulting velocity signal is of less importance. This new filter $\mathcal{H}_{mp}^{-1}(\omega)$ features now a stable response with smooth transitions between frequencies but the resulting signal still contains high frequencies with significant power spectral densities. This can easily be removed by low pass filtering this response. We choose a 20^{th} order Butterworth filter with a cut-off frequency of 500 Hz to this purpose. These successive operations were used to produce velocity disturbances with an almost constant frequency response up to 500 Hz and remove the upper frequencies well above the cut-off frequency of the flame response. The PSD of the resulting velocity signal is shown in

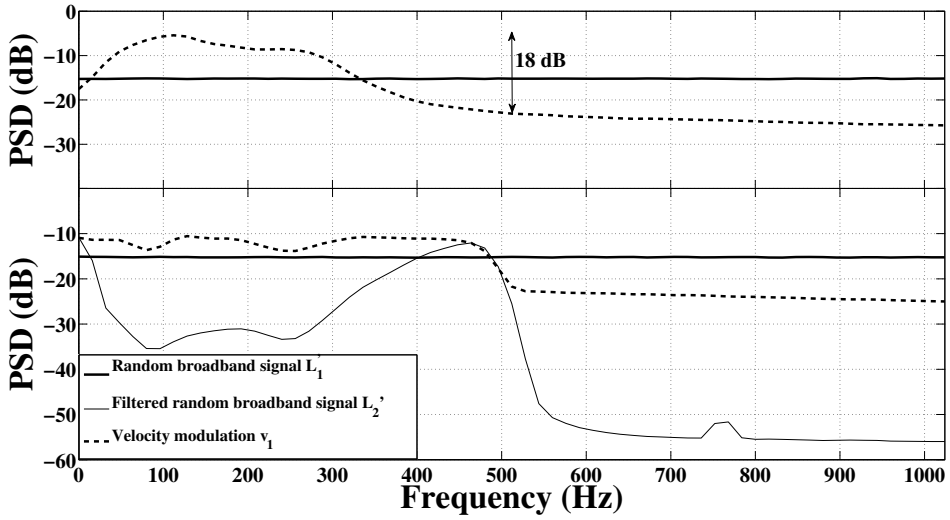

Figure 3.5: *Power spectral densities of* **(top figure)** *(—) the random broadband signal L_1 and (- - -) the uncontrolled velocity perturbations v_1* **(bottom figure)** *(—) the random broadband signal L_1, (...) the broadband signal L_2 resulting from the filtering of L_1 by $\mathcal{H}_{mp}^{-1}(\omega)$ and (- - -) the resulting controlled velocity perturbations v_1.*

Fig. 3.5-bottom. It has a nearly uniform power density over the frequency range of interest. The difference between the maximum and the minimum of the PSD is reduced to less than 5 dB. This value can be compared to the 18 dB difference observed for a velocity signal generated by driving the amplifier with a white electrical noise without correction (see Fig. 3.5-top). This pre-processing procedure can now be used to generate random velocity fluctuations at the burner outlet and compare the flame response to the ones obtained for harmonic flow modulations. The entire procedure is schematically shown in Fig. 3.4-right.

3.4 FTF determination using random signals

The flame response is first examined for small amplitude velocity perturbations. Results for the FTF determined with random and harmonic velocity modulations are presented in Fig. 3.6. Measurements were carried out on a 22 mm-radius burner corresponding to the configuration (b) in Fig. 2.1 and a flame with the following parameters: $v_0 = 1.56$ m.s^{-1} and $\phi = 1.03$. For harmonic perturbations, the FTF is measured between 20 and 250 Hz, with a 5 Hz frequency resolution. The harmonic signals were sampled at a rate $f_s = 4096$ Hz over 20 s, what lead to the acquisition of 81920 samples for each frequency.

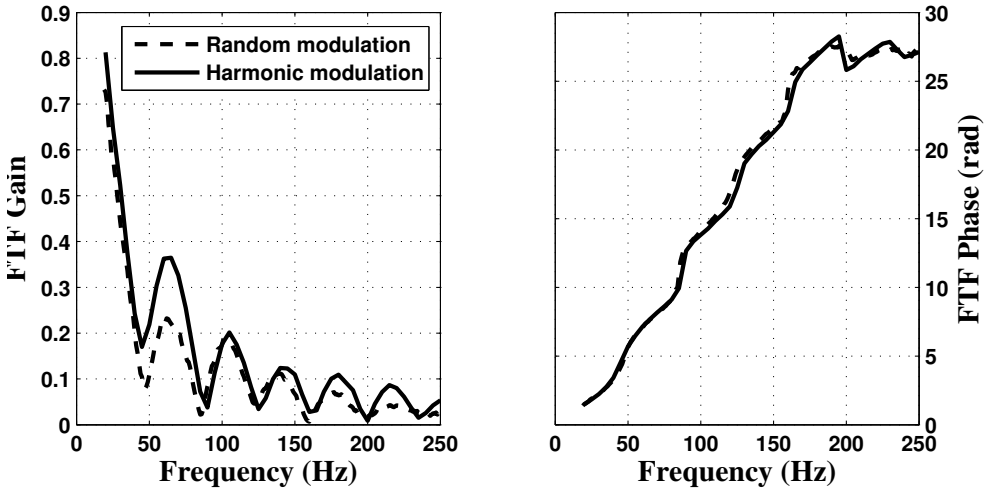

Figure 3.6: *FTF obtained with harmonic and random velocity modulations and power spectral analysis, for a relative rms velocity perturbation of* $v_1^{\mathrm{rms}}/v_0 = 0.04$.

An averaging technique with 20 windows was used. For random perturbations, data were collected and averaged over 600 windows of 4096 samples each. The sampling frequency was also fixed to 4096 Hz yielding a 1 Hz frequency resolution for the FTF measured with random disturbances.
In this case, the results collapse well with both methods of excitation. The random signal method retrieves the main characteristics of the response of this conical flame. The FTF gain is well captured up to 45 Hz, where the flame response is strong. For higher excitation frequencies, the random modulation technique shows some differences on the gain, but it still captures the correct evolution of the gain, as well as the position of the minima and maxima of the FTF gain. For the FTF phase, both methods give the same results. Both random and harmonic modulation techniques show that the phase increases regularly with the frequency up to about 200 Hz. This evolution highlights the convective nature of the flame response. This behavior ceases at higher frequencies when the phase reaches a constant value [Kornilov *et al.* (2007); Durox *et al.* (2009); Karimi *et al.* (2009)]. This saturation is also well predicted by both techniques. This is in agreement with previous theoretical and experimental results on conical flame transfer functions, where the nearly constant slope of the phase can be linked to a convection time lag [Schuller *et al.* (2003a)]. The saturation phenomenon observed at higher frequencies is suspected to be induced by the contribution of the flame base dynamics to the FTF response [Kornilov *et al.* (2007); Karimi *et al.* (2009)]. This issue is considered in detail in Chapter 5.
It is now interesting to briefly examine some advantages of using random flow perturbations. It is first worth noticing that the harmonic modulation method take about 30 mn to determine a FTF, with a 5 Hz frequency resolution, while

the cross-correlation technique was carried out in 10 mn, with a 1 Hz frequency resolution. If it represents some improvement on the reduction of duration of experiments, the main advantage is to improve the frequency resolution. Window overlap could also be used for the average cross-correlation technique, which again could divide by 2 (for a 50% overlap) the number of samples needed to reach statistical convergence of the method. This technique was used here on a specific configuration where the flame response vanishes for frequencies above 250 Hz. There are many configurations where flames feature a significant response at much higher frequencies. The determination of the FTF would require about the same duration with the random modulation technique, but a considerable additional time to conduct the experiments with harmonic modulations at higher forcing frequencies, if the frequency resolution were kept constant. Another advantage is that the better frequency resolution reduces significantly ambiguities about critical points of the FTF near maxima and minima for the gain and for frequencies where the phase lag approaches π (modulo 2π) if no attempt is made to unwrap results. It is known that the FTF may feature large and sudden changes in gain or phase as a function of frequency that may be difficult to capture with harmonic forcing. The alternative technique used herein avoids having an a-priori knowledge of the FTF where these critical points are located and avoids refining the investigation in these frequency bands.
SI tools were also used to post-process the time resolved data obtained with random broadband disturbances. The FTF gain and phase curves (not shown here) obtained with those tools were compared to the FTF determined with averaged cross-spectral density. The FTF gain and phase curves obtained with both post-processing methods collapse for all configurations investigated.

Modulation level effects

FTF determination with multi-tone methods work well for vanishingly small perturbations when the flame response remains linear. It is now interesting to examine effects of the perturbation amplitude. The FTF has been determined for different velocity fluctuation levels. Results for the same configuration, $v_0 = 1.56$ m.s^{-1} and $\phi = 1.03$, are presented in Fig. 3.7 when the overall perturbation level is increased. Measurements with harmonic and random excitation methods are also compared in Figs. 3.8, 3.9 and 3.11, for increasing rms velocity perturbations $v_1^{\text{rms}}/v_0 = 0.07$, 0.12 and 0.18, respectively.
As indicated in Fig. 3.7, both methods result in the same type of curves for the FTF when the velocity perturbation level increases. When the velocity amplitude increases, the gain decreases and an early saturation of the phase is observed. This is in agreement with previous experimental data obtained on the same type of configuration when submitted to harmonic disturbances of increasing perturbation levels [Durox *et al.* (2009); Karimi *et al.* (2009)].
For a modulation level of $v_1^{\text{rms}}/v_0 = 0.07$, both methods yield the same response as shown in Fig. 3.8. There are some differences in the FTF gain values, but

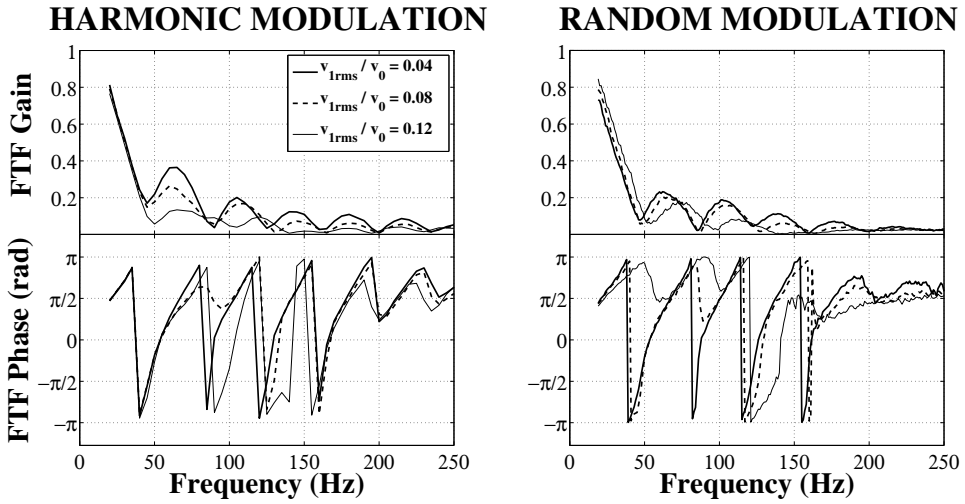

Figure 3.7: *Gain and phase of the FTF obtained for different velocity perturbation levels. Left: results obtained with harmonic modulation. Right: results obtained with random disturbances.*

the global shape of the gain curve and the locations of extrema are still well retrieved. The FTF phase also exhibits a very good match between the two excitation techniques. Results are presented in Fig. 3.9 for a higher perturbation level $v_1^{\text{rms}}/v_0 = 0.12$. The phase curves feature large differences between 50 and 200 Hz. For larger frequencies, the saturation of the phase lag is again retrieved with the two techniques, but the saturation value at high frequencies is different. It is however found that these asymptotic values match modulo 2π.

The main differences observed in the measurements essentially lie in the combined effects of the phase dependence to the perturbation level, and of unwrapping the phase across π where the phase is difficult to define precisely for small values of the gain. At intermediate forcing levels, the phase evolution may switch between a regular increase and a saturation with frequency. This behavior is very sensitive to the perturbation level. A small difference in the rms value of velocity perturbations between harmonic and random excitation methods may trigger the transition between these two regimes at different frequencies. The phase evolution wrapped between 0 and 2π is presented in Fig. 3.10. This figure shows that the saturation frequency shifts from about 170 Hz when the flame is submitted to harmonic modulations to 140 Hz when the flame is submitted to random velocity modulations with the same rms value. Outside of this frequency range, the main behavior and the saturation value are well retrieved.

For a perturbation level of $v_1^{\text{rms}}/v_0 = 0.18$, presented in Fig. 3.11, the FTF gain is underestimated by the random modulation technique between 50 and

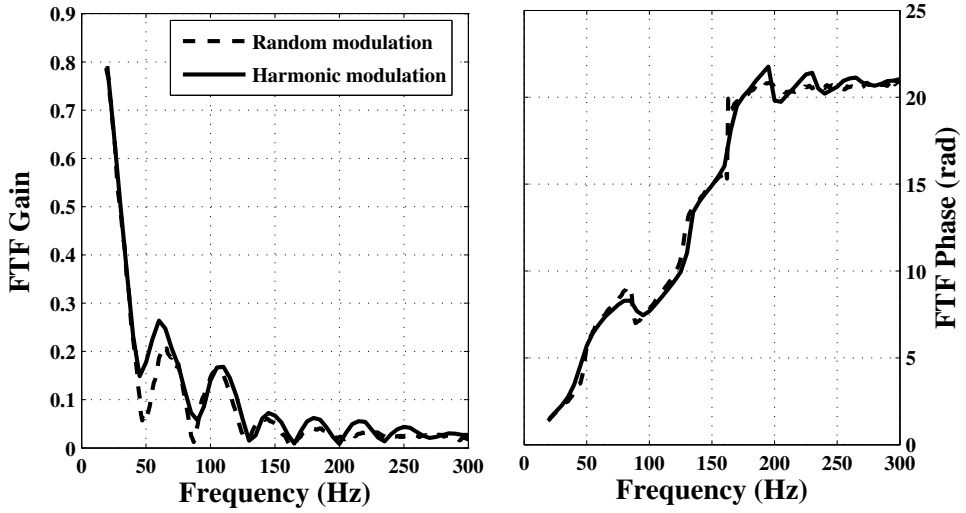

Figure 3.8: *FTF obtained with harmonic and random velocity modulation and cross-correlation techniques, for a relative rms velocity perturbation of* $v_1^{\mathrm{rms}}/v_0 = 0.07$.

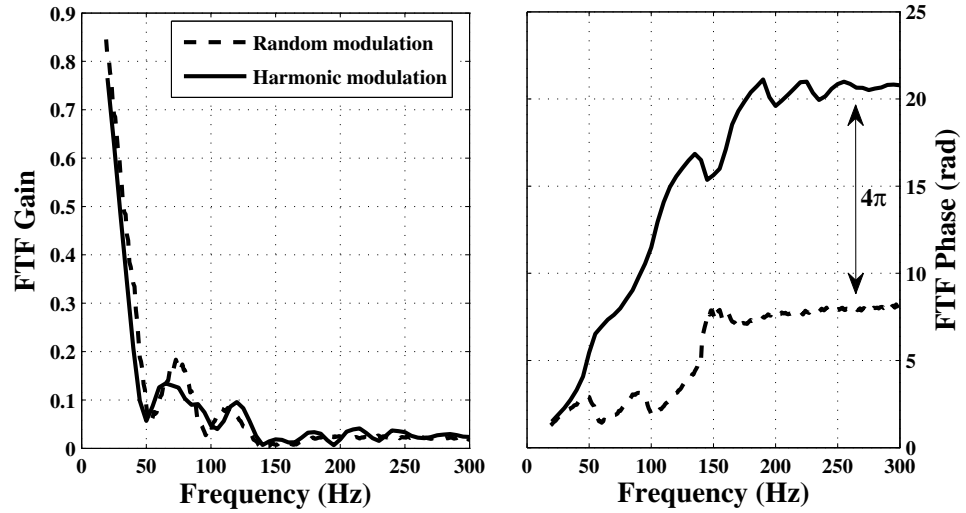

Figure 3.9: *FTF obtained with harmonic and random velocity modulation and cross-correlation techniques, for a relative rms velocity perturbation of* $v_1^{\mathrm{rms}}/v_0 = 0.12$.

150 Hz, while the phase curves still fit well between both measurement techniques. It is however worth noticing that the slope of the phase curve takes a smaller value compared to measurements performed at a lower input level. This phenomenon is due to a shortening of the conical flame when submitted to large velocity perturbations. A reduction in flame height induces a decrease of the average time for a velocity disturbance to produce a heat release rate perturbation. This in turn modifies the slope of the phase of the FTF.

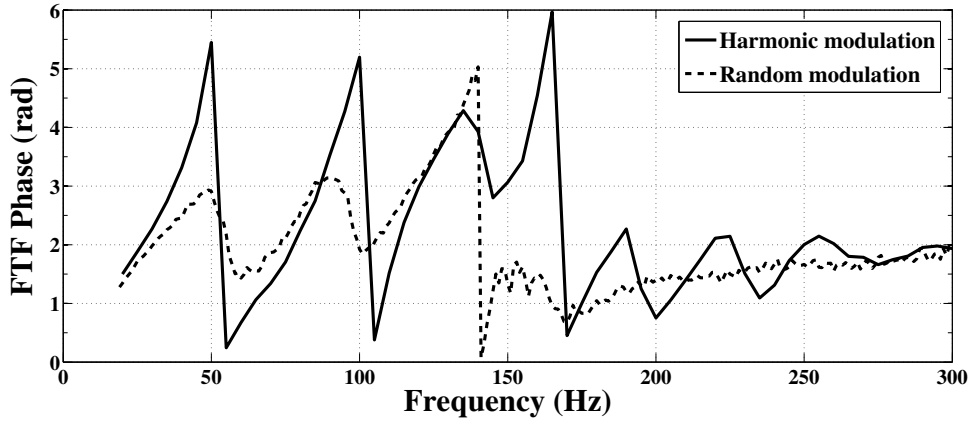

Figure 3.10: *Phase lag of the FTF, wrapped between* 0 *and* 2π*, for a relative rms velocity perturbation of* $v_1^{\mathrm{rms}}/v_0 = 0.12$ *when the flame is submitted to harmonic (-) or random (–) velocity disturbances.*

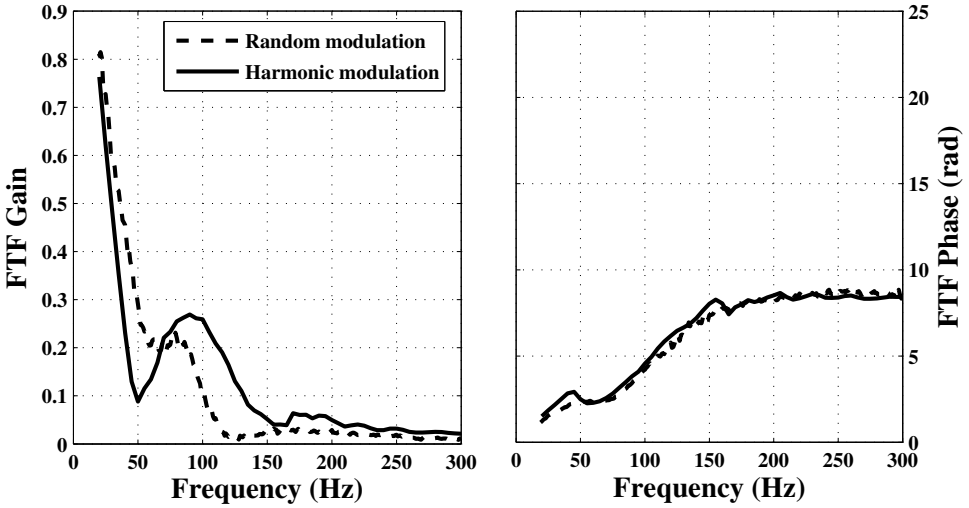

Figure 3.11: *FTF obtained with harmonic and random velocity modulation and cross-correlation techniques, for a relative rms velocity perturbation of* $v_1^{\mathrm{rms}}/v_0 = 0.18$*.*

These results clearly show the limits of the random modulation technique for large velocity disturbances. It is known that the flame response is nonlinear [Dowling (1997)]. Using harmonic perturbations, the gain and the phase lag of the flame response with respect to the incoming perturbations are only analyzed at the forcing frequency. This yields the FTF in the first harmonic approximation while higher harmonics are discarded in this description. Measuring the FTF with random broadband velocity perturbations includes in addition the flame response at different harmonics. The FTF determined with this latter

technique and examined at a certain frequency includes information on the non-linearity of the flame response at others frequencies than the forcing frequency [Moeck and Paschereit (2012)]. This, along with the sensitivity of the phase lag to the velocity input level, explains the differences observed between results for the gain and the phase of the FTF obtained with the two techniques. New techniques must then be developed to characterize the flame frequency response when the input level needs to be considered.

3.5 SI parameter optimization

A sensitivity analysis is carried out in this section on the parameters of the SI method, to emphasize their influence on the determination of the FTF. As mentioned in Section 3.2.2, an important set of parameters that need to be considered for the flame response model in the identification step is the number of forward and reverse filter coefficients n_a and n_b appearing in Eq. (3.7). In this study, n_a and n_b were chosen equal $n = n_a = n_b$. By increasing the number n, more samples in the time series are considered to build an IIR model of the flame response. This number must be chosen to capture the slowest time scale controlling in the flame dynamics. As a first approximation, it can be considered that this number is mainly linked to the largest time lag of the flame response. In the case of a conical flame, this time lag corresponds to the time for a flame front perturbation to travel from the flame base to the flame tip. This time lag is given by [Baillot *et al.* (1992); Blumenthal *et al.* (2013)]:

$$\tau_{\max} = \frac{L}{v_0 \cos\alpha} = \frac{R}{S_d \cos\alpha} \tag{3.9}$$

where v_0 and L respectively stand for the mean flow velocity and the flame front length. In this expression, α denotes the flame angle with respect to the main flow direction. In the case presented here, $v_0 = 1.56$ m.s^{-1}, and $L = R/\sin\alpha$ where $R = 0.011$ m is the burner radius and $\sin\alpha = S_d/v_0$ where $S_d = 0.44$ m.s^{-1} is the flame speed determined by matching the theoretical and experimental steady flame heights. One finds here $\tau_{\max} = 26$ ms. The minimum number of coefficients can be deduced: $n = \tau_{\max}/\Delta t$ where Δt is the sampling time step. For a sampling frequency of 4096 Hz, this yields a value $n = 107$.

A parametric study is conducted to analyze the effect of the number of coefficients n considered in the determination of the gain of the FTF with SI tools. The difference between the gain G_{SI} obtained with the SI method and the gain G_{CC} determined with the cross-correlation technique is calculated for the conical flame $v_0 = 1.56$ m.s^{-1}, $\phi = 1.03$ submitted to random small velocity disturbances when $v_1^{\text{rms}}/v_0 = 0.04$, all other parameters in the signal post-processing remaining identical. Results are shown in Fig. 3.12. They indicate that the difference computed as $|G_{CC} - G_{SI}|$ converges towards zero as

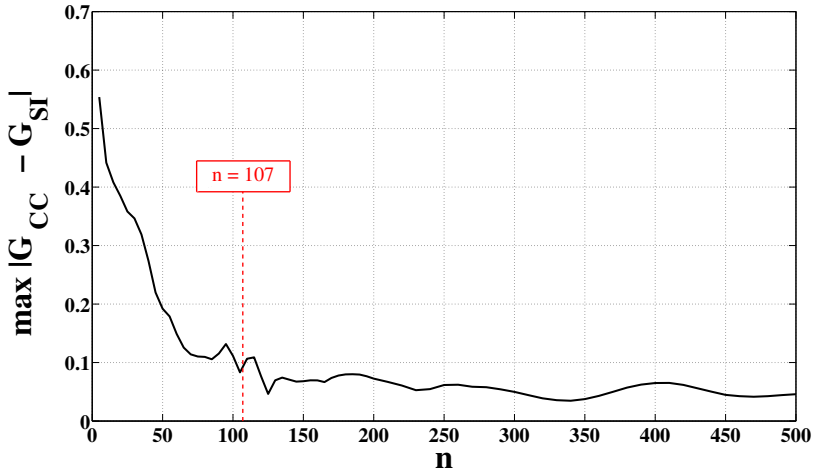

Figure 3.12: *Convergence of the SI method. The gain difference* $|G_{CC} - G_{SI}|$ *is plotted as a function of the number of coefficients* $n = n_a = n_b$ *used to model the IIR flame response.* $v_1^{\text{rms}}/v_0 = 0.04$.

n increases. Results do not improve for a number of coefficients larger than 120, indicating that the estimation in Eq. (3.9) of the minimum number of coefficients required to compute the flame IIR model is a good indicator.

3.6 Conclusion

Different techniques were examined to determine the flame transfer function of laminar conical flames submitted to flow rate disturbances. When random broadband excitation is considered, the flow modulation at the nozzle outlet must be characterized and controlled to obtain a nearly white noise velocity perturbation signal instead of a colored signal filtered by the different responses of the electrical and mechanical elements present in the actuation line. This broadband random velocity signal was then used to determine the FTF with averaged cross-correlation or system identification techniques.
The results were compared to FTF measured with harmonic velocity modulations, when the modulation level was kept constant. The FTF gain and phase curves match well between the different methods for small amplitude perturbations. As the perturbation level amplitude is increased, the FTF gain is underestimated when random perturbations are considered. A general agreement is obtained for the FTF phase lag evolution, even though the FTF phase lag features complex transitions between different behaviors at low and high frequencies. The transition between these two regimes is very sensitive to the velocity perturbation level. This phenomenon was shown to be the cause of the main differences observed between the harmonic and random forcing techniques.

A sensitivity analysis on the number of samples that has to be considered in the SI technique to capture the FTF was conducted. This analysis emphasized the link existing between the largest time lag of the flame response and the optimized SI parameters. The method has to be further tested on flows with higher Reynolds-numbers in the future, but the same type of pre- and post-treatment is thought to be suited also for turbulent flows to separate incoherent disturbances induced by turbulence from coherent perturbations induced by the flow modulation. Moreover, nonlinear system identification techniques has to be designed in order to overcome the issues observed when the perturbation level is increased.

Part II

Combined mechanisms governing the FTF

Chapter 4

Effects of the velocity perturbation model on the FTF

The Flame Transfer Function (FTF) of an axisymmetric conical flame is studied in this chapter using a kinematic description of the flame motion. A new FTF model is derived by taking into account the incompressible and convective natures of the flow perturbations in the fresh stream. This type of perturbation is responsible for the regular increase of the phase lag with the forcing frequency observed in experiments when the flame aspect ratio characterized here by the flame angle with respect to the mean flow direction is not too small. It is shown that the FTF phase lag cannot be approximated by a purely convected one dimensional perturbed flow field and cannot be approximated by assuming a constant time lag delay over the whole frequency range as considered in many previous models. A systematic comparison of predictions is carried out with models that are already available in the literature and with measurements. Analytical developments are also conducted in the time domain to derive the linear unit impulse response of the flame when these incompressible convected perturbations are considered.

4.1 Introduction

Progress has been achieved in experimental determination and numerical simulation of FTF, but theoretical approaches have failed yet in modeling the correct phase lag evolution between flow and heat release rate disturbances over the frequency band of interest for thermo-acoustic instability prediction (see Chapter 1 for a review of the available models). FTF predictions are rarely compared to measurements even in a relatively simple configuration such as a conical axisymmetric flame submitted to flowrate disturbances. This type of laminar flames may be found in some burners for domestic boilers, material processing or multi-port preheaters. A combined theoretical and experimental

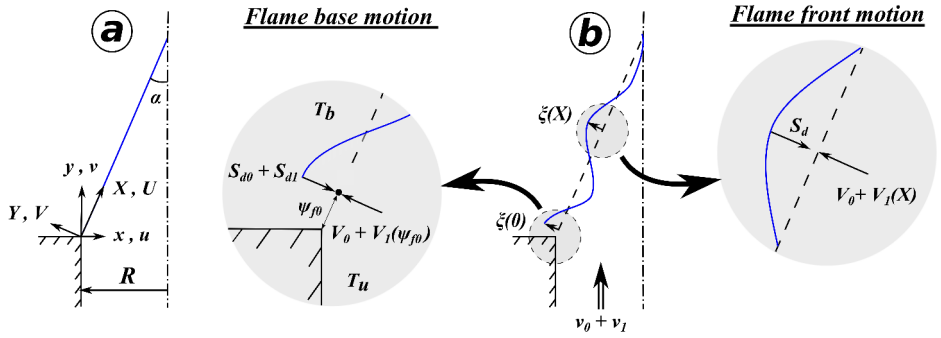

Figure 4.1: *Schematic of the configuration investigated. (a) Steady conical flame along with the different frames used in this article. (b) Acoustically perturbed conical flame, with a focus on the flame base region and the flame front displacement far from the burner lip.*

approach is used here to show that the correct evolution of the FTF phase lag can be predicted by including two essential features of the reactive flow dynamics. The first one is the feedback from the wrinkled flame front on the fresh reactant gas dynamics and the second one is the dynamics of the anchoring point. This second contribution is treated in Chapter 5. The first mechanism is examined here. It is first shown in section 4.2 that it can be well captured by imposing a divergence free convective flow perturbation to the fresh reactant velocity field. Predictions for flame wrinkles and FTF are compared to available data in the literature and to complementary measurements in section 4.3. In section 4.4, the unit impulse response of the flame is examined with a two-dimensional divergence-free convective perturbations and compared to experimental data from Chapter 3.

4.2 Incompressible convective velocity perturbation model

4.2.1 Velocity model

For a conical premixed flame that is compact with respect to the acoustic wavelengths, the perturbed flow resulting from acoustic modulation in the vicinity of the flame front is essentially of incompressible type [Baillot *et al.* (1992); Schuller *et al.* (2002); Birbaud *et al.* (2006)] and velocity perturbations are convected from the burner outlet to the flame front [Sugimoto and Matsui (1982); Baillot *et al.* (1992); Baillot *et al.* (1996); Birbaud *et al.* (2006)]. The perturbed velocity field in the fresh reactants can then be well approximated by:

$$\tilde{u}_1 = ik\frac{(R-x)}{2}v_1\exp(iky) \tag{4.1}$$
$$\tilde{v}_1 = v_1\exp(iky) \tag{4.2}$$

where R denotes the burner radius, $R-x$ is the radial coordinate in the burner frame and $k=\omega/v_0$ indicates the wavenumber of flow disturbances convected along the burner axis (see Fig. 4.1-a). These expressions represent a more detailed modeling of the velocity perturbations in the fresh stream than the uniform model ($\tilde{u}_1=0$, $\tilde{v}_1=v_1$) studied by Ducruix *et al.* (2000) and the convective model ($\tilde{u}_1=0$, $\tilde{v}_1=v_1\exp(iky)$) investigated by Schuller *et al.* (2003a) and Preetham *et al.* (2008). The starting point is to determine the resulting normal flame front displacement $\tilde{\xi}$ from its steady state due to this incoming perturbation (see Fig. 4.1-b).

The local velocity perturbation component normal to the steady front needs first to be determined. In the burner frame, this perturbation takes the following form:

$$\begin{aligned}\widetilde{V}_1(x) &= \tilde{v}_1\sin\alpha - \tilde{u}_1\cos\alpha \\ &= v_1\left[\sin\alpha - i\frac{k}{2}(R-x)\cos\alpha\right]\exp(iky)\end{aligned} \tag{4.3}$$

In the reference frame attached to the steady flame front, this expression becomes:

$$\widetilde{V}_1(X) = v_1\sin\alpha\left[1-i\frac{1}{2}k_*\left(1-\frac{X}{L}\right)\right]\exp\left(ik_*\frac{X}{L}\right) \tag{4.4}$$

where $L=R/\sin\alpha$ is the steady flame front length. This expression is a function of the dimensionless frequency $k_*=\omega_*\cos^2\alpha$, where α is the half-tip flame angle and $\omega_*=\omega R/(S_d\cos\alpha)$ denotes the reduced frequency identified by Ducruix *et al.* (2000). These dimensionless numbers can also be interpreted by considering the different interfering mechanisms controlling flame wrinkling [Lieuwen (2003); Lee and Lieuwen (2003); Blumenthal *et al.* (2013)]. The reduced frequency $\omega_*=\omega R/(S_d\cos\alpha)$ is related to the convection of flame wrinkles along the flame length L at the mean flow velocity component tangential to the steady flame front $U_0=v_0\cos\alpha$. The reduced frequency k_* is related to the convection of velocity disturbances in the fresh gases along the burner axis over a distance H corresponding to the flame height at the mean axial velocity v_0:

$$\omega_* = \frac{\omega R}{S_d\cos\alpha} = \frac{\omega}{U_0}L \tag{4.5}$$
$$k_* = \omega_*\cos^2\alpha = \frac{\omega}{v_0}H \tag{4.6}$$

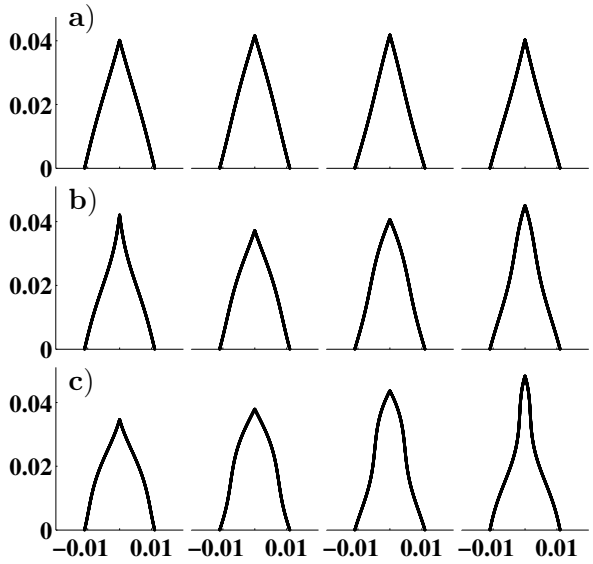

Figure 4.2: *Flame shapes predicted with (a) a uniform velocity perturbation [Ducruix et al. (2000)]; (b) a convected velocity disturbance [Schuller et al. (2003a)]; (c) the model derived in the present chapter. The flame is presented for four different phases of the acoustic period, namely* 0, $\pi/2$, π *and* $3\pi/2$. *Flame motions are calculated for* $\alpha = \pi/12$, $|v_1/v_0| = 0.1$ *and* $\omega_* = 5$.

These two quantities are related by the flame aspect ratio $\cos^2\alpha = k_*/\omega_*$. Schuller *et al.* (2003a) use the first description with ω_* and the flame angle α with respect to the flow direction as independent parameters to analyze the response of conical flames, while Lieuwen and co-workers [Lieuwen (2003); Lee and Lieuwen (2003); Preetham *et al.* (2008)] use two Strouhal numbers corresponding to the last expressions in Eqs. (4.5) and (4.6) to analyze flame wrinkling. While equivalent, the first description is preferred here to emphasize effects of the flame aspect ratio $\cos\alpha = H/L$ on the FTF, where $H = R/\tan\alpha$ is the steady flame height and $L = R/\sin\alpha$ is the steady flame front length.

4.2.2 Flame front perturbation and FTF model

Using the expression Eq. (4.4) for the normal velocity perturbation $\tilde{V}_1(X')$ and assuming that the flame is steadily anchored on the burner rim $\tilde{\xi}(0) = 0$, the normal flame displacement $\tilde{\xi}$ given by Eq. (1.13) may be written:

$$\tilde{\xi}(X) = \frac{\exp\left(i\omega_* \frac{X}{L}\right)}{U_0} \int_0^X \tilde{V}_1\left(X'\right) \exp\left(-i\omega_* \frac{X'}{L}\right) dX' \tag{4.7}$$

By introducing $X_* = X/L$, one finally obtains an expression for the dimensionless flame front displacement as a function of the relative input perturbation

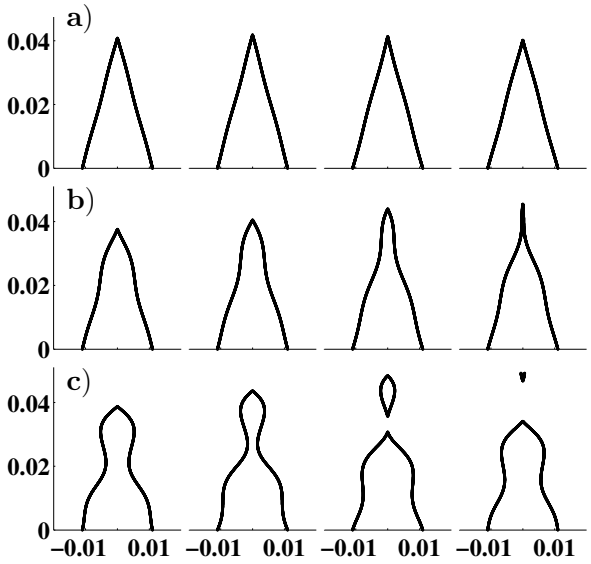

Figure 4.3: *Flame shapes predicted with (a) a uniform velocity perturbation [Ducruix et al. (2000)], (b) a convected velocity disturbance [Schuller et al. (2003a)], and (c) the model derived in the present chapter. The flame is presented for four different phases of the acoustic period, namely* 0, $\pi/2$, π *and* $3\pi/2$. *Flame motions are calculated for* $\alpha = \pi/12$, $|v_1/v_0| = 0.1$ *and* $\omega_* = 10$.

$\tilde{v}_1/v_0$ applied at the burner exit:

$$\frac{\tilde{\xi}(X)\cos\alpha}{R} = \frac{\tilde{v}_1}{v_0}\exp\left(i\omega_* X_*\right) \int_0^{X_*}\left[1-\frac{ik_*}{2}\left(1-X_*'\right)\right]\exp\left[i\left(k_*-\omega_*\right)X_*'\right]dX_*' \tag{4.8}$$

Integration is straightforward and one gets:

$$\frac{\tilde{\xi}(X_*)\cos\alpha}{R} = \frac{\tilde{v}_1}{v_0}\frac{1}{i(k_*-\omega_*)} \left[\left(1-\frac{ik_*}{2}-\frac{1}{2}\frac{k_*}{k_*-\omega_*}\right)\left(\exp(ik_*X_*)-\exp(i\omega_*X_*)\right) -\frac{ik_*}{2}X_*\exp(ik_*X_*)\right] \tag{4.9}$$

This expression shows that the flame front displacement is controlled by the two dimensionless numbers ω_* and $k_* = \omega_*\cos^2\alpha$ identified previously. The predicted flame shapes submitted to velocity modulations are presented in Figs. 4.2-4.4 for different values of the reduced frequency $\omega_* = 5, 10$ and 20 and for a relatively elongated flame $\alpha = \pi/12$. Four phases of the acoustic period are shown in these figures. Predictions (a) with a uniform velocity perturbation and (b) with a unidimensional convected disturbance are compared

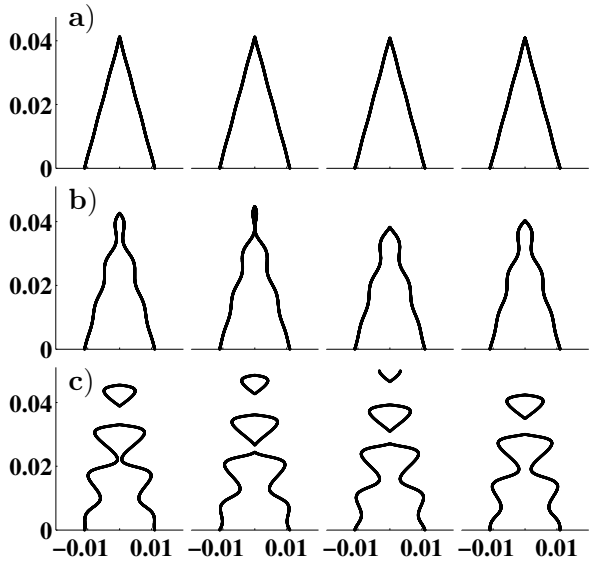

Figure 4.4: *Flame shapes predicted with (a) a uniform velocity perturbation [Ducruix* et al. *(2000)]; (b) a convected velocity disturbance [Schuller* et al. *(2003a)]; (c) the model derived in the present chapter. The flame is presented for four different phases of the acoustic period, namely* 0, $\pi/2$, π *and* $3\pi/2$. *Flame motions are calculated for* $\alpha = \pi/12$, $|v_1/v_0| = 0.1$ *and* $\omega_* = 20$.

to the present model (c) for an input level $|v_1/v_0| = 0.1$. In all cases explored, predictions from model (a) feature tiny imperceptible wrinkles in Figs. 4.2-4.4 (a). The shapes taken by the unsteady flame lie very close to the steady flame front position. The bulk oscillation imposed to the flow is strongly filtered by the flame at these forcing frequencies. This is in contrast with observations for the same reduced frequency [Bourehla and Baillot (1998); Ducruix *et al.* (2000); Schuller *et al.* (2002); Karimi *et al.* (2009)]. Predictions obtained with model (b) feature larger wrinkles around the steady flame shape for the same perturbation level $|v_1/v_0| = 0.1$. Wrinkles convected along the flame front are here clearly visible with a shorter wavelength as the reduced frequency ω_* increases.

Predictions from the incompressible convective model (c) are plotted in the bottom frames of Figs. 4.2-4.4. At low reduced frequency ω_*, the shape taken by the flame closely follows that predicted with the purely convective model (b). The radial component $\tilde{u}_1$ in Eq. (4.1) of the incompressible perturbation convected by the flow is proportional to k_* and thus vanishes at very low frequency. For larger values of ω_*, flame wrinkles are amplified. These large sinusoidal perturbations of the flame front are convected along the steady flame, from the flame base to the flame tip, with the release of pockets of unburnt gases at the flame tip due to the collapse of neighboring flame fronts [Joulin and Sivashinsky (1991); Baillot and Bourehla (1997)]. This phenomenon will

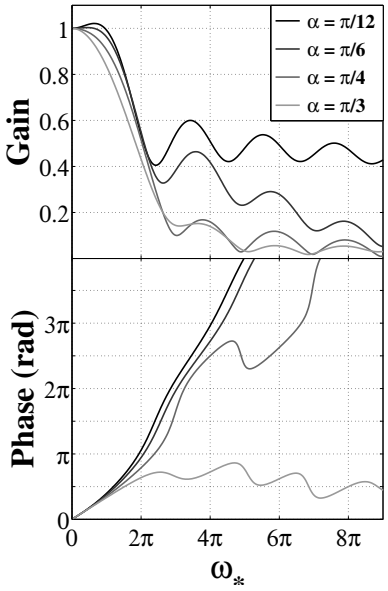

Figure 4.5: *FTF component F_A gain (top) and phase lag (bottom) evolution as a function of the reduced frequency ω_* for different values of the flame angle $\alpha = \pi/3$, $\pi/4$, $\pi/6$ and $\pi/12$ with respect to the flow direction. The darkness is associated to decreasing values of α: $\alpha = \pi/12$ (black). $\alpha = \pi/3$ (light gray).*

not be taking into account in the FTF derivation, where only small perturbations in the linear regime are considered.

The expression Eq. (4.9) for flame wrinkles is now integrated to determine the flame surface area evolution and the FTF. One obtains:

$$\frac{\tilde{\dot{Q}}_1}{\dot{Q}_0} = \frac{\tilde{A}_1}{A_0} = F_A \frac{\tilde{v}_1}{v_0} \tag{4.10}$$

where the transfer function F_A is given by:

$$F_A = \frac{1}{i(k_* - \omega_*)} \left[\left(2 - ik_* - \frac{k_*}{k_* - \omega_*} \right) \left(\frac{\exp(ik_*) - 1}{ik_*} - \frac{\exp(i\omega_*) - 1}{i\omega_*} \right) + \exp(ik_*) - \frac{\exp(ik_*) - 1}{ik_*} \right] \tag{4.11}$$

Table 4.1: *FTF obtained for different flow perturbation models and their low frequency approximation.*

	F_A	$\lim_{\omega_* \to 0} F_A$	$\lim_{\omega_* \to +\infty}^{\alpha \to 0} F_A$
Uniform model [Ducruix *et al.* (2000)]	$\frac{2}{\omega_*^2}(1 - \exp(i\omega_*) + i\omega_*)$	$1 + \frac{i\omega_*}{3}$	$\frac{2i}{\omega_*}$
Convective model [Schuller *et al.* (2003a)]	$\frac{2}{\omega_*^2(1-\cos^2\alpha)}\left[1 - \exp(i\omega_*) + \frac{\exp(i\omega_*\cos^2\alpha) - 1}{\cos^2\alpha}\right]$	$1 + \frac{i\omega_*}{3}(1 + \cos^2\alpha)$	$\frac{\exp(i\omega_*)}{i\omega_*}$
Incompressible convective model	$\frac{1}{i(k_* - \omega_*)}\left[2\left(1 - \frac{ik_*}{2} - \frac{1}{2}\frac{k_*}{k_* - \omega_*}\right)\left(\frac{\exp(ik_*) - 1}{ik_*} - \frac{\exp(i\omega_*) - 1}{i\omega_*}\right) + \left(\exp(ik_*) - \frac{\exp(ik_*) - 1}{ik_*}\right)\right]$	$1 + \frac{i\omega_*}{3}$	$-\frac{\exp(i\omega_*)}{2}$

The gain and phase of $F_A(\omega_*, k_*)$ are plotted in Fig. 4.5 as a function of the reduced frequency ω_* for different values of the flame angle $\alpha = \pi/3$, $\pi/4$, $\pi/6$ and $\pi/12$ with respect to the flow direction. The FTF gain behaves as a low-pass filter with a set of secondary humps. The gain curves almost collapse for all flame angles investigated at low reduced frequencies $\omega_* \leq 2\pi$. Differences appear for $\omega_* > 2\pi$. The gain is in this region a strong function of the flame aspect ratio. For a fixed reduced frequency, the gain and phase rapidly drop for increasing values of the flame angle α. The FTF phase lag is regularly increasing with the reduced frequency for elongated flames and saturates around the value $\varphi = \pi/2$ for large flame angles.

This last behavior can be retrieved by expanding Eq. (4.11) around the value $\alpha = \pi/2$ or equivalently by considering the limit $k_* = 0$:

$$\lim_{k_* \to 0} F_A = \frac{2}{\omega_*^2}(1 + i\omega_* - \exp(i\omega_*)) \tag{4.12}$$

For large flame angles or small k_* values, $F_A(\omega_*, k_*)$ reduces to the expression derived by Ducruix *et al.* (2000) for uniform flow perturbations where the FTF phase lag was shown to saturate around the asymptotic value $\varphi = \pi/2$.

Predictions are further compared to previous FTF models synthesized in Tab. 4.1. Model (a) [Ducruix *et al.* (2000)] considers uniform flow perturbations and model (b) [Schuller *et al.* (2003a)] describes the flame response to a convected unidimensional wave. Model (c) denotes the FTF expression found in this study including a two dimensional incompressible convective perturbation. Comparisons are first conducted in Fig. 4.6-left for a large flame angle $\alpha = \pi/3$. The gain collapses in this case roughly on the same curve for the three models tested. The main differences between the model predictions are observed for the phase lag evolution. It regularly increases with frequency for the convective model (b), while the phase lag of model (c) is shown to saturate at nearly the same value as predictions from the uniform model (a) at high frequencies. For flames with a small aspect ratio $\cos\alpha = H/L \ll 1$, the wavelength of velocity perturbations convected by the mean flow $\lambda = v_0/f$ is relatively large compared to the flame height H and the flame may be considered compact with respect to hydrodynamic velocity perturbations. In this limit case, a correct description of the FTF reduces to predictions of model (a) obtained for uniform flow oscillations.

Predictions between the different models are further compared when the flame angle is reduced to $\alpha = \pi/6$ and $\pi/12$ in Fig. 4.6-center and right respectively. The flame aspect ratio $H/L = \cos\alpha$ regularly increases from left to right. When $\alpha = \pi/6$, the gain predicted by model (c) takes slightly higher values than model (a) and (b) predictions. The main difference is again observed on

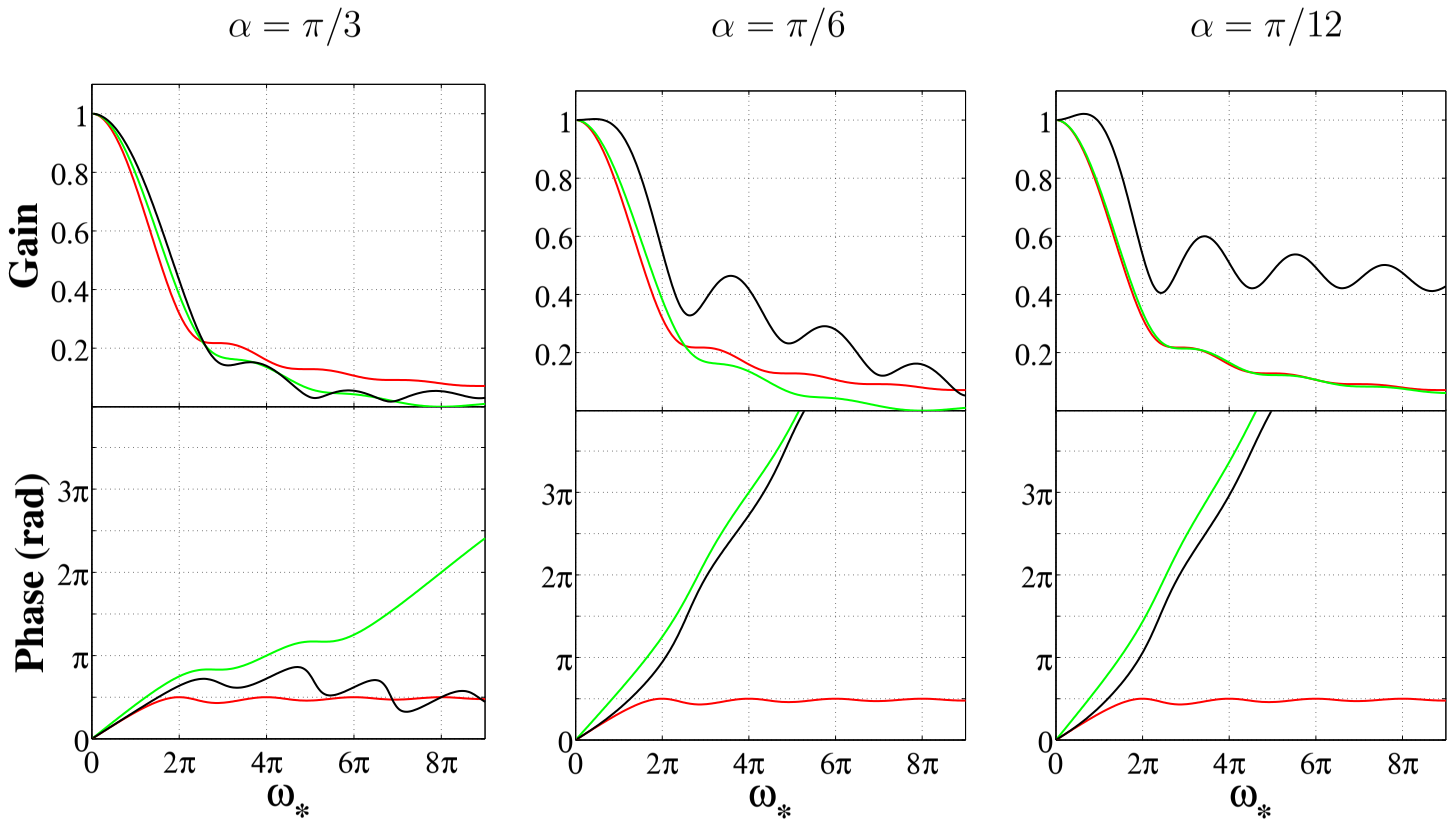

Figure 4.6: *FTF component F_A gain (top) and phase (bottom) evolutions as a function of the reduced frequency ω_* for different values of the flame angle $\alpha = \pi/3$ (left), $\pi/6$ (center) and $\pi/12$ (right) for different flow perturbation models. Red: uniform oscillation - model (a). Green : unidimensional convective wave - model (b). Black: incompressible two dimensional convected wave - model (c).*

the phase lag evolution. Predictions from model (c) closely follow those from the uniform model (a) at low reduced frequencies $\omega_* \leq \pi$ and then deviate for larger frequencies to follow the same trend as model (b) predictions at high frequencies with a regularly increasing phase lag. The same behavior can be noticed for a longer flame when $\alpha = \pi/12$ in Fig. 4.6-right. In this case, large differences may be observed for the predicted gain. Model (a) and (b) collapse on the same curve, but predictions from model (c) indicate that the flame strongly responds to flow perturbations over a wide range of frequencies. This overestimation of the gain with model (c) will be examined in further detail in the next section, but it is first worth analyzing the evolution of the phase lag at low frequency.

The three different models are now compared when the reduced frequency ω_* takes small values. A development in Taylor series around the value $\omega_* = 0$ yields the expressions presented in the third column in Tab. 4.1. The expression found show that the uniform model (a) and the present model (c) have the same limit at low reduced frequencies while the unidimensional convective model (b) features a higher value of the phase slope around $\omega_* = 0$. FTF measurements [Ducruix *et al.* (2000); Durox *et al.* (2009)] indicate that predictions from model (a) are more accurate at low frequency than those from model (b). The reason indicated by Schuller *et al.* (2003a) is that the convective model (b) violates mass balance, but enables to capture a regularly increasing phase lag at high frequency. Model (c) developed in this study satisfies mass balance and improves predictions of the FTF phase lag. The incompressible convected wave satisfying the continuity equation enables to retrieve the correct phase lag behavior at low frequency and the convective behavior is still captured at higher frequency. It is also worth noting that, although they look close, the phase lag curves in Fig. 4.6-right calculated with models (b) and (c) are separated by about $\pi/2$ over a large frequency range. This observation is supported by the expression presented in the fourth column of Tab. 4.1. These expressions indicate the approximation of the FTF of elongated flames ($\alpha \ll 1$) in the high frequency limit for the three different models. The phase lag of model (b) is about $\phi_b = \omega_* - \pi/2$ while the phase lag of model (c) is about $\phi_c = \omega_* - \pi$. It is thus shown that the phase lag slope is equal to unity in both models but a constant gap of $\pi/2$ is predicted between the two phase lags. This difference is significant for a phase lag which values are defined between 0 and 2π. It is well known that small differences on the FTF phase lag may lead to large deviations in the predictions of stability margins of a combustor [Schuller *et al.* (2003b); Noiray *et al.* (2006b); Wolf *et al.* (2012)].

4.2.3 Spatial decay of fresh gas velocity perturbations

One difficulty with model (c) predictions is the large values taken by the FTF gain even at relatively high reduced frequencies which are not observed in ex-

periments. This difference may result from a too crude description of the perturbed flow field or of the flame front dynamics. Laser Doppler velocimetry [Baillot *et al.* (1992)] and particle imaging velocimetry [Schuller *et al.* (2002)] measurements realized in the fresh reactants show that the amplitude of the velocity perturbations is decreasing with the distance above the burner along its centerline. A numerical integration of the G-equation showed that such an accurate description of the decay of the velocity perturbation is an important feature that needs to be considered to retrieve the measured FTF [Schuller *et al.* (2002)]. In the experiments conducted by Durox *et al.* (2004) and by Birbaud *et al.* (2006), the axial velocity perturbation field along the vertical axis was examined in detail in the fresh reactant stream. It was found that velocity perturbations decay exponentially with the distance to the burner nozzle, with an increasing decay rate as the forcing frequency is increased.

Birbaud *et al.* (2006) indicated in their experimental analysis that the feedback from flame wrinkling on the fresh reactant dynamics is the origin of the incompressible convected velocity disturbance observed in the experiments. The region of influence is a function of the amplitude and frequency of flame wrinkling. Model (c) in Eq. (4.11) does not consider flame wrinkles that are attenuated due for example to curvature or stretch effects [Wang *et al.* (2009); Preetham *et al.* (2010)] or because the region of influence is reduced when the frequency increases [Birbaud *et al.* (2006)]. The radial velocity perturbation imposed at the burner outlet in Eq. (4.1) near the burner rim is also probably too large, because the flow perturbation inside the injection tube is unidirectional. These different mechanisms highlight the limits of model (c) and contribute to the decay of flow perturbations when the frequency increases and when the distance to the nozzle outlet increases. One possibility to reproduce these observations is to modify the reduced frequency k_* describing velocity disturbances convected by the mean flow and introduce a complex component:

$$k_* = \frac{\omega}{v_0} H(1 + ib) \tag{4.13}$$

The real part $\omega H/v_0$ still describes the convection of velocity disturbances along the burner axis at the mean flow speed v_0. The imaginary component characterized by the decay rate $-b\omega/v_0$ enables to reproduce the exponential decrease of flow perturbations along the vertical axis observed in experiments. It is also worth noting that in the model proposed in Eq. (4.13), the decay rate increases with the forcing frequency as noted in experiments [Birbaud *et al.* (2006)]. Using Eq. (4.13), the symbolic expression for the FTF with model (c) remains unchanged except for the different definition of k_*. Schuller *et al.* (2002) chose to represent the perturbation decay by a linear approximation that was determined experimentally for a premixed methane/air flame with an equivalence ratio $\phi = 1.05$ stabilized in a flow of mean velocity $v_0 = 0.97\text{m.s}^{-1}$:

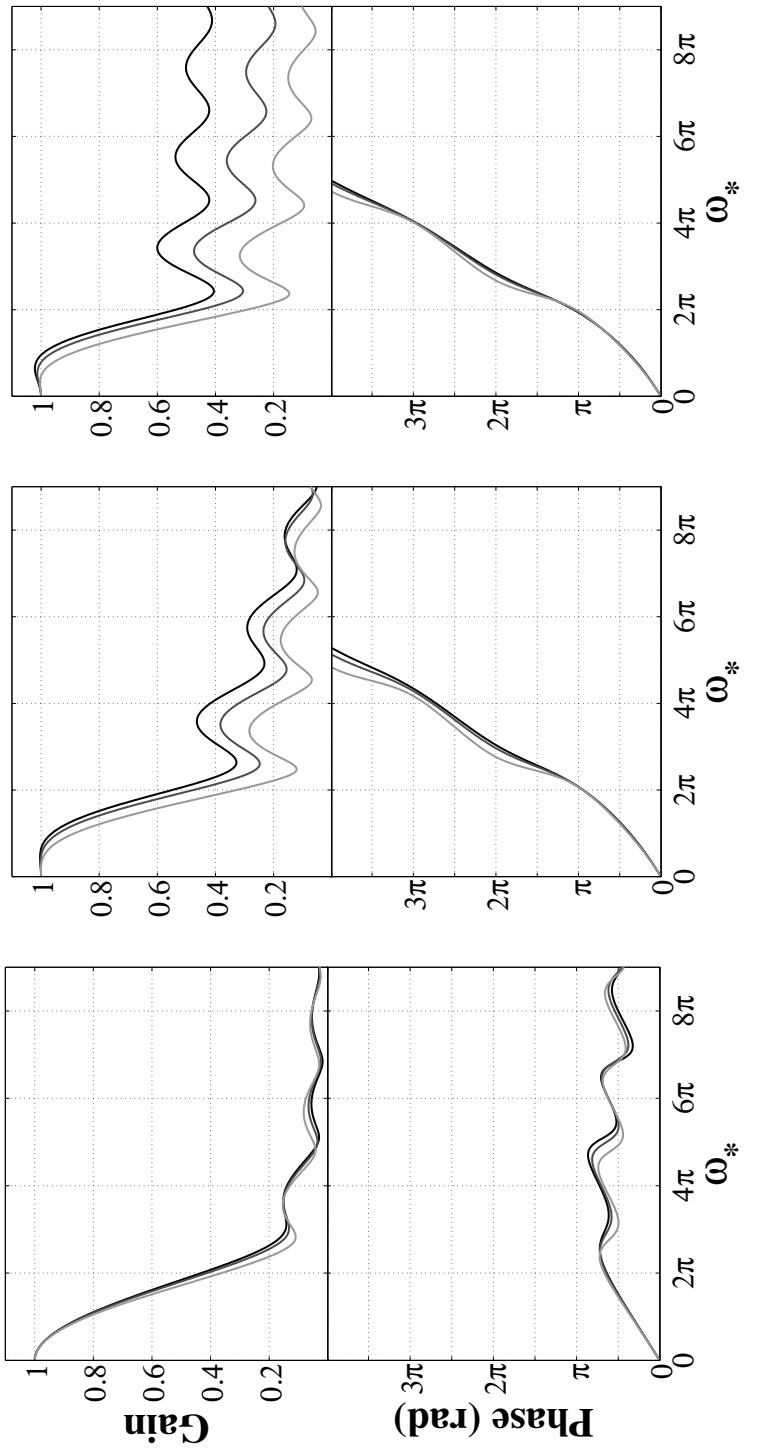

Figure 4.7: *FTF component F_A gain (top) and phase (bottom) evolutions as a function of the reduced frequency ω_* for different values of the flame angle $\alpha = \pi/3$ (left), $\pi/6$ (center) and $\pi/12$ (right). Predictions from model (c) with a spatial decay $b = 0$, 0.1 and 0.4. The darkness of the line decreases with increasing values of b.*

$$|v_1(y)| = 2^{\frac{1}{2}} a_0 \left(1 - \frac{a_1}{a_0} y\right) \tag{4.14}$$

where $a_0 = 0.20$ m.s^{-1} and $a_1 = 5$ m.s^{-1} were measured for a forcing frequency $f = 10.5$ Hz and a relatively large perturbation level $|v_1/v_0| = 0.29$. This leads to the following value for $b = a_1 v_0/(a_0\omega) \simeq 0.4$ at low frequency.

FTF predictions with model (c) are shown in Fig. 4.7 for different values of the decay parameter $b = 0$, 0.1 and 0.4 and flame angle. For short flames, when the aspect ratio is relatively small $\alpha = \pi/3$ ($H/L = 0.5$), the decay parameter barely modifies the gain and phase of the flame response because the fresh reactant region is not large enough for the velocity perturbation to decay significantly before reaching the flame tip. For longer flames, when the flame aspect ratio increases $\alpha = \pi/6$ ($H/L = 0.87$) and $\alpha = \pi/12$ ($H/L = 0.97$), the decay parameter again barely modifies the phase lag evolution except that small undulations appear around the curve obtained for $b = 0$. These undulations were also observed in recent experiments [Cuquel *et al.* (2011a)]. The main effect of the decay parameter is on the FTF gain. When the factor b increases, the gain rapidly drops, particularly for elongated flames.

Model (c) combined with a complex representation of k_* offers a suitable framework to analyze the response of conical flames submitted to flow disturbances when the dynamics of the flame anchoring point can be neglected. It was shown that the decay factor b barely modifies the FTF phase lag, but enables to reproduce the perturbation decay observed in experiments conducted with elongated flames and leading to a strong attenuation of the FTF gain when the forcing frequency increases. These different predictions are validated in the next section with experiments.

4.3 Experimental validation

The experimental results presented in this section were carried out on a burner of radius $R = 11$ mm with a mean flow velocity $v_0 = 1.56$ m.s^{-1} at the burner outlet when the burner is fed by a methane/air mixture with a fixed equivalence ratio $\phi = 1.03$. The flame displacement speed is set to $S_d = 0.44$ m.s^{-1} by matching the experimental and theoretical flame heights as in Schuller *et al.* (2002).

4.3.1 Analysis of flame wrinkling

Flame images are first compared with the flame shapes predicted by the G-equation with an incompressible convective velocity perturbation model, with or without axial decay. The flame shapes are first compared in Fig. 4.8 (a)

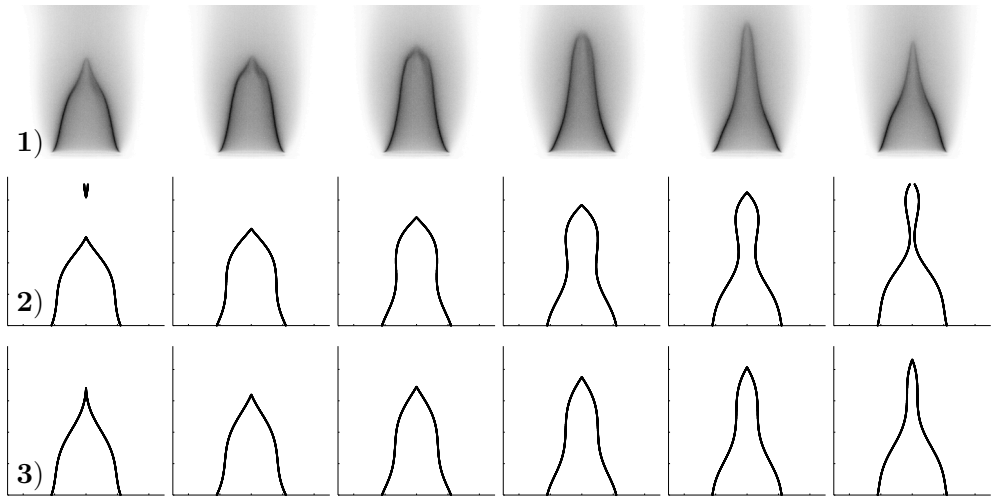

(a) $\omega_* = 6.55$.

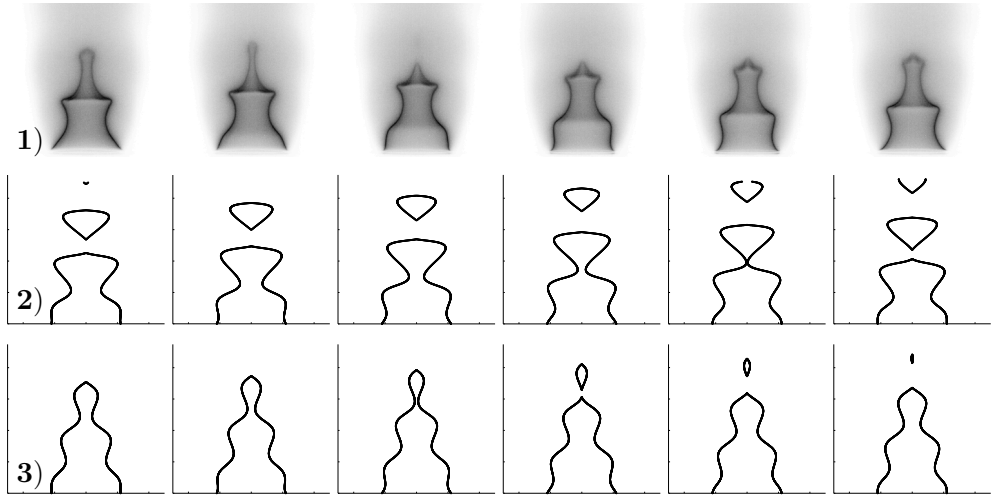

(b) $\omega_* = 16.37$.

Figure 4.8: *(1) Images of the conical flame submitted to a modulation at $f = 40$ Hz (top figures) and $f = 100$ Hz (bottom figures) for a perturbation level $v_1^{\mathrm{rms}}/v_0 = 0.1$. (2) and (3) Flame shapes predicted with the incompressible convective model with (2) $b = 0$ and (3) $b = 0.4$. Flow conditions: $v_0 = 1.56$ $m.s^{-1}$, $S_d = 0.44$ $m.s^{-1}$. Flame geometry: $R = 0.011$ m, $\alpha = 0.286$ rad.*

and (b) for a forcing level of $v_1^{\text{rms}}/v_0 = 0.1$ at two different forcing frequencies $f = 40$ Hz and $f = 100$ Hz, respectively corresponding to reduced frequency values of $\omega_* = 6.55$ and $\omega_* = 16.37$. In both figures, the shape taken by the flame is presented at six successive phases of the periodic excitation, each being separated by a constant phase difference of $\pi/3$ rad. Experimental images presented in Fig. 4.8 in inverted black and white colors are presented in the top row (1), followed by predictions with the incompressible convective model in the second row (2). Shapes predicted with the decaying incompressible convective model are presented in bottom row (3) when the decay rate b is fixed to $b = 0.4$. At relatively low frequency $\omega_* = 6.5$, the flame is executing a quasi-uniform bulk oscillation in the vertical direction because the flame is almost compact with respect to the hydrodynamic velocity perturbation wavelength $\lambda = v_0/f$. Predictions with models (2) and (3) retrieve well the flame shape and in particular, the correct amplitude and phase lag of wrinkles observed along the flame fronts. However, a few differences persist near the flame tip, where the models feature very thin zones of fresh gases. These regions are not observed in the experiments, because curvature effects modify the flame speed near the flame tip and its dynamics [Poinsot *et al.* (1992)]. It is however expected that these small differences do not affect the global response of the flame because only a small part of the flame surface area is located at the flame tip.

At higher reduced frequency $\omega_* = 16.37$, images highlight important flame wrinkles, convected from the flame base to the flame tip. Model (2) retrieves this phenomenon, but the amplitude of the flame front deformation is over estimated. These wrinkles provoke the shedding of large unburnt gas pockets above the flame tip, a feature that has not been observed in experiments conducted for these forcing conditions. These large flame surface fluctuations are responsible of the over prediction of the FTF gain observed in Fig. 4.5. Predictions with the decaying velocity perturbation model (3) match better with the observed shapes, especially in terms of flame front perturbation amplitude. Experiments however indicate that the flame wrinkles form cusps for this forcing level, a nonlinear phenomenon that cannot be anticipated by the linear models considered in this chapter.

4.3.2 Analysis of Flame Transfer Function

The comparison between predictions and measurements of the shapes taken by the flame during the modulation cycle is now completed by analyzing the corresponding FTF. For a fixed perturbation level $v_1^{\text{rms}}/v_0 = 0.04$, the FTF was determined between 20 and 250 Hz, with a frequency resolution of 5 Hz. Experimental results (red line) are presented in Fig. 4.9, along with predictions from a uniform (thin black line) and purely convective (dashed black lines) models and the divergent-free convective model derived in the present study (thick black line). These predictions were obtained with the following set of parameters

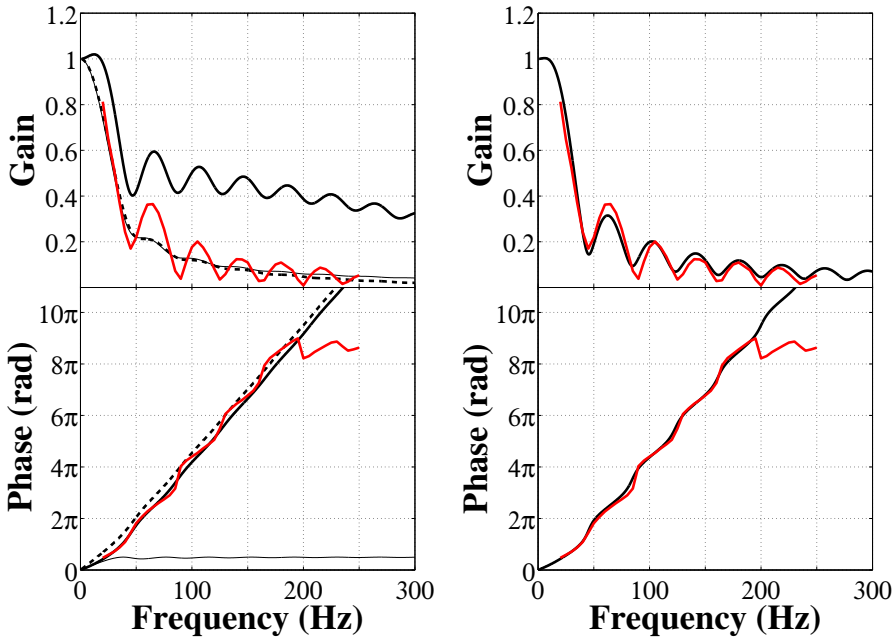

Figure 4.9: **(left)** *FTF gain (top) and phase lag (bottom) as a function of the forcing frequency. Predictions with the non-decaying incompressible convective velocity perturbation model $F_A(\omega)$ (thick black line) are compared to predictions obtained with a uniform flow oscillation (thin black line), with a purely convective perturbation (dashed black line), and to measurements (red line).* **(right)** *FTF gain (top) and phase lag (bottom) as a function of the forcing frequency. Predictions from the decaying incompressible convective velocity perturbation model $F_A(\omega, b)$, with $b = 0.4$ (thick black line) are compared to measurements (red line).*

$R = 0.011$ m, $v_0 = 1.56$ m.s^{-1} and $S_d = 0.44$ m.s^{-1}, where the value chosen for the flame speed S_d does not correspond to the laminar burning velocity $S_L = 0.39$ m.s^{-1} for this mixture equivalence ratio $\phi = 1.03$ [Vagelopoulos and Egolfopoulos (1998)]. This value was fixed in order to match the observed and theoretical steady flame heights [Schuller *et al.* (2002); Cuquel *et al.* (2013b)]. Predictions with a uniform modulation (thin black line in Fig. 4.9-left) reproduce the correct phase lag evolution observed in experiments at very low frequency, but rapidly fail in predicting the phase lag at higher frequencies. The purely convective model (dashed black line in Fig. 4.9-left) retrieves the regular increase of the phase lag but yields too large phase lags at low frequency. Predictions of the FTF gain with these two models are very close. Predictions from Eq. (4.11) derived in this study, with the incompressible convected velocity perturbation field (thick black line in Fig. 4.9-left), retrieve both the right low frequency behavior and the regular increase of the phase lag in the intermediate frequency range. This model however largely over-estimates the measured values of the gain, but it is worth noticing that it reproduces well the correct

frequencies of the secondary extrema observed in the FTF gain measurements.

This problem identified in the prediction of the gain may be overcome by taking into account the decrease of the amplitude of the velocity perturbation observed along the vertical axis. Using a decay rate $b = 0.4$ in Eq. (4.13), predictions with this decaying incompressible convective velocity model are shown to collapse well with experimental results over a large frequency range in Fig. 4.9-right. This improved model enables to reproduce the gain evolution as well as the different humps observed in experiments. Predictions of the phase lag are also slightly improved. The small oscillations superimposed on the phase curve are observed in the measurements as well. This model yields now a satisfactory representation of the FTF in the low and intermediate frequency ranges, but it still fails to reproduce the phase lag saturation observed in the high frequency limit. This features is important for thermo-acoustic instability prediction because it controls the flame response over a wide range of frequencies for high perturbation levels [Durox *et al.* (2009)]. This problem is tackled in Chapter 5 by examining the flame base dynamics.

4.4 Impulse response

Recently, the impulse response of conical and wedge flames has been studied theoretically by Blumenthal *et al.* (2013). Analytical expressions were derived based on two different velocity perturbation models. The uniform flow perturbation model used by Ducruix *et al.* (2000) may be described in the time domain by: $v_1(x, y, t) = v_1\delta(t)$ where δ is the Dirac delta function. It represents a spatially uniform impulse in the time domain corresponding to a sudden increase and decrease of the axial velocity. The convective disturbance considered by Schuller *et al.* (2003a) takes in the time domain the form of a spatially convected velocity impulse: $v_1(x, y, t) = v_1\delta(t - y/v_0)$. The impulse response of conical flames submitted to these disturbances writes:

$$h_U(t) = \frac{2}{\tau_r}\left(1 - \frac{t}{\tau_r}\right)\left(H(t) - H(t - \tau_r)\right) \tag{4.15}$$

$$h_C(t) = \frac{2}{\tau_r - \tau_c}\left[\left(1 - \frac{t}{\tau_r}\right)\left(H(t) - H(t - \tau_r)\right) - \left(1 - \frac{t}{\tau_c}\right)\left(H(t) - H(t - \tau_c)\right)\right] \tag{4.16}$$

where $H(t)$ is the Heaviside step function. Equation (4.15) corresponds to the flame response $h_U(t)$ to the uniform flow impulse. Equation (4.16) denotes the flame response to the convected impulse. The uniform impulse response only depends on the time variable t and on the "restoration" time scale $\tau_r = L/(v_0 \cos\alpha)$ which is linked to the convection of flame wrinkles along the

steady flame front of length L at a speed $v_0 \cos\alpha$ equal to the steady velocity component tangential to the steady flame front. This impulse response decreases linearly with time as shown in Fig. 4.10-top, from the initial instant where $h_U(0^+) = 2/\tau_r$ and vanishes for $t \geq \tau_r$. The impulse response obtained for a convected disturbance depends on two time scales: the "restoration" time scale $\tau_r = L/(v_0 \cos\alpha)$ and the "convection" time scale $\tau_c = H/v_0 = \tau_r \cos^2\alpha$. The convection characteristic time is linked to velocity perturbations in the fresh gases that are convected by the mean flow at a speed v_0 over a distance equal to the flame height $H = R/\tan\alpha$. This impulse response is growing linearly from zero at $t = 0^+$ to a maximum value defined by $h_C(\tau_c) = 2/\tau_r$. From that maximum value, the impulse response decreases linearly for longer times to reach zero for times larger than the restoration time τ_r: $h_C(t > \tau_r) = 0$.

4.4.1 Unit response to an incompressible convected impulse

The unit response to an incompressible convected disturbance is examined below. The model relies on a convective axial velocity perturbation defined by:

$$v_1(r, y, t) = v_1 \delta(t - y/v_0) \tag{4.17}$$

The radial velocity perturbation component $u_1(r, y, t)$ is deduced from a local mass balance in the fresh gases:

$$\frac{\partial v_1}{\partial y} + \frac{1}{r}\frac{\partial r u_1}{\partial r} = 0 \tag{4.18}$$

This leads to the following expression for the radial velocity perturbation component:

$$u_1(r, y, t) = -v_1 \frac{r}{2v_0} \frac{\delta(t - y/v_0)}{t - y/v_0} \tag{4.19}$$

The velocity perturbation component normal to the steady flame front, taken at the flame front location for $Y = 0$, now writes:

$$V_1(X, t) = v_1 \delta(t - X\cos\alpha/v_0) \left[\sin\alpha - \frac{\cos\alpha}{2v_0} \frac{R - X\sin\alpha}{t - X\cos\alpha/v_0}\right] \tag{4.20}$$

The resulting flame wrinkles in a frame attached to the flame front are given by:

$$\xi(X, t) = \frac{1}{U_0} \int_0^X V_1 \left(X', t - \frac{X - X'}{U_0}\right) dX' \tag{4.21}$$

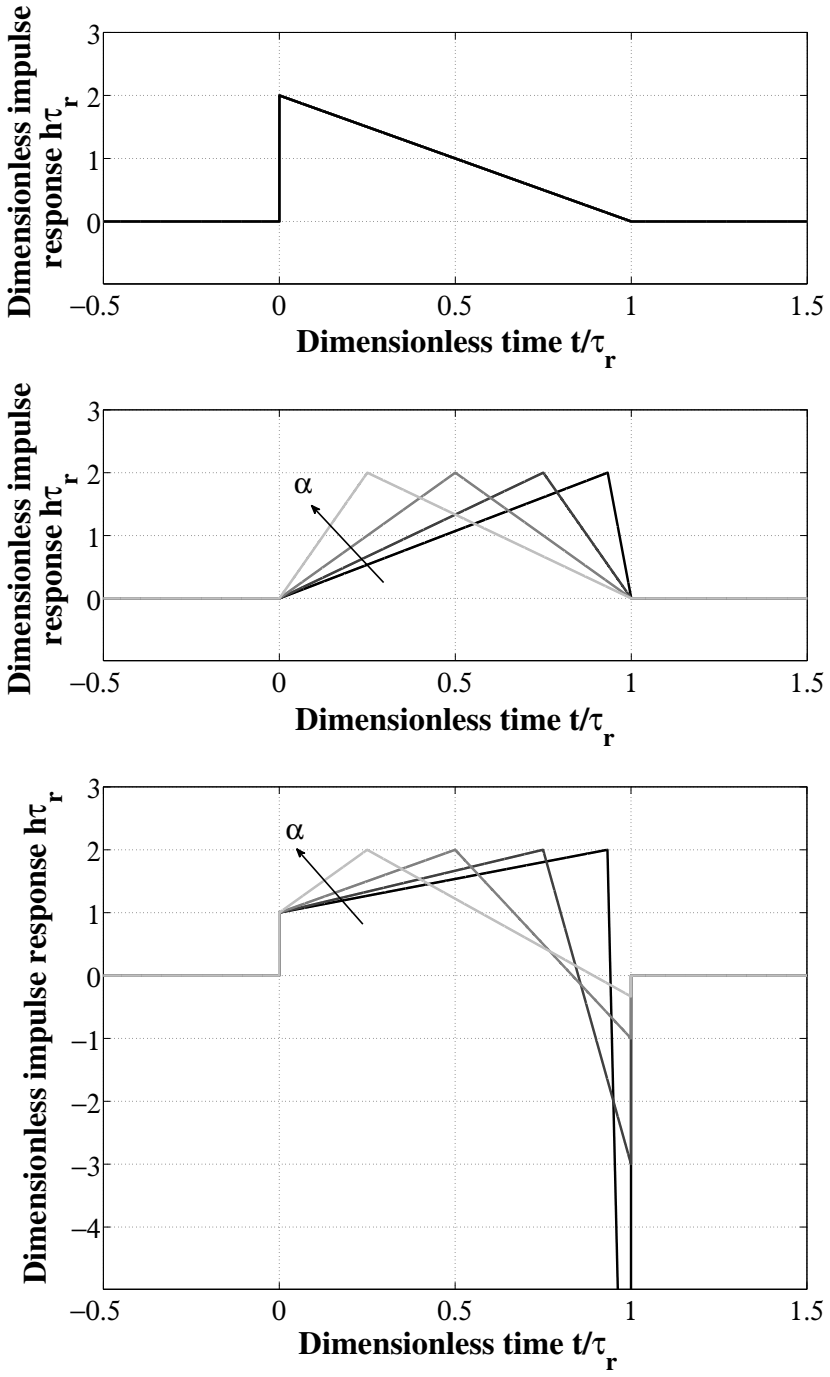

Figure 4.10: *Impulse response of a conical flame. The impulse response is plotted as a function of time, both made dimensionless with the restoration time scale τ_r. The uniform and convective models derived by Blumenthal* et al. *(2013) are plotted on the upper and middle figures. Results from the incompressible convective model are plotted in the bottom figure. Different curves are associated to different values of $\alpha = \pi/3$ (light grey), $\pi/4$, $\pi/6$ and $\pi/12$ (black).*

Integration of this equation yields:

$$\xi(X^*,t) = \frac{v_1}{v_0}\frac{1}{2}\frac{\tau_c}{\tau_r-\tau_c}\left[\frac{2}{\tau_c}\left(1+\frac{1}{2}\frac{\tau_c}{\tau_r-\tau_c}\right)\left(H(t/\tau_c - X^*) - H(t/\tau_r - X^*)\right)\right.$$
$$\left. + (1-X^*)\,\delta(t/\tau_c - X^*) - \delta(t/\tau_c - X^*)\right] \quad (4.22)$$

where $X^* = X/L$ is the dimensionless variable along the steady flame front. The resulting flame surface area perturbations may be obtained by integration (see Eq. (1.19) in Chapter 1):

$$\frac{A_1}{A_0} = \frac{2\sin\alpha\cos\alpha}{R^2}\int_0^L \xi(X,t)dX \quad (4.23)$$

One finally obtains:

$$h_{IC} = \frac{1}{\tau_r-\tau_c}\left[\frac{\tau_r}{\tau_r-\tau_c}\left(1-\frac{t}{\tau_c}\right)\left(H(t-\tau_c) - H(t)\right)\right.$$
$$\left. + \left(\frac{\tau_c}{\tau_r} - \left(1+\frac{1}{1-\tau_c/\tau_r}\right)\left(1-\frac{t}{\tau_r}\right)\right)\left(H(t-\tau_r) - H(t)\right)\right] \quad (4.24)$$

This impulse response is plotted in Fig. 4.10-bottom for different values of the flame tip half-angle $\alpha = \pi/3; \pi/4; \pi/6; \pi/12$. Like the impulse response obtained for a uniform perturbation, the impulse response features first a jump at initial instant $t = 0$ when $h_{IC}(0^+) = \tau_r$. The response then increases linearly until $t = \tau_c$ where $h_{IC}(\tau_c) = 2\tau_r$ before decreasing linearly down to the value:

$$h_{IC}(\tau_r^-) = -\frac{\tau_c/\tau_r}{\tau_r-\tau_c} = -\frac{1}{\tau_r\tan^2\alpha} \quad (4.25)$$

This development around $t = \tau_r^-$ explains why the negative values of the impulse response strongly increases when the flame tip half-angle is close to zero for elongated flames. It is worth noting that these large negatives values of the impulse response are found for elongated flames. In this case, FTF gain over-predictions were observed with the incompressible convective model. For larger times when $t \geq \tau_r$, the incompressible convective impulse response vanishes. This new incompressible convective model appears as a compromise between the two previous models. It reproduces the jump at initial time from the uniform model but also exhibits a non-monotonic behavior as the purely convective model. However, the negative values taken close to $t = \tau_r$ by the model derived here constitute a significant difference compared to previously derived models. These negative values are a consequence of the unity constraint imposing that the impulse response time-integral is equal to unity.

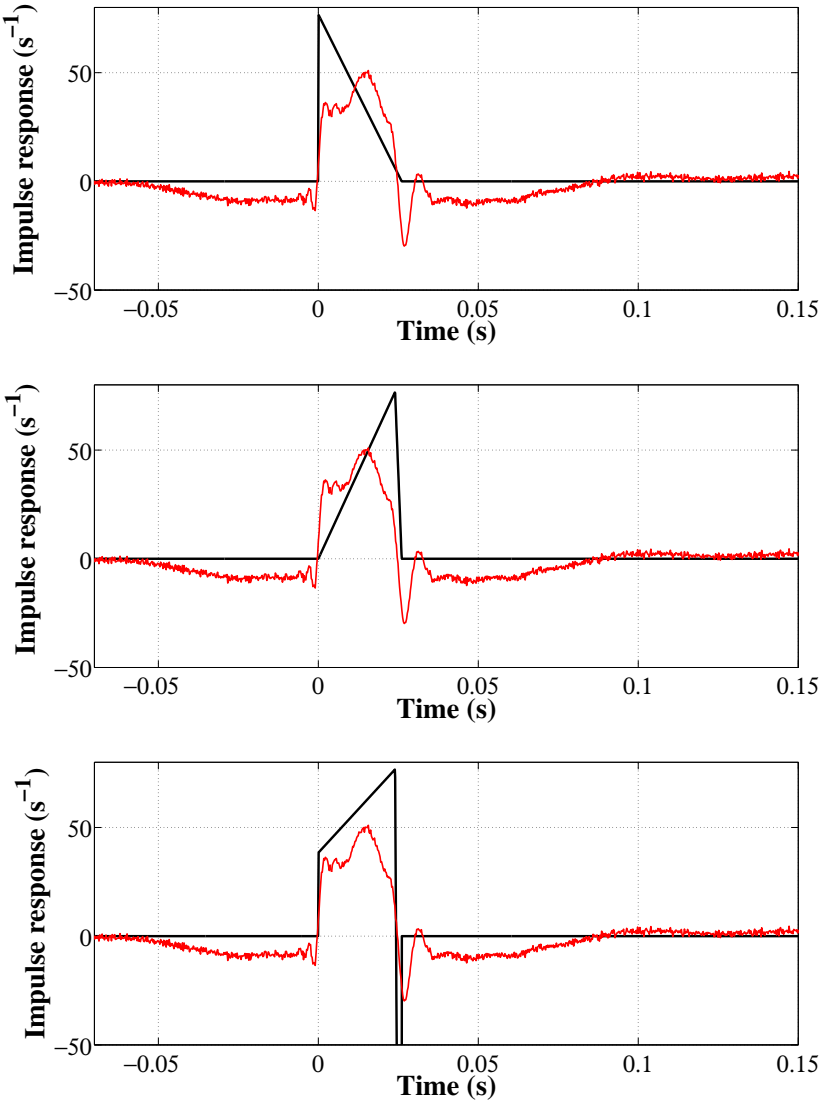

Figure 4.11: *The experimentally determined impulse response (red curves) is plotted as a function of time and compared to predictions from different models (black curves): uniform model (top), convective model (center) and incompressible convective model (bottom).* $\tau_r = 0.261\ s^{-1}.\tau_c = 0.240\ s^{-1}$.

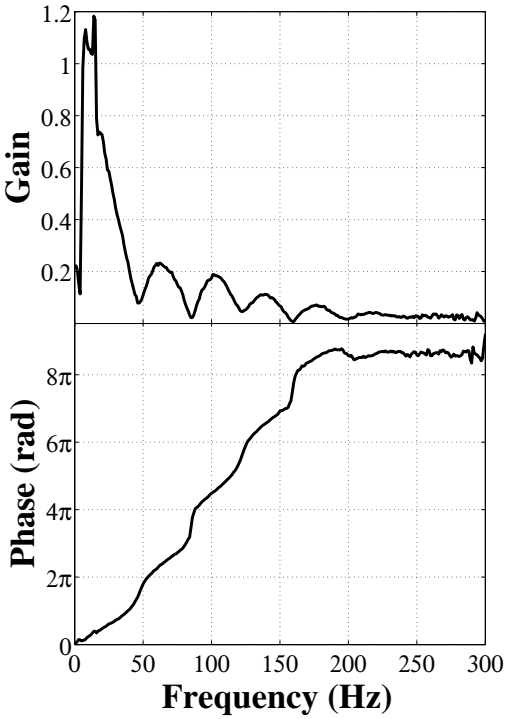

Figure 4.12: *Flame Transfer Function determined with random flow perturbation as a function of the forcing frequency.*

4.4.2 Comparison with experimental data

In Chapter 3, the response of conical flames to random flow perturbations was determined experimentally. These data are used here to determine the impulse response. Matlab is first used to convert the random time signal into a state space model. This model is then used to determine the unit impulse response. Results are compared to predictions for the different models examined in Fig. 4.11. The measured impulse response increases rapidly around $t = 0$ s, then oscillates between $t = 0$ s and $t \sim 0.02$ s and rapidly decreases before vanishing around $t = 0.03$ s. Predictions with the uniform model (top figure) retrieve the jump at initial time but does not capture the later time behavior. The impulse response determined with the convective model (center figure) misses the initial time jump but retrieves the strong decrease of the response around $t = 0.02$ s. Calculations with the incompressible convective model (bottom figure) catch both the sudden increase at $t = 0$ s and the sudden decrease at $t = 0.02$ s, as well as negative values around $t = 0.03$ s.

Differences observed between experimental and theoretical impulse responses can partly be explained by looking more closely at the FTF. By determining

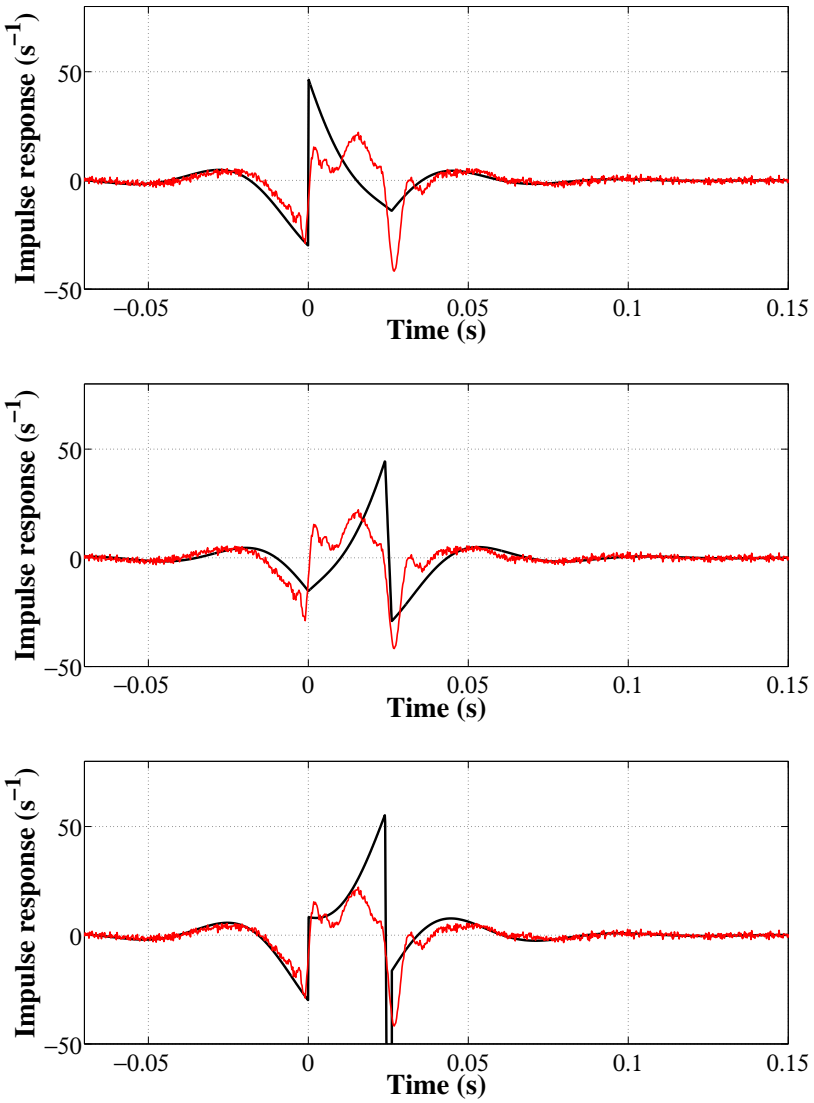

Figure 4.13: *The filtered experimental impulse response (red curves) is plotted as a function of time and compared to predictions from different filtered models (black curves): uniform model (top), convective model (center) and incompressible convective model (bottom).* $\tau_r = 0.261\ s^{-1}.\tau_c = 0.240\ s^{-1}$. *Cut-off frequency of the high-pass filter:* $f_c = 20\ Hz$.

the FTF with random signals, one gather information about all the frequencies comprised between 0 and $f_s/2$, where $f_s = 4096$ Hz stands for the sampling frequency. As explained in Chapter 2, the burnt gases on the top of the flame undergo a shear-layer instability which is associated to buoyant effects and which is not directly related to the acoustic velocity forcing. This instability produces a feedback on the flame front dynamics and generates low frequency coherent heat release rate disturbances and velocity perturbations in the fresh reactants with a characteristic frequency of about 10 Hz [Durox *et al.* (1990); Baillot *et al.* (1992); Li *et al.* (2012)]. This additional phenomenon is an artifact that cannot be eliminated using random velocity disturbances to determine the FTF as shown in Fig. 4.12. When the flame is submitted to harmonic perturbations, velocity and heat release rate large fluctuations are produced at a single frequency. The contribution from the flame flickering to the heat release rate perturbations is thus negligible at that frequency compared to the contribution induced by the acoustic perturbation. When random perturbations are used, the power is distributed over a wide range of frequencies. In that case, the contribution from the flame flickering can be larger than the contribution from the acoustic perturbations around 10 Hz and strongly impact the FTF measured with random velocity modulations. This instability is not included in the unit impulse response models examined in this work. To get rid of that low frequency hydrodynamic instability, both experimental and theoretical impulse responses are filtered using a 5^{th} order Butterworth low-pass filter with a cut-off frequency of 20 Hz. This operation is combined with a zero phase shift filter to ensure that no phase difference is introduced by the filtering operation. The results are shown in Fig. 4.13 for the uniform model (top figure), the convective model (center figure) and the incompressible convective model (bottom figure). The incompressible convective model features the best fit with experiments for the conical flame impulse response. However, large negative values are predicted in the time interval between $t = \tau_r$ and $t = \tau_c$. This behavior does not match well with experimental data. This feature may probably be improved by accounting for the axial decrease of the velocity impulse along the burner axis, as shown in section 4.2.3 in the frequency domain.

4.5 Conclusion

The FTF of conical flames submitted to different velocity perturbations has been studied in the case of an axisymmetric conical flame. It was shown that the FTF phase lag may be captured by considering an incompressible convective velocity perturbation model with a constant decay rate along the burner axis in the frequency domain. This was emphasized by several comparisons with predictions from different models and with experimental data. An analysis was also carried out in the time domain to determine the flame unit impulse response. Including a two-dimensional incompressible convected disturbance

was shown to greatly improve the FTF or unit impulse response, but the high frequency evolution of the FTF phase lag is still not well modeled. The FTF phase lag features a saturation at high frequency that is promoted as the perturbation level increases. This phenomenon is studied in the next chapter by considering the flame base contribution $F_B(\omega)$ to the FTF.

Chapter 5

Impact of flame-wall unsteady heat transfer on FTF

Effects of heat loss on the Flame Transfer Function (FTF) of an axisymmetric premixed conical flame is studied in this chapter. It is shown that unsteady heat transfer from the flame to the burner rim determines the dynamics of the anchoring point. A model for the contribution $F_B(\omega)$ to the FTF from the flame base displacement is derived. It takes into account unsteady heat losses from the flame base to the burner rim and the convection of the resulting flame wrinkles along the steady flame front. A model for enthalpy waves traveling between the flame base and the burner rim is used to derive the flame base motion frequency response and ultimately, the contribution to the FTF. This contribution to flame wrinkling becomes predominant at high frequencies and is responsible for saturation of the FTF phase lag at a nearly constant value. Experiments indicate that this phase lag saturation occurs at lower frequencies when the velocity modulation level is increased. Predictions from models including the flame base motion and the FTF phase lag saturation are compared to measurements. It is in particular shown that the flame anchoring point dynamics is responsible for the nonlinear response of the FTF phase lag when the perturbation level increases.

5.1 Introduction

Significant progresses were achieved in the previous chapter concerning the theoretical modeling of the phase lag between flow and heat release rate disturbances in the case of a premixed laminar conical flames. The FTF phase lag was shown to be well reproduced in the low and intermediate ranges of frequencies. However, the high frequency behavior of the FTF phase lag was not captured. It was also shown in Chapter 1 (see Eq. (1.21)) that the FTF can be split into two different contributions corresponding to two features of the reactive flow dynamics. The first one is the feedback from the wrinkled

flame front on the fresh reactant gas dynamics. This mechanism examined in the previous chapter can be well captured by imposing a divergence free convective flow perturbation to the fresh reactant velocity field. This type of perturbation is responsible for the regular increase of the phase lag with the forcing frequency observed in experiments when the flame aspect ratio is not too small. In this chapter, a second mechanism associated to the dynamics of the anchoring point is examined. It was shown that the flame base motion is controlled by unsteady heat losses from the flame to the burner rim. Perturbations of the flame anchoring point are further convected along the flame front.

The contribution of the flame base motion to flame front wrinkling is often neglected in theoretical models of conical FTF [Fleifil *et al.* (1996); Ducruix *et al.* (2000); Schuller *et al.* (2003a); Preetham and Lieuwen (2004)] by assuming that the flame is fixed to the anchoring device $\xi(X = 0, t) = 0$ (see Eq. 1.13 in Chapter 1). Experiments [Kornilov (2006); Karimi *et al.* (2009)] however indicate that this is a crude approximation. Kornilov *et al.* (2007) designed an experiment to control the flame motion at its base and analyzed its effects on FTF. They showed that perturbations from the flame base are convected along the flame front (as indicated by Eq. (1.13) and that the flame front, perturbed by the flame base motion, produces as a feedback a velocity perturbation in the fresh reactants around the flame. These authors also found that in this configuration, the corresponding FTF exhibits a saturation at high frequencies. This problem was also examined theoretically. Lee and Lieuwen (2003) used a kinematic description of the flame motion to derive an expression of the FTF as a function of flame base perturbations. The link between these perturbations and the incoming acoustic velocity perturbations was however not properly addressed and thus no results from that modeling were presented in their study. In the case of a ducted V-flame, Dowling (1999) also found that the motion at the flame base needs to be considered and was responsible of the nonlinear saturation of the FTF gain. It is shown here that in the case of a conical flame, the flame base motion mainly modifies the phase lag of the FTF.

In their FTF model of small conical flames anchored on a perforated plate, Altay *et al.* (2009) combined the kinematic description of the flame motion from Fleifil *et al.* (1996) to treat regions where the flame front is inclined, with a dynamic model for fluctuations of the mass burning rate where planar flame elements lie in front of the burner [Rook *et al.* (2002); Rook and de Goey (2003)]. It is shown in this chapter that the motion at the flame base needs also to be considered to describe the response of larger flames, *a priori* weakly interacting with the anchoring device. This feature will be shown to be essential to reproduce the high frequency and nonlinear evolutions of the FTF phase lag of single conical flames.

5.2 Flame base motion and its link to the FTF

Heat release rate fluctuations produced by perturbations at the flame base correspond to the contribution $F_B(\omega)$ appearing in Eq. (1.21) in Chapter 1. This contribution results from flame wrinkles, described by the second term in Eq. (1.13), which are generated at the flame origin $X = 0$ and are convected along the flame front towards the flame tip by the mean flow velocity component tangential to the steady flame front $v_0 \cos\alpha$ (see Section 1.2.1). These wrinkles integrated over the flame surface produce in turn surface area perturbations and thus heat release rate disturbances.

The starting point to model this contribution is to examine the resulting flame surface area fluctuations. Considering only the contribution from flame base disturbances in Eq. (1.13), one obtains (see Chapter 1 for more details):

$$\tilde{A}_{1B} = 2\pi \int_0^L \tilde{\xi}(X) \cos\alpha dX = 2\pi \cos\alpha \frac{e^{iKL} - 1}{iK} \tilde{\xi}(0) \tag{5.1}$$

By dividing this expression by the steady flame surface area A_0, it is possible to determine the flame transfer function F_B component:

$$F_B(\omega) = \frac{\tilde{A}_{1B}/A_0}{\tilde{v}_1/v_0} = \frac{\tilde{A}_{1B}/A_0}{\tilde{\xi}(0)/R} \frac{\tilde{\xi}(0)/R}{\tilde{v}_1/v_0} = F_C(\omega_*, \alpha)\ \Xi(\omega) \tag{5.2}$$

that can be decomposed as a product of two contributions $F_c(\omega_*, \alpha)$ and $\Xi(\omega)$, where:

$$F_C(\omega_*, \alpha) = 2\cos\alpha \frac{e^{i\omega_*} - 1}{i\omega_*} \tag{5.3}$$

is a filter which is a function of the flame angle α and of the reduced frequency $\omega_* = \omega R/(S_d \cos\alpha)$, and

$$\Xi(\omega) = \frac{\tilde{\xi}(0)/R}{\tilde{v}_1/v_0} \tag{5.4}$$

which links the flame base motion normal to the flame front to the axial velocity modulation at the burner outlet.

Equation 5.2 describes how small displacements at the flame base are filtered by the flame and produce heat release rate disturbances. The frequency response of the flame base motion with respect to the velocity modulation at the burner outlet is represented here by $\Xi(\omega)$ as a function of the forcing frequency. Flame displacements at the flame foot are then convected along the flame front and their contribution to heat release rate perturbations is filtered by $F_C(\omega_*, \alpha) = G_C(\omega_*, \alpha) \exp(i\varphi_C(\omega_*))$ plotted in Fig. 5.1 with respect to the reduced frequency ω_* for different values of the flame tip half-angle $\alpha = \pi/3$,

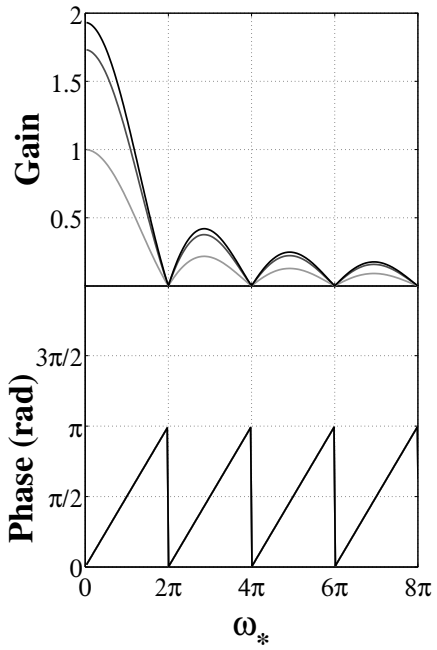

Figure 5.1: *Transfer function $F_C(\omega_*, \alpha)$ plotted as a function of reduced frequency ω_* for different angles $\alpha = \pi/12$ (black), $\pi/6$ (dark grey), and $\pi/3$ (light grey).*

$\pi/6$ and $\pi/12$. The gain G_C is a low-pass filter with decreasing amplitudes for increasing flame angles α. The unwrapped phase lag φ_C is independent of the flame angle and is characterized by oscillating values comprised between 0 and π when the reduced frequency increases, without any values between π and 2π. This feature indicates that, although wrinkles produced at the flame base are convected along the flame front, the resulting heat release rate disturbances do not feature a regular increase of the phase lag with the reduced frequency. The remaining problem is to model the flame base displacement induced by the velocity modulation at the burner outlet to determine $\Xi(\omega)$. This issue is addressed in the next section.

5.3 Modeling the flame base displacement frequency response $\Xi(\omega)$

To model $\Xi(\omega)$, it is natural to examine the motion of a planar premixed flame stabilized close to a solid boundary and submitted to acoustic perturbations. Away from the solid elements, one may reasonably consider that the flame dynamics obey to an adiabatic evolution. In the vicinity of the anchoring device, heat transfer between the flame and the solid wall is of significant importance. The dynamics of a planar flame front interacting with a solid permeable injection unit has already been treated theoretically [Joulin (1982); McIntosh

and Clarke (1984); Mclntosh (1990)]. Models derived in these studies were used to determine the corresponding transfer function of planar and inclined flames stabilized above porous burners [Rook *et al.* (2002); Altay *et al.* (2009)].

It was shown that planar flame elements stabilized on the top of the burner are perturbed in two ways. Firstly, acoustic velocity perturbations produce regular flame front displacements with respect to the burner position. These perturbations in the flame position modify in turn the injection conditions at the burner outlet. When synchronized they may lead to a resonant coupling in certain circumstances [Rook *et al.* (2002)]. Enthalpy $h = \Delta h_f^0 Y_f + c_p T$ disturbances between the flame front and the burner control this interaction, where Δh_f^0 is the heat value per unit mass of fuel, Y_f is the fuel mass fraction in the mixture, c_p is the mixture specific heat at constant pressure and T is the mixture temperature.

In Rook *et al.* (2002) analysis, the fuel mass fraction Y_f is fixed at the flame front and the temperature T remains constant at the burner outlet and equal to T_u. Fluctuations of the flame front distance with respect to the burner outlet induce enthalpy disturbances that are transported by both convection and diffusion processes, from the burner to the flame resulting in temperature fluctuations. When these disturbances reach the flame front, they induce in turn perturbations in flame speed producing a displacement of the flame front. These phenomena can couple and lead to resonance when the enthalpy disturbance wavelength is of the order of $4\psi_{f_0}$ [Rook *et al.* (2002); Rook and de Goey (2003)], where ψ_{f_0} is the flame stand-off distance with respect to the burner outlet (see Fig. 1.3). Using this mechanism, Rook *et al.* (2002) obtained an expression for the transfer function linking flame speed perturbations $\tilde{S}_{d1}$ to acoustic velocity disturbances $\tilde{V}_1(X = \psi_{f_0})$ at the flame base. This relation is rewritten here in a slightly modified form with compact notations to highlight the main dimensionless numbers controlling the flame anchoring point dynamics:

$$\begin{aligned}\mathcal{A}(\mathrm{Ze}, \hat{\omega}, \Psi_f) &= \frac{\tilde{S}_{d1}}{\widetilde{V}_1(X = \psi_{f_0})} \\ &= \left[1 - \frac{i\hat{\omega}}{\mathrm{Ze}} \sinh(\Psi_f) \exp\left(\Psi_f (1 - i\hat{\omega})^{1/2}\right)\right]^{-1}\end{aligned} \tag{5.5}$$

where

$$\begin{aligned}\hat{\omega} &= 4\omega \frac{\delta}{S_{d0}} \\ \mathrm{Ze} = \frac{T_a}{T_b}\frac{T_b - T_u}{T_b} \quad &\text{and} \quad \Psi_f = \frac{\psi_{f_0}}{2\delta} = \frac{1}{2}\log\left(\frac{T_{ad} - T_u}{T_{ad} - T_b}\right)\end{aligned} \tag{5.6}$$

In these expressions, ω denotes the angular forcing frequency, δ indicates the thermal flame thickness, S_{d0} is the steady flame speed, T_a is the activation

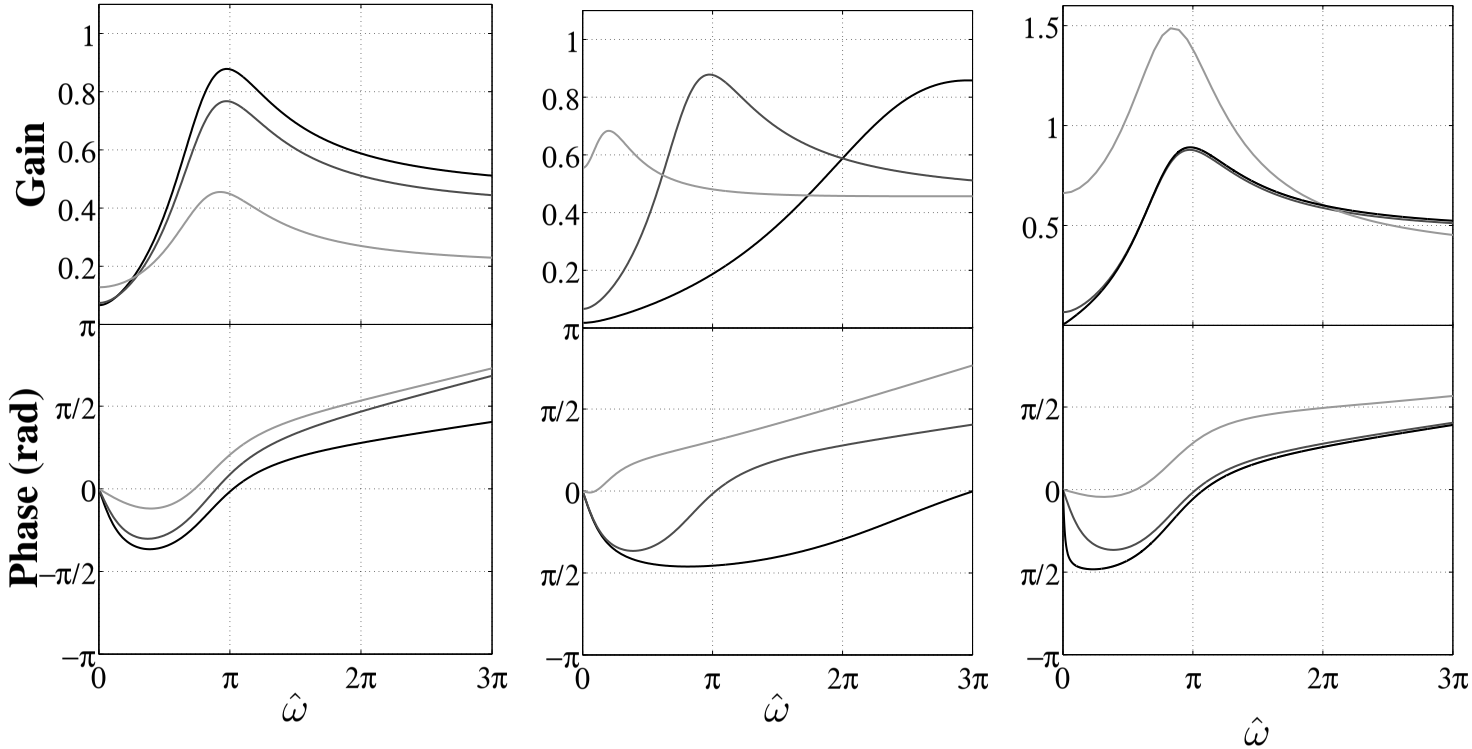

Figure 5.2: *Transfer Function* $\Xi(\hat{\omega}, \Psi_f, \alpha, \delta_*, \mathrm{Ze})$ *plotted as a function of reduced frequency* $\hat{\omega}$. *The Zeldovich number* $\mathrm{Ze} = 10$ *is kept constant in all figures.*
(left) *Effects of the flame tip half-angle* $\alpha = \pi/12$ *(black),* $\pi/6$ *(dark grey) and* $\pi/3$ *(light grey).* $\Psi_f = 1$. $\delta_* = 0.05$.
(center) *Effects of the flame stand-off distance* $\Psi_f = 0.5$ *(black),* 1 *(dark grey), and* 2 *(light grey).* $\alpha = \pi/12$ *rad.* $\delta_* = 0.05$.
(right) *Effects of the thermal flame thickness* $\delta_* = 0.005$ *(black),* 0.05 *(dark grey) and* 0.5 *(light grey).* $\alpha = \pi/12$ *rad.* $\Psi_f = 1$.

temperature, T_b is the burnt gas temperature, T_u is the fresh mixture gas temperature, also taken here equal to the burner temperature, ψ_{f_0} corresponds to the steady flame stand-off distance above the burner and T_{ad} is the adiabatic flame temperature.
Dimensional analysis indicates that the problem can be fully described by only three dimensionless numbers, namely the Zeldovich number Ze, a reduced frequency associated with a flame time scale $\hat{\omega}$, and the dimensionless flame stand-off distance Ψ_f with respect to the flame thickness. It is here interesting to further introduce the ratio δ_* between the thermal flame thickness projected along the horizontal direction $\delta \cos\alpha$ divided by the burner radius R:

$$\delta_* = \frac{\delta \cos\alpha}{R} \quad \text{and} \quad \hat{\omega} = 4\delta_*\omega_* \tag{5.7}$$

This new ratio enables as a first approximation to take into account the fact that the flame front near the anchoring device is not parallel to the burner lip but features an angle α with respect to the axial direction [Cuquel *et al.* (2013a)]. It also clarifies the link between the reduced frequencies ω_* controlling the dynamics of the inclined flame far from the solid boundary and $\hat{\omega}$ controlling the flame base motion near solid elements. As the flame angle α does not appear explicitly in the expression of $\hat{\omega}$, relations in Eq. (5.7) only yield approximate estimates of the influence of the flame angle. They are however useful to sort out the different mechanisms controlling the flame dynamics depending on the size of the injector. These relations indicate that for small burner outlet radius which dimension is of the same order of magnitude as the thermal flame thickness $\delta_* \simeq 1$, and $\hat{\omega} \sim \omega_*$. This is for example the case in porous burners used to stabilize planar or small conical flames [Schreel *et al.* (2002); Rook and de Goey (2003); Schreel *et al.* (2005); Altay *et al.* (2009); Kedia *et al.* (2011)]. In many situations, the flame thickness is however much smaller than the injection tube radius and $\delta_* \ll 1$, indicating that the reduced frequencies $\hat{\omega}$ and ω_* are well separated for larger flames. This analysis emphasizes that in many practical burners, flame wrinkling resulting from velocity and anchoring point disturbances produce contributions to heat release rate disturbances in different frequency bands.

It is now possible to use Eq. (5.5) to determine the motion imparted to the flame base of a conical flame using a local kinematic description. The flame base lies close to the burner rim shear layer where the mean flow velocity is significantly reduced. Therefore, the convective term appearing in Eq. (1.11) in Chapter 1 may be neglected. In this case, this equation reduces to:

$$\frac{\partial \xi(0)}{\partial t} = V_1(\psi_{f_0}, t) - S_{d1}(t) \tag{5.8}$$

where $V_1(\psi_{f_0}, t)$ indicates the velocity perturbation normal to the flame front at the flame base $X = \psi_{f_0}$ and $S_{d1}(t)$ denotes disturbances of the flame speed

at the same location. The Fourier transform of Eq. (5.8) yields the following model for the flame base motion transfer function:

$$\Xi(\omega) = -\frac{v_0}{i\omega R}\left(1 - \frac{\tilde{S}_{d1}}{\tilde{V}_1(\psi_{f_0})}\right)\frac{\tilde{V}_1(\psi_{f_0})}{\tilde{v}_1} \tag{5.9}$$

An expression for the remaining term $\tilde{V}_1(\psi_{f_0})/\tilde{v}_1$, linking the normal velocity perturbation at the flame base at $X = \psi_{f_0}$ to the axial velocity modulation at the burner outlet $\tilde{v}_1$, was proposed in Chapter 4:

$$\frac{\tilde{V}_1(\psi_{f_0})}{\tilde{v}_1} = \sin\alpha\left[1 - \frac{ik_*}{2}\left(1 - \frac{\psi_{f_0}}{L}\right)\right]\exp\left(ik_*\frac{\psi_{f_0}}{L}\right) \tag{5.10}$$

where $L = R/\sin\alpha$ is the steady flame front length and $k_* = \omega H/v_0 = \omega_* \cos^2\alpha$ denotes the wavenumber associated to flow perturbations convected along the axial direction. By combining Eqs. (5.9) and (5.10), one finally obtains the desired expression linking perturbations at the flame base due to incoming velocity disturbances:

$$\begin{aligned}\Xi(\mathrm{Ze}, \hat{\omega}, \Psi_f, \alpha, \delta_*) &= \frac{\tilde{\xi}(0)/R}{\tilde{v}_1/v_0} \\ &= -4\delta_* \frac{1 - \mathcal{A}(\mathrm{Ze}, \hat{\omega}, \Psi_f)}{i\hat{\omega}\cos\alpha}\exp\left(i\frac{1}{2}\hat{\omega}\Psi_f\cos\alpha\sin\alpha\right) \\ &\quad \left(1 - i\frac{1}{8}\frac{\hat{\omega}}{\delta_*}\cos^2\alpha\,(1 - 2\delta_*\Psi_f\tan\alpha)\right)\end{aligned} \tag{5.11}$$

For a given mixture and operating conditions, the Zeldovich number is fixed, the transfer function Ξ is then a function of the reduced frequency $\hat{\omega}$ and its geometrical characteristics α, Ψ_f and δ_*. Predictions for $\Xi(\mathrm{Ze}, \hat{\omega}, \Psi_f, \alpha, \delta_*)$ are plotted in Fig. 5.2 as a function of $\hat{\omega}$, in terms of gain and phase for different values of the remaining parameters. The Zeldovich number is kept constant in all figures: $\mathrm{Ze} = 10$. This value corresponds to the order of magnitude of Zeldovich numbers for methane/air flames at atmospheric pressure [Gu *et al.* (2000)]. In the left figure, the flame tip half angle is changed $\alpha = \pi/12; \pi/6; \pi/3$ for fixed values of the normalized stand-off distance $\Psi_f = 1$ and of the dimensionless flame thickness $\delta_* = 0.05$. In the center figure, the dimensionless flame stand-off distance is changed $\Psi_f = 0.5; 1; 2$ for fixed values of $\alpha = \pi/12$ and $\delta_* = 0.05$. In the right figure, the dimensionless flame thickness is changed $\delta_* = 0.005; 0.05; 0.5$ for fixed values of $\alpha = \pi/12$ and $\Psi_f = 1$. The response corresponds to a frequency passband filter with a resonance-like behavior which frequency peak location is strongly dependent on the dimensionless flame stand-off distance Ψ_f. The gain reaches an almost constant value as the reduced frequency $\hat{\omega}$ is increased. This asymptotic behavior mainly depends on the flame tip half-angle. The phase lag decreases at low frequencies, before increasing again and reaching a very small but constant slope at high reduced frequencies

$\hat{\omega}$. The resonance frequency shifts to higher frequencies as Ψ_f decreases. All other parameters remaining constant, a drop in the flame stand-off distance corresponds to a shorter resonance wavelength and a larger peak frequency. The phase lag minimum is also shifted to higher frequencies when Ψ_f decreases. The maximum value of the gain depends on the dimensionless flame thickness δ_*. When the flame thickness is of the order of the burner outlet radius, the gain maximum value almost doubles compared to a situation where the flame thickness is much smaller than the burner radius. The phase lag keeps the same global trends when δ_* is modified but does not feature the same asymptotic value at high frequencies when δ_* is increased. A modification in the flame tip half-angle has a significant impact on both the gain and the phase lag, especially at high frequencies.

This analysis shows that the contribution $F_B(\omega) = F_C(\omega_*, \alpha)\ \Xi(\mathrm{Ze}, \hat{\omega}, \Psi_f, \alpha, \delta_*)$ to the FTF $F(\omega)$ resulting from wrinkles induced by the flame base motion features a saturation of the phase lag at high frequencies originating from $\Xi(\mathrm{Ze}, \hat{\omega}, \Psi_f, \alpha, \delta_*)$ which is modulated by the oscillation of $F_C(\omega_*, \alpha)$. An experimental validation of these predictions is presented in the next section. The flame base motion is first examined. Its frequency response is measured and is compared to the predictions from the model derived in the present section.

5.4 Experimental determination of the flame base motion

The following measurements were conducted on a burner exit featuring a plateau shape without quartz tube to confine the flame (see Fig. 2.1 in Chapter 2). A methane/air mixture was used to stabilize a premixed flame above that burner with the following parameters: $R = 0.011$ m, $\phi = 1.03$ and $v_0 = 1.56$ m.s^{-1}. Two modulation levels were investigated: $v_1^{\mathrm{rms}}/v_0 = 0.1$ and 0.05.

5.4.1 Analysis of the flame base motion

Six phase conditioned average images, separated by a constant phase lag, are presented in Fig. 5.3 over a modulation cycle for a forcing frequency $f = 100$ Hz and a velocity perturbation level fixed to $v_1^{\mathrm{rms}}/v_0 = 0.1$. The steady flame position is also plotted in these figures as dashed-dotted white lines to provide a reference. These images clearly show that the flame base is not motionless, but undergoes a periodic oscillation around its steady position. These perturbations are then convected along the flame front. Figures 5.4-a and -b plot the displacement of the flame base around its mean position during one forcing period, for two different forcing frequencies $f = 100$ and 200 Hz. This periodic motion of the flame base is roughly oriented along a main direction, supporting the fact that the perturbations at the flame base can effectively be well

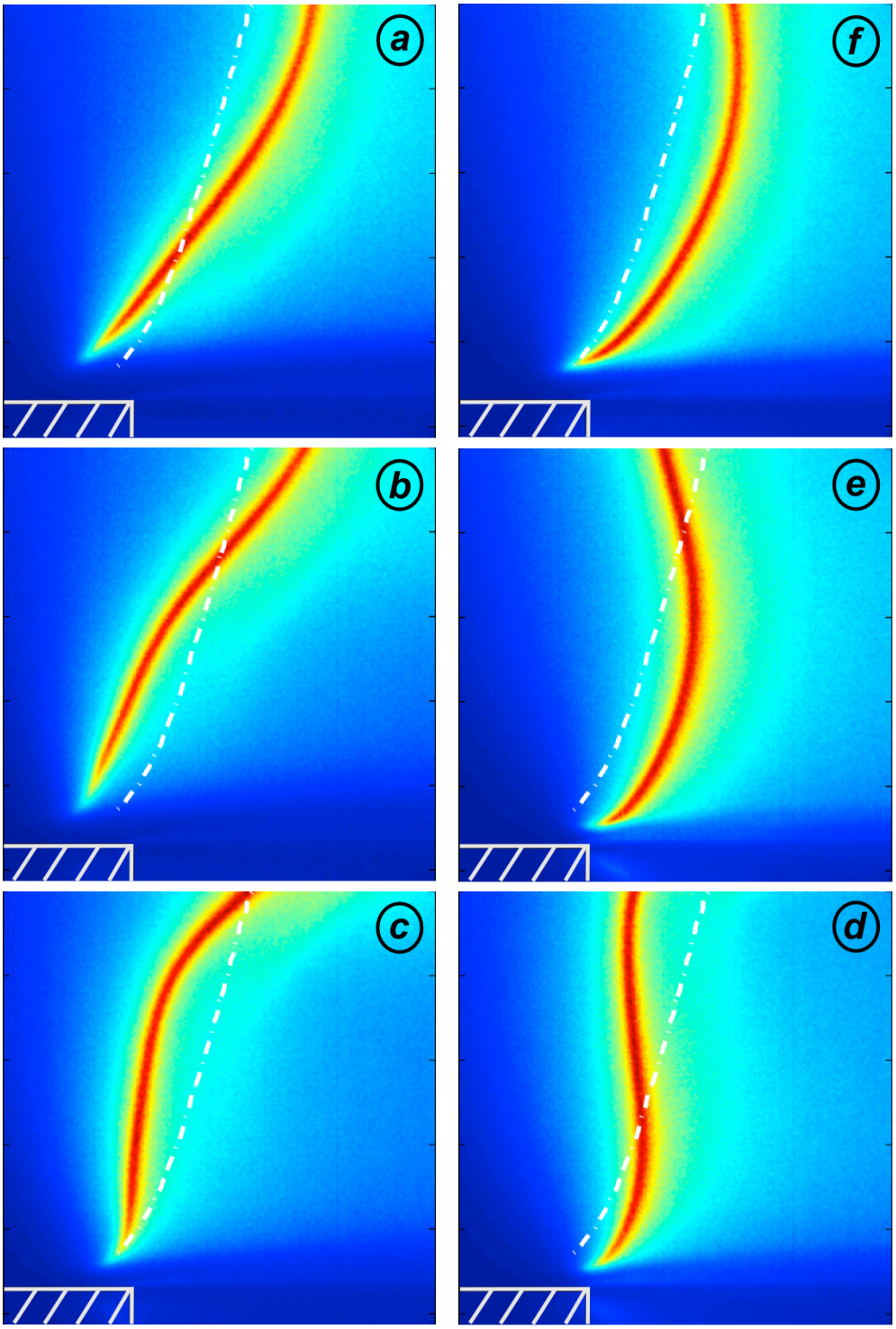

Figure 5.3: *Images of the flame base motion taken at six regularly spaced phases during a modulation cycle for a forcing frequency $f = 100$ Hz and a velocity fluctuation level $v_1^{\mathrm{rms}}/v_0 = 0.1$. The steady flame position is indicated as white dashed-dotted lines. The burner edge is represented in white in the bottom left part of the images. A premixed methane/air mixture flows out of the burner with at a velocity $v_0 = 1.56$ $m.s^{-1}$ and an equivalence ratio $\phi = 1.03$.*

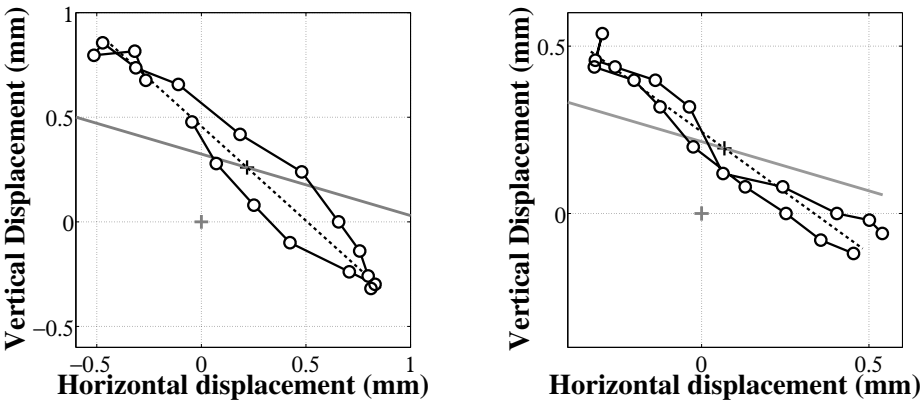

(a) $f = 100$ Hz. (b) $f = 200$ Hz.

Figure 5.4: *Flame base motion for a modulation amplitude of* $v_1^{\mathrm{rms}}/v_0 = 0.1$ *(grey +) Steady flame base location. (black +) Mean location of the flame base displacement. (black line) Flame base motion determined experimentally. (black dashed line) Measured direction normal to the flame front at the flame base, defined by* α_{base}*. (grey solid line) Theoretical direction normal to the flame front, defined by* $\alpha = \arcsin(S_{d0}/v_0)$*.*

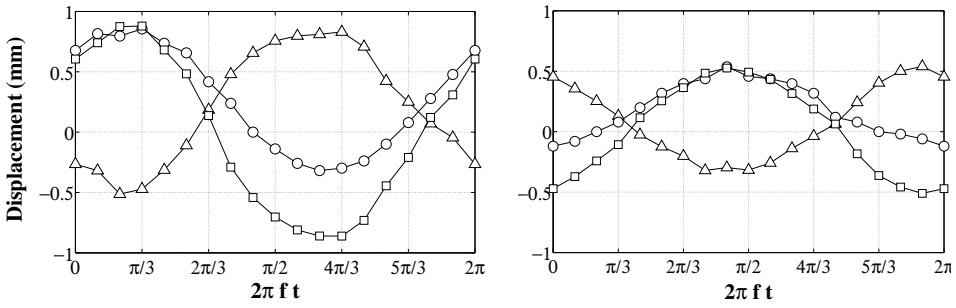

(a) $f = 100$ Hz. (b) $f = 200$ Hz.

Figure 5.5: *Flame base displacement as a function of the phase in the excitation cycle for a modulation amplitude of* $v_1^{\mathrm{rms}}/v_0 = 0.1$*. The horizontal (△) and vertical displacements (○) with respect to the steady flame location are represented, as well as the displacement in the normal direction with respect to the flame front (□).*

described only by a displacement normal to the mean flame front. It was also found that the mean and steady flame front positions coincide well.

These observations are further supported by Fig. 5.5-a and -b where the flame base displacement is plotted with respect to the phase of the forcing signal. The three curves represent the horizontal, vertical and normal to the steady flame front displacement components. They all feature a periodic signal which is nearly a harmonic function of time. The amplitude of this displacement is

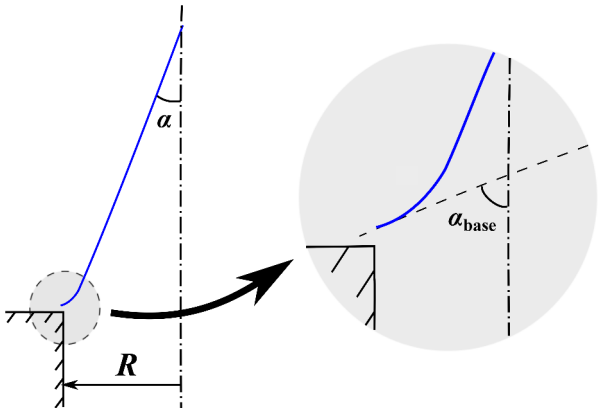

Figure 5.6: *Scheme of a conical flame with a zoom on the flame base showing the difference between the flame tip half-angle α and the flame base angle α_{base}.*

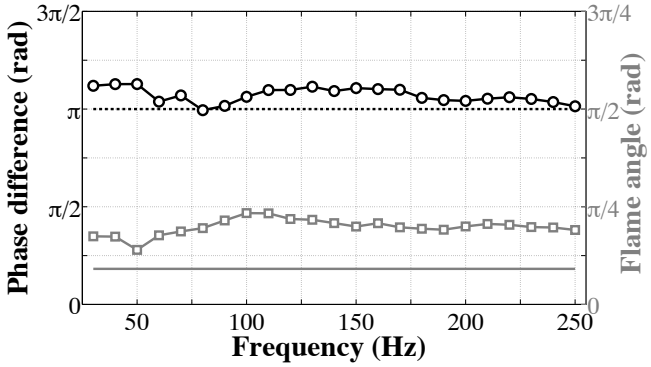

Figure 5.7: *Evolutions of the (black curve and circles) phase difference between the horizontal and the vertical flame front displacement at its base, (grey line) flame tip half-angle defined by $\alpha = \arcsin(S_d/v_0)$ and (grey circles) angle α_{base} between the flame front at the flame base and the vertical axis. Perturbation level $v_1^{\text{rms}}/v_0 = 0.1$.*

of the order of 1 mm, a value which is consistent with other studies conducted with similar flames in the same flow and forcing conditions [Kornilov (2006); Karimi *et al.* (2009)]. Moreover, the phase differences between the horizontal and vertical displacements, shown in Fig. 5.7 (black lines) as a function of the forcing frequency, are very close to phase opposition (π). This observation further supports the assumption used in the model that the flame base oscillation is mainly oriented along a single direction. The measured amplitudes of the horizontal and vertical displacements of the flame base are used to identify the principal direction of the flame base motion. This information enables to determine the angle α_{base} formed by the flame front and the vertical axis near the flame base (see Fig. 5.6 for the difference with the flame tip half-angle α). This direction is indicated as black dashed lines in Fig. 5.4-a and -b.

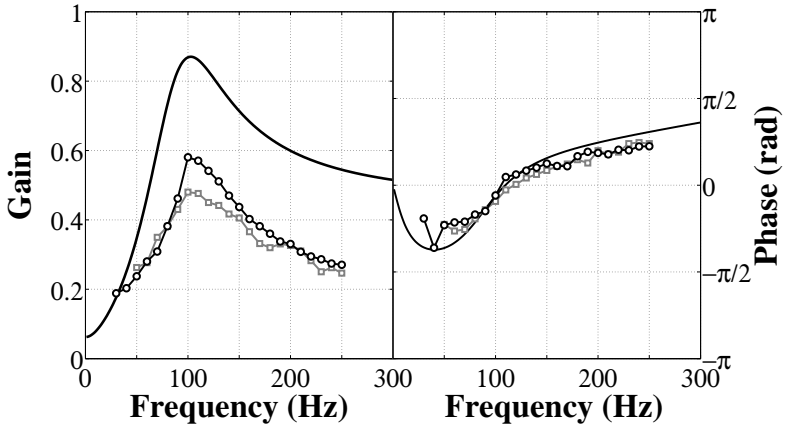

Figure 5.8: *Transfer function $\Xi(\omega)$ gain (left) and phase (right) as a function of the forcing frequency. The theoretical transfer function (black curve) is compared to measurements for two input levels $v_1^{\mathrm{rms}}/v_0 = 0.05$ (grey curve with square symbols) and $v_1^{\mathrm{rms}}/v_0 = 0.1$ (black curve with circle symbols).*

The normal direction with respect to the theoretical flame front direction defined by the half-angle at the flame tip $\alpha = \arcsin(S_{d0}/v_0)$ is also indicated as black dashed dotted lines for comparison in Fig. 5.4. Predictions largely deviate from measurements because the flame angle α_{base} at the flame base differs significantly from the one at the flame tip α. The value of the angle at the flame base is determined by a balance between the flow velocity and the flame burning velocity at this location. The burning velocity at the flame base is reduced due to heat loss to the burner rim and the flow velocity in the wake of the burner edge takes also small values. These effects combine and modify the flame angle with respect to its value far from the burner edges [Altay *et al.* (2010); Kedia *et al.* (2011); Kedia and Ghoniem (2013)]. In Fig. 5.7 (grey lines), the values taken by the angles α (plain line) and α_{base} (circles) are plotted as a function of the forcing frequency. It is shown that the difference between the two angles is significant on all the frequency range of interest. This phenomenon is also highlighted in the images of the steady flame, where the flame front is slightly bent close to the burner edge (dashed-dotted lines in Fig. 5.3).

Measurements of the flame base motion are now post-processed to determine the transfer function $\Xi_{\mathrm{exp}}(\omega)$. These data are compared to predictions from Eq. (5.11). The flame stand-off distance was determined using images of the steady flame. In the configuration explored, it was found that $\psi_{f_0} = 1$ mm (Fig. 5.3). For the methane/air flame investigated stabilized on a plateau-shaped burner with a outlet radius $R = 0.011$ m and a for a methane/air mixture with $\phi = 1.03$ and $v_0 = 1.56$ m.s^{-1}, the following parameters were used to compute $\Xi(\hat{\omega})$: $T_{ad} = 2234$ K, $T_b = 2000$ K, $T_u = 300$ K, $T_a = 24000$ K, $\bar{S}_{d0} = 0.44$ m.s^{-1} and $\delta = 0.47$ mm.

The corresponding dimensionless numbers are Ze = 10.2 [Gu *et al.* (2000)], $\delta_* = 0.037$ and $\Psi_f = 1.056$. Measurements were conducted for two velocity modulation levels $v_1^{\rm rms}/v_0 = 0.05$ and $v_1^{\rm rms}/v_0 = 0.10$ over the frequency range 30 to 250 Hz with a frequency resolution of 10 Hz. Results are presented in Fig. 5.8. The measured gain shows a resonance-like behavior with a peak frequency reached at about 100 Hz and an amplitude of almost 0.6. Data for the two modulation levels collapse on the same curve except in the region near the peak value of the gain, which slightly increases with the perturbation level. The flame base response remains linear for these modulation levels except near resonance. This observation is in agreement with previous measurements [Karimi *et al.* (2009)], where the mean value of the flame base diameter was found to be equal to its steady value up to a very high forcing level $|v_1/v_0| \simeq 1$. The authors also found that the amplitude of the dimensionless flame base diameter perturbations scaled linearly with the perturbation level $|v_1/v_0|$, even when $|v_1/v_0|$ approaches unity. The phase lag plotted in Fig. 5.8 decreases first with increasing frequencies before reaching an almost constant value for frequencies higher than 170 Hz. This behavior is in good agreement with predictions, except that the predicted gain exceeds by far measurements. The global behavior is however well retrieved including the correct location of the peak frequency for the gain of the flame base response. The phase lag is well reproduced by the model.

5.4.2 Analysis at high frequency

It is now possible to examine the evolution of the phase lag at high frequency. Expressions from Eqs. (5.3) and (5.11) for $F_C(\omega)$ and $\Xi(\omega)$ are combined and used to estimate the contribution $F_B(\omega) = F_C(\omega)\ \Xi(\omega)$ to the conical flame response. Results are plotted in Fig. 5.9-left, where predictions for $F_B(\omega)$ (grey solid lines) are compared to the FTF $F(\omega)$ (black circles) determined experimentally. The phase lags of the functions F_B and F match well at high frequency and are characterized by a saturation. The gains have the same behavior in this frequency range as well. This demonstrates that saturation of the FTF phase lag at high frequency may be captured by including the description of the flame base motion in the analysis. This motion at the flame base determines the high frequency behavior of the flame response to velocity perturbations.

5.5 Nonlinear behavior of the FTF of conical flames

It is now worth examining effects of the perturbation level. For small amplitudes, it was shown that the FTF of conical flames may be captured over the frequency range of interest by including two main features:

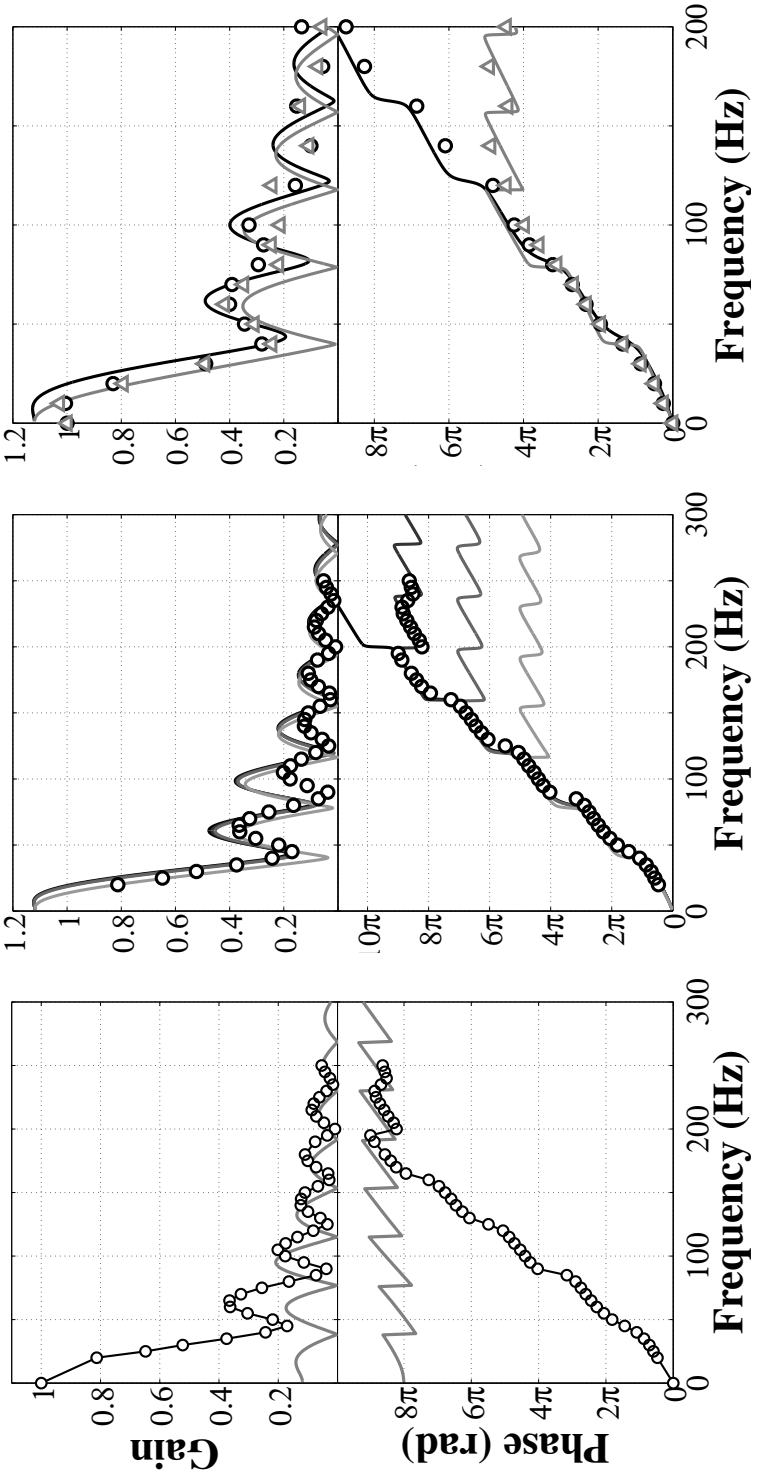

Figure 5.9: *Transfer function gain (top) and phase (bottom). Left: FTF component $F_B(\omega)$ as a function of the forcing frequency. The theoretical contribution $F_B(\omega)$ (grey curve) is compared to FTF measurements $F(\omega)$ for $v_1^{\mathrm{rms}}/v_0 = 0.04$ (black circles). Center : Comparison between measurements (black circles) and predictions of the FTF $F(\omega)$ obtained with the incompressible convective model for increasing values of $b = 0.4$, 0.45, 0.5, and 2 that are associated to lines with decreasing darkness. Right: FTF measurements from Durox et al. (2009) for $|v_1/v_0| = 0.04$ (black circles) and $|v_1/v_0| = 0.07$ (grey triangles) are compared to predictions $F(\omega)$ with $b = 0.4$ (black line) and $b = 6$ (grey line).*

- The first is the interaction of the flame front with velocity perturbations convected in the fresh gases. This mechanism was thoroughly analyzed in Chapter 4. This interaction controls the dynamics of the conical flame in the low and intermediate frequency ranges. It determines the shape of the FTF gain as well as the regular increase of the FTF phase lag with the forcing frequency. It was also shown that the perturbed flow field needs to satisfy the continuity equation to reproduce the correct FTF behavior observed in experiments at low frequency. These features cannot be captured by prescribing a uniform bulk oscillation or a one dimensional convective wave to the perturbed flow field. One possibility is to use an incompressible convected wave to improve the description of the FTF at low and intermediates frequencies. This has led to the derivation of an expression for the FTF component F_A.

- The second mechanism was examined in the previous sections and considers the interaction of the flame base with the local perturbed flow field and unsteady heat loss to the burner. Disturbances originating from the motion of the flame base are convected along the flame front and result in additional contributions to the FTF gain and phase lag. It was shown that this contribution is responsible for the FTF phase lag saturation at high frequency. By coupling the velocity disturbance model proposed in Chapter 4 with a description of enthalpy waves originating from the burner rim and traveling to the flame base, it was possible to capture the correct flame base motion and retrieve the FTF behavior observed in experiments at high frequency. This analysis has led to an expression for the FTF component F_B.

These features are not specific to this configuration and can be identified by examining the different data set of responses to flow perturbations gathered on single conical flames [Ducruix *et al.* (2000); Kornilov *et al.* (2007); Karimi *et al.* (2009)] and multiple conical flames [Kornilov *et al.* (2009); Duchaine *et al.* (2011)] stabilized on various burners with different injector sizes. In several cases, it is found that the FTF phase lag features a saturation at high frequency, but this is not always the case [Noiray *et al.* (2008); Kornilov *et al.* (2009); Boudy *et al.* (2011)]. It is also known from studies considering effects of the input level that the frequency at which this FTF phase lag saturation occurs strongly depends on the perturbation amplitude [Durox *et al.* (2009)]. When the perturbation amplitude increases, the FTF gain decreases and saturation of the FTF phase lag is triggered at a lower forcing frequency.

Effects of the input level may be interpreted with the model devised in this study. The two contributions F_A and F_B to the FTF feature distinct responses to the amplitude of incoming velocity disturbances. The gain of the component F_A decreases rapidly as the velocity modulation level increases at the burner

outlet [Preetham *et al.* (2008); Durox *et al.* (2009)], whereas it was shown by Karimi *et al.* (2009) and confirmed in this study that the amplitude of the flame base motion features a linear response even at very large forcing levels $|v_1/v_0| \simeq 1$. This indicates that the component F_B can take over F_A on a larger frequency range as the velocity modulation level increases. The influence of the motion at the flame base on the FTF is becoming increasingly predominant at lower frequencies over effects of flame wrinkling resulting from velocity perturbations when the disturbance level increases. This behavior may be reproduced using the following approximation, where the nonlinear FTF component F_A is modeled with an increasing value of the parameter b when the perturbation level increases and the FTF component F_B is supposed to be unchanged:

$$F_{\mathrm{nl}}(\omega, b) = F_A(\omega, b) + F_B(\omega) \tag{5.12}$$

It was shown in Section 4.2.3 that when the decay rate b increases the gain of F_A drops while the phase lag remains merely unaffected. This ad-hoc description of effects of the input level cannot be used to fully describe the nonlinear response of F_A, but it features some similarities with measured flame describing functions [Durox *et al.* (2009); Boudy *et al.* (2011)]. The coefficient b is used here to modify the relative magnitudes of the two terms F_A and F_B in Eq. (5.12) to simulate their responses as the velocity modulation is increased. The function $F_A(\omega, b)$ considered here uses the decaying incompressible convective velocity disturbance model derived in Section 4.2.3. The function $F_B(\omega)$ is that derived in the Section 5.2.

Predictions from Eq. (5.12) are plotted in Fig. 5.9-center for different values of the decay rate $b = 0.4,\ 0.45,\ 0.5,\ 2.0$ (solid black and grey curves), which are compared to the measured FTF for a small perturbation level $v_1^{\mathrm{rms}}/v_0 = 0.04$ (black circles). The modeled FTF shows different saturation levels for different values of b. The frequency where the phase lag saturates decreases as b decreases, i.e. when $|v_1/v_0|$ increases. One may also note that the phase lags reached at saturation are all the same, modulo 2π. This feature is also consistent with previous experimental observations [Durox *et al.* (2009); Kornilov *et al.* (2009)]. Measurements from Durox *et al.* (2009) are plotted as dark circles and grey triangles in Fig. 5.9-right for two disturbance levels $|v_1/v_0| = 0.04$ and $|v_1/v_0| = 0.07$ where they are compared with predictions from Eq. (5.12) for $b = 0.4$ and $b = 6.0$. These values were tuned to reproduce the experiments. This figure clearly confirms that saturation of the phase lag occurs at lower frequencies when the contribution F_A to the FTF is reduced and that it is possible to match the FTF gain and phase evolutions over the full frequency range of interest for different perturbation levels with Eq. (5.12) by tuning the velocity disturbance decay rate b.

This analysis highlights the nonlinear response of conical flames submitted to flow perturbations and shows that this behavior results from a competition between flame wrinkling resulting from velocity and flame base motion disturbances, the former mechanism being strongly altered by the disturbance level while the latter one remains essentially insensitive to the perturbation amplitude. The dynamics at the flame anchoring device is pointed here as controlling the nonlinear response of the flame to flow perturbations. This was already recognized by Dowling (1999) in her analysis of the response of a ducted V-flame to flow perturbations. When the perturbation level reached a certain threshold level, the amplitude of the flame response saturated due to flashback at the flame anchoring device. In the case of conical flames, it was shown in this study that the anchoring point dynamics triggered an abrupt change of the phase lag when the perturbation amplitude increased. In more complex configurations, it may be inferred that the dynamics of the flame near anchoring devices is an important element to consider to understand the nonlinear dynamics of the combustor.

5.6 Conclusion

The heat loss contribution $F_B(\omega)$ to the FTF has been studied in the case of an axisymmetric conical flame submitted to acoustic flow perturbations. It was shown that these perturbations produce disturbances of the flame base motion. This motion can be modeled by taking into account enthalpy waves traveling between the flame base and the burner rim. These disturbances wrinkle the flame front and lead to additional heat release rate perturbations. Their contribution $F_B(\omega)$ to the global FTF may be deduced. This expression features a phase lag that saturates at an almost constant value. Measurements were carried out to determine the flame base motion and the FTF. Predictions were compared to these data. The model reproduces the resonant peak location of the flame base disturbance frequency response. Furthermore, the phase lag of the FTF contribution $F_B(\omega)$ matches well with the measured FTF phase lag in the high frequency range where the phase lag saturates. This saturation of the FTF phase lag occurs at lower frequencies as the perturbation level is increased. This behavior can be reproduced by a description including a change in the relative magnitude of the two contributions $F_A(\omega)$ and $F_B(\omega)$. Increasing in the perturbation levels are here modeled by higher decay rates of axial velocity perturbations. This model enables to reproduce measurements and to observe a change of the FTF phase lag in the high frequency range as the perturbation level is increased.

Chapter 6

Confinement effects on the FTF

The influence of confinement side walls on the response of a premixed conical flame submitted to velocity disturbances is investigated experimentally and theoretically in this chapter. In that case, the confinement ratio defined here by $C_r = R_0/R_1$, where R_0 and R_1 denote the burner and flame tube radii and the burnt to unburnt gas volumetric expansion ratio $E = \rho_u/\rho_b$ need to be taken into account in the description of the FTF. The main effect of confinement is an acceleration of the fresh stream of reactants induced by the over-pressure of the confined burnt gases when they cannot fully expand. Experiments on steady flames reveal that the flame height increases for increasing confinement ratios C_r, leading to a gain shift and a phase drop for the FTF. A theoretical analysis is conducted to model this acceleration and examine its impact on the steady flame shape and flame response to flow disturbances. The change in the FTF phase is shown to be related to a reduction of the mean time lag for perturbations to reach the flame front. An expression to scale the FTF of confined flames is derived based on a modification of the reduced frequency ω_* used to analyze the response of unconfined flames. This new reduced frequency includes explicitly the confinement ratio C_r and the volumetric expansion ratio E. This relation may be used to transpose the FTF determined on a burner with a certain flame tube to a configuration with a different flame tube or to transpose results determined on single burners to multiple injection configurations when the burnt gases cannot fully expand due to the presence of neighboring flames. Finally, the FTF models derived in the previous chapters are used to simulate the response of a collection of small laminar premixed conical flames and these predictions are compared to measurements.

6.1 Introduction

In many laboratory scale experiments and numerical simulations, the flame response to flow perturbations is analyzed on a single burner or on a limited

numerical domain, which generally does not exactly coincide with the flow and geometrical arrangement of the real configuration investigated. Practical combustors often feature multiple injectors with a limited space for the flame to expand due to the presence of neighboring flames, but in many simulations and experiments, the analysis of flame dynamics is often limited to a single burner. The location of the combustion chamber walls with respect to the burner position may also vary between generic and real configurations to ease instrumentation for diagnostics, reduce computational cost in simulations, or because of limitations in admissible power rate or due to other flow and thermal restrictions.

Fanaca *et al.* (2010) have recently shown that a turbulent swirling flame does not take the same shape in a single burner and in an annular combustor equipped with the same injectors. It is well known that for the same flow conditions, the flame frequency response also strongly depends on the steady flame shape [Durox *et al.* (2009)]. Duchaine *et al.* (2011) conducted numerical simulations on a single laminar conical flame with periodic lateral boundaries to reproduce the response of a collection of small conical flames stabilized over a perforated plate and submitted to flow disturbances [Boudy *et al.* (2011)]. It was necessary to take into account a diverging angle of the numerical domain on the burnt gas side to reproduce measurements. A modification of only a few degrees led to a significant change of both the axial velocity profile and the flame response to acoustic perturbations. These examples indicate that it is difficult to transpose results obtained for the flame dynamics with a certain geometrical arrangement to situations with different boundaries or geometries.

The present investigation aims at characterizing effects of confinement of the burnt gases on the dynamics of flames operated under the same flow conditions. The objective is to show that the expansion of the burnt gases with respect to confinement is an important parameter that should be taken into account when examining FTF. It is well known that confinement strongly modifies the flow and flame structures of turbulent swirling flames [Beltagui and Maccallum (1976); Rao *et al.* (1983)], but measurements or numerical determinations of FTF with different confinements are more seldom [Hauser *et al.* (2011); Tay-Wo-Chong and Polifke (2012)]. One important element considered by Mehta *et al.* (2005) in an analysis of the dynamics of a ducted V-flame is the effect of exothermicity. Due to the fixed density jump across the flame front, the confined burnt gases induce an acceleration of the mean flow field in the fresh reactant stream, which modifies the FTF with respect to its unconfined response to flow perturbations. The presence of side walls also strongly modifies the motion of the flame tip near the solid wall resulting in large deviations of the FTF when the confinement is modified [Birbaud *et al.* (2007a)]. The impact of the first mechanism is studied here in a situation where there is no direct interaction between the flame tip and solid walls. This problem is examined for

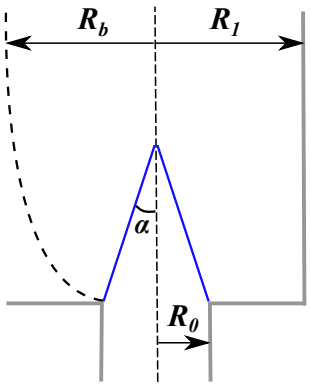

Figure 6.1: *Scheme of a conical flame showing the different notations needed in this study. The injection unit radius R_0 has to be compared to the burnt gas plume radius R_b occupied by the flame if it would be unconfined (left side of the figure) and to the radius of the flame tube R_1 confining the burnt gases (right side of the figure). The flame tip half-angle α is also indicated in this figure.*

conical flames submitted to velocity disturbances, the FTF being defined by:

$$F(\omega) = \frac{\tilde{\dot{Q}}_1/\dot{Q}_0}{\tilde{v}_1/v_0} = G\exp(i\varphi) \tag{6.1}$$

where $\tilde{\dot{Q}}_1/\dot{Q}_0$ is the dimensionless heat release rate disturbance caused by the dimensionless velocity fluctuation $\tilde{v}_1/v_0$ at the burner outlet, G denotes the FTF gain and φ the FTF phase lag.

The response of laminar unconfined conical flames to velocity disturbances has already received considerable attention and was reviewed in Chapter. 1. Effects of the confinement side walls were not documented yet. Successive theoretical expressions for the FTF of unconfined flames were proposed [Schuller *et al.* (2003a); Preetham *et al.* (2008); Cuquel *et al.* (2011b)] based on two independent dimensionless numbers. One generally uses the flame tip half-angle $\alpha = \arcsin(S_d/v_0)$ [Schuller *et al.* (2003a)], where S_d is the flame speed and v_0 denotes the mean bulk velocity in the fresh gases, and the reduced frequency $\omega_* = \omega R_0/(S_d\cos\alpha)$, where R_0 stands for the burner exit radius and ω is the forcing angular frequency [Fleifil *et al.* (1996); Ducruix *et al.* (2000)].
When the flame is confined, the burnt gases may be in contact with the combustor walls depending on the value taken by the ratio between the unconfined flame plume radius R_b and the confinement tube radius R_1 as shown in Fig. 6.1. For a conical flame, this ratio is defined by [Remie *et al.* (2006)]:

$$C_b = \frac{R_b}{R_1} = C_r\left[1 - \frac{E-1}{E}\cos\alpha\right]^{-\frac{1}{2}} \tag{6.2}$$

where $E = \rho_u/\rho_b$ is the burnt to unburnt gas volumetric expansion ratio and $C_r = R_0/R_1$. It was recently demonstrated that a change of velocity in the stream of fresh reactants needs to be considered to describe the shape of unconfined conical flames for large injection velocities and large gas expansion ratios E due to an adverse pressure gradient exerted by the burnt gases [Higuera (2009)]. This effect is strongly amplified when the burnt gases cannot fully expand due to confinement for $C_b \geq 1$. This acceleration of the fresh reactant stream represents one important difference between unconfined and confined flame configurations [Mehta *et al.* (2005)]. The flame response to flow perturbations was not fully documented yet in these situations. It is shown in this study how to take this phenomenon into account to scale the FTF obtained for different confinements.

The experimental setup and results for the flame shape and FTF are presented in section 6.2. A theoretical analysis is then conducted to model the acceleration of the flow as a function of the confinement ratio C_r. It is used in section 6.4 to model the steady shape taken by a confined conical flame. An analysis of the travel time of flow and flame front disturbances convected along the mean shape is then carried out to define a new dimensionless reduced frequency that explicitly accounts for confinement effects. This parameter is finally used to rescale the FTF of conical flames gathered for different confinements.

6.2 Experimental setup

The configuration studied here features a cylindrical feeding manifold equipped with a set of laminarization grids and a convergent nozzle used to reduce remaining velocity fluctuations and to get a nearly uniform top-hat velocity profile at the burner exit. The burner outlet is circular with a radius $R_0 = 11$ mm. More details about this burner can be found in Chapter 2. By changing the mixture flow rate, the mean bulk velocity at the burner outlet can be varied. In these experiments methane and air are perfectly premixed before entering the manifold with a fixed equivalence ratio $\phi = 0.86$. The mixture is injected at $T_u = 300$ K and flows out of the confinement tube at a temperature $T_b = 1800$ K, corresponding to a burnt to unburnt gas volumetric expansion ratio $E = 6$. When the flame is not confined, the flame speed is taken here equal to $S_d = 0.37$ m.s^{-1}. This value is obtained by matching predicted and measured flame heights assuming a perfect conical shape (see Schuller *et al.* (2002) and Fig. 6.8-right row). The flow and the geometrical parameters modified in these experiments are indicated in Tab. 6.1. Measurements are carried out for three different mass flow rates. The radius of the hot gas plume generated by the unconfined flame is given by Eq. (6.2), and one finds $R_b = 23.8$, 25.2 and 26.0 mm respectively, for the three mass flow rates explored.
Three quartz tubes of length $L = 0.3$ m with different radius R_1 were used

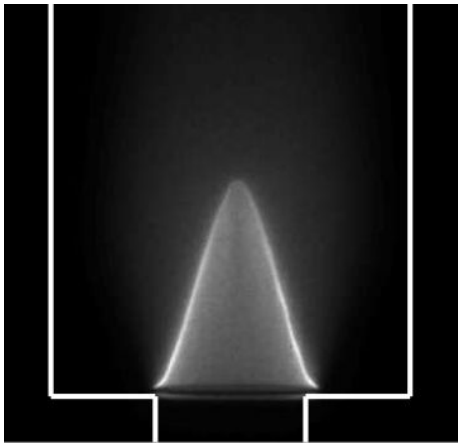

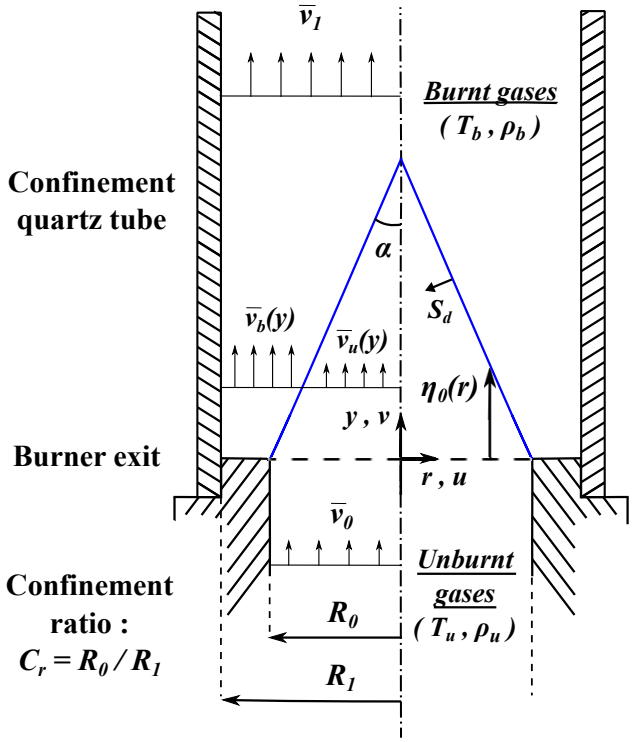

Figure 6.2: **(top)** *Image of an axisymmetric confined conical flame with* $C_r = 0.44$ *and* $C_b = 0.95$.
(bottom) *Schematic of the axisymmetric confined conical flame considered in this study.*

Table 6.1: *Table of experimental parameters considered in this study. The different values of the flame tube radius R_1 and the mass flow rate $\dot{m}$ are used to determine the confinement ratios $C_r = R_0/R_1$ and $C_b = R_b/R_1$.*

		$\dot{m}$ (g.s^{-1})		
		0.396	0.566	0.792
R_1(mm)	C_r	C_b	C_b	C_b
$+\infty$	0	0	0	0
25.00	0.44	0.95	1.01	1.04
18.35	0.60	1.30	1.37	1.42
13.55	0.81	1.76	1.86	1.92

to confine the flame. The confinement ratio is defined here as $C_r = R_0/R_1$ where $C_r = 0$ corresponds to the limiting case of an unconfined flame when $R_1 \to +\infty$. It is interesting to first look at values of C_b characterizing the ratio of the burnt gas plume radius R_b of the same but unconfined flame and the flame tube radius R_1 (see Tab. 6.1). The largest flame tube $R_1 = 25$ mm is expected to have a limited impact on the burnt gas expansion because $C_b \approx 1$. For the two other tested tubes, $C_b > 1$, the burnt gases cannot fully expand and the confinement tube is expected to have an impact on the flame and its response to flow perturbations.

The bottom of the burner is equipped with a loudspeaker to modulate the flow and perturb the flame. The loudspeaker is driven by a harmonic signal generated with LabVIEW®, which feeds a HiFi-amplifier that is connected to the loudspeaker as described in Chapter 2. Harmonic velocity perturbations are produced at the burner outlet and are measured by LDV at the base of the flame, 2.8 mm above the burner outlet on the burner axis. A photodiode equipped with an OH* filter is used to collect the chemiluminescence emission from the flame, which is roughly proportional to the heat release rate in this case [Hurle *et al.* (1968)].

The velocity and heat release rate time records are all sampled at once with a National Instrument analog-to-digital converter board controlled by LabVIEW®. The sampling frequency is $f_s = 4096$ Hz. These signals are further post-processed to determine the cross- and auto-power spectrum densities and obtain the FTF as a function of frequency for a fixed velocity modulation level at the burner exit $|v_1/v_0| = 0.1$. LDV was also used to measure the axial velocity distribution $v_{0u}(y)$ along the burner axis in the unburnt gases. Flame images were gathered with an intensified CCD camera (ICCD). The signal-to-noise ratio was improved through an averaging method by taking over 50 snapshots for each image.

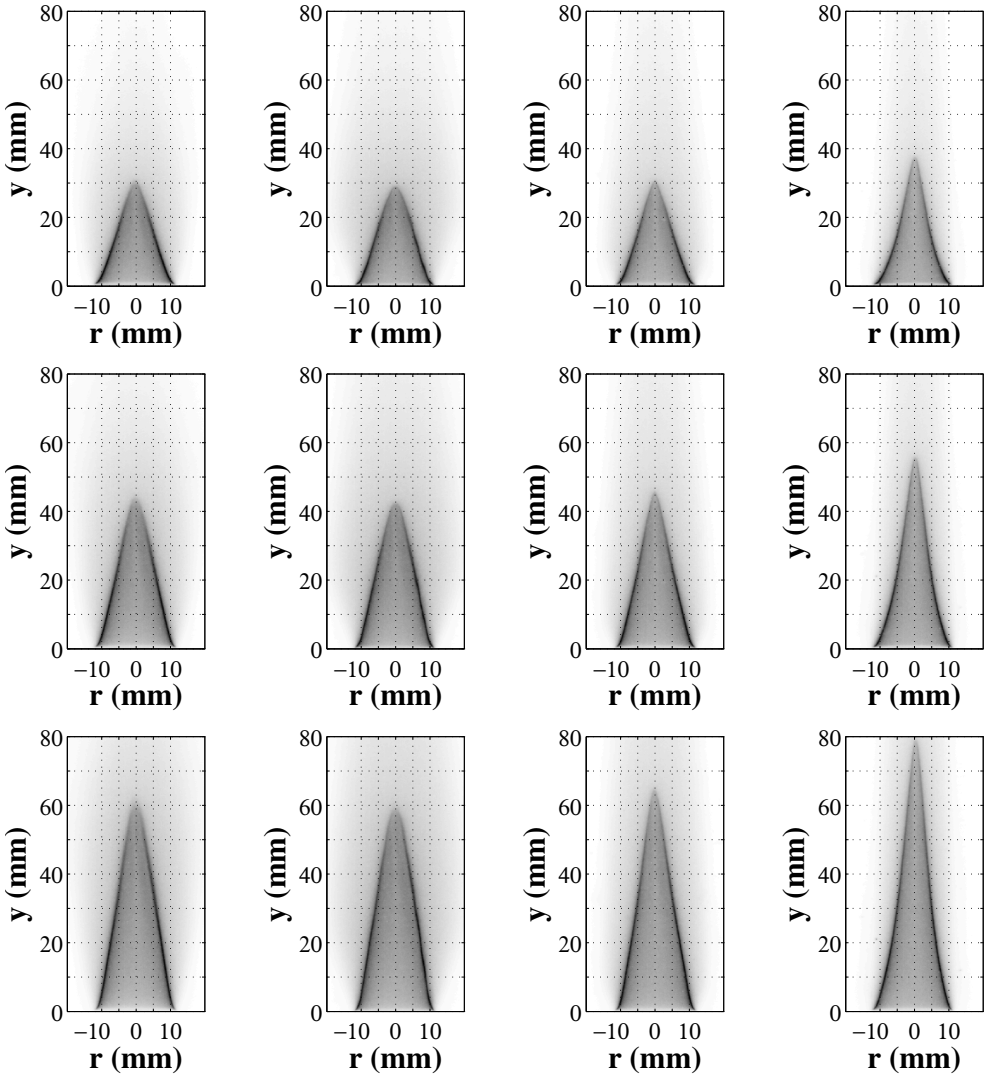

Figure 6.3: *Flame images for different confinement tubes and flow conditions. From left to right : C_r = 0, 0.44, 0.60 and 0.81. Upper row: $\dot{m}$ = 0.396 $g.s^{-1}$. Middle row: $\dot{m}$ = 0.566 $g.s^{-1}$. Lower row: $\dot{m}$ = 0.792 $g.s^{-1}$.*

6.3 Experimental results for steady confined conical flames

Confining the burnt gases modifies the shape of the steady conical flames as shown in Fig. 6.3 for the three different mass flow rates $\dot{m} = 0.396$, 0.566 and 0.792 g.s^{-1} investigated when the confinement ratio C_r is modified. The unconfined flame takes a conical shape with a straight flame front for all mass flow rates explored (first column in Fig. 6.3). As the confinement ratio is increased, the flame shape remains unchanged up to $C_r = 0.44$ (second column) and its height starts to increase for higher confinement ratios $C_r = 0.60$ (third column), up to a flame that has grown by almost a third of its initial height for $C_r = 0.81$ (fourth column). For this last confinement ratio, the flame fronts are bent towards the fresh gases. A better interpretation can be given if one looks at the steady flame shapes shown with the confinement tube dimensions in Fig. 6.4. For $\dot{m} = 0.369$ and 0.792 g.s^{-1}, the flame height increases as the flame tube radius is decreased. In these situations, it is interesting to compare the maximal width taken by the burnt gas plume of the unconfined flame R_b (shown in the first column in Fig. 6.4 and reproduced with a black arrow in the other columns) with the confinement tube radius R_1. The ratio of these two quantities is $C_b = R_b/R_1$. As long as the hot gases can fully expand in the

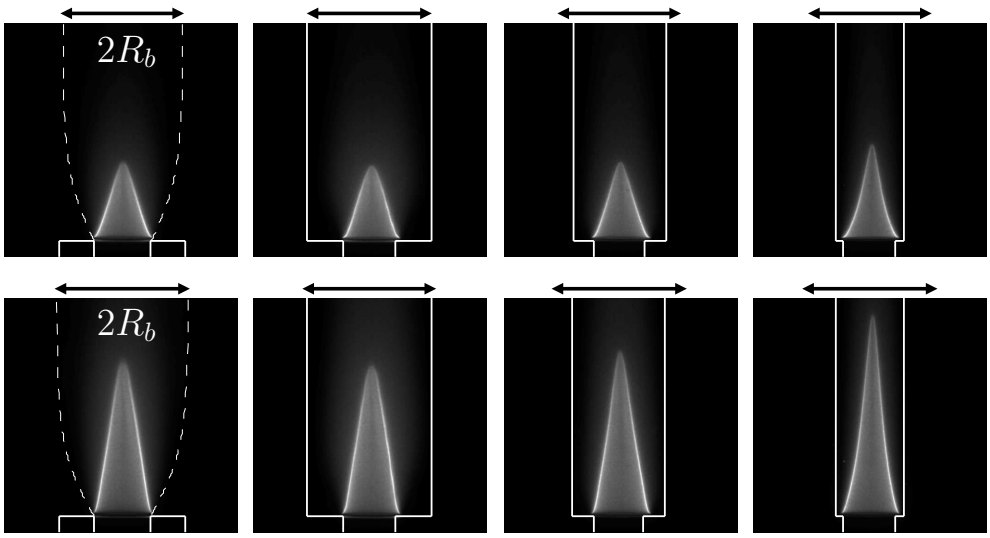

Figure 6.4: *Flame images for different confinement tubes and flow conditions. From left to right : C_r = 0, 0.44, 0.60 and 0.81. Upper row: $\dot{m}$ = 0.396 g.s^{-1}. Lower row: $\dot{m}$ = 0.792 g.s^{-1}. The plume of burnt gases is represented schematically by the white dashed lines in the left images. The burner exit and the confinement tubes are represented with white plain lines. The width of the unconfined flame plume radius R_b is shown as a black arrow on the top of each image. This quantity can be compared to the width of the flame tube.*

confinement tube, i.e. $C_b \leq 1$, the flame shape remains unchanged. This is the situation in the unconfined case when $C_r = 0$ and in the slightly confined case when $C_r = 0.44$. When the confinement further increases ($C_r = 0.60$, third column in Fig. 6.4), the burnt gases are in contact with the quartz tube and the flame height slightly increases. This effect is more noticeable for the highest flow rate $\dot{m} = 0.792$ g.s^{-1}. For an even larger confinement ratio $C_r = 0.81$, the ratio C_b approaches 2 as indicated in Table 6.1. The hot gases are compressed by the lateral walls. The flame height is considerably increased and the flame front bends towards the fresh gases. These effects are more important for elongated flames, indicating an influence of the flame tip half-angle α.

It is now worth examining the velocity field in the fresh reactants to understand changes in flame shapes when the flame is confined. The dimensionless axial velocity $v_{0u}(r = 0, y)/v_0$ was determined with LDV along the burner axis $r = 0$ under steady flow conditions as a function of y/H_0, where $v_{0u}(r, y)$ is the axial velocity component in the unburnt gases at a distance y from the burner outlet, $v_0 = v_{0u}(y = 0)$ indicates the axial velocity at the burner outlet and $H_0 = R_0/\tan\alpha$ is the unconfined steady flame height. These data are plotted in Fig. 6.5 (circles), for three mass flow rates $\dot{m} = 0.392, 0.566$ and 0.792 g.s^{-1}, and for three different confinement ratios $C_r = 0.44$, 0.60 and 0.81. The same changes in the axial velocity field may be observed when the mass flow rates is varied. For $C_r = 0.44$, the axial velocity remains almost constant along the burner centerline up to the flame tip as in the unconfined case (not represented here). This again emphasizes the small influence of the flame tube when $C_b \leq 1$. For higher confinement ratios, the axial velocity increases roughly linearly along the burner centerline up to the flame tip. This velocity gradient in the fresh gases increases for higher confinement ratios. For the highest confinement ratio presented here, the axial velocity has almost doubled between the burner exit and the flame tip. These observations may be used to explain the evolution of the flame images presented in Fig. 6.3. First, an increase of the mean axial velocity leads to longer flames compared to a flame with a uniform velocity field. The flame front then necessarily bends towards the fresh gases when the confinement ratio increases because, for a constant injected mass flow rate and a constant flame speed, the heat release rate and flame surface area are fixed as shown in Fig. 6.6.

6.4 Modeling the steady conical flame shape

The observations made in the previous sections are here predicted by theoretical means, starting by modeling the velocity field in the fresh gases to ultimately retrieve the shape of confined conical flames.

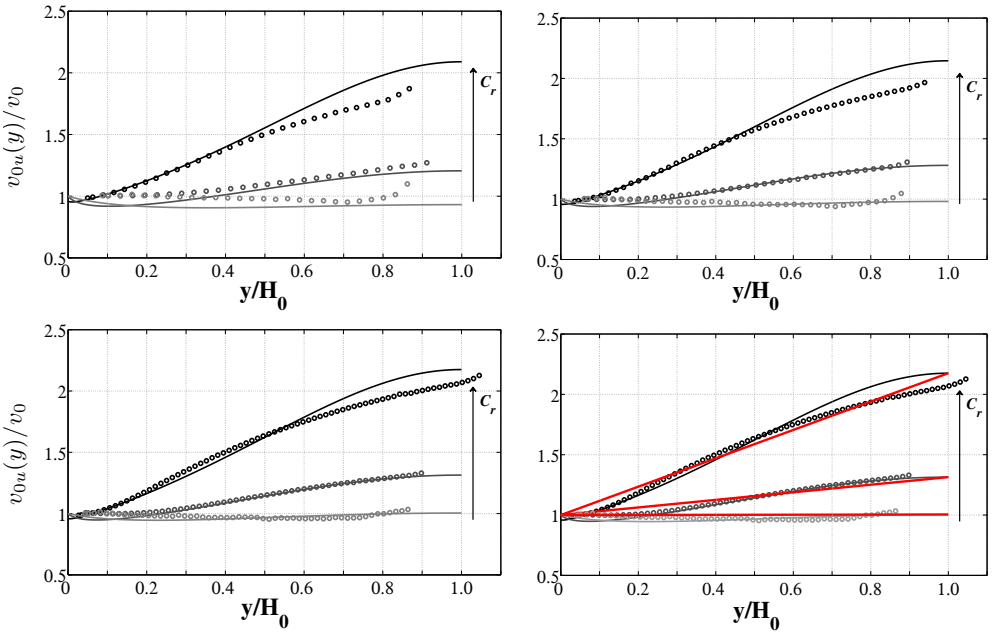

Figure 6.5: *Dimensionless fresh gas axial velocity $v_{0u}(r=0,y)/v_0$ as a function of the axial coordinate y/H_0, where $v_0 = v_{0u}(y=0)$ is the mean flow velocity at the exit of the burner and $H_0 = R_0/\tan\alpha$ is the unconfined steady flame height. Results are plotted for three mass flow rates (***top-left***) $\dot{m} = 0.396$ g.s^{-1}, (***top-right***) $\dot{m} = 0.566$ g.s^{-1} and (***bottom-left***) $\dot{m} = 0.792$ g.s^{-1} and for three confinement ratios: $C_r = 0.44$ (light grey), 0.60 (dark grey) and 0.81 (black). Circles stand for measurements and lines represent model predictions from Eq. (6.10). In the bottom right figure, results for $\dot{m} = 0.792$ g.s^{-1} are superimposed with the linear approximation from Eq. (6.16).*

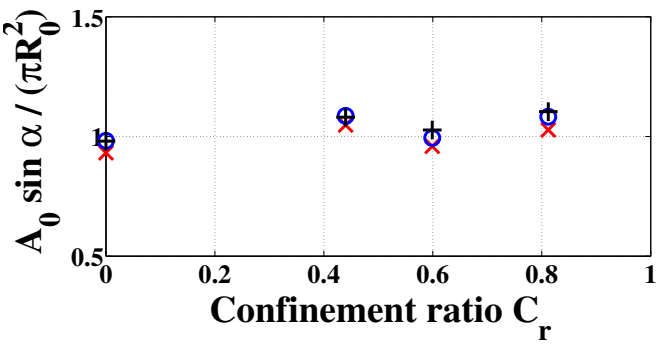

Figure 6.6: *Evolution of the flame surface area A_0 as a function of the confinement ratio. Measurements for three different mass flow rates: $\dot{m} = 0.396$ g.s^{-1} (red cross); 0.566 g.s^{-1} (blue circles); 0.792 g.s^{-1} (black cross). The flame surface area is made dimensionless with the theoretical unconfined steady flame surface area $A_0 = \pi R_0^2/\sin\alpha$.*

6.4.1 Modeling the steady velocity field

A conical flame is considered here and effects of confinement are analyzed using the simplified flow model presented in Fig 6.2, when the confinement tube downstream the flame front is filled with burnt gases, i.e. $C_b > 1$. The first objective is to derive an expression for the increase of the axial velocity in the stream of fresh reactants during steady operation. The reactive mixture flows out the burner in section (0) at $y = 0$ with a uniform velocity v_0 and the burnt gases leave the confinement tube in section (1) also with a uniform velocity v_1 that satisfy mass balance:

$$v_1/v_0 = C_r^2 E \tag{6.3}$$

where $C_r = R_0/R_1$ is the confinement ratio and $E = \rho_u/\rho_b$ is the unburnt to burnt gas volumetric expansion ratio. A momentum balance for the control volume comprised between sections (0) and (1) in Fig. 6.2 then yields:

$$\left(p_1 + \rho_b v_1^2\right) R_1^2 = \left(p_0 + \rho_u v_0^2\right) R_0^2 + p_R \left(R_1^2 - R_0^2\right) \tag{6.4}$$

where p_R is the pressure exerted on the combustor back plane located at $y = 0$ between $R_0 < r < R_1$. The flow around the flame is supposed here in a first approximation to be described by two axial velocity fields $v_{0u}(y)$ in the unburnt gases and $v_{0b}(y)$ in the burnt gases that are only a function of the distance y to the injection plane $y = 0$. Assuming a conical shape of the flame front, mass and momentum balances between the injection plane $y = 0$ and a horizontal plane at a height y can be written:

$$\rho_u v_0 R_0^2 = \rho_b v_{0b}(y) \left[R_1^2 - r_f^2(y)\right] + \rho_u v_{0u}(y) r_f^2(y) \tag{6.5}$$

$$\begin{aligned} &\left[\rho_u v_{0u}^2(y) + p_u(y)\right] r_f^2(y) + \left[\rho_b v_{0b}^2(y) + p_b(y)\right] \left[R_1^2 - r_f^2(y)\right] \\ &\qquad = \left(\rho_u v_0^2 + p_0\right) R_0^2 + p_R \left(R_1^2 - R_0^2\right) \end{aligned} \tag{6.6}$$

where the flame front position r_f is given by $r_f = R_0(1 - y \tan\alpha/R_0)$. The pressure jump across the flame is constant and fixed by:

$$p_u(y) - p_b(y) = \rho_u S_d^2 (E - 1) \tag{6.7}$$

The pressure p_R acting on the back plane is taken here as the pressure right behind the base of the flame:

$$p_R = p_0 - \rho_u S_d^2 (E - 1) \tag{6.8}$$

In the fresh stream, the flow is assumed incompressible and unidirectional. The Bernoulli equation along a streamline starting from the injection plane writes:

$$\frac{1}{2}\rho_u v_0^2 + p_0 = \frac{1}{2}\rho_u v_{0u}^2(y) + p_u(y) \tag{6.9}$$

This system of equations leads after a few manipulations to a second-order algebraic equation for $v_{0u}(y)/v_0$:

$$a_1 \left(\frac{v_{0u}(y)}{v_0} \right)^2 + a_2 \frac{v_{0u}(y)}{v_0} + a_3 = 0 \tag{6.10}$$

where the coefficient a_i are functions of $C_r = R_0/R_1$, $E = \rho_u/\rho_b$, $r_f^*(y) = r_f/R_0$ and $\sin\alpha = S_d/v_0$, and are given by:

$$a_1(y) = \left(C_r r_f^*\right)^2 + E\left(C_r r_f^*\right)^4 \left(1 - \left(C_r r_f^*\right)^2\right)^{-1} - \frac{1}{2} \tag{6.11}$$

$$a_2(y) = -2EC_r^2 \left(C_r r_f^*\right)^2 \left(1 - \left(C_r r_f^*\right)^2\right)^{-1} \tag{6.12}$$

$$a_3(y) = \frac{1}{2} - C_r^2 \left[C_r^2 E \left(1 - \left(C_r r_f^*\right)^2\right)^{-1} - \sin^2\alpha (E-1)\left(1 - r_f^{*2}\right) \right] \tag{6.13}$$

This lengthy expression is solved with Matlab and the predictions for the axial velocity are plotted in Fig. 6.5 in terms of the evolution of dimensionless axial velocity $v_{0u}(y)/v_0$ as a function of the dimensionless length y/H_0, where H_0 is the unconfined flame height. These predictions match well measurements for the different confinement ratios C_r explored, even if the velocity is slightly over-predicted with this model near the flame tip when $C_r = 0.81$. This is due to the crude assumption on the flow field in this region. Comparisons for data gathered for all mass flow rates injected give similar results. These results indicate that the axial velocity gradient in the reactant stream may be suitably reproduced by the proposed model when the confinement and mass flow rates are modified.

It is interesting to determine the velocity at the height $y = H_0$. This quantity will be used later. By considering that $r_f^* = 0$ at this location, Eq. (6.10) reduces to:

$$\left(\frac{v_{0u}}{v_0} \right)^2_{y=H_0} = 1 - 2C_r^2 \left[1 + \sin^2\alpha\,(E-1) - EC_r^2 \right] \tag{6.14}$$

It is important to remind that the expressions developed in this section are only valid when the flame tube is filled with burnt gases, i.e. when $C_b = R_b/R_1 \geq 1$. The domain of validity of these expressions is delimited by (see Eq. 6.2):

$$C_r \geq \left[1 - \frac{E-1}{E} \cos\alpha \right]^{\frac{1}{2}} \tag{6.15}$$

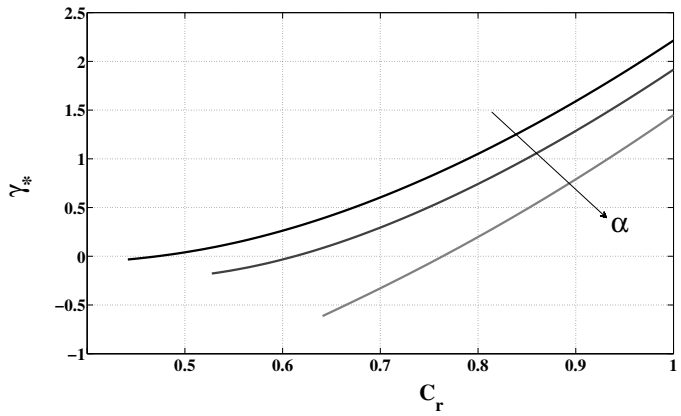

Figure 6.7: *Evolution of γ_* as a function of the confinement ratio C_r for values of C_r satisfying Eq. (6.15). Different flame tip half-angles are considered: $\alpha = \pi/12$ (black), $\pi/6$ (dark grey) and $\pi/4$ (light grey). $E = 6$.*

In Fig. 6.7, the function $\gamma_* = (v_{0u}(H_0) - v_0)/v_0$ is plotted as a function of the confinement ratio C_r for values satisfying Eq. (6.15) for three flame tip half-angles corresponding to $\alpha = \pi/12; \pi/6$ and $\pi/4$. One observes that γ_* increases significantly with the confinement ratio, meaning that the fresh reactant stream is more and more accelerated as the confinement ratio is increased. This is consistent with measurements. Moreover, negative values of γ_* are found for large flame tip half-angles and for moderate confinement ratios. In these cases, the axial velocity in the fresh gases decreases with the distance y to the burner exit and the flame would be shorter. These configurations were not investigated in the experiments conducted in this work. For the different mass flow rates explored, the flame tip angle was relatively small and it is probably difficult to stabilize conical flames with larger flame angles and to observe these regimes where confined flames would shorten.

To simplify the problem, the axial velocity component $v_{0u}(y)$ is approximated by a linearly increasing function of the coordinate y, which is equal to v_0 at $y = 0$. A radial component $u_{0u}(r)$ is added to obtain an incompressible steady flow field satisfying continuity:

$$\mathbf{v} = \begin{cases} v_{0u}(y) &= v_0 \left(1 + \gamma_* \dfrac{y}{H_0}\right) \\ u_{0u}(r) &= -v_0 \gamma_* \dfrac{r}{2H_0} \end{cases} \tag{6.16}$$

The expression for the dimensionless velocity slope γ_* is deduced from the expression of the axial velocity at $y = H_0$ obtained in Eq. (6.14). One finds:

$$\gamma_*(C_r,\alpha,E) = \frac{v_{0u}(H_0) - v_0}{v_0} = \left[1 - 2C_r^2\left(1 + \sin^2\alpha\,(E-1) - EC_r^2\right)\right]^{\frac{1}{2}} - 1 \tag{6.17}$$

Predictions from Eq. (6.16) are plotted in Fig. 6.5-bottom-right for different confinement ratios and a mass flow rate $\dot{m} = 0.792$ g.s^{-1}. This model gives a good overall approximation of the axial velocity in the fresh gases of a confined conical flame. This model is used in the next section to examine the shape taken by the flame.

6.4.2 Modeling the shape of confined flames

The steady flame front position is given by $y = \eta_0(r)$ (Fig. 6.2) and is determined by the steady G-equation that reduces to:

$$S_d = \mathbf{v}\cdot\mathbf{n} \tag{6.18}$$

where S_d is the flame speed that is assumed here to be constant for a given equivalence ratio, $\mathbf{v}$ is the velocity vector in the fresh gases, $\mathbf{n} = \nabla G_0/|\nabla G_0|$ the unit vector normal to the flame front and $G_0(y,r) = y - \eta_0(r)$ is the level set variable. It is now possible to obtain an expression for the slope taken by steady confined conical flames. The following developments are derived in the elongated flame approximation when $\alpha \ll 1$. The acceleration γ_* is then a positive increasing function of the confinement ratio C_r. The steady G-equation determining the flame position may be written:

$$v_{0u} - u_{0u}\frac{\partial\eta_0}{\partial r} = S_d\left[1 + \left(\frac{\partial\eta_0}{\partial r}\right)^2\right]^{\frac{1}{2}} \tag{6.19}$$

In the limit of elongated flames $\alpha \ll 1$, i.e. $|\partial\eta_0/\partial r| \gg 1$, one may writes:

$$\left[1 + \left(\frac{\partial\eta_0}{\partial r}\right)^2\right]^{\frac{1}{2}} \simeq \left|\frac{\partial\eta_0}{\partial r}\right| = -\frac{\partial\eta_0}{\partial r} \tag{6.20}$$

This approximation finally leads to:

$$v_{0u} - u_{0u}\frac{\partial\eta_0}{\partial r} = -S_d\frac{\partial\eta_0}{\partial r} \tag{6.21}$$

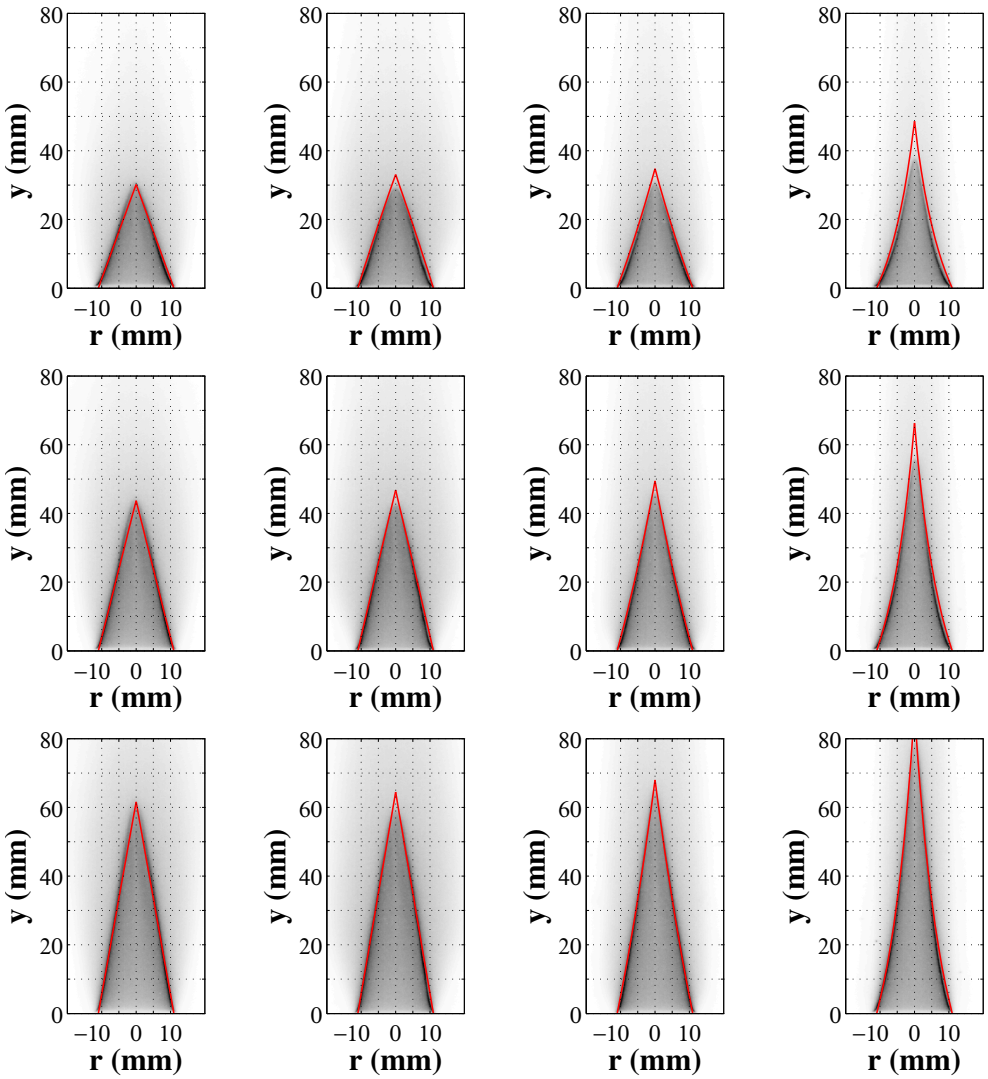

Figure 6.8: *Flame images for different confinement tubes and flow conditions. From left to right : C_r = 0, 0.44, 0.60 and 0.81. Upper row: $\dot{m}$ = 0.396 $g.s^{-1}$. Middle row: $\dot{m}$ = 0.566 $g.s^{-1}$. Lower row: $\dot{m}$ = 0.792 $g.s^{-1}$. Predictions with Eq. (6.23) are plotted in red.*

It is interesting to make this expression dimensionless:

$$1 + \gamma_* \eta_0^* = -\left(\frac{\partial \eta_0}{\partial r}\right)^* \left[\gamma_* \frac{r^*}{2} + \cos\alpha\right] \tag{6.22}$$

where $\eta_0^* = \eta_0/H_0$ and $r^* = r/R_0$. Spatial integration of Eq. (6.22) up to the zero$^{\text{th}}$ order in α leads to the following expression for the position of the steady flame front:

$$\eta_0^*(r^*) = \frac{1}{\gamma_*}\left[\left(1 - \frac{1-r^*}{1+2/\gamma_*}\right)^{-2} - 1\right] \tag{6.23}$$

A comparison between the predicted shapes obtained with this expression and flame images is presented in Fig. 6.8 for the different mass flow rates and confinement ratios studied. The predicted flame front bends towards the burner axis and the flame height H increases compared to the unconfined flame height H_0 when the confinement ratio increases. Predictions match well with flame images, except in some cases near the flame tip, where the constant flame displacement speed assumption is too crude to capture the flow field when the flame fronts are close to each other. Flame curvature also modifies the propagation of the flame front near the tip [Poinsot *et al.* (1992)], a phenomenon which is not included in the present description. For the highest confinement ratio $C_r = 0.81$, the flame height is slightly over-predicted. These small differences near the flame tip have a limited impact on the flame surface area of axisymmetric flames. This might be an issue to deal with for two-dimensional conical flames.

These modifications of the steady flame shape have an impact on the response of these confined flames to flow perturbations. It is well known that flames with different shapes feature different frequency responses [Durox *et al.* (2009)]. It is also known that flow perturbations are convected by the mean flow in the fresh reactants [Sugimoto and Matsui (1982); Baillot *et al.* (1992); Baillot *et al.* (1996); Birbaud *et al.* (2006)], the slope of the FTF being related, in the low frequency range, to the mean time lag taken by flame front disturbances originating at the flame base to produce a flame surface area perturbation. When the flame is confined, the resulting distortions of the mean flow field and the shape taken by the flame also modify the travel time of these disturbances. This problem is first examined experimentally and then theoretically in the next sections.

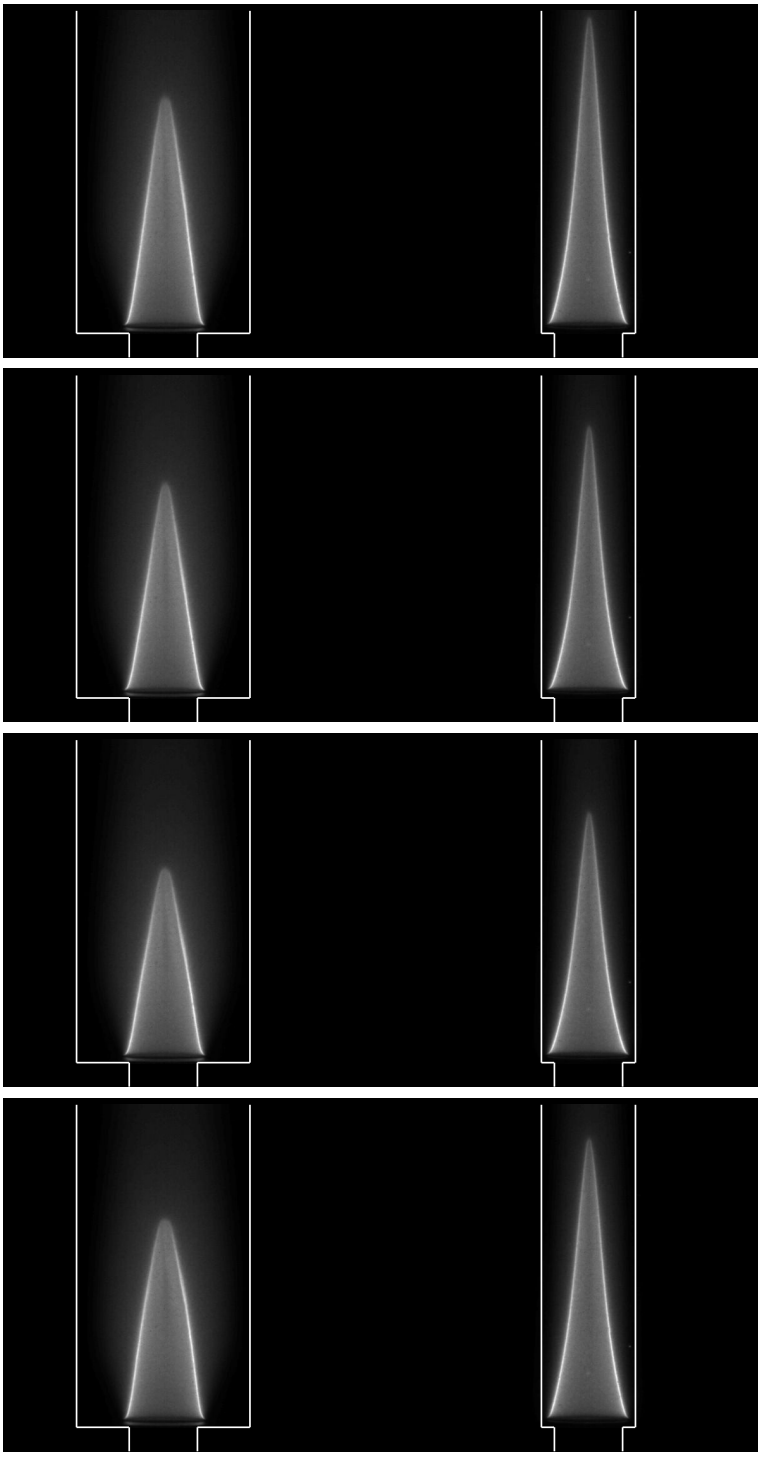

Figure 6.9: *Images of acoustically perturbed confined conical flames for four equidistant phases during the forcing period. Left column:* $C_r = 0.44$. *Right column:* $C_r = 0.81$. $f = 10$ *Hz.* $\dot{m} = 0.792$ *g.s*$^{-1}$. $|v_1/v_0| = 0.1$. $\phi = 0.86$.

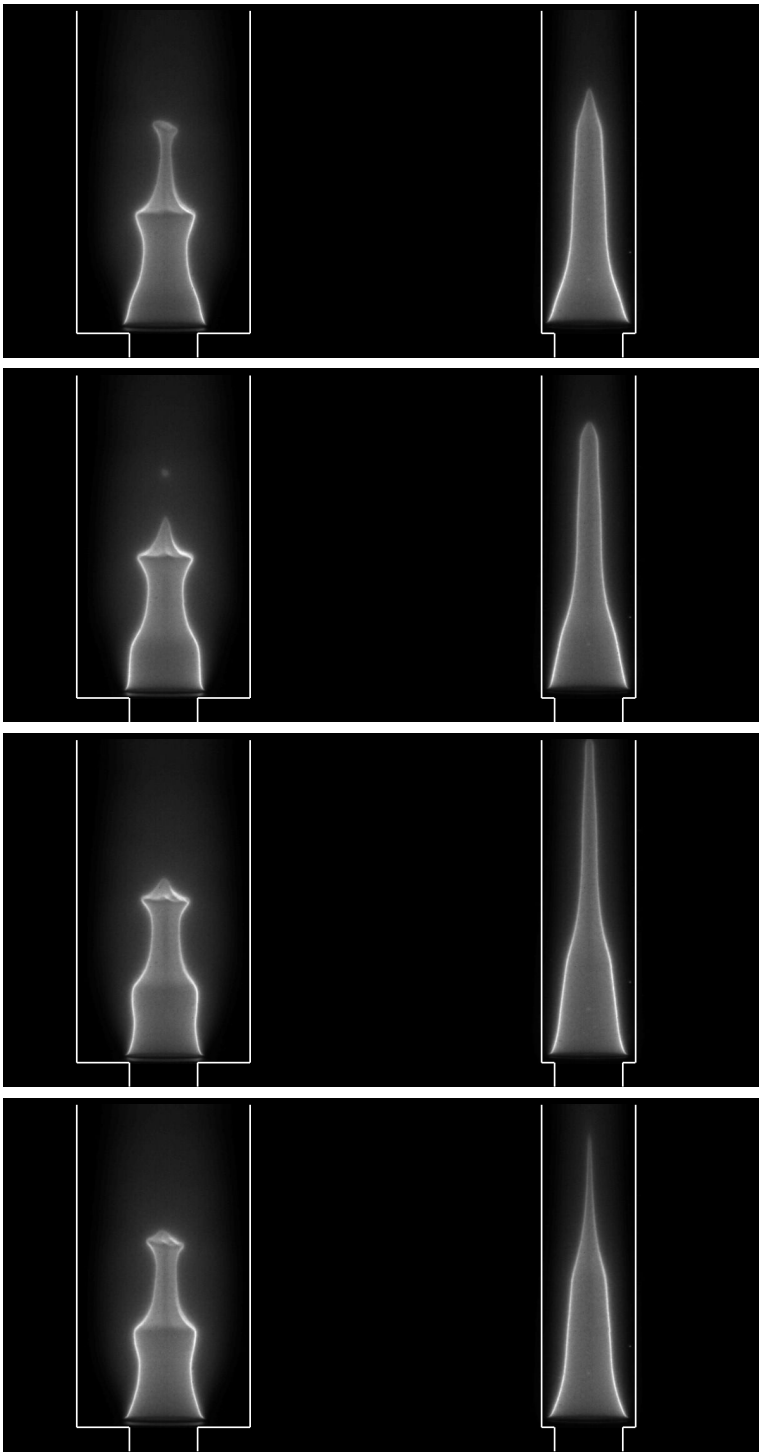

Figure 6.10: *Images of acoustically perturbed confined conical flames for four equidistant phases during the forcing period. Left column:* $C_r = 0.44$. *Right column:* $C_r = 0.81$. $f = 80$ *Hz.* $\dot{m} = 0.792$ $g.s^{-1}$. $|v_1/v_0| = 0.1$. $\phi = 0.86$.

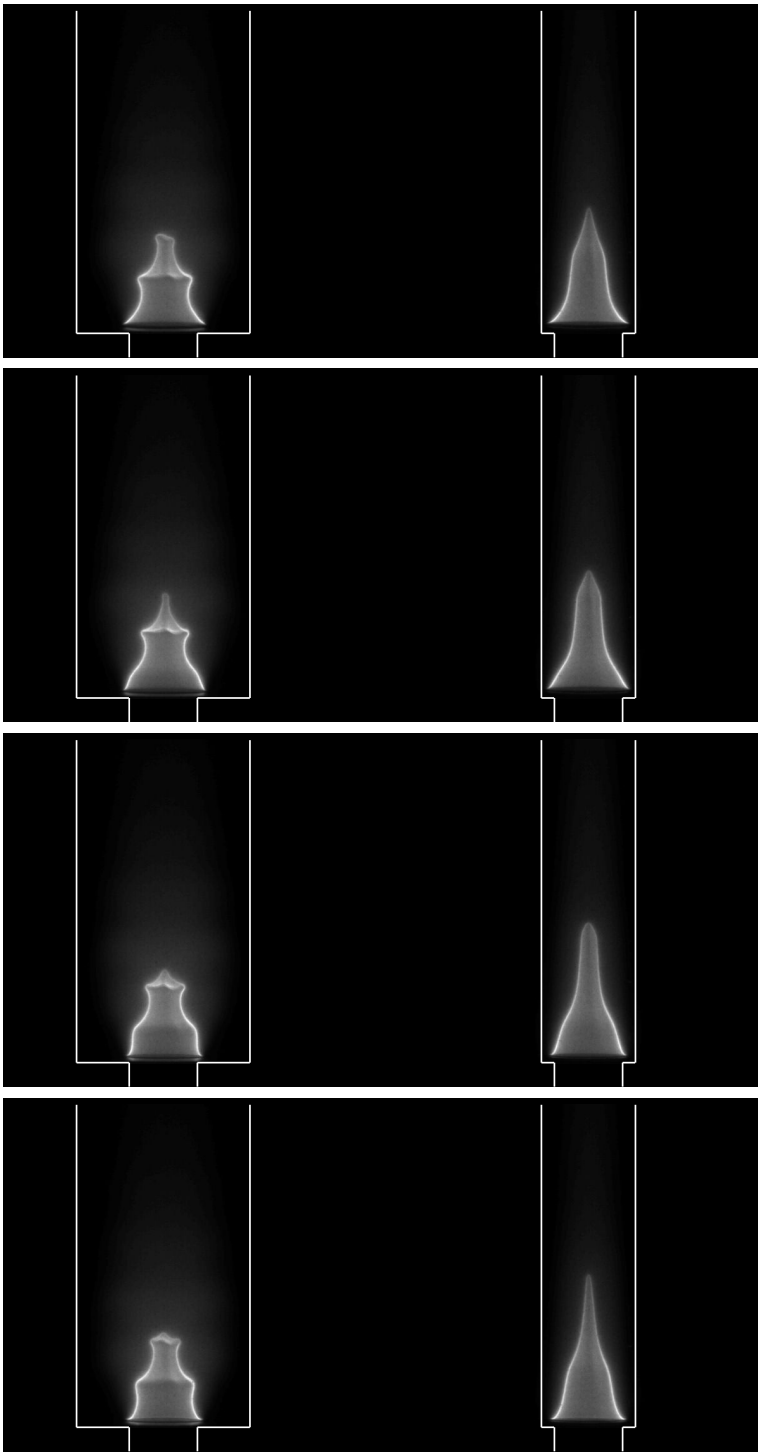

Figure 6.11: *Images of acoustically perturbed confined conical flames for four equidistant phases during the forcing period. Left column:* $C_r = 0.44$. *Right column:* $C_r = 0.81$. $f = 80$ *Hz.* $\dot{m} = 0.396$ $g.s^{-1}$. $|v_1/v_0| = 0.1$. $\phi = 0.86$.

6.5 Experimental investigation of the response of confined flames to flow perturbations

In this section, effects of the confinement are investigated first by analyzing images of acoustically perturbed confined conical flames and then by determining their FTF.

6.5.1 Confined flame dynamics

Phase-conditioned images of confined conical flames have been taken for two mass flow rates ($\dot{m} = 0.396$ and 0.792 g.s^{-1}), two confinement ratios ($C_r = 0.44$ and 0.81), two forcing frequencies ($f = 10$ and 80 Hz) and one input level $|v_1/v_0| = 0.1$. Images for a mass flow rate $\dot{m} = 0.792$ g.s^{-1} and an excitation frequency $f = 10$ Hz are presented in Fig. 6.9. At low frequency, the flame features a quasi-steady response to the imposed perturbations. For both confinement ratios, the flame undergoes a bulk oscillation with a flame tip that is successively stretched and compressed during the modulation cycle. At low frequency, the flame motion is similar to that observed for unconfined flames and results for both confinements are close. Images for the same mass flow rate are presented in Fig. 6.10 but with a different perturbation frequency $f = 80$ Hz. Significant differences between images obtained for both confinement ratios may now be underlined. For $C_r = 0.44$, the flame front exhibits large wrinkles and several cusps. For $C_r = 0.81$, the flame front features smaller wrinkles without cusps. Moreover, for that confinement ratio, the flame wrinkle wavelength is larger, due to the higher mean velocity component tangential to the flame front. This emphasizes the increasing axial velocity in the fresh reactant flow when the confinement ratio is increased. The same observations can be made for a flame with a mass flow rate $\dot{m} = 0.396$ g.s^{-1} and perturbed at 80 Hz, as shown in Fig. 6.11.

6.5.2 FTF of confined conical flames

The FTF are measured for the different confinement ratios and mass flow rates explored. Results are plotted in terms of the FTF gain G and phase lag φ as a function of the reduced frequency $\omega_* = \omega R_0/(S_d \cos\alpha)$. The analysis is first conducted by comparing FTF measured for different mass flow rates for a fixed confinement ratio: $C_r = 0$ (Fig. 6.12-left), 0.44 (Fig. 6.12-right), 0.60 (Fig. 6.13-left) and 0.81 (Fig. 6.13-right). For all confinements, the gain features a low-pass filter behavior with several secondary humps and a slight excess to unity at low frequency. The phase lag regularly increases with frequency, indicating that flow perturbations are convected by the mean flow. This behavior ceases at high frequencies, except for $C_r = 0.81$ in Fig. 6.13-right. For each confinement, the FTF collapse roughly on the same curve when plotted as a function of the reduced frequency ω_* for data gathered at different injection velocities. These

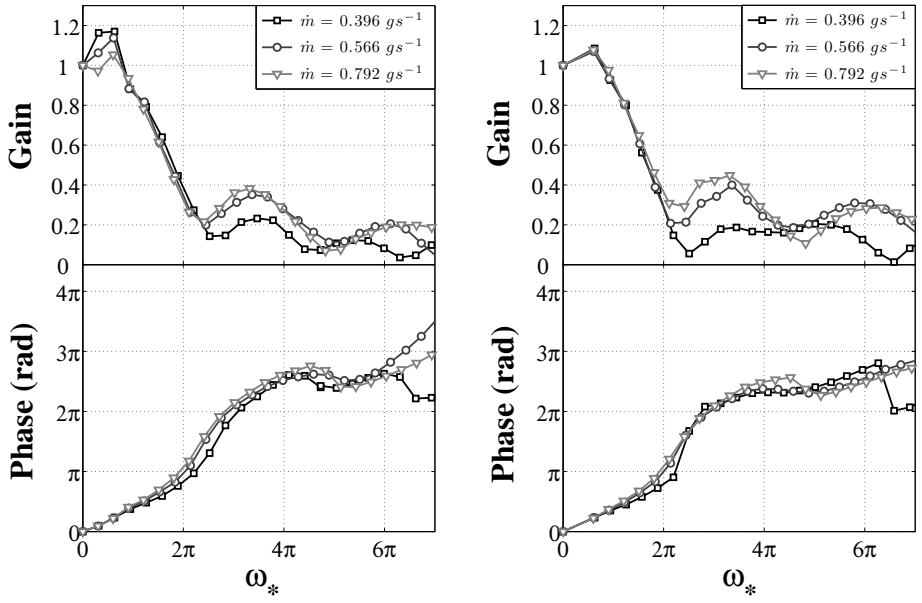

Figure 6.12: *FTF gain (top) and phase (bottom) as a function of the reduced frequency ω_*, for three different inlet mass flow rates and for two confinement ratios: $C_r = 0$ (left) and $C_r = 0.44$ (right).*

results indicate that the reduced frequency ω_* is still a relevant dimensionless number that characterizes the frequency response of a conical flame for a fixed confinement ratio. It is however worth mentioning that these experiments at fixed C_r values were also conducted by keeping the dimensionless parameter C_b roughly constant as well (see Tab. 6.1). It would be interesting to investigate effects of changes in the value of C_b while keeping C_r constant. That can be achieved by either changing the mixture equivalence ratio or the fuel used.
The measured FTF are now further studied for different confinement ratios C_r by keeping the inlet mass flow rates constant. Results are examined for $\dot{m} = 0.396$ g.s^{-1} in Fig. 6.14-left, $\dot{m} = 0.566$ g.s^{-1} in Fig. 6.14-center and $\dot{m} = 0.792$ g.s^{-1} in Fig. 6.14-right. These figures indicate that the slope of the FTF phase lag as well as the location of the extrema of the FTF gain are modified when the confinement ratio C_r is changed. For the two largest mass flow rates, the frequency responses of the unconfined flame obtained for $C_r = 0$ and the weakly confined flame $C_r = 0.44$ collapse on a single curve at low frequency, emphasizing the limited influence of confinement when $C_b \leq 1$. For higher confinement ratios, both gain and phase curves feature the same trends as the unconfined configuration, but the response is stretched out to higher reduced frequencies as the confinement ratio is increased. By examining for example the measurements for the reduced frequency $\omega_* = 3\pi$, where the gain still takes high values, differences larger than π for the phase lag may be observed between the different responses. Such a phase distortion can make the difference between

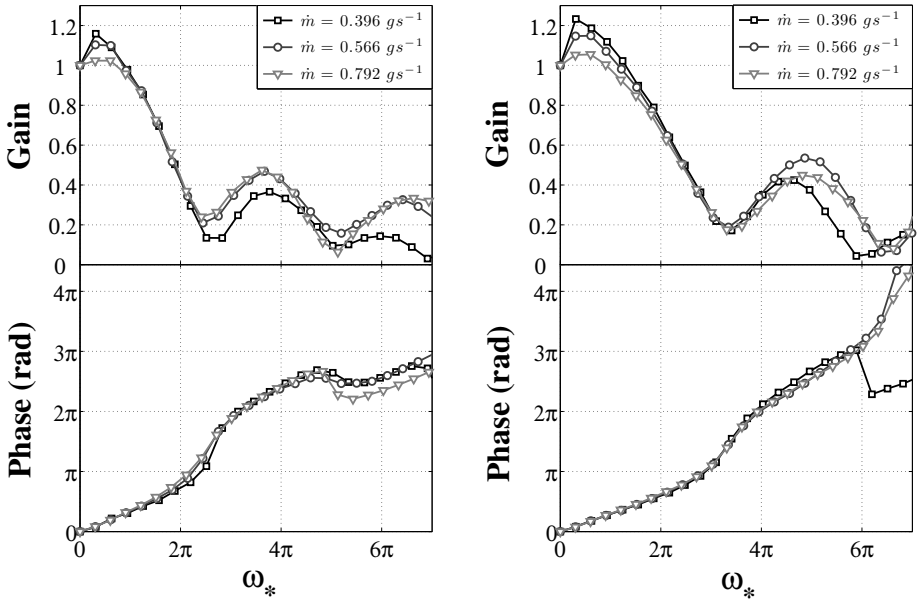

Figure 6.13: *FTF gain (top) and phase (bottom) as a function of the reduced frequency ω_*, for three different inlet mass flow rates and for two confinement ratios: $C_r = 0.60$ (left) and $C_r = 0.81$ (right).*

a stable and an unstable combustor regarding thermo-acoustic instabilities. Differences are also observed on the FTF gain. Values of the secondary gain peaks increase when the confinement ratio increases in the case of a flame with a small aspect ratio (see Fig. 6.14-left). This effect disappears in the case of elongated flames (see Fig. 6.14-right). It is also worth noting that the FTF phase lag saturates at high frequency in all cases explored, except for the two largest confinement ratios and the two most elongated flames.
These observations motivate further analysis and indicate that the reduced frequency ω_* needs to be corrected to explicitly take into account the confinement ratio. This problem is investigated in the next section.

6.6 Reduced frequency for the FTF of confined conical flames

Knowing the steady flame front location in a confined configuration, it is now possible to determine an approximate expression for the time lag between heat release rate and flow perturbations controlling the FTF of a confined conical flame. It is known that for an unconfined axisymmetric elongated conical flame stabilized in a uniform velocity field, this time lag is about $\tau = (1/3)H_0/v_0$ [Sugimoto and Matsui (1982); Durox *et al.* (2009)] at low frequency. The exact expression was derived for any flame angle. This time lag is given

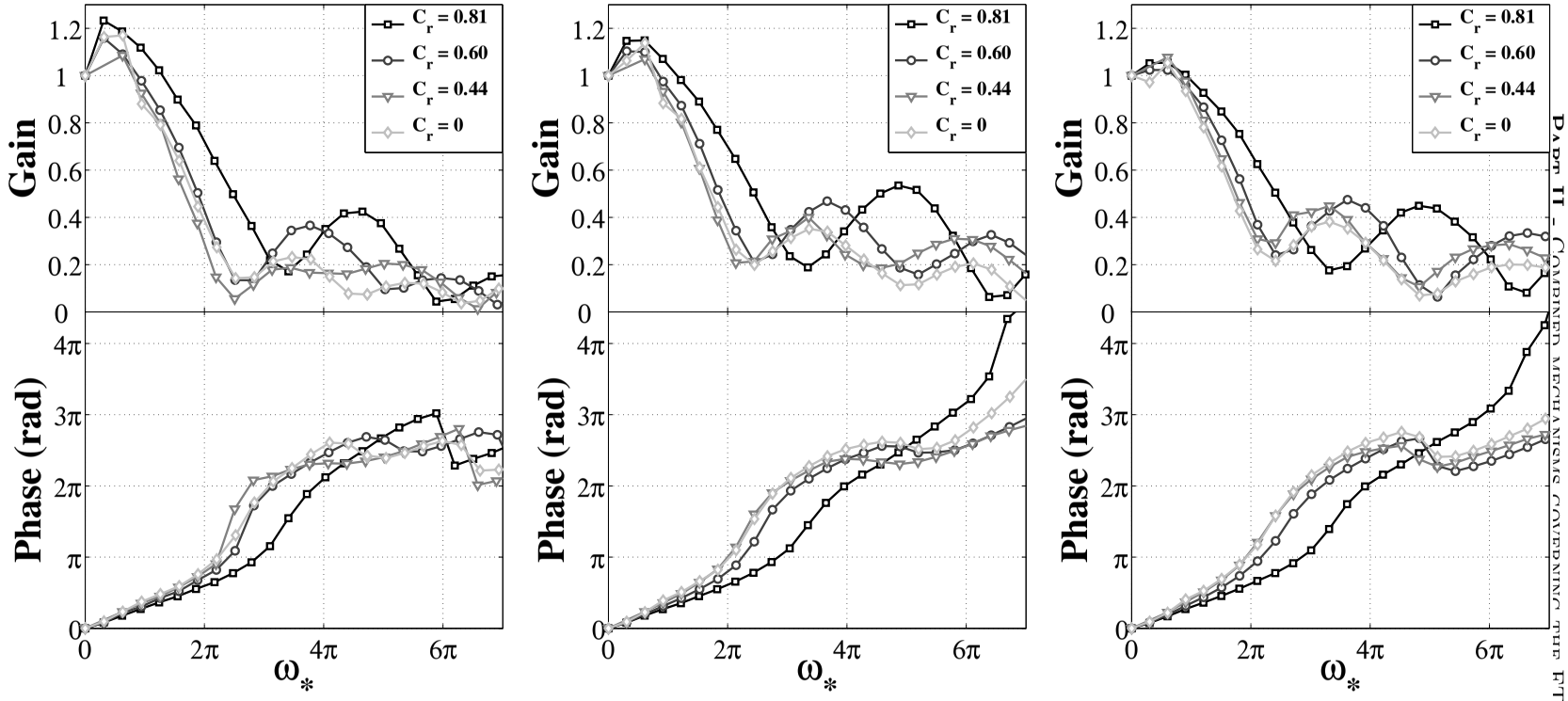

Figure 6.14: *Gain G (top) and phase lag φ (bottom) of the FTF as a function of the reduced frequency ω_*, for different confinements and flow rates. Left plot: $\dot{m} = 0.396$ g.s^{-1}. Center plot: $\dot{m} = 0.566$ g.s^{-1}. Right plot: $\dot{m} = 0.792$ g.s^{-1}.*

by $\tau = (1/3)R_0/(S_d \cos\alpha) = (1/3\cos^2\alpha)H/v_0$ [Merk (1957); Ducruix *et al.* (2000)]. At high frequencies, this time lag is modified. In particular, it was shown to be equal to $\tau = H_0/v_0$ in the case of elongated flame [Schuller *et al.* (2003a); Cuquel *et al.* (2011b)] (see also Tab. 4.1 in Chapter 4). The FTF of an unconfined premixed conical flame depends on two time scales [Baillot *et al.* (1992); Blumenthal *et al.* (2013)] associated to the convection of either velocity or flame front perturbations. The first time scale is given by $\tau_r = L/(v_0 \cos\alpha)$ and is associated to the convection of flame front perturbations at a speed $v_0 \cos\alpha$ along the steady flame front over a distance $L = R_0/\sin\alpha$ corresponding to the steady flame front length. The second time scale is equal to $\tau_c = H_0/v_0$ and is associated to the convection of flow disturbances by the mean flow v_0 over a length $H = R_0/\tan\alpha$ corresponding to the flame height. These two time scales can be retrieved analytically by determining the averaged time that perturbations take to travel from the flame base to the flame tip. At low frequency, one may write:

$$\tau_{\xi_1} = \frac{1}{\pi R_0^2}\int_0^{R_0} 2\pi r\ \tau_{\xi_1}^{\mathrm{loc}}(r)\ dr \qquad \text{with} \qquad \tau_{\xi_1}^{\mathrm{loc}}(r) = \frac{L - r/\sin\alpha}{v_0\cos\alpha} \tag{6.24}$$

$$\tau_{v_1} = \frac{1}{\pi R_0^2}\int_0^{R_0} 2\pi r\ \tau_{v_1}^{\mathrm{loc}}(r)\ dr \qquad \text{with} \qquad \tau_{v_1}^{\mathrm{loc}}(r) = \frac{H_0 - r/\tan\alpha}{v_0} \tag{6.25}$$

These expressions give the following results linking the time lags τ_{ξ_1} and τ_{v_1} to the two time scales τ_r and τ_c :

$$\tau_{\xi_1} = \frac{1}{3}\frac{L}{v_0\cos\alpha} = \frac{\tau_r}{3} \tag{6.26}$$

$$\tau_{v_1} = \frac{1}{3}\frac{H_0}{v_0} = \frac{\tau_c}{3} \tag{6.27}$$

For a confined flame, these travel times are modified due to the increase of the mean axial velocity $v_{0u}(y)$ and the change of the location of steady flame front $\eta_0(r)$. The starting point is to examine resulting changes on the average time taken by either flow or flame front disturbances originating from the burner outlet to induce a flame surface area perturbation. In the elongated flame approximation, these local time lags are given by:

$$\tau_{v_1}^{\mathrm{loc}}(r) = \int_0^{\eta_0(r)} \frac{dy}{v_{0u}(y)} \qquad \tau_{\xi_1}^{\mathrm{loc}}(r) = \int_{R_0}^{r} \frac{1}{v_{0u}(\eta_0(r))}\frac{\partial\eta_0}{\partial r}dr \tag{6.28}$$

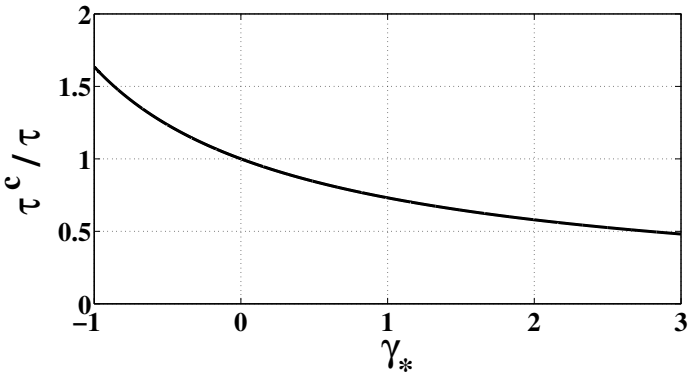

Figure 6.15: *Evolution of the ratio of the time lag derived for elongated confined conical flames (Eq. 6.32) divided by the time lag* $\tau = (1/3)H_0/v_0$ *of an elongated unconfined conical flame as a function of the parameter* γ_*.

The first expression $\tau_{v_1}^{\mathrm{loc}}(r)$ stands for the time lag needed by a flow perturbation originating from the burner outlet and being convected vertically towards the flame front at a speed $v_{0u}(y)$ to cover a distance $\eta_0(r)$. The second expression $\tau_{\xi_1}^{\mathrm{loc}}(r)$ represents the time lag induced by a flame front disturbance originating from the flame base and being convected along the steady flame front at a speed equal to the velocity component tangential to the steady flame front $v_{0t}(\eta_0(r)) = v_{0u}(\eta_0(r))\cos\alpha_l - u_{0u}(\eta_0(r))\sin\alpha_l$, where $\alpha_l(r)$ is the local angle between the flame front and the burner axis. This speed reduces to $v_{0t}(\eta_0(r)) = v_{0u}(\eta_0(r))$ in the elongated flame approximation. These flame front disturbances are being convected over an infinitesimal distance equal to $dl = d\eta_0(r)/\cos\alpha_l$. This distance reduces to $(\partial\eta_0/\partial r)dr$ for an elongated flame. These quantities need to be integrated over the flame surface to determine their average values:

$$\tau_{v_1}^c = \frac{1}{\pi R_0^2}\int_0^{R_0} 2\pi r \int_0^{\eta_0(r)} \frac{dy}{v_{0u}(y)} dr \tag{6.29}$$

$$\tau_{\xi_1}^c = \frac{1}{\pi R_0^2}\int_0^{R_0} 2\pi r \int_{R_0}^{r} \frac{1}{v_{0u}(\eta_0(r'))}\frac{d\eta_0}{dr'} dr' dr \tag{6.30}$$

$$\tag{6.31}$$

After a series of calculations, one obtains the same result for $\tau_{v_1}^c$ and $\tau_{\xi_1}^c$ in the elongated flame approximation:

$$\tau^c = \tau_{v_1}^c = \tau_{\xi_1}^c = \frac{1}{3}\frac{H_0}{v_0}\left[\frac{6}{\gamma_*}\left(\frac{1}{2} - \frac{2}{\gamma_*} + \left(\frac{2}{\gamma_*}\right)^2 \ln\left(1+\frac{\gamma_*}{2}\right)\right)\right] \tag{6.32}$$

The time lag τ^c of a confined flame is reduced compared to its value $\tau = (1/3)H_0/v_0$ for an elongated unconfined flame by the factor indicated between

the square brackets in Eq. (6.32). It is then natural to consider a modified expression for the reduced frequency $\omega_* = \omega R_0/(S_d \cos\alpha)$ used to rescale unconfined FTF by accounting for the reduced mean time lag when the flame is confined. This can be done by replacing ω_* with the following modified expression:

$$\omega_*^c = \omega_* \frac{6}{\gamma_*} \left[\frac{1}{2} - \frac{2}{\gamma_*} + \left(\frac{2}{\gamma_*} \right)^2 \ln\left(1 + \frac{\gamma_*}{2} \right) \right] \tag{6.33}$$

The scaling factor $\omega_*^c/\omega_* = \tau^c/\tau$ is a function of γ_* and is plotted in Fig. 6.15. This figure shows that when the confinement ratio is taken into account (i.e. when $\gamma_* \neq 0$), the scaling factor takes values between 0 and 1 for positive values of γ_*.

This new reduced frequency takes into account the flow acceleration in the fresh reactants $\gamma_*(C_r, E, \alpha)$ when the flame is confined and can be used to rescale FTF measured for different confinement ratios as shown in Fig. 6.16. For the highest mass flow rate investigated, the flames are elongated (see Fig. 6.16-right). The gain curves obtained for different confinements collapse well on each other up to $\omega_*^c = 3\pi$. The first local minimum value of the gain response is also well retrieved even if at higher reduced frequencies some deviations can be observed for the case $C_r = 0.81$, i.e. when the flame is strongly confined. The phase lag evolutions also collapse on a single curve for all confinement ratios up to $\omega_*^c = 3\pi$. There are however some differences at high frequencies. The phase lag for $C_r = 0.81$ still features a regular increase for frequencies larger than $\omega_*^c \geq 3\pi$ and diverges from other data exhibiting a saturation like behavior in this frequency range. It is clear that this phenomenon cannot be anticipated with the model proposed herein and additional physics must be included in the analysis to investigate the high frequency behavior of confined conical flames. For the smallest flames investigated, when the mass flow rate is reduced to $\dot{m} = 0.396$ g.s^{-1}, the curves for the FTF gain and phase lag still collapse but results are not as good as for the elongated flame case. This emphasizes the limit of the present time lag model that was derived in the elongated flame approximation when $\alpha \ll 1$. In Fig. 6.16, the FTF expression Eq. (4.11) derived with an incompressible convective velocity perturbation model is also plotted in red lines on top of the experimental data. This model captures the correct phase lag evolution of the FTF for all confinement ratios when the reduced frequency ω_*^c is taken into account. This analytical expression can then be used to model the frequency response of confined conical flames up to $\omega_*^c = 3\pi$.

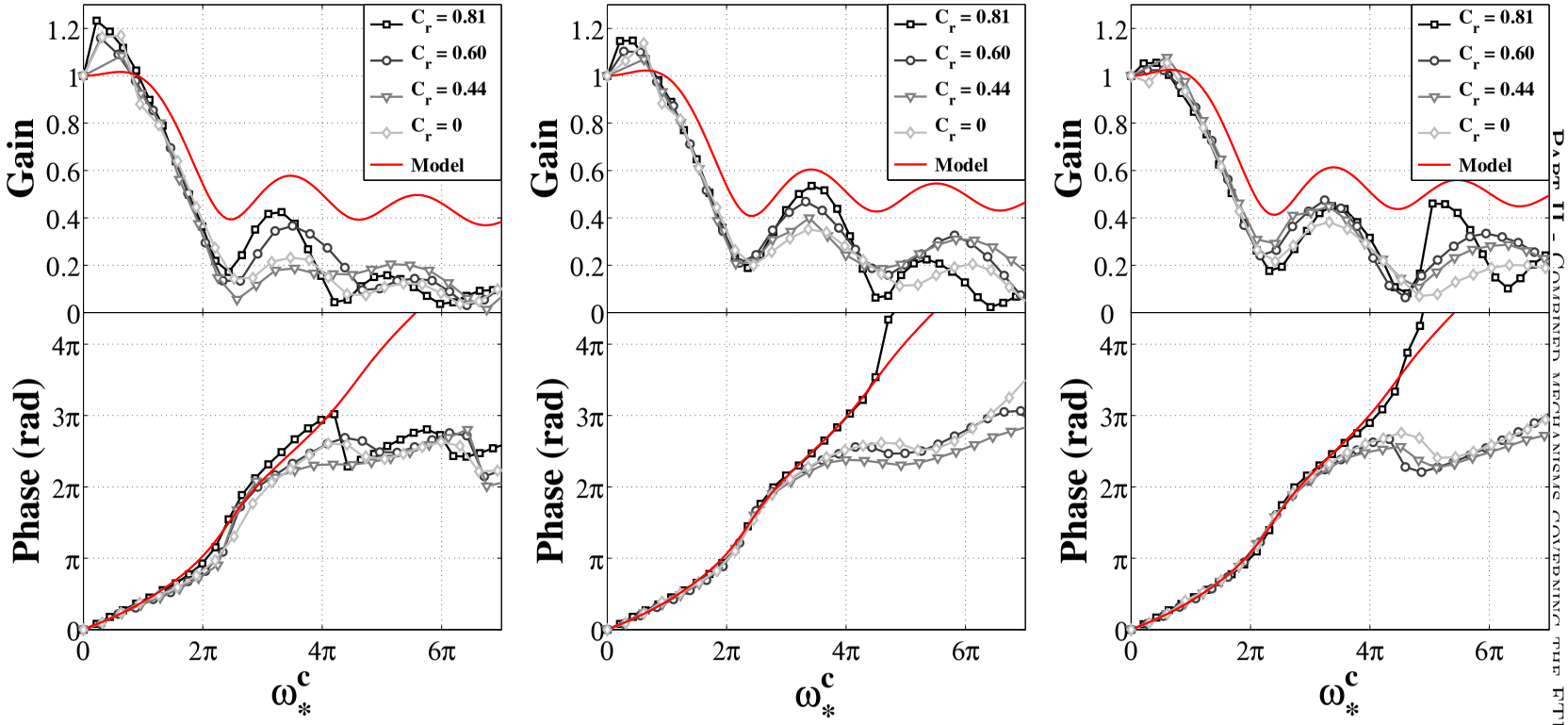

Figure 6.16: *Gain G (top) and phase lag φ (bottom) of the FTF as a function of the reduced frequency ω_*^c, for different confinement ratios and flow rates. Left plot: $\dot{m} = 0.396$ g.s^{-1}. Center plot: $\dot{m} = 0.566$ g.s^{-1}. Right plot: $\dot{m} = 0.792$ g.s^{-1}. In all figures, the model $F_A(\omega_*, \alpha)$ is plotted in red lines.*

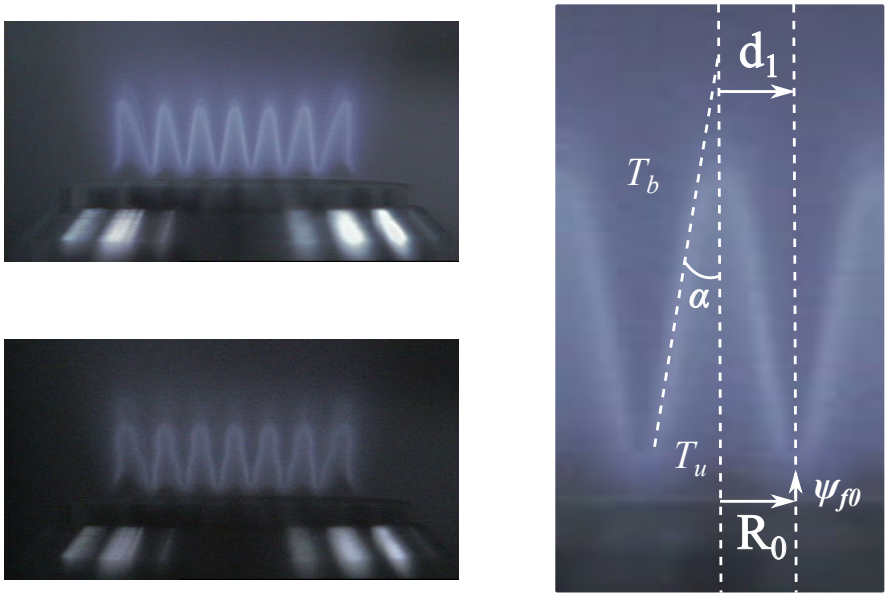

Figure 6.17: (left) *Collection of conical flames anchored on a perforated plate: steady flames (top) and a snapshot of acoustically perturbed flames (bottom).* **(right)** *Zoomed image of the central flame used to determine some of the parameters used in the theoretical models.*

6.7 FTF of a collection of conical flames

The FTF models developed in the Chapters 4, 5 and 6 are used in this section to compare predictions with FTF measurements carried out on a collection of small premixed laminar conical flame anchored on a perforated plate. This configuration is presented in Fig. 6.17. These experiments were conducted during the Ph.D. work of F. Boudy [Boudy *et al.* (2011); Boudy *et al.* (2011); Boudy *et al.* (2013); Boudy (2012)]. The experimental setup features a perforated plate where the flames are anchored, with 129 holes of radius $r_h = 1$ mm that are distributed over a square mesh with a hole pitch $d_1 = 1.5$ mm. Zoomed images of the steady flames presented in Fig. 6.17-right are used to determine some quantities such as the flame base radius R_0, the flame front slope related to the flame tip half-angle α and the flame quenching distance ψ_{f0} to model the flame response. In the following, different combinations of the models derived in the present work are envisaged. Measurements of FTF from Boudy (2012) are compared to predictions with five different degrees of approximation.

6.7.1 FTF model $F_A(\omega_*, \alpha)$

The FTF model $F_A(\omega_*, \alpha)$ given by Eq. (4.11) is first considered with the following parameters. The mean flow velocity at the burner exit and on the burner axis was measured by Boudy (2012). This velocity is equal here to $v_0 = 4.8$ m.s^{-1}. The flame front angle with respect to the vertical axis was determined from the image shown in Fig. 6.17-right. The value found for the flame tip half-angle is $\alpha = 0.174$ rad. These values are used to determine the corresponding flame speed $S_d = v_0 \sin\alpha = 0.83$ m.s^{-1}. Finally, images in Fig. 6.17-left shows that the flame bases from neighboring injectors are in contact. No planar flame front is present in between the conical flames, contrary to the configuration studied by Altay *et al.* (2009). Thus, the flame base radius is taken here equal to the hole pitch and one has $R_0 \simeq d_1 = 1.5$ mm. Predictions from this model are plotted in Fig. 6.18-top (black line) and compared to FTF measurements (red circles). The model retrieves the global trend of the FTF gain and phase lag. However, it does not yield the correct frequencies of the extrema of the FTF gain measurements. The modeled FTF gain also features much smaller values than experimental data. The modeled FTF phase lag collapses on measurements at low frequencies, but predictions rapidly diverge from experiments at higher frequencies. Large phase lag differences of about π may be observed in certain frequency range.

6.7.2 FTF model $F_A(\omega_*, \alpha) + F_B(\omega_*, \alpha, \Psi_f, \delta_*, \mathrm{Ze})$

The contribution from the flame base motion F_B is added to the previous model. The same values for v_0, R_0 and S_d are considered. The flame quenching distance is estimated from the zoomed image in Fig. 6.17-right. The value found is of the order of $\psi_{f0} = 0.5$ mm. The fresh gas temperature is taken here equal to $T_u = 300$ K and the burnt gas temperature is taken equal to $T_b = 900$ K. This last quantity was tuned to obtain a good fit with FTF measurements. These values lead to the following dimensionless numbers $\Psi_f = 0.225$ and $\delta_* = 0.73$ needed to determine the contribution F_B from Eq. (5.11). The activation temperature was taken equal to $T_a = 20000$ K corresponding to a Zeldovich number equal to $\mathrm{Ze} = 14$. Predictions with this model are plotted in Fig. 6.18-center (black line) and compared to FTF measurements (red circles). This new model exhibits only small differences on the FTF phase lag compared to the previous model. The predicted gain now features slightly larger values than with $F_A(\omega)$ and thus compares slightly better with measurements. However, the frequencies of the extrema are still not correctly reproduced.

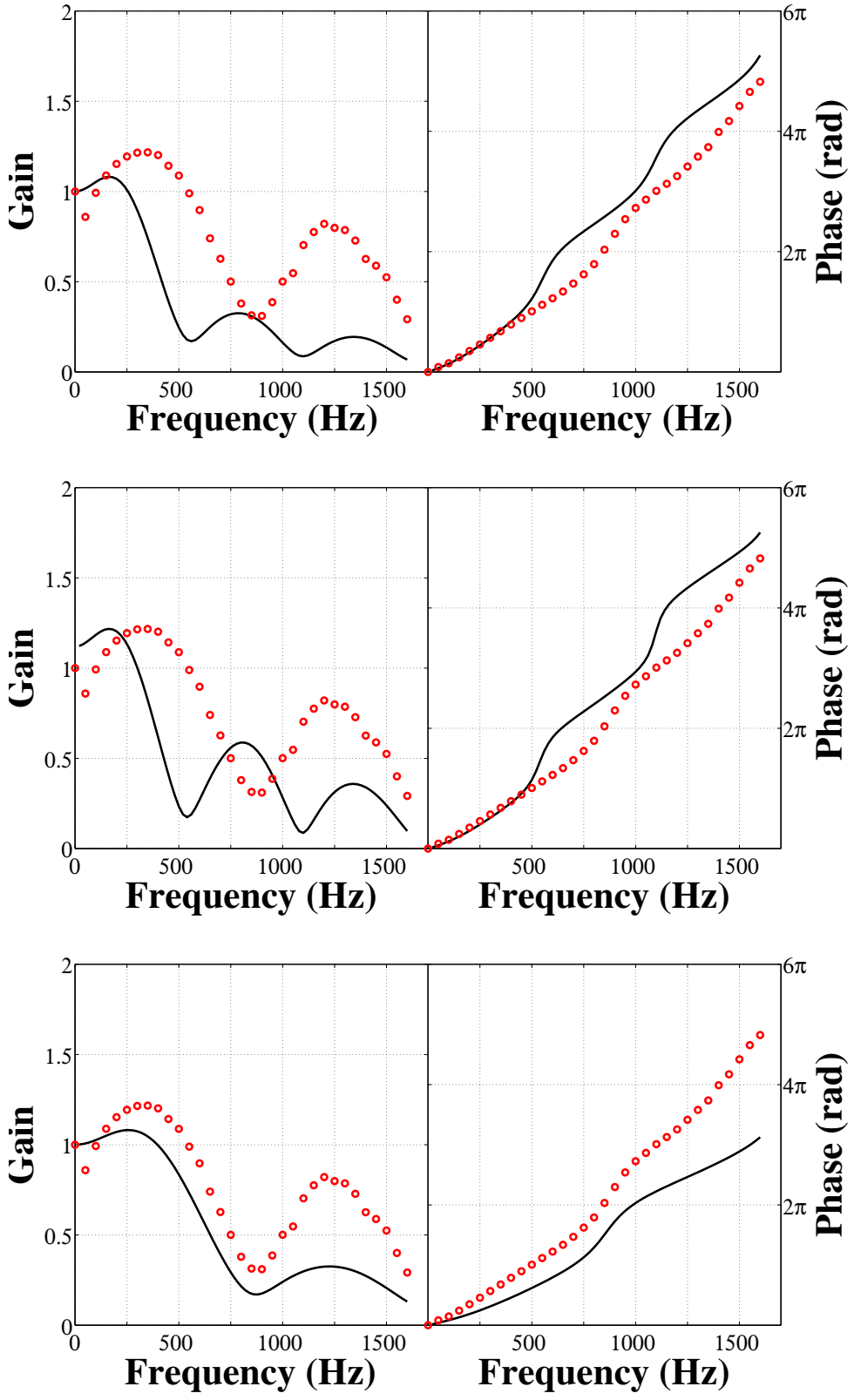

Figure 6.18: *Comparisons between FTF measurements (red circles) and different FTF models (black lines).* **(top)** $F_A(\omega_*, \alpha)$. **(center)** $F_A(\omega_*, \alpha) + F_B(\omega_*, \alpha, \Psi_f, \delta_*, Ze)$.**(bottom)** $F_A(\omega_*^c, \alpha)$.

6.7.3 FTF model $F_A(\omega_*^c, \alpha)$

The previous models do not take into account the fact that the burnt gases cannot fully expand due to the presence of neighboring flames. This phenomenon is here taken into account by using the modified reduced frequency ω_*^c into the FTF expression F_A instead of ω_*. The confinement ratio is here defined by the square root of the ratio between the cross-section area of the flame base πR_0^2 and the cross-section of the volume occupied by the burnt gases $(2d_1)^2$:

$$C_r = \frac{\pi^{\frac{1}{2}} R_0}{2d_1} = 0.89 \tag{6.34}$$

A burnt to unburnt gas volume expansion ratio $E = \rho_u/\rho_b = 6$ is considered. Using these parameters, the dimensionless acceleration is equal to $\gamma_* = 1.57$. Results from model $F_A(\omega_*^c, \alpha)$ are plotted in Fig. 6.18-bottom as a function of the forcing frequency. This new model reproduces the correct frequencies of the extrema of the FTF gain, but the gain is globally underestimated. The model does not match FTF phase lag measurements. It features the same trend as the FTF measurements and the change in the slope of the FTF phase lag near 800 Hz corresponding to a local minimum of the gain is well retrieved.

6.7.4 FTF model $F_A(\omega_*^c, \alpha) + F_B(\omega_*^c, \alpha, \Psi_f, \delta_*, \mathrm{Ze})$

The last two models are now combined to take into account two important features of the flame response to flow perturbations:

(1) Effects due to the confinement of the burnt gases,
(2) Effects of unsteady losses from the flame to the burner rim.

Predictions from this model are plotted in Fig. 6.19-top. Results match well experiments for the FTF gain. The frequencies and the values of the gain extrema are well reproduced. Predictions for the FTF phase lag show differences with measurements. However, the global trend is well retrieved, including the frequency corresponding to a change of the slope of the phase lag. It is also interesting to note that the difference between the modeled FTF phase lag and experimental data increases with the forcing frequency. This observation is used to improve the model in the next section.

6.7.5 FTF model $[F_A(\omega_*^c, \alpha) + F_B(\omega_*^c, \alpha, \Psi_f, \delta_*, \mathrm{Ze})] \exp(i\omega\tau_1)$

In order to match phase lag measurements, an additional time lag $\tau_1 = 4.10^{-4}$ s is added to the previous model. Results are presented at the bottom of Fig. 6.19. The gain curve is not modified by this correction and thus still compares well

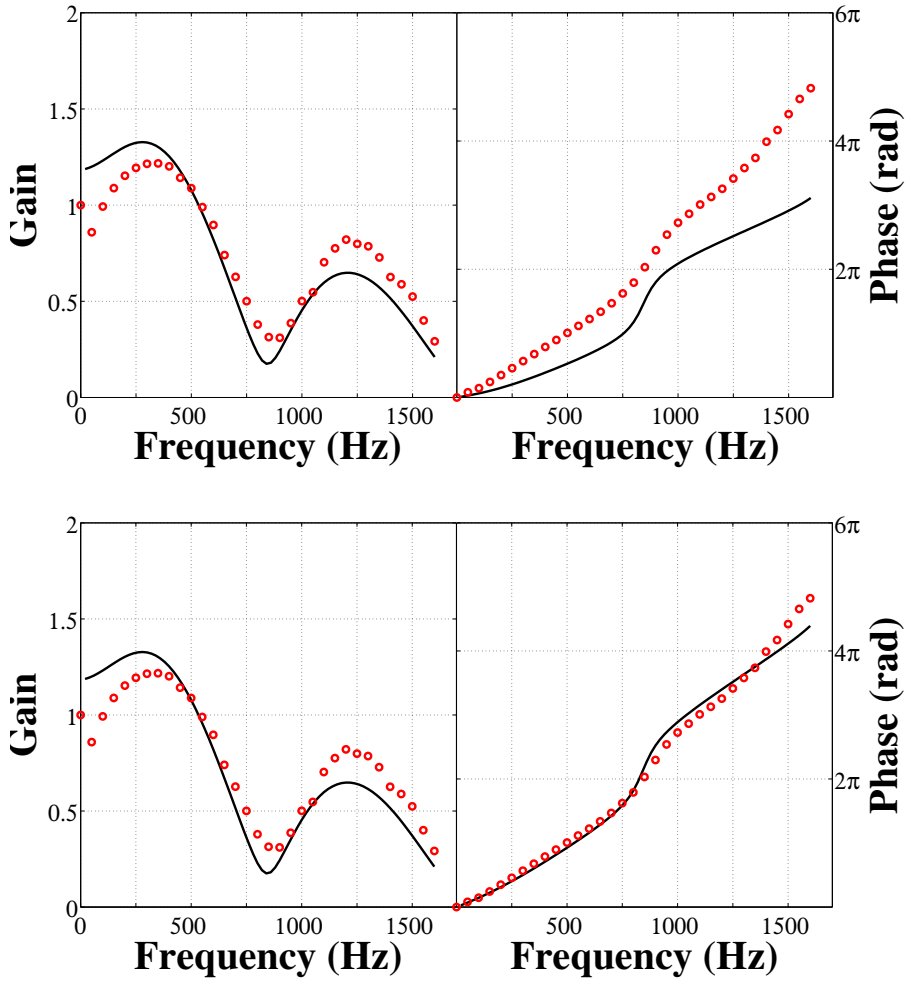

Figure 6.19: *Comparisons between FTF measurements (red circles) and different FTF models (black lines).* **(top)** $F_A(\omega_*^c, \alpha) + F_B(\omega_*^c, \alpha, \Psi_f, \delta_*, Ze)$. **(bottom)** $[F_A(\omega_*^c, \alpha) + F_B(\omega_*^c, \alpha, \Psi_f, \delta_*, Ze)] \exp(i\omega\tau_s)$.

with measurements. This correction corresponding to an additional phase lag $\omega\tau_1$ modifies the slope of the phase lag and enables to collapse predictions on the experimental data over the whole range of frequencies explored. The physical mechanism associated to this time lag remains to be elucidated. Different conjectures can be made that were not checked experimentally. It is interesting to indicate an associated length scale $\delta_{\tau_1} = v_0\tau_1 = 1.9$ mm based on the mean flow velocity.

A combination of the different models derived in this thesis shows that it is possible to model the FTF of a collection of small laminar premixed conical flames anchored on a perforated plate by taking into account different important

features: (1) the incompressible nature of the velocity perturbations in the fresh stream of reactants, (2) the unsteady heat losses from the flame base to the perforated plate and (3) the effects of confinement taking place when the burnt gases cannot fully expand. To obtain these predictions, different parameters need to be determined and fixed. A sensitivity analysis of the FTF to these parameters has to be carried out but the results presented in this section already show that the FTF can be reasonably approximated by carefully taking into account the different physical mechanisms controlling the response of these flames.

6.8 Conclusion

It was shown that effects of the confinement of the burnt gases must be taken into account to transpose data for FTF gathered for premixed unconfined conical flames or for FTF of flames obtained with a certain geometrical confinement to a situation with a different confinement. This is necessary when the burnt gases cannot fully expand. This situation takes place when the confinement ratio identified in this study C_b exceeds the threshold value of unity. In this case, the FTF is a function of the confined reduced frequency ω_*^c and flame angle α. This dimensionless frequency ω_*^c is the product of the unconfined flame reduced frequency ω_* and a correction that accounts for a change in the mean time lag between heat release rate and velocity disturbances. These modifications result from the acceleration of the fresh stream of reactants and the deformation of the flame shape when the flame is confined. In this work, these two phenomena were explicitly linked to the confinement ratio $C_r = R_0/R_1$ and volumetric burnt to unburnt gas expansion ratio $E = \rho_u/\rho_b$. These phenomena are also present in situations where the flames are not confined by walls, but when the hot gases of neighboring flames are in contact as in many multiple injection systems. One example was considered in the last section of this chapter by examining the response of a collection of small conical flames anchored on a perforated plate. The models derived in the present thesis were tested and compared to experiments gathered on this multiple flame burner. It is shown that the global shape of the FTF can be reproduced correctly with a model taking into account incompressible velocity perturbations, heat losses from the flame to the burner and the fact that the burnt gases cannot fully expand.

Part III

Instability prediction using a Helmholtz solver and the FDF methodology

Chapter 7

The Helmholtz solver AVSP and the FDF methodology

It has been recently shown that the Flame Describing Function (FDF), an extension of the Flame Transfer Function (FTF) including effects of perturbation amplitude, can be used in combination with low-order acoustic network models to predict a wide range of nonlinear behaviors such as limit cycle amplitudes and frequencies, mode triggering, mode switching and hysteresis observed during unstable operation of a combustor. This nonlinear description of the flame response to flow perturbations is used in this chapter in a finite element solver that solves the inhomogeneous Helmholtz equation on multidimensional unstructured grids. This combination enables to perform simulations of the nonlinear stability analysis of a combustor in complex geometries with complex impedances. The FDF methodology is first introduced before introducing the multidimensional Helmholtz solver AVSP. The way unsteady heat release rate is included in the solver, the response of the perforated plate used to stabilize conical flames is modeled and the treatment at the combustor boundaries are described.

7.1 Introduction

Thermo-acoustic instability prediction has for a long time relied on the determination of the acoustic eigenmodes of the combustor coupled to a linear stability analysis through the use of the Flame Transfer Function (FTF) [Krebs *et al.* (2002); Schuller *et al.* (2003b); Noiray *et al.* (2006b); Nicoud *et al.* (2007); Schuermans *et al.* (2010)]. Such linear methods yield the set of modes that might grow at the instability onset but in many cases, these methods fail to determine the right mode or the right frequency that was reached by the thermo-acoustic instability. In addition, these methods lead to the prediction of an exponential instability growth and thus are unable to determine the limit cycle amplitude, due to the nonlinear nature of the saturation mechanisms involved

[Balachandran *et al.* (2005); Bellows *et al.* (2007)].

7.2 The FDF methodology

7.2.1 Nonlinear flame dynamics

While nonlinear acoustics can be of significant importance in the case of thermo-acoustic instabilities in rocket engines [Culick (1994)], it was shown that the flame is often the main nonlinear component of the system in the case of gas turbines [Dowling (1999); Balachandran *et al.* (2005); Durox *et al.* (2009); Palies *et al.* (2011); Schimek *et al.* (2011)]. Various experiments have been carried out to investigate the effects of perturbation amplitude on the FTF. Images of the perturbed flame shapes and FTF were measured in generic laminar flame configurations by sweeping the perturbation level [Durox *et al.* (2009)]. The most noticeable effects is a continuous decrease of the FTF gain for increasing perturbation levels. In many premixed configurations where the mixture composition remains homogeneous, the FTF phase remains almost unchanged, except in the case of single conical flames. The same conclusions were drawn for turbulent bluff body stabilized flames [Balachandran *et al.* (2005)] and turbulent swirling flames [Bellows *et al.* (2007); Palies *et al.* (2011); Schimek *et al.* (2011)]. LES simulations were recently carried out by Krediet *et al.* (2012), Krediet *et al.* (2013) to retrieve the FDF measured by Schimek *et al.* (2011) but significant differences between experiments and simulations were observed. In particular, differences between experiments and simulations of about $\pi/2$ were noticed on the phase lag between heat release rate and velocity disturbances. It is well known that instability predictions are very sensitive to small phase lag mismatch.

A novel method borrowed from control theory was developed to extend the linear stability analysis based on the FTF to nonlinear stability analysis based on the FDF. The Describing Function (DF) was first introduced in combustion dynamics analysis by Dowling (1999) in a theoretical study where the gain was considered to saturate at some constant value above a certain perturbation level threshold. It enabled to model the saturation of the flame response to flow perturbation so that the instability reached a limit cycle. This method was then generalized to the Flame Describing Function (FDF) and first put to use by Noiray *et al.* (2008) by considering a set of experimentally determined FTF that depend on both the frequency and perturbation level:

$$\mathcal{F}(\omega, |\widetilde{v}_1|) = G(\omega, |\widetilde{v}_1|)e^{i\varphi(\omega,|\widetilde{v}_1|)} = \frac{\widetilde{\dot{Q}}_1/\dot{Q}_0}{\widetilde{v}_1/v_0} \tag{7.1}$$

where $|\widetilde{v}_1|$ denotes the velocity perturbation amplitude. Each FTF in this description is determined for a fixed input level as shown in Fig. 7.1. The FDF

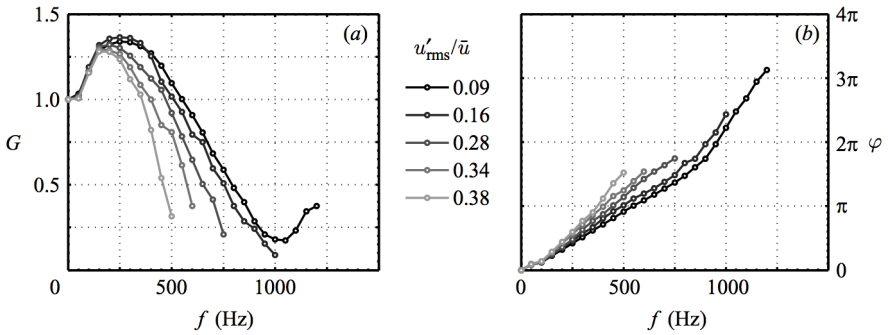

Figure 7.1: *Flame Describing Function gain G and phase φ as a function of frequency f and perturbation level $u_{\mathrm{rms}}/\bar{u}$. Reproduced from Noiray et al. (2008).*

was used by Noiray (2007), Noiray *et al.* (2008) in combination with an analytical low order acoustic network model of a combustor (see Fig. 7.2) to predict instabilities in a single cavity burner featuring small conical flames anchored at one extremity of a perforated plate. It enabled the authors to retrieve a wide range of nonlinear phenomena often observed in practical configurations. First, predictions of the limit cycle frequency and amplitude were possible thanks to modifications of either the FDF gain or phase lag. Secondly, it was also shown that mode triggering or mode switching can occur and be predicted in generic thermo-acoustic systems. Finally, this method enabled to predict a hysteresis phenomenon that was observed experimentally.
This nonlinear methodology was extended to confined systems by Boudy *et al.* (2011), Boudy *et al.* (2011), Boudy (2012). A second cavity was added on top

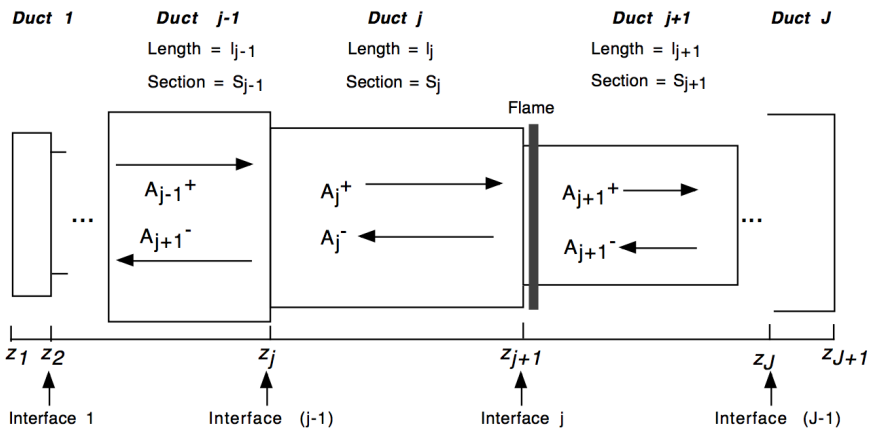

Figure 7.2: *Scheme of the acoustic network method. Reproduced from Poinsot and Veynante (2012).*

of the perforated plate. In addition to the previous studies, the influence of the boundary condition at the flame tube outlet and at the plenum inlet was thoroughly investigated. The same nonlinear phenomena were observed and it was possible to anticipate them for small confinement tube lengths. For longer flame tubes, more complex behaviors appeared during experiments featuring limit cycle destabilizations by different mechanisms [Boudy *et al.* (2012); Boudy *et al.* (2013)]. This raises the problem of multi-frequency interactions that can not be taken into account for now in the FDF framework.
Stability analysis based on FDF was also conducted with turbulent flames by Palies *et al.* (2011) in a combustor featuring a confined swirling flame. Limit cycle amplitude were also successfully predicted for several geometrical configurations of the combustor. This configuration was further studied with the numerical code AVSP by Silva *et al.* (2013) and the results also compared well with experimental data. In addition, the use of a numerical solver allowed to investigate the effects of modifications in the combustor geometry and the flame spatial distribution within the combustor chamber. Only the former was found to have a significant influence on the combustor stability.

7.2.2 Methodology for nonlinear stability analysis using the FDF

The nonlinear stability analysis making use of the Flame Describing Function (FDF) is based on several stability analyses that are each performed for a different perturbation level. The acoustic velocity and pressure are first developed as normal modes with the following form:

$$p_1(\mathbf{x},t) = \widetilde{p_1}(\mathbf{x})e^{-i\omega t} \tag{7.2}$$

$$\mathbf{v_1}(\mathbf{x},t) = \widetilde{\mathbf{v}}_\mathbf{1}(\mathbf{x})e^{-i\omega t} \tag{7.3}$$

where the angular frequency is a complex number $\omega = \omega_r + i\omega_i$, where ω_r stands here for the real part of the angular frequency and is linked to the instability frequency f by $\omega_r = 2\pi f$ and ω_i represents the imaginary component of the angular frequency and the growth rate of the instability. These normal modes are then injected in the linearized acoustic equations leading to either a dispersion relation if one uses a relatively simple low-order acoustic network representation of the combustor dynamics (see for example [Noiray *et al.* (2008); Kim *et al.* (2010); Boudy *et al.* (2011); Palies *et al.* (2011)]) or an eigenvalue problem if one uses a numerical solver (see the next section or [Nicoud *et al.* (2007); Camporeale *et al.* (2011)] for more details). As a result, one can obtain values for the angular frequency ω_r of the oscillation. One can also conclude on the system stability following the sign of $\omega_i - \delta$ where δ indicates the acoustic damping rate in the system. If this difference is negative (resp. positive), the acoustic variables will decay (resp. grow) exponentially and the system is thus stable (resp. unstable). In the cases where $\omega_i - \delta$ goes from positive to negative,

it means that a limit cycle is reached for $\omega_i - \delta = 0$.

The methodology that is used in the present work slightly differs than those used in the previous analyses and is synthesized in Fig. 7.3. The matricial equations considered here are solved with an iterative procedure. As such, one needs to choose a first approximation of the result for the first iteration. Thus, at each step, one has to consider an initial frequency value, an equation to solve and the result of that equation. The first step usually consists in the determination of the acoustic eigenmode of the system. In that case, no unsteady flame effects are considered. Therefore, the equation to consider is homogeneous:

$$M(\omega)P = 0 \tag{7.4}$$

where $M(\omega)$ is a matrix that is frequency dependent and P is the pressure eigenvector. The solution of that equation is the acoustic eigenfrequency ω_A that is a real number if no damping is considered (through perfectly reflective boundary conditions for example) or a complex number if damping is added in the model.

The next steps consider unsteady flame effects. The same equation than Eq. (7.4) is solved but with a right-hand side source term including the response by the flame to flow perturbation and modeled by a FDF. In this description, the FDF depends only on the real part of the angular frequency ω_r because it is determined with constant amplitude harmonic acoustic waves as the input signal. One is now left with the following inhomogeneous system:

$$M(\omega)P = F(\omega_r, v_1^k) \tag{7.5}$$

where the different velocity perturbation levels considered here are noted v_1^k for $k \in$ [1,N] and with $v_1^N > ... > v_1^k > ... > v_1^1$. At this stage, the method developed to solve the problem slightly differs from previous work. In the second step, the flame frequency response determined for the highest perturbation level $F(\omega_r, v_1^N)$ is used in the stability analysis instead of the smallest value as in the studies of Noiray *et al.* (2008) and Palies *et al.* (2011). The reason is that at high perturbation level, heat release rate perturbations correspond to very low FDF gain values and thus the inhomogeneous equation Eq. (7.5) almost reduces to the homogeneous acoustic equation Eq. (7.4) without source term. Results from the first step are thus used as an initial frequency for the second step. Next steps consider the equation with frequency responses corresponding to decreasing velocity perturbation levels. The initial frequency considered is taken from the result of the previous step. By covering all perturbation amplitudes, one obtains the values of the real angular frequency and growth rate for the set of perturbation levels considered:

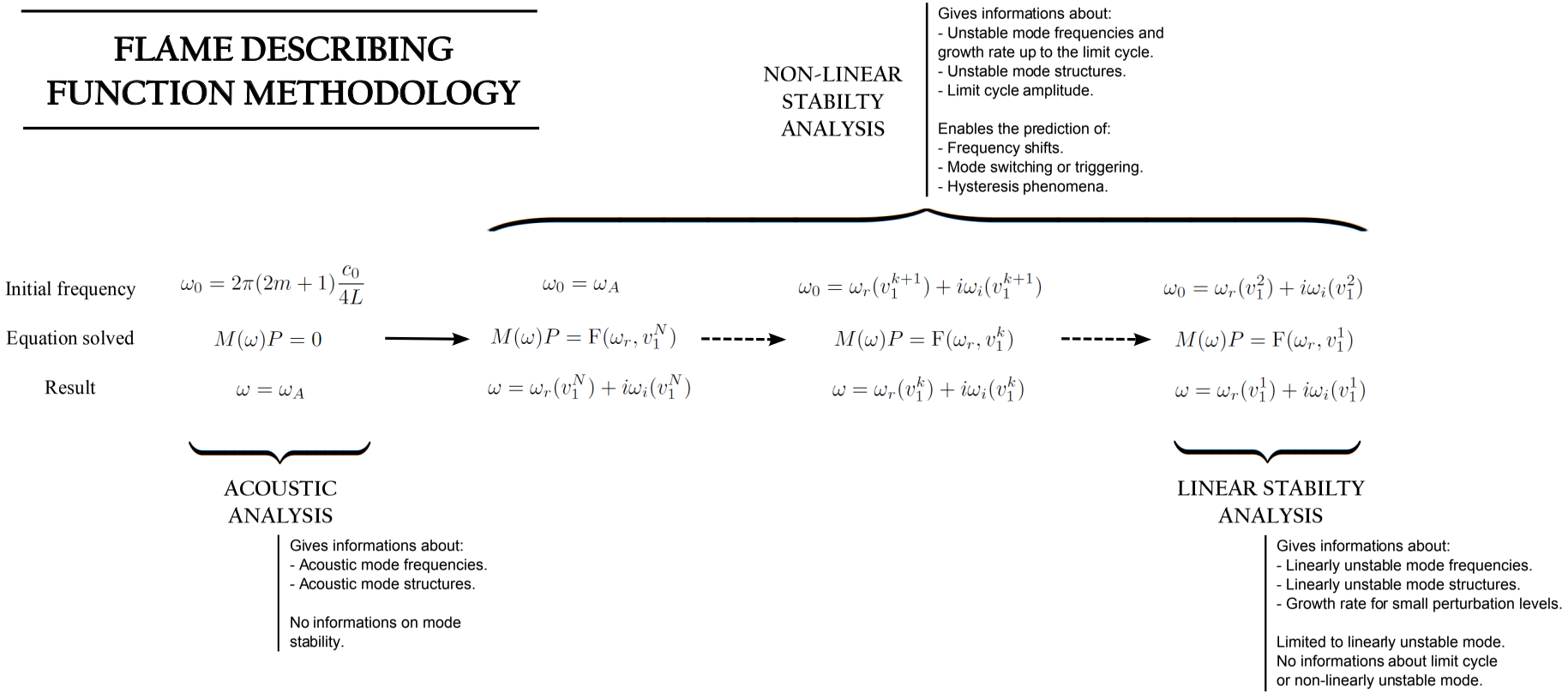

Figure 7.3: *Schematic of the FDF methodology using a Flame Describing Function* $\mathrm{F}(\omega_r, v_1^k)$ *defined for a set of perturbation level* v_1^k *for* $k \in [1,N]$ *where* $v_1^N > ... > v_1^k > ... > v_1^1$. *The method starts with an acoustic analysis and continue by considering unsteady flame effects. The flame frequency response determined for the largest perturbation level* $\mathrm{F}(\omega_r, v_1^N)$ *is considered first. The nonlinear stability analysis is pursued by considering all perturbation levels, from the largest* v_1^N *down to the smallest* v_1^1.

$$\omega_r = \omega_r(v_1^k) \tag{7.6}$$
$$\omega_i = \omega_i(v_1^k) \tag{7.7}$$
$$\tag{7.8}$$

These trajectories are plotted as a function of the perturbation level and the stability of the system can be deduced from these trajectories as shown by Noiray *et al.* (2008). This nonlinear stability analysis allows to determine the evolution of the growth rate with the perturbation level and thus to determine if a mode is either:

- stable, i.e. $\omega_i(v_1^k) < 0$ for all k.
- linearly unstable, i.e. $\omega_i(v_1^1) > 0$.
- nonlinearly unstable, i.e. $\omega_i(v_1^1) < 0$ but $\omega_i(v_1^k) > 0$ for at least a value of $k > 1$.

Limit cycles are identified by examining the evolution of the growth rate with the perturbation level. The limit cycle is reached when the growth rate goes from positive values to $\omega_i = 0$ in systems where the damping can be neglected [Noiray *et al.* (2008); Boudy *et al.* (2011)]. In systems where the damping is significant, the limit cycle condition is modified. In [Palies *et al.* (2011)], a damping rate of $\delta = 55 \pm 10\ \mathrm{s}^{-1}$ was determined in a set of separate experiments and was used to retrieve the limit cycle amplitude by using the relation: $\omega_i = \delta$.

The FDF methodology may be used to predict different nonlinear behaviors. Nonlinearly unstable modes can be triggered by external perturbations [Noiray *et al.* (2008); Boudy *et al.* (2011)] or external noise [Jegadeesan and Sujith (2013)]. Comparison of the growth rate evolutions of each mode also enables to delineate regions where mode switching occurs, i.e. when a linearly unstable mode triggers a nonlinearly unstable mode. Finally, drawing the stability map of a combustor can reveal domains where the system can undergo a bifurcation, inducing a hysteresis phenomenon. This problem was highlighted for example in a two-cavity combustor where the plenum length was modified and used as a bifurcation parameter [Noiray *et al.* (2008); Boudy *et al.* (2011)].

After this brief introduction on FDF-based stability analysis methodology, it is now worth describing the numerical Helmholtz solver which will be used to perform that nonlinear stability analysis.

7.3 The Helmholtz solver ASVP

Stability analyses based on network of compact elements are difficult to conduct when the combustor geometry features many details. In these situations, one

possibility is to rely on a numerical solver to determine the structure of the acoustic field in the chamber. This can be realized with a Helmholtz solver such as ASVP, a solver developed at CERFACS and Université Montpellier II [Benoit (2005); Sensiau (2008); Gullaud (2010)]. This type of code was developed to determine the solution of the Helmholtz equation in cavities with sophisticated geometries and with complex boundaries. These equations are first presented before introducing the way the boundary conditions are treated. The way unsteady combustion is introduced in the solver is then presented. The method used to solve the eigenvalue problem is finally described.

7.3.1 The Helmholtz equation

The Helmoltz equation is derived from the first principles and rules the propagation of acoustic waves in a quiescent flow. If one considers the decomposition of the different fields as the sum of a steady and a perturbation components, such as $a(\mathbf{x},t) = a_0(\mathbf{x}) + a_1(\mathbf{x},t)$, linearization of mass and momentum balances yields:

$$\frac{\partial \rho_1}{\partial t} + \mathbf{v_1} \cdot \nabla \rho_0 = 0 \tag{7.9}$$

$$\rho_0 \frac{\partial \mathbf{v_1}}{\partial t} = -\nabla p_1 \tag{7.10}$$

where the contributions from viscous stress and body forces are neglected. Neglecting heat diffusion and the dissipation terms in the energy equation also yields:

$$\frac{1}{\gamma}\rho_0 \frac{\partial p_1}{\partial t} - p_0 \frac{\partial \rho_1}{\partial t} - p_0 \mathbf{v_1} \cdot \nabla \rho_0 = \frac{\gamma - 1}{\gamma} \rho_0 \dot{q}_1 \tag{7.11}$$

where $\dot{q}_1$ stands for the heat release rate perturbations and γ denotes the specific heat capacity ratio.

By combining these three equations, one obtains the wave equation describing the propagation of sound waves:

$$\nabla(c_0^2 \nabla p_1) - \frac{\partial^2 p_1}{\partial t^2} = -(\gamma - 1)\frac{\partial \dot{q}_1}{\partial t} \tag{7.12}$$

This equation shows that heat release rate disturbances are the source of sound waves and that propagation may be altered by the gradient of the speed of sound within the flow. By considering acoustic waves developed as normal modes in the frequency domain, one may write:

$$p_1(\mathbf{x},t) = \Re(\widetilde{p_1}(\mathbf{x})e^{-i\omega t}) \tag{7.13}$$
$$\mathbf{v_1}(\mathbf{x},t) = \Re(\widetilde{\mathbf{v}_\mathbf{1}}(\mathbf{x})e^{-i\omega t}) \tag{7.14}$$
$$\rho_1(\mathbf{x},t) = \Re(\widetilde{\rho_1}(\mathbf{x})e^{-i\omega t}) \tag{7.15}$$
$$\dot{q}_1(\mathbf{x},t) = \Re(\widetilde{\dot{q}_1}(\mathbf{x})e^{-i\omega t}) \tag{7.16}$$

This leads to the Helmholtz equation defined in the frequency domain:

$$\nabla(c_0^2\nabla\widetilde{p_1}) + \omega^2\widetilde{p_1} = i\omega(\gamma-1)\widetilde{\dot{q}_1} \tag{7.17}$$

This equation shows that some parameters are necessary to compute the sound pressure distribution. The specific heat capacity ratio must be fixed. It is chosen here as constant and equal to $\gamma = 1.4$. The speed of sound that may deduced from the gas temperature and composition needs also to be specified. On the right hand side, the heat release rate perturbation $\widetilde{\dot{q}_1}$ distribution needs to be fixed. This information can be provided from different sources using numerical simulations, experimental data or theoretical models.

This equation is solved by the AVSP code with a set of possibilities for the acoustic boundary conditions at the system limits [Nicoud *et al.* (2007)].

7.3.2 Boundary and jump conditions

The AVSP solver allows different type of boundary conditions that can be used:

- A pressure node:
  This condition is used to enforce a pressure node at the boundary to simulate an atmospheric outlet for example where:

  $$\widetilde{p_1} = 0 \tag{7.18}$$

- A velocity node:
  This condition is used to enforce a velocity node at the boundary. It simulates the presence of a rigid wall where the acoustic velocity component normal to the wall vanishes. Using the momentum conservation equation, it goes down to a condition on the pressure gradient:

  $$\nabla\widetilde{p_1}\cdot\mathbf{n} = 0 \tag{7.19}$$

  where $\mathbf{n}$ is the unit vector normal to the wall.

- An acoustic impedance condition:
  This condition is used when the system studied is connected to other cavities with a complex acoustic response. In that case, the specific acoustic

impedance of the boundary is defined as the dimensionless ratio between the acoustic pressure and the acoustic velocity component normal to the boundary.

$$Z = \frac{\zeta}{\zeta_0} = \frac{\widetilde{p_1}}{\rho_0 c_0 \widetilde{\mathbf{v}}_\mathbf{1} \cdot \mathbf{n}} \tag{7.20}$$

where $\zeta_0 = \rho_0 c_0$ is the specific impedance of the medium considered. The complex value of the impedance becomes then an input of the code. It can be either provided by an analytical model or by measurements and is usually a function of the angular frequency ω. Knowing the specific impedance, the boundary condition goes down to a mixed condition:

$$\nabla \widetilde{p_1} \cdot \mathbf{n} - \frac{i\omega}{c_0 Z} \widetilde{p_1} = 0 \tag{7.21}$$

- A pressure jump condition:
  This function of the AVSP code allows to link two boundaries by a pressure jump. This type of model may be used for example to describe the response of a small element compact with respect to the acoustic wavelength considered like perforations in a rigid wall without solving either hydrodynamic equations or the Helmholtz equation in the small cavities formed by the perforations. In this case, the continuity of the acoustic volume flowrate is imposed on both sides of the plate with a jump in the pressure acoustic field:

$$\widetilde{\mathbf{v}}_\mathbf{1}^+(\mathbf{x}^+) \cdot \mathbf{n_{pp}} = \widetilde{\mathbf{v}}_\mathbf{1}^-(\mathbf{x}^-) \cdot \mathbf{n_{pp}} = \widetilde{\mathbf{v}}_\mathbf{1}(\mathbf{x}) \cdot \mathbf{n_{pp}} \tag{7.22}$$

$$\left[\widetilde{p_1}^+(\mathbf{x}^+) - \widetilde{p_1}^-(\mathbf{x}^-)\right] = \frac{i\omega\rho_0}{K_a} d^2 \ \widetilde{\mathbf{v}}_\mathbf{1}(\mathbf{x}) \cdot \mathbf{n_{pp}} \tag{7.23}$$

where $\mathbf{x}^-$ is a location on the upstream side of the perforations, $\mathbf{x}^+$ is the corresponding location on the downstream side of the perforations, $\mathbf{n_{pp}}$ is the unit vector normal to the perforated plate, d is the perforated plate hole radius and K_a is the Rayleigh conductivity. Different models can be used for the Rayleigh conductivity depending on the situation investigated.
In [Gullaud *et al.* (2009); Gullaud (2010); Gullaud and Nicoud (2012)], the Rayleigh conductivity K_a was linked to the perforated plate characteristics using the expression derived by Howe (1979). This model enables to reproduce sound production through the perforation traversed by a bias flow in the absence of combustion. This model was for example used to compute the eigenmodes of a full helicopter annular chamber to simulate the presence of multiperforations around the combustion chamber.
In the present work, the presence of small conical flames anchored on the perforated plate prevent the flow from generating vortex shedding

that are responsible for sound emission or attenuation. It thus makes the Howe model not valid for the present configuration. We used here an alternative model to take into account the inertia of the unsteady flow in the small channels and viscous effects. This model leads to the following expression for the pressure jump [Melling (1973)]:

$$\left[\widetilde{p_1^+}(\mathbf{x}^+) - \widetilde{p_1^-}(\mathbf{x}^-)\right] = i\omega\rho_0 h \left[1 + \frac{l_\nu}{a}(1+i)\right] \frac{\widetilde{\mathbf{v_1}}(\mathbf{x}) \cdot \mathbf{n_{pp}}}{\sigma} \tag{7.24}$$

$$= \frac{h\left(1 + \frac{l_\nu}{a}(1+i)\right)}{\sigma} \nabla\widetilde{p}_1(\mathbf{x}) \cdot \mathbf{n_{pp}} \tag{7.25}$$

where h is the perforated plate thickness, $l_\nu = (2\nu/\omega)^{1/2}$ is the viscous acoustic boundary layer thickness in the perforations, ν is the kinematic viscosity, a is the perforated plate hole radius and σ is the perforated plate porosity.

The solutions of the Helmholtz equation coupled with this set of conditions enable to determine the eigenmodes of cavities in the absence of unsteady combustion. Combustion dynamics may now be included as well using the following description.

7.3.3 Unsteady flame modeling

Steady combustion modifies the distribution of the speed of sound in the combustion chamber and thus alters sound propagation. Unsteady flame effects appear in the right hand side of Eq. (7.17) through perturbations in heat release rate $\widetilde{\dot{q}_1}$. These perturbations need to be modeled. It is usually done by linking the heat release rate perturbations to the acoustic velocity perturbations determined at a reference point $\mathbf{x_{ref}}$ upstream of the flame.

$$\nabla(c_0^2\nabla\widetilde{p}_1) + \omega^2\widetilde{p}_1 = i\omega(\gamma-1)\widetilde{\dot{q}_1} \tag{7.26}$$

$$= i\omega(\gamma-1)\left[\frac{\widetilde{\dot{q}_1}/\dot{q}_0}{\widetilde{v}_1(\mathbf{x_{ref}})/v_0(\mathbf{x_{ref}})}\right]\dot{q}_0\frac{\widetilde{v}_1(\mathbf{x_{ref}})}{v_0(\mathbf{x_{ref}})} \tag{7.27}$$

The term between brackets is defined as a local Flame Transfer Function :

$$\mathcal{F}_{\text{loc}}(\omega_r, |\widetilde{v}_1(\mathbf{x_{ref}})/v_0(\mathbf{x_{ref}})|) = \frac{\widetilde{\dot{q}_1}/\dot{q}_0}{\widetilde{v}_1(\mathbf{x_{ref}})/v_0(\mathbf{x_{ref}})} \tag{7.28}$$

while the velocity perturbation at the reference point is related to the pressure gradient at the reference point using the momentum balance :

$$\widetilde{v}_1(\mathbf{x_{ref}}) = \frac{1}{\rho_{\text{ref}} i\omega}\nabla_{\mathbf{ref}}\widetilde{p}_1(\mathbf{x_{ref}}) \cdot \mathbf{n_{ref}} \tag{7.29}$$

where $\mathbf{n_{ref}}$ is a unit vector. Its direction is the same as the velocity component considered for the velocity perturbation determination. In the present case, it corresponds to the axial direction. Equation (7.27) may then be rewritten as:

$$\nabla(c_0^2\nabla\widetilde{p_1}) + \omega^2\widetilde{p_1} = \frac{(\gamma-1)\dot{q}_0}{\rho_{\text{ref}}v_0(\mathbf{x_{ref}})}\mathcal{F}_{\text{loc}}\nabla_{\mathbf{ref}}\widetilde{p_1}(\mathbf{x_{ref}})\cdot\mathbf{n_{ref}} \tag{7.30}$$

The remaining issue is to link the local FTF $\mathcal{F}_{\text{loc}}$ to the global FTF $\mathcal{F}$ that is measured in experiments. The global FTF is constructed with the global heat release rate, which is the local heat release rate integrated over the flame volume V_f:

$$\mathcal{F}(\omega_r, |\widetilde{v}_1(\mathbf{x_{ref}})/v_0(\mathbf{x_{ref}})|) = \frac{\widetilde{\dot{Q}}_1/\dot{Q}_0}{\widetilde{v}_1(\mathbf{x_{ref}})/v_0(\mathbf{x_{ref}})} \tag{7.31}$$

where the integrated heat release rate perturbations $\widetilde{\dot{Q}}_1$ and mean value $\dot{Q}_0$ are defined by the following expressions:

$$\widetilde{\dot{Q}}_1 = \int_{V_F}\widetilde{\dot{q}}_1 dV \tag{7.32}$$

$$\dot{Q}_0 = \int_{V_F}\dot{q}_0 dV \tag{7.33}$$

Starting from Eq. (7.28) that is rewritten as:

$$\widetilde{\dot{q}}_1 = \mathcal{F}_{\text{loc}}(\omega_r, |\widetilde{v}_1(\mathbf{x_{ref}})/v_0(\mathbf{x_{ref}})|)\dot{q}_0\frac{\widetilde{v}_1(\mathbf{x_{ref}})}{v_0(\mathbf{x_{ref}})} \tag{7.34}$$

One finds after integration over the flame volume V_f:

$$\widetilde{\dot{Q}}_1 = \frac{\widetilde{v}_1(\mathbf{x_{ref}})}{v_0(\mathbf{x_{ref}})}\int_{V_f}\mathcal{F}_{\text{loc}}(\omega_r, |\widetilde{v}_1(\mathbf{x_{ref}})/v_0(\mathbf{x_{ref}})|)\dot{q}_0 dV \tag{7.35}$$

For a compact flame, i.e. a flame which dimensions are much smaller than the acoustic wavelength, the local FTF $\mathcal{F}_{\text{loc}}$ can be considered as constant over the flame volume. It then leads to:

$$\widetilde{\dot{Q}}_1 = \mathcal{F}_{\text{loc}}(\omega_r, |\widetilde{v}_1(\mathbf{x_{ref}})/v_0(\mathbf{x_{ref}})|)\frac{\widetilde{v}_1(\mathbf{x_{ref}})}{v_0(\mathbf{x_{ref}})}\int_{V_f}\dot{q}_0 dV \tag{7.36}$$

$$= \mathcal{F}_{\text{loc}}(\omega_r, |\widetilde{v}_1(\mathbf{x_{ref}})/v_0(\mathbf{x_{ref}})|)\frac{\widetilde{v}_1(\mathbf{x_{ref}})}{v_0(\mathbf{x_{ref}})}\dot{Q}_0 \tag{7.37}$$

By comparing Eq. (7.37) with Eq. 7.31, one deduces that:

$$\mathcal{F}_{\text{loc}}(\omega_r, |\widetilde{v}_1(\mathbf{x_{ref}})/v_0(\mathbf{x_{ref}})|) = \mathcal{F}(\omega_r, |\widetilde{v}_1(\mathbf{x_{ref}})/v_0(\mathbf{x_{ref}})|) \tag{7.38}$$

The local and global flame transfer functions are then considered equal for a compact flame. These developments show that in the case of compact flames, the global FTF determined experimentally may directly be used in the numerical solver.

7.3.4 The AVSP solver

The discretization of the Helmholtz equation Eq. (7.30) along with the boundary conditions over an unstructured grid with a finite volume method leads to an eigenvalue problem that reduces to the following form [Nicoud *et al.* (2007)]:

$$\mathcal{A}\mathbf{P} + \omega\mathcal{B}(\omega)\mathbf{P} + \omega^2\mathcal{C}\mathbf{P} = \mathcal{D}(\omega)\mathbf{P} \tag{7.39}$$

where $\mathbf{P}$ is a vector containing the eigenvector values, $\mathcal{A}$ and $\mathcal{C}$ are matrices containing coefficients coming from the discretization of the homogeneous Helmholtz equation, $\mathcal{B}(\omega)$ contains the information about the boundary conditions (see Eqs. (7.18) to (7.25)) and $\mathcal{D}(\omega)$ represents the unsteady flame source term including the FDF.
When using frequency dependent boundary or jump conditions (such as an impedance condition or pressure jump through a perforated plate) or a frequency dependent heat release rate perturbation field (when using a FTF or a FDF for example), the matrices $\mathcal{B}(\omega)$ and $\mathcal{D}(\omega)$ are a function of the angular frequency. This results in a nonlinear eigenvalue problem that is resolved with a fixed-point iterative method [Nicoud *et al.* (2007)]. Equation (7.39) is first reduced to a linear eigenvalue problem that is defined for the k^{th} iteration, by:

$$[\mathcal{A} + \Omega_k\mathcal{B}(\Omega_k)) - \mathcal{D}(\Omega_k)]\mathbf{P} + \omega_k^2\mathcal{C}\mathbf{P} = 0 \tag{7.40}$$

where $\Omega_k = f(\omega_{k-1})$ is a function of the previous iteration result. This linear eigenvalue problem is solved by an Arnoldi iterative method. More details about that procedure can be found in [Sensiau (2008); Nicoud *et al.* (2007); Gullaud (2010)]. The fixed-point method is pursued until the error defined by $\epsilon = |\omega_k - \Omega_k|/\omega_k$ is lower than a specified value, typically of the order of 1%. Two fixed-point algorithms were tested here. The simplest algorithm possible states that $\Omega_k = \omega_{k-1}$. It uses the result from the previous iteration to compute the acoustic variables at the boundaries and to estimate unsteady flame effects. This method is effective when it comes to find attractive fixed points but it is not able to retrieve repulsive fixed points. To tackle that problem, a second algorithm was developed by introducing a relaxation coefficient β and stating

that $\Omega_k = (1-\beta)\omega_{k-1} + \beta\Omega_{k-1}$ [Silva *et al.* (2013)]. When using the relax value $\beta = 0$, this algorithm reduces to the first fixed point method. In cases where the first algorithm does not converge, a value of $\beta = 0.5$ is usually used with the second algorithm.

7.4 Conclusion

The Flame Describing Function (FDF) methodology, an extension of the Flame Transfer Function (FTF) including the perturbation level, has been presented in this chapter. It relies on measuring a set of FTF for different fixed perturbation levels and performing successive quasi-linear analyses for each perturbation level investigated. It enables to retrieve some nonlinear characteristics of thermo-acoustic instabilities such as their limit cycle frequency and amplitude, mode switching and hysteresis phenomena. This nonlinear method will be used in the next chapter in combination with the Helmholtz solver AVSP. This solver was already validated on numerous configurations and successively implemented with numerous features. It is able to take into account complex boundary conditions, to model the response of perforated plates to acoustic disturbances and to include a description of the unsteady heat release rate in the calculations of thermo-acoustic eigenmodes. This type of solver enables to take into account the complexity of practical 3D geometrical configurations. The combination of this numerical tool and the FDF methodology is validated on a generic configuration in the next chapter.

Chapter 8

Validation of the AVSP/FDF methodology

A generic configuration is considered to validate the methodology described in the previous chapter. The system comprises an adjustable injection tube, a perforated plate to stabilize small conical flames and different quartz tubes to confine the flames. This configuration was extensively studied by Boudy (2012) with detailed experiments. A thorough theoretical investigation of the stability of this setup was also conducted with low-order acoustic network models. The corresponding numerical setup is first described in terms of numerical domain, mesh and necessary inputs to the AVSP code. The acoustic eigenmodes of the burner determined experimentally are presented for different feeding manifold lengths and perforated plate thicknesses. They are compared to a numerical estimates by solving the homogeneous Helmholtz equation with the AVSP code. Finally, a nonlinear stability analysis is performed on the same configuration using the AVSP solver in combination with the Flame Describing Function (FDF) methodology. Simulations for different plenum lengths are investigated. Various nonlinear behaviors are predicted and compared to experimental data gathered at limit cycles.

8.1 Experimental configuration

8.1.1 Experimental setup

The burner considered here is sketched in Fig. 8.1. The experimental setup includes a feeding manifold with an adjustable length, a perforated plate on top of which small laminar premixed conical flames are anchored and a confinement quartz tube [Boudy *et al.* (2011); Boudy *et al.* (2011); Boudy (2012)]. Methane and air are premixed upstream of the burner. The mixture is injected in the plenum through six small apertures drilled in the piston head. The mixture then flows through the perforated plate and burns on top of it. The reaction

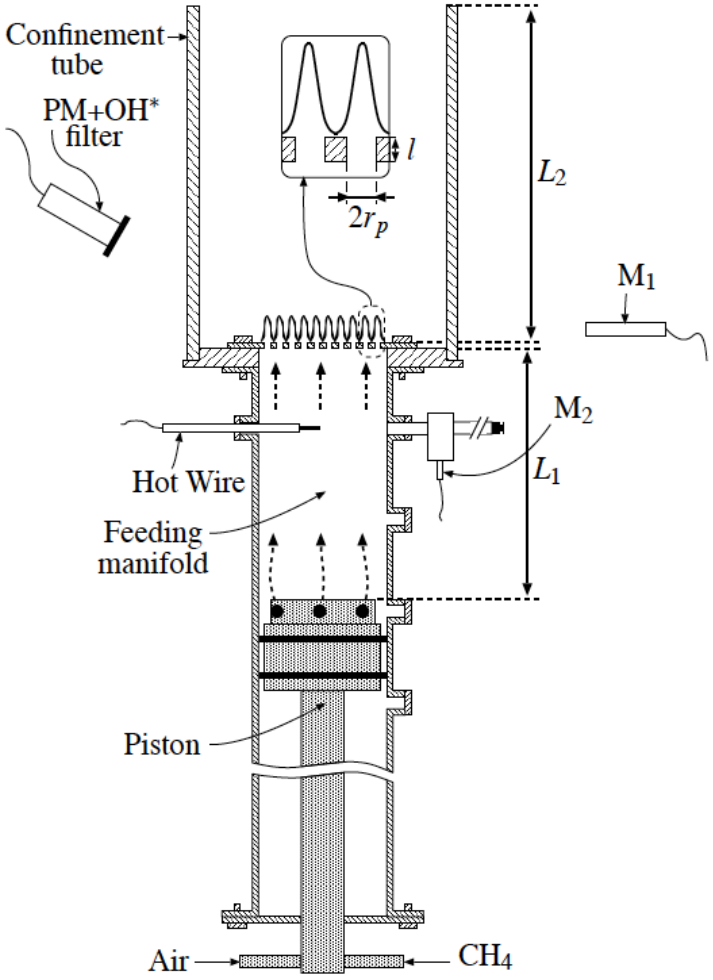

Figure 8.1: *Experimental setup used to characterize self-sustained thermo-acoustic oscillations involving combustion [Boudy (2012)]. Reactants are premixed upstream and a piston is used to modify the feeding manifold length L_1. A perforated plate of thickness l and hole radius r_p acts as an anchoring device for a collection of small laminar conical flames. The flame tube, made out of quartz and of length $L_2 + l$, allows the confinement of the combustion zone.*

forms a collection of small conical flames that are anchored on the perforated plate. A quartz tube is also placed on the top of the perforated plate and acts as a combustion chamber by confining the flames and the burnt gases.
The piston can be moved to adjust the feeding manifold length from $L_1 = 100$ to 750 mm, allowing to vary the acoustic response of the burner. The piston head is flat to provide a nearly perfectly reflective surface to sound waves. More details are given in the next sections on the burner inlet impedance. The plenum diameter is constant and equal to 69 mm. The perforated plate is composed of

421 circular holes with a radius $r_p = 1$ mm that are regularly distributed over a 3 mm square mesh pattern. It results in a global porosity of 0.34. Two plates with different thicknesses are available: $l = 3$ and 15 mm. The combustion chamber is a 65 mm radius quartz tube with different lengths: 100, 200, 300 and 400 mm. The investigation is conducted here only with the 100 mm tube. In these experiments, the mass flow rate and the equivalence ratio are fixed to $\dot{m} = 4.71$ g.s^{-1} and $\phi = 1.03$, resulting in a thermal power of 13.3 kW. The quartz tube outer temperature was measured and averaged over its length to yield an estimation of the temperature in the combustion chamber. It was found that $T_b = 900, 1100, 1300$ and 1400 K for the flame tube of length 100, 200, 300 and 400 mm, respectively [Boudy (2012)].
The thermo-acoustic behavior of the burner was characterized in terms of pressure, heat release rate and velocity records at limit cycles. These measurements were performed by F. Boudy and are reported in details in his Ph.D. thesis [Boudy (2012)]. The plenum velocity is determined by a hot wire anemometer and the heat release rate was deduced from a photomultiplier. The pressure signals are measured by three microphones, located in the plenum, on the combustion chamber backplane and outside of the combustion chamber. All signals were recorded simultaneously at limit cycles of unstable regimes. These data will be compared to numerical results in the next sections in terms of limit cycle frequencies and amplitudes.

8.2 Numerical setup

The geometrical configuration explored by F. Boudy was first included in a design software and meshed with tetrahedral elements. An example of one of the geometries investigated numerically is presented in Fig. 8.2. It features two cavities corresponding to the plenum and the combustion chamber. These domains are separated but their boundaries may communicate. The geometrical details of the piston (ring cavity, injection holes, airtight joint...) are not included in the numerical design and the plenum is thus represented by a cylindrical manifold. The plenum upper boundary represents the perforated plate lower side which is exchanging information with the corresponding boundary at the bottom of the combustion chamber. The combustion chamber is also modeled with a cylindrical domain, except at its bottom where a cylindrical zone of height $l = 3$ mm and of diameter 78 mm was removed to model the presence of a protruding perforated plate. The numerical domain thus includes the ring cavity formed between the perforated plate and the flame tube as int he experiments. An example of mesh is shown in Fig. 8.2-right. All the meshes used are composed of about $100,000$ nodes. They are however not distributed regularly over the whole numerical domain. The region above the perforated plate has been refined to easily introduce the distribution of heat release rate. As explained in Chapter 7, the AVSP solver needs as an input the distribution

Figure 8.2: *Numerical domain for $L_1 = 0.12\ m$, $L_2 = 0.088\ m$ and $l = 0.003\ m$.* **Left:** *Half of the numerical domain.* **Middle:** *2D vertical slice of the numerical domain.* **Right:** *The mesh is superimposed on a fourth of the numerical domain.*

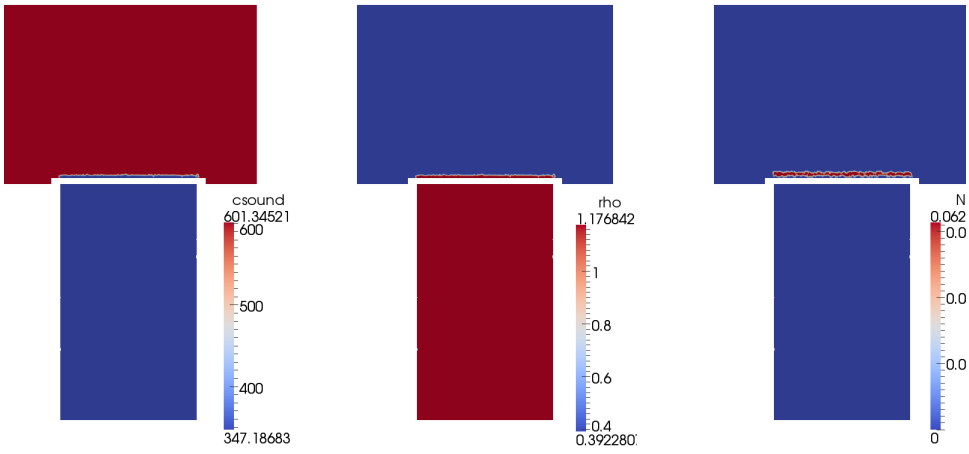

Figure 8.3: **Left:** *Field of the speed of sound modeling effects of steady combustion (in $m.s^{-1}$).* **Middle:** *Corresponding field of density (in $g.m^{-3}$).* **Right:** *Field of magnitude of the source term appearing in the right-hand side of the Eq. (7.17) corresponding to a compact flame location above the perforated plate.*

of the speed of sound, density and heat release rate in the entire numerical domain. Two different fields for the speed of sound are used here. A constant field $c_0 = 347$ m.s^{-1}, corresponding to a temperature of $T_u = 300$ K, is first used to retrieve the acoustic eigenmodes of the burner without combustion. A different speed of sound field was used to compute the eigenmodes of the burner when combustion is considered as shown in Fig.8.3-left. It includes a region where $c_0 = 601$ m.s^{-1}, corresponding to a burnt gas temperature $T_b = 900$ K uniformly distributed over the tube length $L_2 + l = 0.091$ m. It is important to mention that a small region (about 1 mm high) over the perforated plate has been kept at $T_u = 300$ K, to enforce the correct pressure drop through the perforated plate and to model the presence of fresh gases between the flame and the downstream side of the perforated plate. The corresponding density field is also shown in Fig. 8.3-center. This field follows the temperature distribution defined by the fresh and burnt gas temperatures. The flame location is highlighted by a jump in density above the perforated plate.
The flame region lies here above the perforated plate, as indicated in Fig. 8.3-right. The heat release rate is distributed over a cylindrical zone, of radius $R_f = 345$ mm and height $l = 2$ mm. This zone is located 1 mm above the perforated plate. Heat release rate perturbations are distributed uniformly over that volume. The flame being compact with respect to the acoustic wavelengths considered in this work, the real shape of the flame does not need to be reproduced with accuracy to retrieve the thermo-acoustic instability characteristics.

8.3 Flame Describing Function and boundaries conditions

Several inputs are needed to properly describe the thermo-acoustic properties observed with this combustor [Boudy (2012)]. The main elements are:

- A Flame Transfer Function or a Flame Describing Function to represent the flame response to flow perturbations.
- A reflection coefficient representing the piston head as a non-perfectly reflective surface.
- A reflection coefficient modeling acoustic losses and sound radiation at the flame tube outlet.
- An unsteady pressure drop associated to the unsteady flow going through the perforated plate.

These elements were shown to have a significant influence on the acoustic response of the combustor and its nonlinear dynamics [Boudy (2012)]. The FDF was measured by Boudy (2012) on a separate experiment. This burner features a smaller diameter with a collection of conical flames that are anchored on a 129 hole perforated plate, all the other parameters remaining the same.

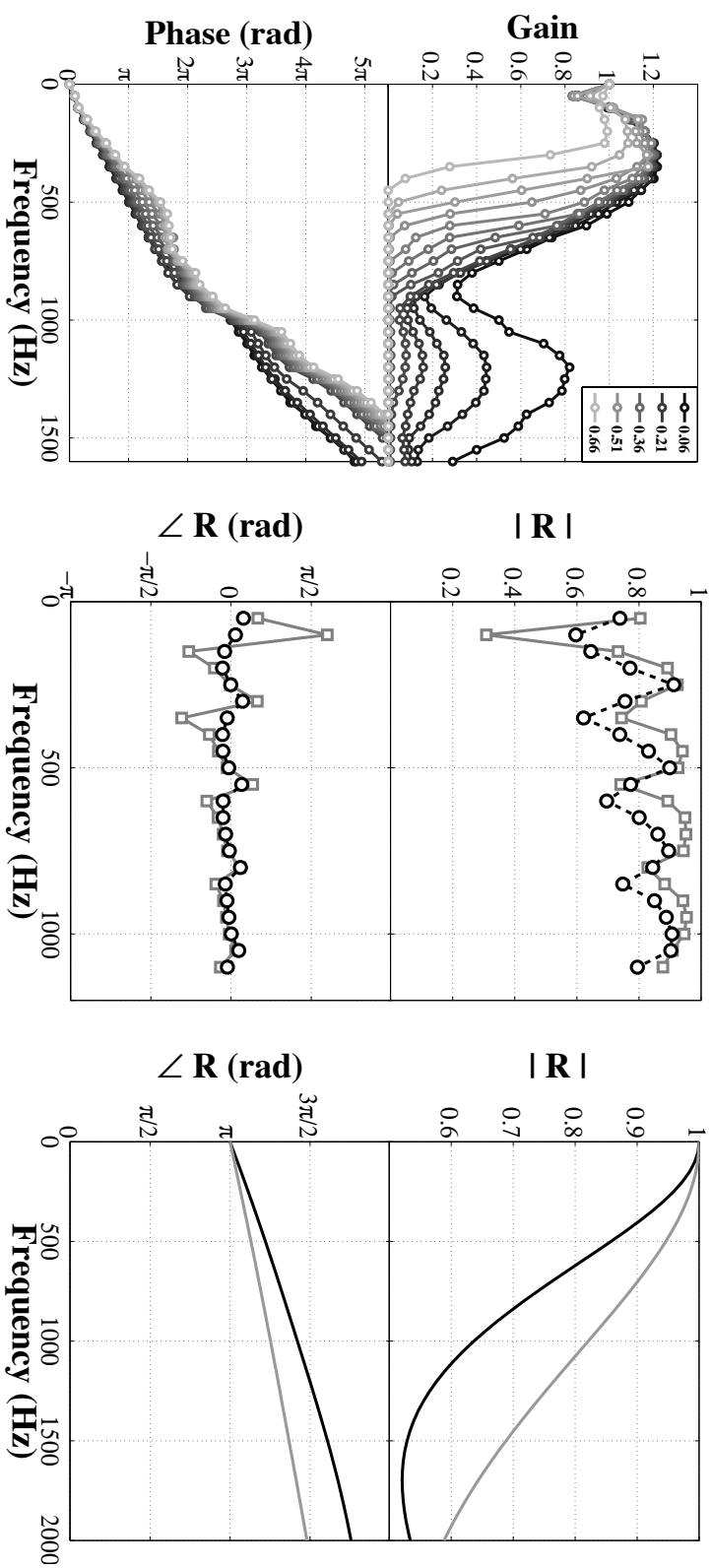

Figure 8.4: **(left)** *Flame Describing Function gain (top) and phase lag (bottom) of a collection of small conical flames anchored on a perforated plate of thickness $l = 3$ mm, as a function of the frequency for increasing perturbation levels. The velocity perturbation level is varied continuously from $v_1^{\mathrm{rms}}/v_0 = 0.06$ (black line) to $v_1^{\mathrm{rms}}/v_0 = 0.66$ (light gray line) with a constant increment of 0.05. The perturbation levels v_1^{rms}/v_0 are indicated in the legend only for five curves, including the highest and lowest perturbation level values.* **(center)** *Piston-head reflection coefficient determined experimentally with flow (black dashed line with ○) and without flow (grey line with □).* **(right)** *Theoretical outlet reflection coefficient of an unflanged open pipe, for $T_b = 300$ K (black line) and $T_b = 900$ K (gray line).*

These measurements are plotted in Fig. 8.4-left for a plate thickness $l = 3$ mm as a function of the acoustic forcing frequency up to 1600 Hz. The FDF gain exhibits a low-pass filter behavior with several humps. The FDF phase lag increases almost linearly with the frequency. These features are commonly observed for single [Ducruix *et al.* (2000); Schuller *et al.* (2002); Schuller *et al.* (2003a); Kornilov *et al.* (2007); Cuquel *et al.* (2013b)] and multiple [Noiray *et al.* (2006b); Noiray *et al.* (2008); Kornilov *et al.* (2009); Kornilov *et al.* (2009)] conical flame responses to flow perturbations. The FDF also features changes with the velocity perturbation level. The phase lag is shifted when the amplitude increases and the gain drops. These modifications need to be considered to predict the limit cycles reached by thermo-acoustic instabilities.

The reflection coefficient of the piston head was also characterized on a separate experiment [Boudy (2012)] and is plotted in Fig. 8.4-center. The reflection coefficient with (black dashed line with circles) and without (gray line with square signs) flow exhibits strong deviations from a perfectly reflective surface characterized by $|R| = 1$ and $\angle(R) = 0$, especially in the low frequency range.

The reflection coefficient of the confinement tube outlet is modeled here by a radiation impedance for an unflanged open pipe [Levine and Schwinger (1948); Rienstra and Hirschberg (2012)]:

$$Z(\omega) = \frac{1}{4}\left(\frac{\omega R}{c}\right)^2 - i0.61\frac{\omega R}{c} \tag{8.1}$$

The real part describes the acoustic power radiated out of the tube and the imaginary part represents the inertia of the flow in the region near the tube outlet. This last contribution is often modeled by an end correction, taken here as $\delta = 0.61R$, that represents the location of the pressure node downstream of the tube exit. The resulting impedance is plotted in Fig. 8.4-right for different gas temperatures corresponding to the case without combustion ($T_b = 300$) and the case with combustion ($T_b = 900$) for $L_2 = 0.088$ m. This figure reveals that, in the frequency range of interest, the reflection coefficient strongly differs from an acoustic pressure node, for which $|R| = 1$ and $\angle(R) = \pi$.

8.4 Determination of the acoustic eigenmodes

Simulations with AVSP are first conducted in the absence of combustion. The objective is to determine the acoustic eigenmodes of the numerical domain simulated and compare these results with measurements. An acoustic network analysis is also performed to compare the numerical and experimental data with results from a low-order acoustic model (LOM). These results were obtained with the code developed by F. Boudy in his Ph.D. thesis [Boudy (2012)].

Burner configuration	Experiments	Δf	α
$L_1 = 0.12$ m	462 Hz	4 Hz	-12.6 s^{-1}
$l = 0.003$ m	882 Hz	42 Hz	-131.9 s^{-1}
$L_1 = 0.12$ m	456 Hz	8.5 Hz	-26.7 s^{-1}
$l = 0.015$ m	882 Hz	38 Hz	-119.4 s^{-1}
$L_1 = 0.35$ m	225 Hz	8 Hz	-25.1 s^{-1}
$l = 0.003$ m	604 Hz	12 Hz	-37.7 s^{-1}
	792 Hz	30 Hz	-94.2 s^{-1}
	1190 Hz	32 Hz	-100.5 s^{-1}
$L_1 = 0.35$ m	221 Hz	8.5 Hz	-26.7 s^{-1}
$l = 0.015$ m	604 Hz	11 Hz	-34.6 s^{-1}
	792 Hz	30 Hz	-94.2 s^{-1}
	1155 Hz	20 Hz	-62.8 s^{-1}

Table 8.1: *Measurements of the first acoustic eigenfrequencies and damping rates for the different geometrical configurations investigated.*

8.4.1 Experimental determination

The burner presented in Fig. 8.1 was equipped with a loudspeaker and two microphones to determine the eigenmodes for two different plenum lengths $L_1 = 120$ and 350 mm, and for two plate thicknesses $l = 3$ and 15 mm. In these experiments, the loudspeaker is placed outside the burner, close to the confinement tube exit. A reference microphone is located between the loudspeaker and the burner exit to measure the external acoustic modulation p_e. The second microphone is installed at the bottom of the plenum to measure the internal acoustic pressure fluctuation p_i inside the burner plenum. The frequency response of the system is investigated by determining the quantity $(\tilde{p_i}/\tilde{p_e})^2$ where $\tilde{(.)}$ denotes the Fourier transform of the signal. This response is a function of the excitation frequency and exhibits strong peaks when resonance is reached. The frequency of these peaks depends on the burner dimensions as shown in Fig. 8.5. The measured frequencies of the first eigenmodes are summed up in Table 8.1 for all the geometrical configurations investigated. The resonant frequencies are smaller for longer plenum lengths. For a fixed plenum length, the resonance frequencies are weakly impacted by the perforated plate thickness. The peak frequency decreases by only a few Hertz when the plate thickness is increased for the configurations considered here.

The damping rate of the acoustic system can also be determined by this method. It is done here by assuming that the system behaves like a second order oscillator with a forcing term. The damping rate can then be deduced from a measurement of the quality factor $Q = f/\Delta f$ that is defined as the ratio between the resonance frequency f and the frequency width Δf of the resonance curve taken at half height of the resonance peak [Durox *et al.* (2009); Palies

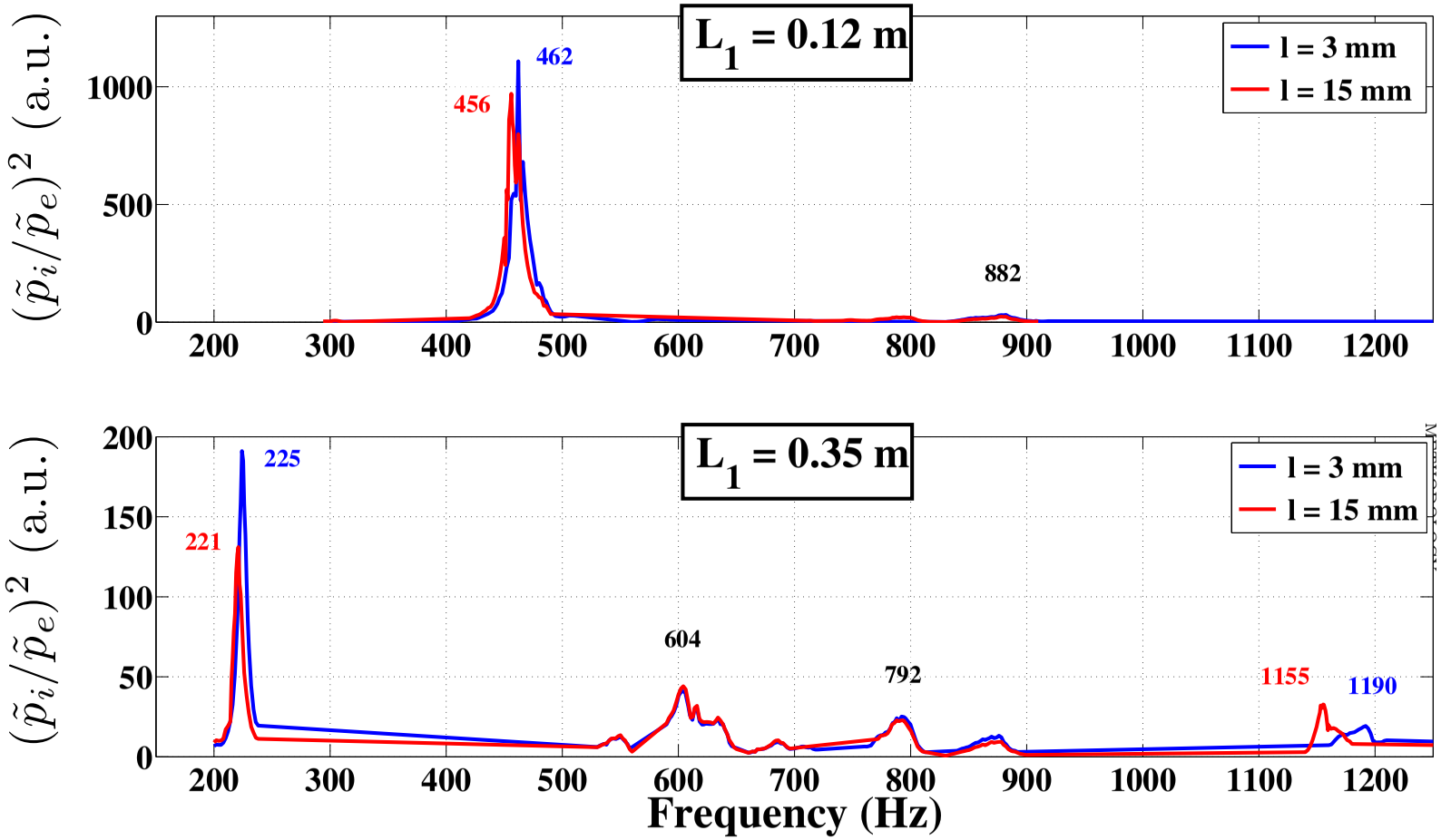

Figure 8.5: *Acoustic eigenmode measurements. Plenum length:* $L_1 = 0.12$ *m (top figure).* $L_1 = 0.35$ *m (bottom figure). Plate thickness:* $l = 3$ *mm (blue line).* $l = 15$ *mm (red line).*

Plenum length	Exp.	AVSP	LOM
$L_1 = 0.12$ m	462 Hz	472 Hz	482 Hz
	882 Hz	881 Hz	909 Hz
$L_1 = 0.35$ m	225 Hz	219 Hz	228 Hz
	604 Hz	608 Hz	609 Hz
	792 Hz	814 Hz	844 Hz
	1190 Hz	1194 Hz	1225 Hz

Table 8.2: *Acoustic eigenmodes of the combustor determined experimentally, numerically with the AVSP solver and with a low-order model (LOM). In the simulations, the following temperatures were considered:* $T_u = T_b = 300$ *K.* $l = 3$ *mm.*

(2010); Palies *et al.* (2011)]. The damping rate α is thus defined by:

$$\alpha = -\pi \Delta f \tag{8.2}$$

Measurements of Δf and α are summarized in Table 8.1. The damping rate of the system strongly increases as the resonance frequency increases.

8.4.2 Numerical determination

Simulations with AVSP are carried out here to determine the acoustic eigenmodes of the configuration investigated without combustion. The acoustic eigenfrequencies were determined numerically with a constant temperature of $T_u = T_b = 300$ K in the whole combustor. This temperature was also used to determine the corresponding outlet boundary condition fixed by Eq. (8.1) which is plotted in Fig. 8.4-right with a black line. The piston reflection coefficient measured without flow is used as an inlet boundary condition (grey line in Fig. 8.4-center) in these simulations. The numerical results from these simulations and the predictions from the LOM are compared to the experimental data in Table 8.2 for two different geometrical configurations corresponding to two plenum lengths $L_1 = 0.12$ and 0.35 m. The calculated eigenfrequencies of the combustor match well those measured, with relative differences lower than 3 %. The numerical results obtained with AVSP also exhibit an improvement compared to LOM results.

8.5 Nonlinear stability analysis

Simulations with AVSP are now carried out with unsteady combustion. A temperature of $T_u = 300$ K is considered in the plenum and the burnt gas temperature in the confinement tube is set to $T_b = 900$ K (see Fig. 8.3-center for the corresponding mixture density field.). This last temperature was also used to determine the outlet boundary condition from Eq. (8.1) which is plotted in

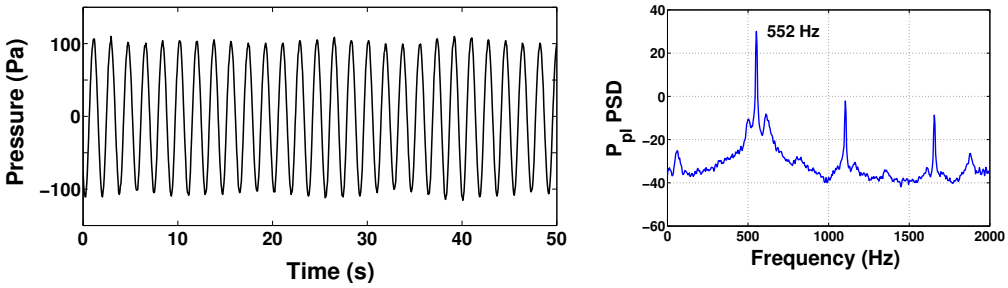

Figure 8.6: Left: *Pressure evolution in the plenum at limit cycle.* **Right:** *Power spectral density of the pressure signal measured at limit cycle.* $L_1 = 0.12$ *m and* $l = 0.003$ *m.*

Fig. 8.4-right with a grey line. The piston reflection coefficient measured with flow is used as an inlet boundary condition (black line in Fig. 8.4-center). The Flame Describing Function (FDF) measured on a perforated plate featuring a thickness $h = 3$ mm is used in this section to model the nonlinear response of the conical flames to acoustic perturbations. The nonlinear stability analysis described in the previous chapter is carried out by calculations with the thirteen FTF composing that FDF (see Fig. 8.4-left). Results are examined for increasing plenum lengths.

8.5.1 First case: $L_1 = 0.12$ m

A first geometrical configuration is considered here for a plenum length of $L_1 = 0.12$ m with a perforated plate of thickness $l = 0.003$ m. Experimental data reveal that the system gets unstable and reaches a limit cycle with a constant amplitude (Fig. 8.6-left) and a frequency of 552 Hz (Fig. 8.6-right). Calculations with the LOM indicate that only the first acoustic mode of the plenum is linearly unstable, *i.e.* this mode features a positive growth rate $\omega_i > 0$ for small amplitude disturbances. The LOM further predicts that the system reaches a limit cycle when $\omega_i = 0$ with a frequency equal to $f = 550$ Hz and an amplitude equal to $v_1^{\text{rms}}/v_0 = 0.55$ as indicated by Fig. 8.7-left (black solid line). Results from AVSP simulations are presented in Fig. 8.7-left (circles) in terms of the first eigenfrequency f and its growth rate ω_i as a function of the perturbation level v_1^{rms}/v_0. This mode is linearly unstable ($\omega_i > 0$ for small perturbation levels) but the growth rate decreases as the perturbation level increases until it reaches a zero value when $v_1^{\text{rms}}/v_0 = 0.55$. This value determines the limit cycle amplitude and allows one to read the predicted limit cycle frequency that is roughly equal to 550 Hz. Results from AVSP simulations (black circles) are very close to LOM predictions (black line), especially when considering the frequency evolution. For small perturbation levels, a difference between numerical and LOM results can be observed on the growth rate evolution. However, it does not impact the limit cycle amplitude predic-

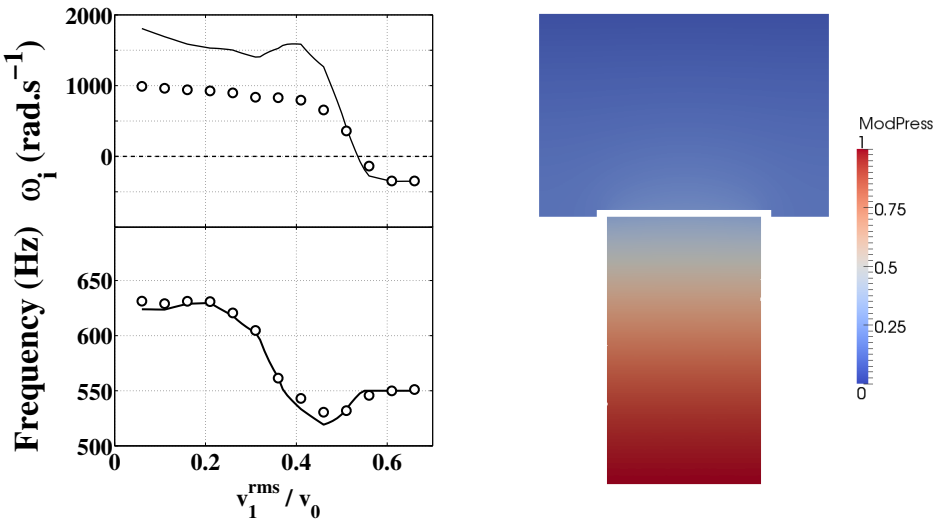

Figure 8.7: Left: *Oscillation frequency f and growth rate ω_i are plotted as a function of the perturbation level v_1^{rms}/v_0. Numerical results from AVSP ($\circ$) are compared to results from LOM (-).* **Right:** *Pressure modulus distribution calculated by AVSP indicating the structure of the corresponding eigenmode at limit cycle. $L_1 = 0.12$ m and $l = 0.003$ m.*

tion. Numerical simulations with AVSP also yield the corresponding eigenmode structure as shown in Fig. 8.7-right. The mode structure corresponds here to the 1/4-wavelength eigenmode of the combustor.

The first other eigenmodes of the combustor were also determined with the AVSP solver. Results are not presented here, but these modes were all found stable over the perturbation level range investigated. This is in agreement with experimental data and with LOM results. The 1/4-wavelength eigenmode of the combustor is the only unstable mode when the plenum length is set to $L_1 = 0.12$ m.

8.5.2 Second case: $L_1 = 0.35$ m

A second geometrical configuration is investigated for a longer plenum when $L_1 = 0.35$ m. Experimental data reveal that the system gets unstable and reaches a limit cycle with a constant amplitude of $v_1^{\text{rms}}/v_0 = 0.4$ (Fig. 8.8-left) and a frequency of 676 Hz (Fig. 8.8-right). Simulations with AVSP are presented in Fig. 8.9 as circles. A mode with a frequency of about 660 Hz is found unstable with a positive growth rate ($\omega_i > 0$) for small perturbation levels. This mode is linearly unstable. The growth rate decreases as the perturbation level increases until reaching a zero value for a perturbation level of

about $v_1^{\text{rms}}/v_0 = 0.4$. This value determines the limit cycle amplitude. When the oscillation amplitude increases, the oscillation frequency is modified but reaches a value at limit cycle close to the one observed in experiments. It is worth noticing that results from AVSP simulations (blue circles) are close to the LOM predictions (blue line). A comparison between the different predictions and experimental data measured at the limit cycle (red squares) show that the AVSP solver retrieves correctly the limit cycle found experimentally at $v_1^{\text{rms}}/v_0 = 0.4$ and $f = 676$ Hz. The corresponding calculated modal structure, presented in Fig. 8.9-right, corresponds to the 3/4-wavelength eigenmode

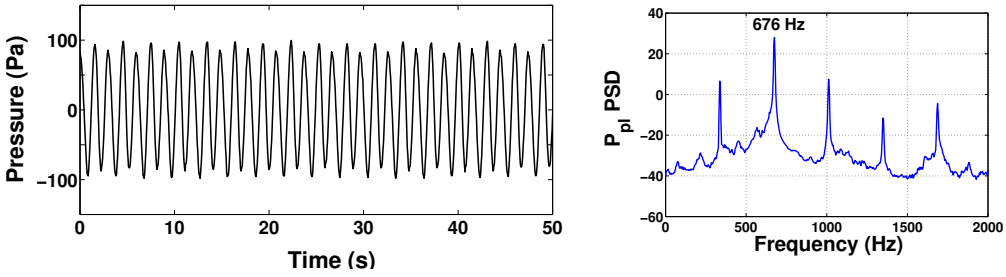

Figure 8.8: Left: *Pressure evolution in the plenum at limit cycle.* **Right:** *Power spectral density of the pressure signal measured at limit cycle.* $L_1 = 0.35$ *m and* $l = 0.003$ *m.*

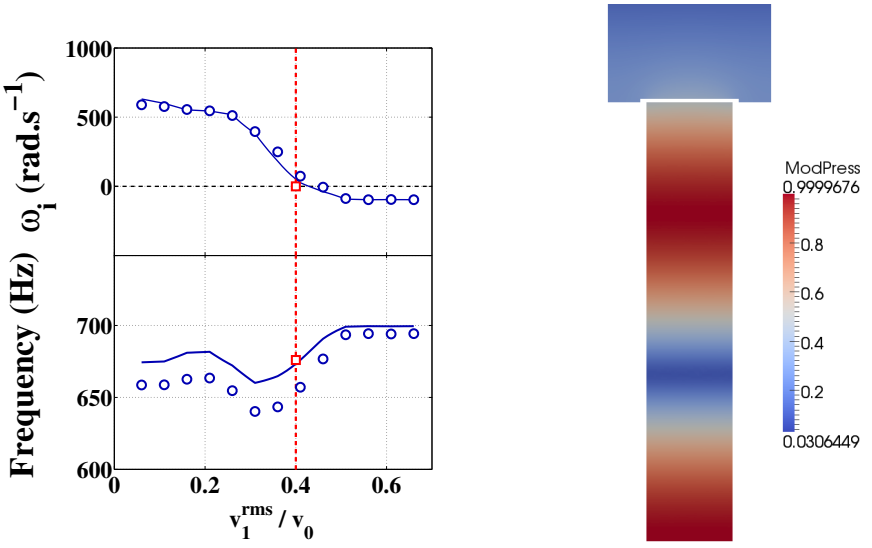

Figure 8.9: Left: *Oscillation frequency* f *and growth rate* ω_i *are plotted as a function of the perturbation level* v_1^{rms}/v_0*. Numerical results from AVSP (*$\circ$*) and from LOM (-) are compared to experimental data (*$\square$*) from [Boudy et al. (2011)].* **Right:** *Pressure modulus distribution calculated by AVSP indicating the structure of the corresponding eigenmode at limit cycle.* $L_1 = 0.35$ *m and* $l = 0.003$ *m.*

of the combustor.

The two previous cases investigated demonstrate that AVSP combined with an FDF and appropriate boundary conditions may be used confidently to analyze the dynamics of linearly unstable modes for small disturbances to a finite amplitude level at limit cycles. These validations were conducted with the 1/4-wavelength and the 3/4-wavelength eigenmodes of the combustor. The last case investigated envisages a configuration featuring a nonlinearly unstable mode.

8.5.3 Third case: $L_1 = 0.54$ m

A third validation is carried out with a different geometrical configuration for a longer plenum length $L_1 = 0.54$ m. Experimental data reveal that the system gets unstable and reaches a limit cycle with a constant amplitude of $v_1^{\text{rms}}/v_0 = 0.7$ (Fig. 8.8-left) and a frequency of 472 Hz (Fig. 8.8-right). Analysis of the transient signal during growth of the instability reveals a mode switching phenomenon occurring shortly after ignition. The system is unstable and oscillate first with a frequency equal to 750 Hz, but it rapidly switches to a lower frequency equal to 472 Hz (see Fig. 8.11-top). By filtering the dimensionless velocity signal $v_1(t)/v_0$ with a 4^{th}-order passband Butterworth filter around 750 Hz, it is possible to isolate the onset and the decrease of the initial high frequency instability that is plotted in Fig. 8.11-bottom. The maximum amplitude reached by this mode can thus be determined and is roughly equal to $|v_1/v_0| = 0.45$ corresponding to a perturbation level $v_1^{\text{rms}}/v_0 = 0.32$.

This transient behavior was already explored by Boudy *et al.* (2011). The same simulations are performed here, the only difference lying in the use of complex boundary conditions instead of real reflection coefficients. Results from LOM and AVSP simulations are compared to experimental data in the following. The third mode is first considered and the second mode is investigated later.

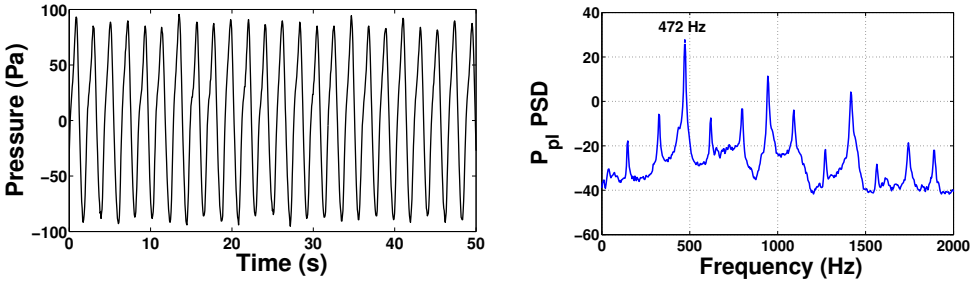

Figure 8.10: Left: *Pressure evolution in the plenum at limit cycle.* **Right:** *Power spectral density of the pressure signal measured at limit cycle.* $L_1 = 0.54$ *m.* $l = 0.003$ *m.*

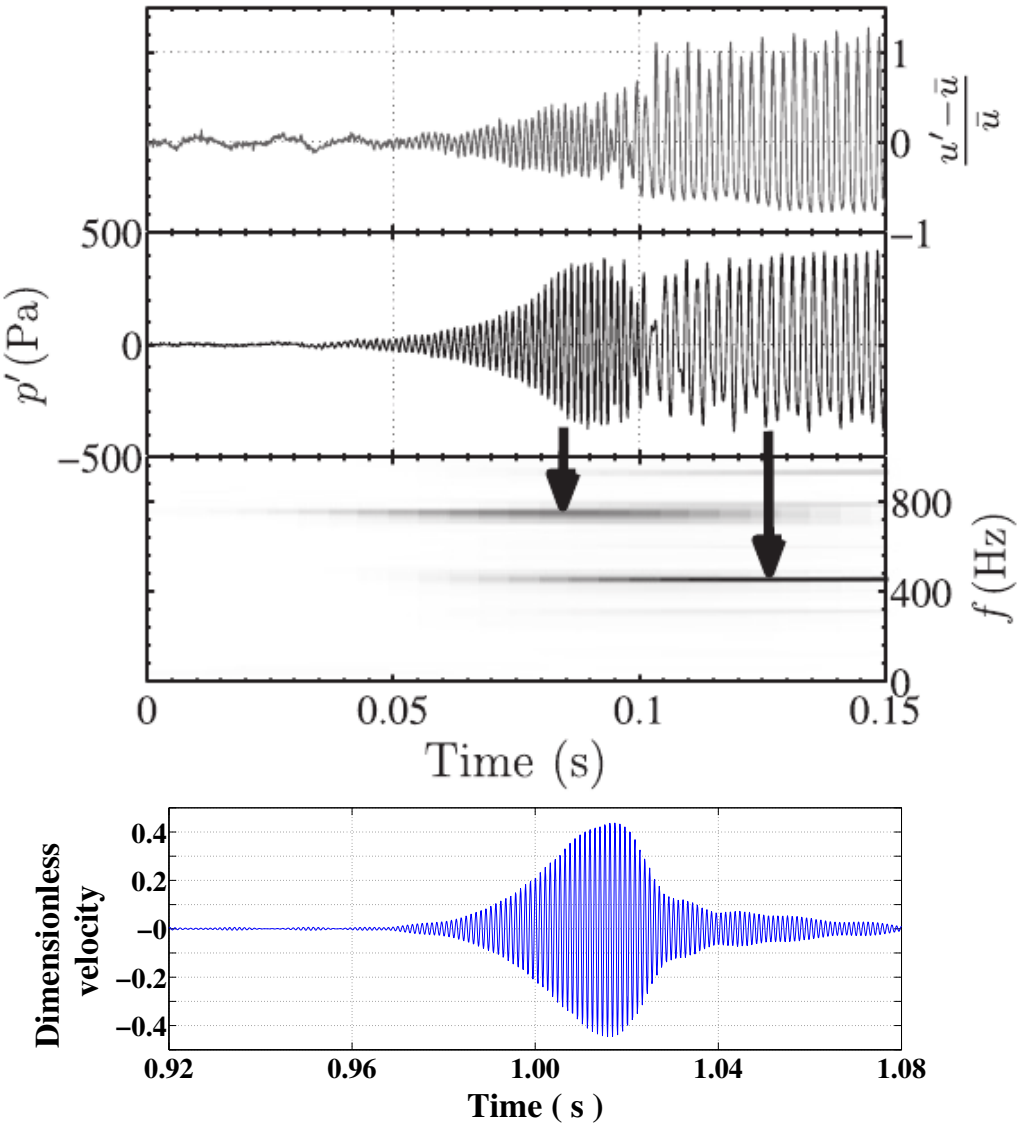

Figure 8.11: Top: *Temporal signals of the self-sustained instability. The two upper plots show the normalized velocity and the pressure oscillations in the plenum. The lower plot corresponds to the short-time Fourier spectral density of the pressure signal. Reproduced from Boudy* et al. *(2011).* **Bottom:** *Dimensionless velocity perturbation signal filtered around the high frequency of the instability.* $L_1 = 0.54\ m.$ $l = 0.003\ m.$

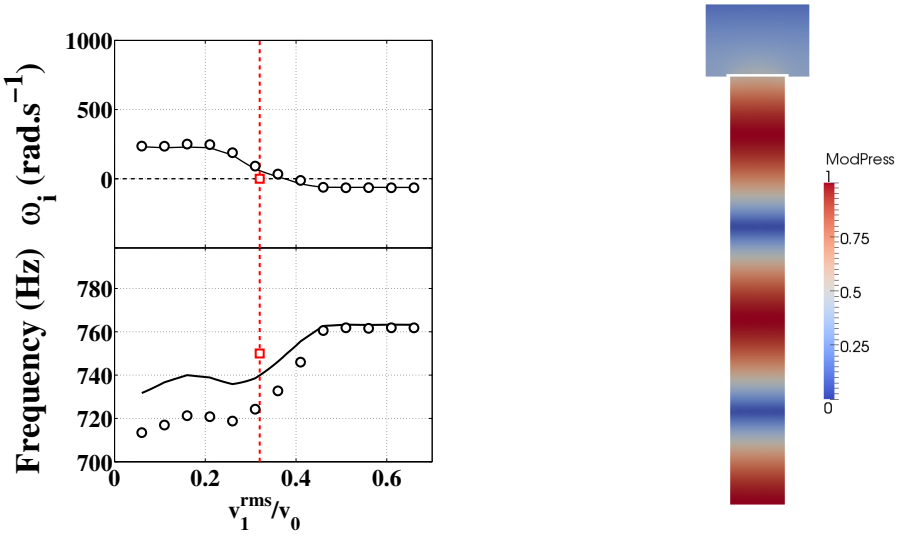

Figure 8.12: Left: *Oscillation frequency f and growth rate ω_i of the third eigenmode are plotted as a function of the perturbation level v_1^{rms}/v_0. Numerical results from AVSP (○) and from LOM (-) are compared to experimental data (□) from Boudy et al. (2011).* **Right:** *Pressure modulus distribution calculated by AVSP indicating the structure of the third eigenmode at limit cycle. $L_1 = 0.54$ m and $l = 0.003$ m.*

Simulations with the LOM indicate that the third acoustic mode of the plenum is linearly unstable ($\omega_i > 0$ for small perturbation levels). The oscillation frequency and growth rate of this mode are plotted in Fig. 8.12. This growth rate rapidly decreases to reach $\omega_i = 0$ when $v_1^{\text{rms}}/v_0 = 0.35$. Results from the AVSP simulations are plotted in Fig. 8.12 as circles for the third eigenmode of the combustor. These results show that this mode is linearly unstable and that the instability grows until the perturbation amplitude reaches a value of $v_1^{\text{rms}}/v_0 = 0.35$. If the instability amplitude is further increased, the growth rate becomes negative and higher fluctuation levels cannot be sustained for this mode. The amplitude of the third mode determined when $\omega_i = 0$ represents the maximum amplitude reached by this mode, before its amplitude decreases as the perturbation level increases when the system switches to another mode. In Fig. 8.12 -left, results from AVSP are compared to LOM predictions and experimental data. Predictions from AVSP or LOM are very close, with differences limited to 20 Hz. The measurements presented in Fig. 8.12-left are determined from the velocity signal plotted in Fig. 8.11-bottom. These experimental data match predictions very closely. The value obtained with AVSP and LOM $v_1^{\text{rms}}/v_0 = 0.35$ is in good agreement with the one measured $v_1^{\text{rms}}/v_0 = 0.32$. The simulations with AVSP also yield the eigenmode spatial structure. The initial eigenmode appearing around 750 Hz corresponds to the 5/4-wavelength

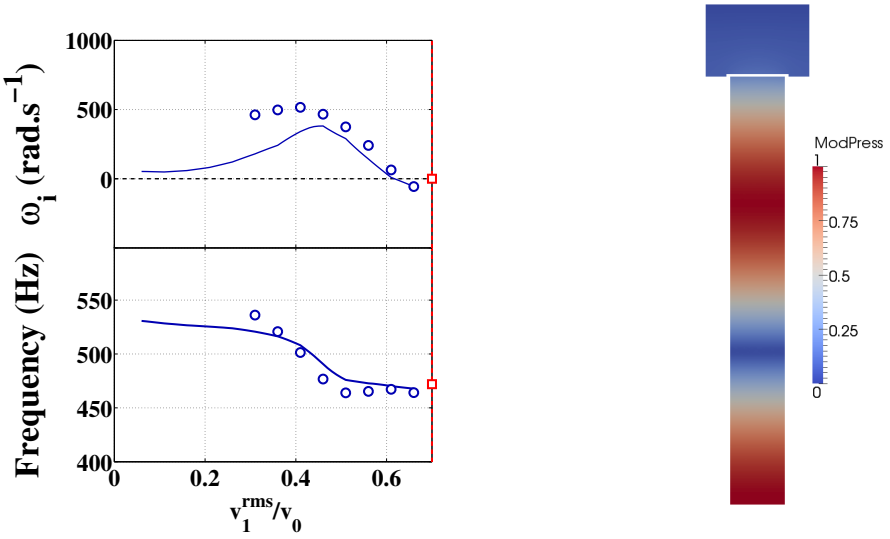

Figure 8.13: Left: *Oscillation frequency f and growth rate ω_i of the second eigenmode are plotted as a function of the perturbation level v_1^{rms}/v_0. Numerical results from AVSP ($\circ$) and from LOM (-) are compared to experimental data ($\square$) from Boudy et al. (2011).* **Right:** *Pressure modulus distribution calculated by AVSP indicating the structure of the second eigenmode at limit cycle. $L_1 = 0.54$ m and $l = 0.003$ m.*

eigenmode of the combustor and is represented in Fig. 8.12-right.

Considering now the results for the second mode in Fig. 8.13, simulations with the LOM indicate that this mode is linearly unstable but with a growth rate much smaller than the one of the third mode for small perturbation levels. The growth rate of the second mode increases as the perturbation level increases before decreasing towards the limit cycle condition $\omega_i = 0$. The LOM thus predicts that the system reaches a limit cycle with a frequency equal to $f = 470$ Hz and an amplitude equal to $v_1^{\text{rms}}/v_0 = 0.6$. Simulations with ASVP are shown as circles in Fig. 8.13 and indicate that the second mode is triggered only for perturbation levels larger than $v_1^{\text{rms}}/v_0 = 0.3$. This mode is thus nonlinearly unstable in the intermediate range of perturbation levels. Its growth rate decreases for higher oscillation amplitudes and reaches zero when $v_1^{\text{rms}}/v_0 = 0.65$, yielding the limit cycle amplitude predicted by these simulations. Oscillations at the limit cycle that have a frequency of about 470 Hz are associated to the 3/4-wavelength eigenmode of the combustor, as shown in Fig.8.13-right.

Predictions for the second mode and experimental data are compared in Fig. 8.13-left. A first difference can be observed between predictions from AVSP and LOM. For small perturbation amplitudes, calculations from the LOM indicate a very small growth rate but the AVSP solver does not detect any mode.

At intermediate perturbation levels comprised between $v_1^{\text{rms}}/v_0 = 0.3$ and $v_1^{\text{rms}}/v_0 = 0.5$, the growth rates calculated with the LOM and AVSP slightly differ, but the oscillation frequencies match well. At high perturbation levels, predictions from AVSP and LOM collapse leading to the same limit cycle with a frequency of 460 Hz and an amplitude $v_1^{\text{rms}}/v_0 = 0.65$. The limit cycle frequency observed in experiments is well retrieved. The limit cycle amplitude is however slightly underestimated compared to the measured one $v_1^{\text{rms}}/v_0 = 0.7$.

Boudy *et al.* (2011) studied the same case where the third mode oscillation starts to grow and then naturally switches to the second mode oscillation for a certain oscillation threshold level. This phenomenon was well retrieved by the LOM predictions. By comparing the growth rate evolutions in Figs. 8.12 and 8.13, the AVSP results show that the third mode is linearly unstable. The situation changes for a certain threshold level when the oscillation reaches an amplitude $v_1^{\text{rms}}/v_0 = 0.35$. At that amplitude, the growth rate of the third mode drops to zero, meaning that this mode has reached a maximum amplitude. Simultaneously, the growth rate of the second mode features a large positive value for this perturbation level. The second mode amplitude thus keeps increasing. At higher amplitudes, the growth rate of the third mode becomes negative and this mode is damped. Therefore, only the second mode remains because its growth rate remains positive up to a larger perturbation amplitude $v_1^{\text{rms}}/v_0 = 0.65$. This mode switching phenomenon is thus retrieved by AVSP even though slight differences were observed in the way the system reaches the limit cycle.

8.6 Conclusion

A nonlinear stability analysis combining the AVSP multidimensional Helmholtz solver with the FDF methodology was conducted by examining the dynamics of a generic multipoint injection combustor. The experimental setup and the corresponding numerical configuration were first introduced. The acoustic eigenmodes of the burner were characterized experimentally and numerically for different geometrical configurations. A good overall agreement was found for the first acoustic eigenfrequencies of the combustor. Simulations were conducted with unsteady flames modeled by the FDF. A nonlinear stability analysis was then carried out to determine the system unstable frequencies and the corresponding growth rates as a function of the perturbation level. Predictions were compared to measurements gathered at limit cycles. A good agreement was found between experimental data, numerical results and simulations with a low-order model of the burner acoustics for linearly unstable modes. It was shown that the AVSP solver catches the correct oscillation frequencies and perturbation levels of the limit cycles reached by these modes. Another configuration featuring a nonlinearly unstable mode was investigated as well. The

FDF/AVSP was shown to retrieve the mode switching phenomenon that was observed experimentally.

Conclusion and Perspectives

The present work deals with the dynamics of laminar premixed conical flames that are submitted to flow perturbations and their interactions with the burner acoustics. This investigation builds on a considerable work conducted at EM2C on this configuration [LeHelley (1994); Ducruix (1999); Schuller (2003); Birbaud (2006); Noiray (2007); Boudy (2012)]. The objective was to improve the description of the flame response by modeling new mechanisms and by using a combination of experimental methods, numerical simulations and theoretical developments. The main results of this work are summed up here:

- A novel method for the experimental determination of the Flame Transfer Function (FTF) was developed. The method uses random flow modulations to perturb a single laminar premixed conical flame. Measurements with this alternative technique compared well with measurements conducted with harmonic signals for low perturbation levels. These comparisons enabled to delineate the limits of this method when the perturbation level is increased.

- Modeling of the FTF of a single conical laminar flame was improved by considering incompressible convective velocity perturbations. It was shown that this is an important feature that needs to be taken into account to satisfy the continuity equation and retrieve the correct phase lag evolution of the FTF observed in experiments at low and intermediate frequencies. The decay of the velocity perturbation amplitude along the burner axis was also shown to be an important feature that needs to be considered to correctly describe the FTF gain evolution.

- New physical mechanisms considering unsteady heat losses from the flame base to the burner rim were taken into account to model the FTF of a single conical premixed laminar flame. Unsteady heat loss was shown to control the motion of the flame base determining the high frequency behavior of the FTF. This mechanism is also responsible for the saturation of the FTF phase lag observed in experiments at high frequencies.

- Transition to nonlinearity was shown to be controlled by a competition

between the flame response to oscillations of the flame base and the flame response resulting from velocity disturbances. These observations were used to guide modeling of the FDF and propose a first analytical semi-heuristic description of effects of the input level on FTF.

- Interactions between walls and burnt gases were investigated by considering a single conical laminar flame placed into a cylindrical flame tube. It was shown that confinement effects need to be taken into account to capture the correct shape of the flame when the burnt gases cannot fully expand. Large differences were observed between FTF measured for different flame tube diameters. These differences were explained by a modification of the averaged time lag taken by flame and flow disturbances to generate heat release rate perturbations. A new reduced frequency was proposed to rescale FTF obtained with different confinements. It was shown that this model may be used to capture the response of a collection of small conical flames stabilized on a perforated plate.

- The Flame Describing Function (FDF) methodology was combined to a numerical tool (AVSP) to solve the Helmholtz equation over 3D combustor geometries. This combination was here validated on a generic multipoint injection combustor by performing a nonlinear stability analysis. It revealed that this numerical method enables to predict linearly unstable modes and their evolution to limit cycle. It was also shown that the FDF/AVSP combination may be used to retrieve some nonlinear features such as nonlinearly unstable modes which are triggered above a certain amplitude threshold and mode switching.

This series of conclusions lead to the following perspectives. On the experimental side, the method developed for FTF determination with non-harmonic signals improves significantly the frequency resolution of the FTF. This method also reduces the amount of time required to determine a FTF. However, more work is required to improve this technique based on system identification tools:

- The technique using random perturbations has to be further tested and validated on other burner configurations, especially in the case of turbulent flames where effects of the turbulence background noise that were not considered here may interact with the forcing signal.

- A complete description of flame nonlinearities in the frequency domain is difficult and can become untractable if more than one single frequency has to be considered simultaneously [Moeck and Paschereit (2012)]. More work should thus be envisaged in the time domain. For example, a generalization of the impulse response including effects of the input level has to be designed in order to extend random perturbation techniques to the

measurement of nonlinear flame response. This can be done for example by considering Volterra series as recently suggested by Selimefendigil *et al.* (2012).

On the modeling side, significant improvements on the response of premixed laminar conical flames submitted to flow disturbances were achieved in this thesis in terms of flame front perturbations and Flame Transfer Function (FTF). In particular, it was shown how to reproduce the FTF of a single conical flame accurately over the whole frequency range of interest. All these models were validated by systematic comparisons with experiments for a single premixed laminar conical flame by detailed velocimetry, chemiluminescence and flame imaging measurements.
These models were also shown to reproduce the observed FTF of a collection of conical flames that are anchored above a perforated plate. By taking into account a correct description of the fresh gas velocity perturbation, the interaction of the flame base with the perforated plate and effects of the confinement due to neighboring flames, a relative good agreement was found between experiments and predictions.

This work leads to new perspectives in flame dynamics modeling:

- A general framework for FTF modeling was proposed. It lead to expressions of the FTF as a function of the fresh stream velocity perturbations at the burner outlet and of the flame base motion. The case of laminar premixed conical flames was examined, but this framework can easily be extended to other premixed flame configurations such as V-flames, M-flames and swirling flames in the future.

- In the present work, the feedback from the flame front perturbations onto the fresh gas flow was modeled by an incompressible convected velocity wave. These velocity perturbations were related here to incoming acoustic perturbations. It was shown by Birbaud *et al.* (2006) that these disturbances originate from the flame front perturbations. To further improve the premixed flame dynamics predictions, this link should be addressed for inclined flames. This problem becomes especially important for flames that are only submitted to mixture composition disturbances or to a motion of the flame base. In these cases, convective velocity perturbations have to be considered [Kornilov *et al.* (2007); Hemchandra (2012)], but they cannot be related to any incoming acoustic perturbations.

- The interaction between the flame base and the burner rim was examined in this work. The same type of model may be used to analyze the interactions of the unsteady flame front with the combustion chamber walls.

- Motions at the flame base were shown to result in large heat release rate disturbances that were linked to heat losses from the flame base to the burner rim. In the case of aerodynamically stabilized flames, the flame base can also execute a periodic motion [Borghesi *et al.* (2009); Stohr *et al.* (2011)] in the absence of unsteady heat losses. There is a wide field of investigation that needs to be conducted to understand the motion of the flame base and its impact on the FTF for aerodynamically stabilized flames.

- Different new physical mechanisms (incompressible convective velocity perturbations, unsteady heat losses, confinement effects) were included to improve the FTF description in the linear regime. Interactions between these mechanisms in the nonlinear regime still need to be investigated. Level set tracker solvers based on the G-equation are probably one natural way to perform these studies.

- Analysis of the impact of the confinement on conical flames can be extended to other premixed flame configurations. For example, in the case of unconfined V-flames, the burnt gases are deviated toward the burner centerline and exert an overpressure on the fresh gases. The streamlines in the fresh gases are thus deviated. The shape of the steady flame is in turn modified [Schuller (2003)]. This has also a great impact on the flame dynamics. A thorough analysis of the steady configuration, similar to the one carried in this work for confined conical flames, should be performed to model the mean flow in the fresh gases and the mean flame shape. This may be used to examine the impact of that overpressure on the FTF of V-flames.

- It was previously shown that confinement effects have a strong impact on steady and perturbed swirling flames [Tay-Wo-Chong and Polifke (2012)] resulting in large modifications of the FTF [Hauser *et al.* (2011); Tay-Wo-Chong and Polifke (2012)]. The same type of analysis that was devised here may be used to understand these changes in FTF and identify the correct dimensionless numbers needed to transpose FTF of swirling flames from one configuration to a burner with different flame tubes.

Finally, a significant step has been achieved by extending and validating a nonlinear stability methodology based on the FDF. It is here combined with a numerical solver of the Helmholtz equation capable to handle complex 3D geometries with complex boundaries. Several issues remain to tackle for thermoacoustic instability prediction:

- The FDF/AVSP methodology was only validated on generic configurations featuring laminar (the present work) or turbulent flames [Silva *et al.*

(2013)]. The next step should be to apply this type of methodology to a practical combustor featuring a 3D complex geometry. The main difficulty remains to determine the FDF in such a configuration at high pressure and high temperature.

- Another challenge is to improve the nonlinear stability analysis methodology by using Describing Functions not only for the flame response but also for the damping rate and for boundary conditions. The damping rate often depends on the input level [Tran *et al.* (2009); Schuller *et al.* (2009)]. There are also a few work initiated regarding the determination of the damping rate. This may be obtained experimentally [Palies *et al.* (2011)] or numerically by solving the linearized Euler equations [Gikadi *et al.* (2013)]. These features are essential to obtain a complete nonlinear description of the system and accurately predict limit cycles on practical combustors which are characterized by a balance between acoustic energy production and damping.

- Other issues recently emphasized by experiments like limit cycle with variable amplitude and multifrequency galloping modes remain difficult to capture [Kabiraj and Sujith (2012); Boudy *et al.* (2013)]. A modeling effort based on the interaction between multiple unstable modes is necessary to better predict these phenomena.

Appendix A

Heat release rate perturbations induced by a flame base motion

It was shown in Chapter 5 that when a conical flame anchored on the rim of a burner is submitted to harmonic flow disturbances, the flame base is not motionless and undergoes a periodic motion. These perturbations of the flame position at its base are convected along the flame front. The resulting flame wrinkles produce flame surface area perturbations and ultimately, heat release rate disturbances. In Chapter 1, this link was only considered for a flame base that moves along a direction normal to the steady flame front. It was also confirmed by experiments in Chapter 6. In a different configuration, Kornilov *et al.* (2007) explored the flame response when the flame base is submitted to either an horizontal or a vertical oscillating motion. It is shown in this appendix that the flame response changes when submitted to oscillations of different directions at the flame base. The different expressions obtained for the FTF are compared for normal, horizontal and vertical disturbances of the flame base position.

The analysis is conducted for a straight laminar conical flame anchored on a circular burner of outlet radius R and in a uniform axial flow of velocity v_0. The flame speed S_d fixes the flame position (see Fig. A.1-a). The following developments make use of the G-equation:

$$\frac{\partial G}{\partial t} + \mathbf{v} \cdot \nabla \mathbf{G} = S_d |\nabla \mathbf{G}| \tag{A.1}$$

A.1 Flame base motion normal to the steady flame front

The conical flame is submitted to harmonic disturbances of the flame base $\xi(X = 0, t)$ in a direction normal to the steady flame front (see Fig. A.1-b).

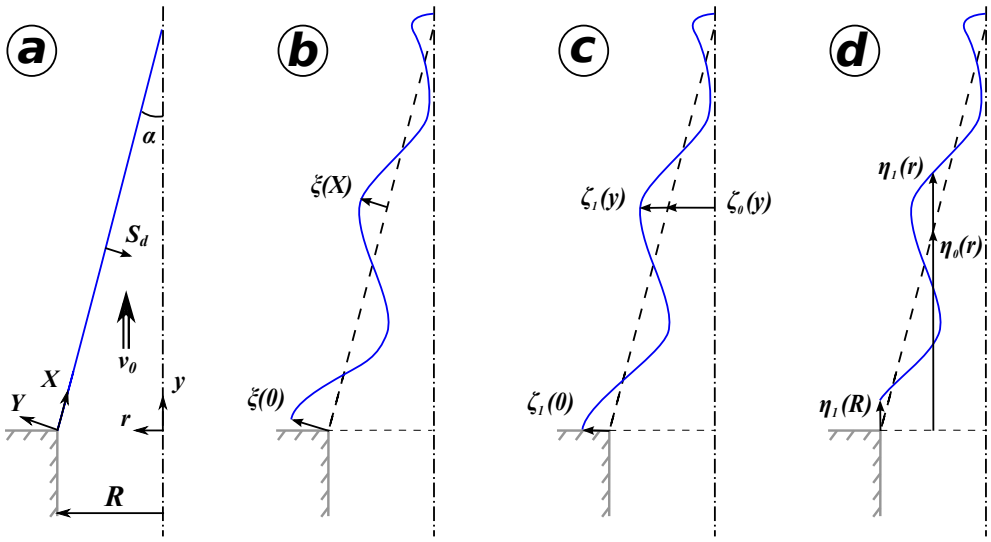

Figure A.1: *Different configurations explored. (a) Steady laminar conical flame. (b) Unsteady flame perturbed by a flame base displacement along a direction normal to the steady flame front $\xi(X = 0)$. (c) Unsteady flame perturbed by a horizontal flame base displacement $\zeta_1(y = 0)$. (d) Unsteady flame perturbed by a vertical flame base displacement $\eta_1(r = R)$.*

These disturbances are convected along the flame front resulting in flame wrinkles $\xi(X, t)$ and flame surface area perturbations $A_1(t)$. In the frame attached to the flame front, the G-equation reduces to:

$$\frac{\partial \xi}{\partial t} + v_0 \cos\alpha \frac{\partial \xi}{\partial X} = 0 \tag{A.2}$$

where $G(X, Y, t) = \xi(X, t) - Y$. In the case of harmonic perturbations of the form $\xi(X, t) = \tilde{\xi}(X) \exp(-i\omega t)$, the solution of Eq. (A.2) is:

$$\tilde{\xi}(X) = \tilde{\xi}(0) \exp\left(\frac{i\omega X}{v_0 \cos\alpha}\right) \tag{A.3}$$

The link between normal flame front perturbations and flame surface area disturbances is given by:

$$\frac{\tilde{A}_1}{A_0} = \frac{\sin\alpha}{\pi R^2} \int_0^L 2\pi \tilde{\xi}(X) \cos\alpha dX \tag{A.4}$$

It finally comes:

$$F_{C_N} = \frac{\tilde{A}_1/A_0}{\tilde{\xi}(0)/R} = 2\cos\alpha \frac{e^{i\omega_*} - 1}{i\omega_*} \tag{A.5}$$

This transfer function is plotted in Fig. A.2-left as a function of the reduced frequency ω_* and for three flame tip half-angles $\alpha = \pi/12$ (black line), $\pi/4$ (dark grey line) and $\pi/3$ (light grey line). This figure shows that the gain of F_{C_N} has a low-pass filter behavior featuring several humps. This gain reduces as α increases. The phase lag of F_{C_N} is increasing linearly from 0 to π when ω_* increases from $2k\pi$ to $2(k+1)\pi$, $k = 1, 2...$, without taking any values between π and 2π. The phase lag does not depend on the flame tip half-angle α.

A.2 Horizontal flame base motion

The flame is now submitted to harmonic horizontal disturbances of the flame base $\zeta(y = 0, t)$ as in Fig. A.1-c. These disturbances are convected along the flame front and result in flame front wrinkles $\zeta_1(y, t)$ and flame surface area perturbations $A_1(t)$. In the frame attached to the burner rim, the G-equation reduces now to:

$$\frac{\partial \zeta_1}{\partial t} + v_0 \cos^2\alpha \frac{\partial \zeta_1}{\partial y} = 0 \tag{A.6}$$

where $G(r, y, t) = \zeta(y, t) - r$. For harmonic perturbations $\zeta_1(y, t) = \tilde{\zeta_1}(y) \exp(-i\omega t)$, the solution of Eq. (A.6) is:

$$\tilde{\zeta_1}(y) = \tilde{\zeta_1}(0) \exp\left(\frac{i\omega y}{v_0 \cos^2\alpha}\right) \tag{A.7}$$

The resulting flame surface area disturbances are given by:

$$\frac{\tilde{A}_1}{A_0} = \frac{\sin\alpha}{\pi R^2} \int_0^H 2\pi \left[\tilde{\zeta_1}(y) - (R - y\tan\alpha)\sin\alpha\cos\alpha \frac{\partial \tilde{\zeta_1}}{\partial y}\right] \frac{dy}{\cos\alpha} \tag{A.8}$$

It finally comes:

$$F_{C_H} = \frac{\tilde{A}_1/A_0}{\tilde{\zeta_1}(0)/R} = 2\left[\frac{e^{i\omega_*} - 1}{i\omega_*} - \sin^2\alpha \frac{e^{i\omega_*} - 1 - i\omega_*}{i\omega_*}\right] \tag{A.9}$$

It is important to note that F_{C_H} reduces to F_{C_N} when the flame tip half-angle α tends to 0. This transfer function F_{C_H} is plotted in Fig. A.2-center as a function of the reduced frequency ω_* and for three flame tip half-angles $\alpha = \pi/12$ (black line), $\pi/4$ (dark grey line) and $\pi/3$ (light grey line). The gain of F_{C_H} is equal to 2 at low frequency and decreases before oscillating around an almost constant value at high frequencies. This constant value decreases when the flame tip half-angle α decreases. The phase lag of F_{C_H} is oscillating between 0 and π

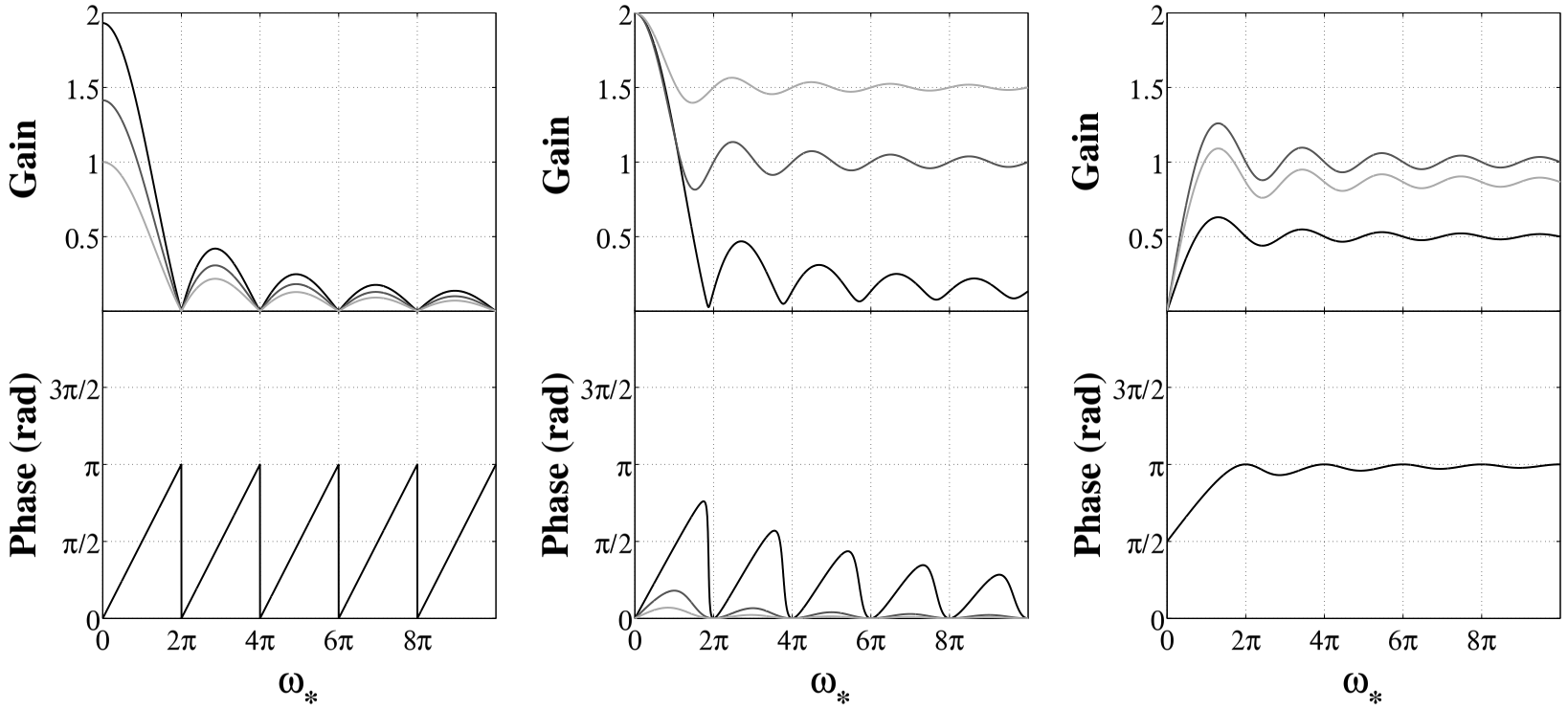

Figure A.2: *Transfer Function $F_C(\omega_*, \alpha)$. It is derived from a flame base motion in the direction normal to the steady flame front $\tilde{\xi}(X = 0)$ (left), from a horizontal flame base motion $\tilde{\zeta}_1(y = 0)$ (center) and from a vertical flame base motion $\tilde{\eta}_1(r = R)$ (right). $\alpha = \pi/12$ (black line), $\pi/4$ (dark grey line) and $\pi/3$ (light grey line).*

and the amplitude of these oscillations is reduced as α increases. It is interesting to note that these oscillations of the phase lag are smaller than the ones of the phase lag of F_{C_N} and that the gain of F_{C_H} takes larger values than the gain of F_{C_N}. The flame response to disturbances at the flame base is thus a strong function of the disturbance direction. It is interesting to explore a last case when perturbations of the flame base position are vertical.

A.3 Vertical flame base motion

The flame is now submitted to harmonic vertical flame base oscillations $\eta_1(r = R, t)$ as shown in Fig. A.1-d. These disturbances are convected along the flame front. They produce flame wrinkles $\eta_1(r, t)$ and flame surface area perturbations $A_1(t)$. In the frame attached to the burner rim, the G-equation reduces to:

$$\frac{\partial \eta_1}{\partial t} - v_0 \cos\alpha \sin\alpha \frac{\partial \eta_1}{\partial r} = 0 \tag{A.10}$$

where G is now given by $G(r, y, t) = \eta_1(r, t) - y$. For harmonic perturbations $\eta_1(r, t) = \tilde{\eta}_1(r) \exp(-i\omega t)$, the solution of Eq. (A.10) writes:

$$\tilde{\eta}_1(r) = \tilde{\eta}_1(R) \exp\left(\frac{i\omega(R - r)}{v_0 \sin\alpha \cos\alpha}\right) \tag{A.11}$$

The resulting flame surface area disturbances are given by:

$$\frac{\tilde{A}_1}{A_0} = \frac{\sin\alpha}{\pi R^2} \int_0^R 2\pi r \left(-\sin\alpha \cos\alpha \frac{\partial \tilde{\eta}_1}{\partial r}\right) \frac{dr}{\sin\alpha} \tag{A.12}$$

It finally comes:

$$F_{C_V} = \frac{\tilde{A}_1/A_0}{\tilde{\eta}_1(R)/R} = 2\sin\alpha\cos\alpha \frac{e^{i\omega_*} - 1 - i\omega_*}{i\omega_*} \tag{A.13}$$

This transfer function F_{C_V} is plotted in Fig. A.2-right as a function of the reduced frequency ω_* and for three flame tip half-angles $\alpha = \pi/12$ (black line), $\pi/4$ (dark grey line) and $\pi/3$ (light grey line). This figure shows that the gain of F_{C_V} is equal to 0 at low-frequency and decreases before oscillating around an almost constant value at high frequencies. The transfer function F_{C_V} corresponds here to a high-pass filter. This constant value is highly dependent on the flame tip half-angle α. The phase lag of F_{C_V} is equal to $\pi/2$ at low frequencies and is oscillating around π at higher frequencies. The phase lag of F_{C_V} does not depend on the flame tip half-angle α.

A.4 Synthesis

These different analytical developments show that flame surface area and heat release rate disturbances resulting from the perturbations imposed at the base of a conical flame strongly depend on the direction of these oscillations of the flame base. In modeling the response of conical flames to flow disturbances, it is important to examine the motion at the flame base and in particular its direction in order to capture the correct contribution to the FTF.

Appendix B

FTF as a function of a complex angular frequency

Flame Transfer Function are usually determined experimentally or numerically by perturbing the flow with a harmonic signal featuring a constant amplitude. The FTF is thus generally determined for real forcing angular frequencies. However, in order to predict thermo-acoustic instabilities, FTF or FDF should in principle be introduced in dispersion relations or numerical acoustic solvers as quantities that depend on a complex frequency. Because the FTF is only known for real frequencies, it is generally introduced as real-frequency-dependent quantities in thermo-acoustic stability analysis. Two problems are considered in this appendix. The first one is:

$$M(\omega)P = F(\omega_r) \tag{B.1}$$

where ω_r is the real part of the complex frequency ω. The second one is:

$$M(\omega)P = F(\omega_r + i\omega_i) \tag{B.2}$$

where ω_i is the imaginary part of the complex frequency ω. In these expressions, M denotes a matrix that depends on the angular frequency and P is the pressure eigenvector. The source term F includes the unsteady flame frequency response to flow perturbations and depends on the angular frequency.

These two problems are used to investigate the influence of FTF with a complex frequency in the determination of thermo-acoustic eigenmodes of a combustor. Analytical expressions of the FTF that were derived in Chapter 4 are first considered and plotted as a function of both the real component ω_r and the imaginary component ω_i of the angular frequency. Analytical calculations are then considered in a generic case with a $n - \tau$ sensitive time lag model to emphasize effects of complex angular frequencies $\omega = \omega_r + i\omega_i$. A method to

compute complex frequency dependent FTF from experimental data is finally described before using it in combination with low-order acoustic network for the determination of the oscillation modes of a generic combustor.

B.1 Effects of ω_i on analytical FTF models

To illustrate this problem, analytical FTF models derived for incompressible convective velocity perturbations and for unidimensional convective velocity perturbations (see Chapter 4) are considered in this study when the real reduced frequency ω_r^* is replaced by a complex frequency $\omega_* = \omega_r^* + i\omega_i^*$. Results are plotted in Fig. B.1 as a function of the reduced frequency $\omega_* = \omega R/(S_d \cos\alpha) = \omega_r^* + i\omega_i^*$. One can observe that the main effect of taking into account finite

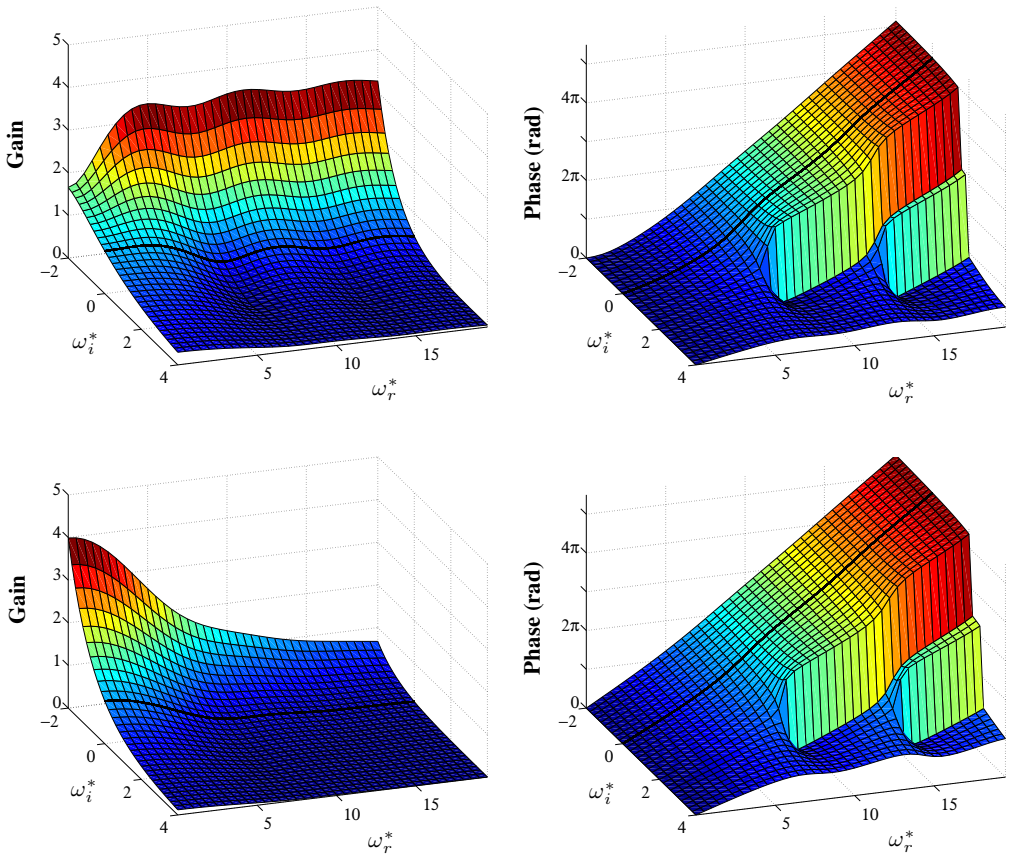

Figure B.1: *Flame Transfer Function gain (left) and phase (right) as a function of the reduced real frequency ω_r^* and the reduced growth rate ω_i^*. The models used are derived from an incompressible convective model (top figures) and from a convective model [Schuller et al. (2003a)]. The FTF values derived for $\omega_i^* = 0$ are highlighted as a thick black curve. $\alpha = \pi/12$.*

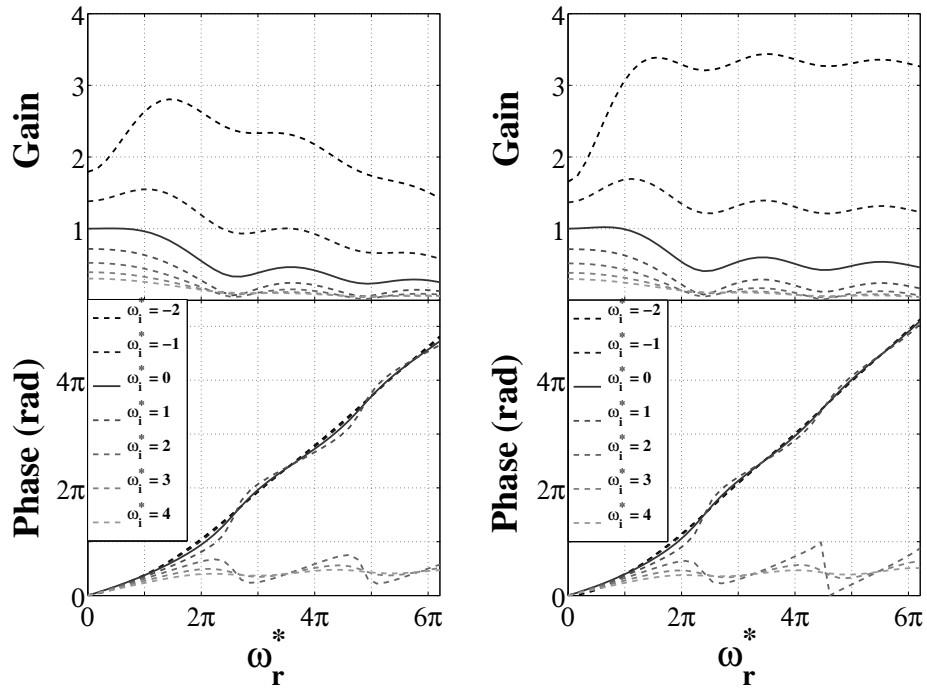

Figure B.2: *Flame Transfer Function as a function of the reduced frequency ω_r^* for different values of the dimensionless reduced growth rate ω_i^*. $\alpha = \pi/6$ (left figure) and $\alpha = \pi/12$ (right figure).*

values for ω_i^* is a strong increase of the FTF gain for large negative values of the reduced growth rate. For large positive values of the growth rate, the FTF gain reduces to zero. Effects of the growth rate ω_i on the FTF phase are less obvious. Only some differences can be observed with a jump of 2π for the unwrapped phase.

The effect of the growth rate ω_i^* is further studied by examining FTF determined for different flame tip half-angles α in the case of incompressible convective perturbations. The FTF are plotted in Fig. B.2 as a function of the reduced real frequency for different growth rates and for two flame tip half-angles $\alpha = \pi/6$ and $\pi/12$. One can see that the sensitivity of the FTF to changes in the reduced growth rate differs when the flame tip half-angle α is varied. For negative values of the growth rate, the FTF gain increases when the flame tip half-angle decreases. The FTF phase weakly depends on the flame tip half-angle. A phase saturation phenomenon appears for large positive values of the growth rate for the two flame tip half angles considered.

Large differences can be observed between $\mathrm{F}(\omega_r)$ and $\mathrm{F}(\omega_r + i\omega_i)$. However, the impact of these differences on the prediction of thermo-acoustic instability

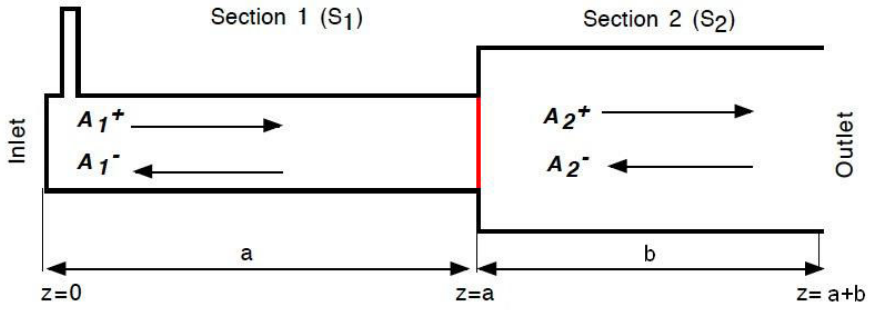

Figure B.3: *Open-close double-duct system where a compact flame is located in between the ducts (red line). Adapted from Poinsot and Veynante (2012).*

has to be assessed. This is achieved in the next section by means of a simplified analytical model.

B.2 Effect of F($\omega_r + i\omega_i$) on thermo-acoustic instability prediction

In this section, a simplified combustor model is considered. This configuration represents an acoustic system comprising two cavities of different lengths and section areas (see Fig. B.3). It represents an open-close double-duct system that models a generic combustor where a compact flame is located in between the two cavities. The eigenmodes of this combustor are determined with a low-order model. This method leads to a dispersion relation which solutions are the eigenfrequencies $f = \omega_r/(2\pi)$ and the growth rates ω_i. Different stability analyses are conducted to investigate the influence of the growth rate ω_i on the system dynamics.
First, calculations are carried out without taking into account the growth rate in the description of the flame response:

$$\cos(\omega a/c_1)\cos(\omega b/c_2) - \Gamma \sin(\omega a/c_1)\sin(\omega b/c_2)\left[1 + \left(\frac{T_2}{T_1} - 1\right)\mathrm{F}(\omega_r)\right] = 0 \tag{B.3}$$

Then, calculations are conducted on the same configuration but by also considering the growth rate in the FTF:

$$\cos(\omega a/c_1)\cos(\omega b/c_2) - \Gamma \sin(\omega a/c_1)\sin(\omega b/c_2)\left[1 + \left(\frac{T_2}{T_1} - 1\right)\mathrm{F}(\omega)\right] = 0 \tag{B.4}$$

$\Gamma = (\rho_2 S_2 c_1)/(\rho_1 S_1 c_2)$ is a cavity coupling index and T_1, a, S_1, ρ_1 and c_1 (resp. T_2, b, S_2, ρ_2 and c_2) are the temperature, length, cross section area, density and speed of sound relative to the upstream cavity (resp. the downstream cavity) (see Fig. B.3).

The linear stability analysis is performed with a n-τ sensitive time lag model. In the frequency domain, one may write: $\mathrm{F}(\omega) = ne^{i\omega\tau}$. Different stability analyses are conducted by sweeping both the flame/acoustic interaction index n, over four values $n = 10^{-5}, 10^{-2}, 10^{-1}$ and 1, and the time lag in a range from $\tau = 0$ to $\tau = 0.03$. Eqs. (B.3) and (B.4) are solved for the following values: $a = b = 0.5$ m, $S_2 = 2S_1$, $T_2 = 6T_1$, $c_1 = 340$ m.s^{-1}, $c_2 = 6^{1/2}c_1$, $\rho_2 = \rho_1/6$. Results are plotted in Fig. B.4, in blue for the solution of Eq. (B.3) (when $\mathrm{F}(\omega_r) = ne^{i\omega_r\tau}$ is considered). They are plotted in red for the solution of Eq. (B.4) (when $\mathrm{F}(\omega_r + i\omega_i) = ne^{-\omega_i\tau}e^{i\omega_r\tau}$ is considered). The influence of the growth rate ω_i on the results of a linear stability analysis appears to be limited for very small values of n (left figures in Fig. B.4). As the coupling parameter n increases, differences appear if one takes into account the growth rate in the FTF expression. For $n = 0.1$, one can see that the frequency of the instability is significantly modified. The system linear stability is also modified for large time lags τ. If the growth rate is not considered in the FTF formulation, the system alternates between stability and instability (depending on the sign of the growth rate) as the time lag τ increases. If the growth rate is considered in the FTF expression, the system features a wider range of stable regimes over the range of time lags investigated. For the last case where $n = 1$, the system stability and the mode frequency are not modified but it is interesting to notice that the resulting growth rates are greatly reduced in the case where they are taken into account in the FTF expression.

Including the growth rate in the FTF was shown to have a strong impact on the stability of the eigenmodes of the system. However, available experimental FTF are only limited to real forcing frequencies where $\omega_i = 0$. A procedure to extend these data to the whole complex frequency plane has to be designed. It is the topic of the next section.

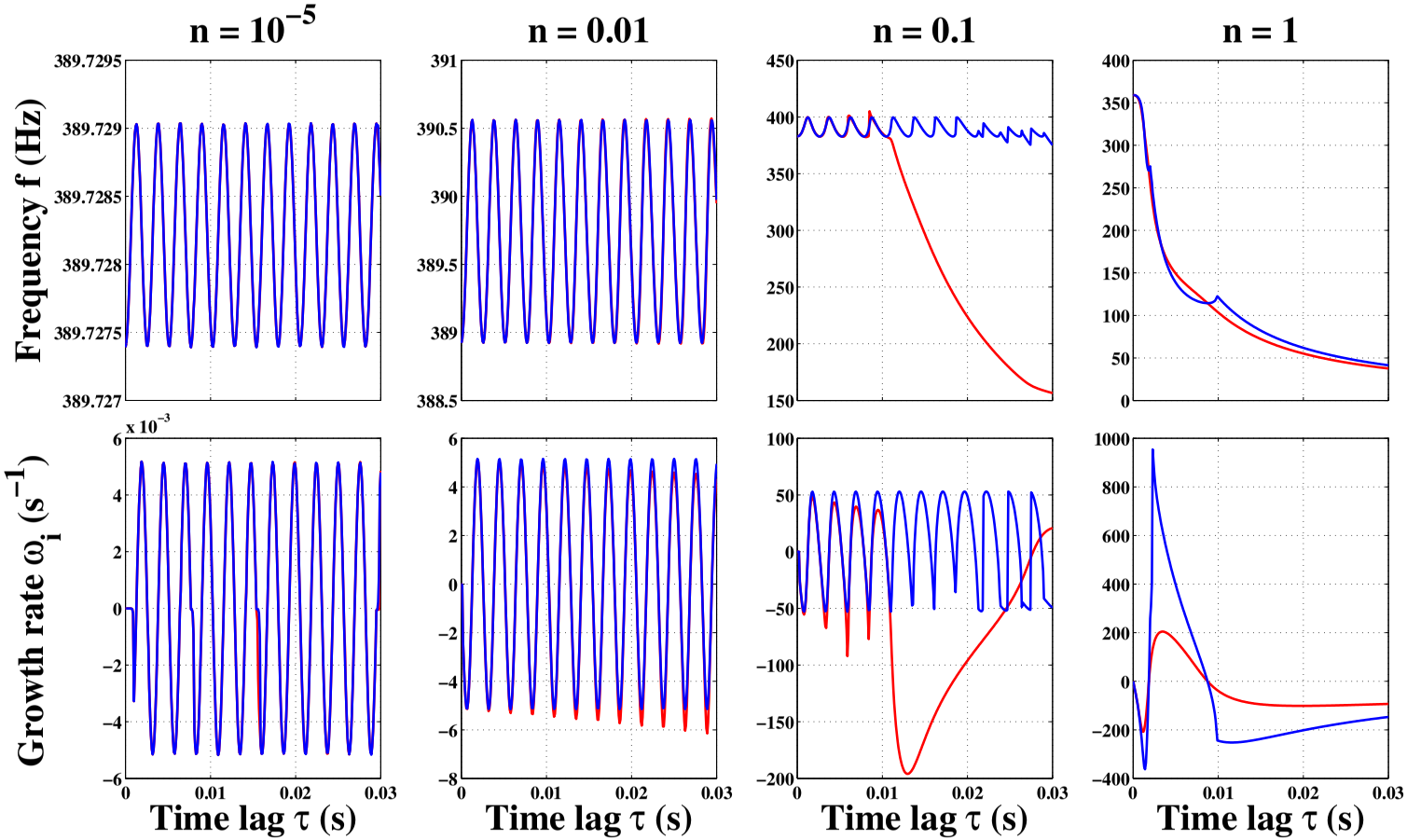

Figure B.4: *Results of a linear stability analysis in terms of frequency f (top row) and growth rate ω_i (bottom row) for four different values of the acoustic/flame coupling index n. Results are plotted as a function of the time lag τ between heat release rate disturbances and velocity modulations. Blue: Solution of Eq. (B.3). Red: Solution of Eq. (B.4).*

B.3 From $\mathrm{F}(\omega_r)$ to $\mathrm{F}(\omega_r + i\omega_i)$

B.3.1 Theoretical method

In practical cases, the FTF is measured or numerically determined using harmonic waves of constant amplitude, i.e. with a growth rate $\omega_i = 0$. These experiments yield $\mathrm{F}(\omega_r)$. However, as shown in the previous section, strong differences can appear between stability analyses that use a FTF that depends or not on the growth rate ω_i. Therefore, a specific algorithm has to be designed and applied to determine $\mathrm{F}(\omega_r + i\omega_i)$ from discrete measurements of $\mathrm{F}(\omega_r)$. This can be done for example by transforming the experimental data from the frequency domain to the time domain, and then apply a Laplace transform. The first step consists in applying an inverse Fourier transform to the FTF determined for real frequencies $\mathrm{F}(\omega_r)$, what results in the impulse response (IR):

$$h(t) = \mathrm{Re}\left[\int_{-\infty}^{+\infty} \mathrm{F}(2\pi f) e^{2i\pi f t} df\right] \tag{B.5}$$

where Re[] denotes the real part of a complex number. An experimental FTF is only determined for a limited number of frequencies with a discrete set of values for the FTF $\mathrm{F}(2\pi f_n)$ measured for a set of real frequencies $(f_n)_{0\leq n\leq N}$ equally spaced by Δf where $f_0 = 0$ Hz, $f_N = f_s/2$ is the Nyquist frequency and f_s is the sampling frequency of the discrete IR. The previous expression thus reduces to:

$$h(t_k) = \mathrm{Re}\left[\mathrm{F}(0)\Delta f + 2\sum_{n=1}^{N} \mathrm{F}(2\pi f_n) e^{2i\pi f_n k\Delta t}\Delta f\right] \tag{B.6}$$

where $\Delta f = f_{n+1} - f_n$, $\Delta t = 1/f_s$ and $t_k = k\Delta t$. To obtain a FTF that depends on the complex angular frequency $\omega = \omega_r + i\omega_i$, a Laplace transform is used:

$$\mathrm{F}(s) = \int_0^{+\infty} h(t) e^{-st} dt \tag{B.7}$$

In the case of a discrete-value IR, this corresponds to:

$$\mathrm{F}(s) = \sum_{k=0}^{N} h(t_k) e^{-st_k}\Delta t \tag{B.8}$$

where $t_k = k\Delta t$ and $\Delta t = 1/f_s = t_{k+1} - t_k$ is the sampling period. The FTF is obtained by setting $s = i(\omega_r + i\omega_i)$.

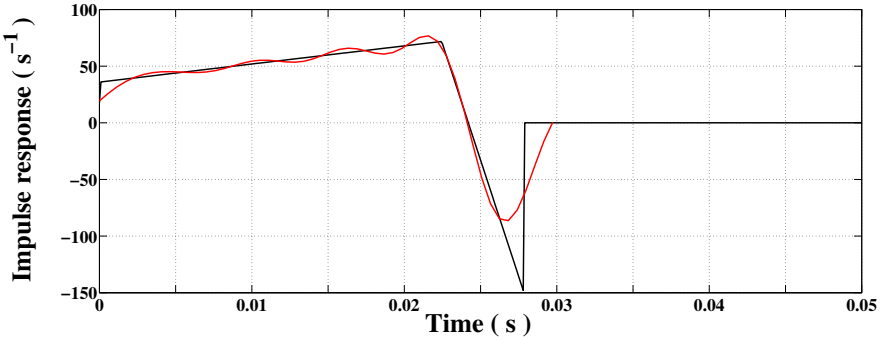

Figure B.5: *Impulse response of a single premixed laminar conical flame. (black line) Analytical model that considers incompressible convective perturbations. (red line) Impulse response determined from a discrete set of samples of an analytical FTF and the application of the reconstruction algorithm.*

B.3.2 Validation of the method

This method is tested by comparison with an analytical expression of the FTF of a single laminar premixed conical flame that was derived in Chapter 4 by considering incompressible convective velocity perturbations. The following parameters are used: the mean velocity is equal to $v_0 = 1$ m.s^{-1} and the flame speed is equal to $S_d = 0.44$ m.s^{-1}. It leads to a flame tip half-angle $\alpha = 0.45$ rad. A burner exit radius $R = 0.011$ m is also considered. The continuous FTF expression is plotted as a function of the reduced frequency ω_r^* in Fig. B.6-top-left as a black line. To simulate discrete values corresponding to FTF measurements, the model is then sampled between $\omega_r^* = 0$ and $\omega_r^* = 30$ with a reduced frequency resolution $\Delta\omega_r^* = 1$. To improve the sampling frequency of the impulse response, the flame response is padded with zero up to $\omega_r^* = 150$. The result is plotted in Fig. B.6 as black circles. The reconstruction algorithm presented in Section B.3.1 is applied to that discrete-value FTF and the resulting impulse response is plotted in Fig. B.5 (red line) along with the model derived in Section 4.4 (black line). The reconstruction algorithm retrieve well the trend of the analytical IR. Some differences can be observed because the frequency response above $\omega_* = 30$ is not taken into account. Some additional tests (not shown here) showed that, by taking into account the whole frequency response up to a frequency where the gain is negligible, the reconstruction algorithm retrieve the IR almost perfectly. The full reconstruction algorithm is then applied for $s = i\omega_r$ (with $\omega_i = 0$). Results are plotted in Fig. B.6-bottom-left. One can see that the FTF is perfectly retrieved after applying reverse and forward Fourier Transforms. The same algorithm is then applied for different values of ω_i. Results from calculations carried out with six values of the growth rate ω_i are plotted in Fig. B.6 and the comparison between analytical predictions (plain black lines) and results of the FTF reconstruction (dashed red lines) shows a good match. The FTF discrete samples (black circles) are

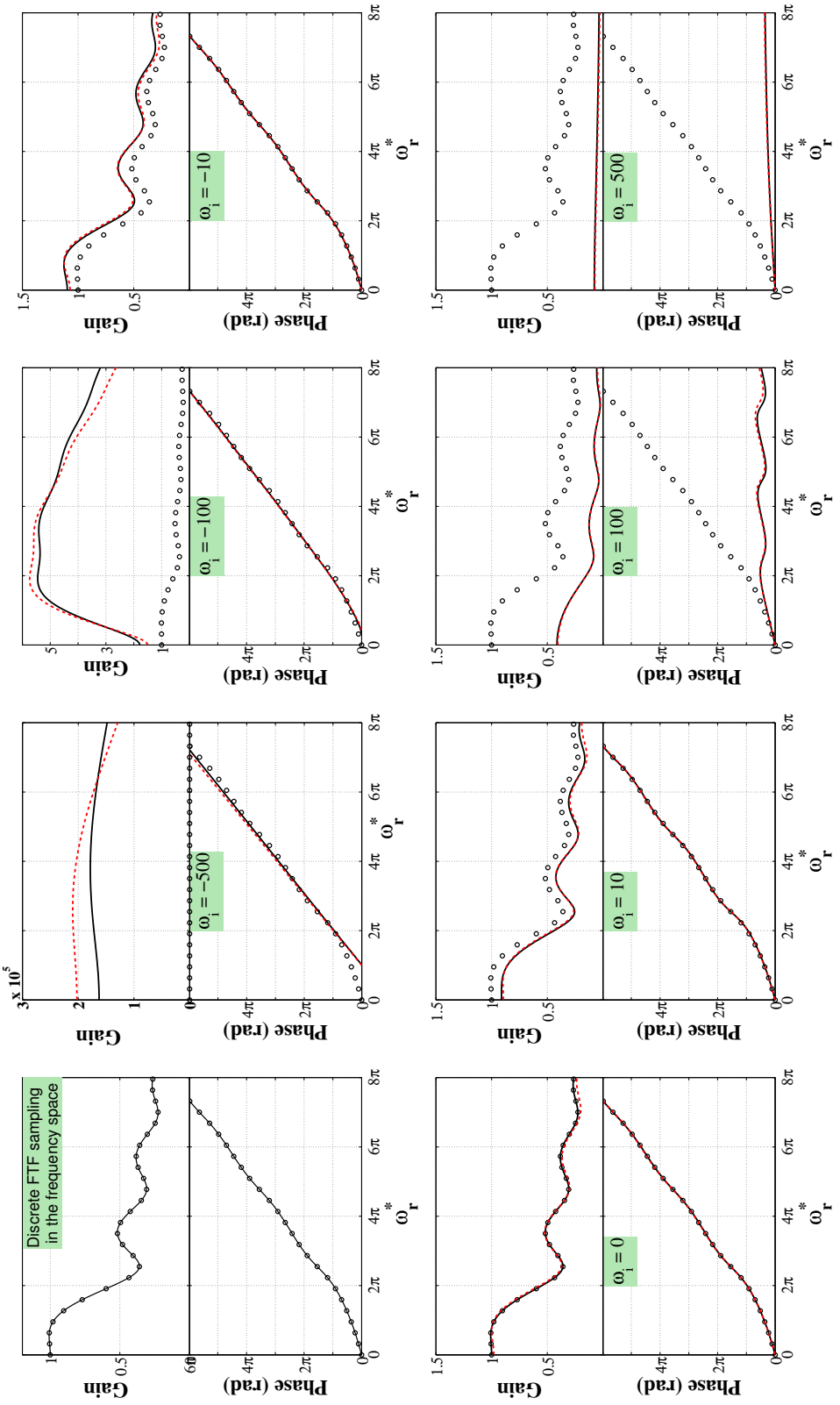

Figure B.6: *FTF as a function of the real part ω_r^* of the reduced frequency ω_*. (black ○) Sampled analytical FTF for $\omega_i = 0$. (black line) Analytical FTF plotted for different growth rates. (red line) FTF for different growth rates determined from the reconstruction based on the sampled FTF determined for $\omega_i = 0$. $\alpha = 0.45$ rad.*

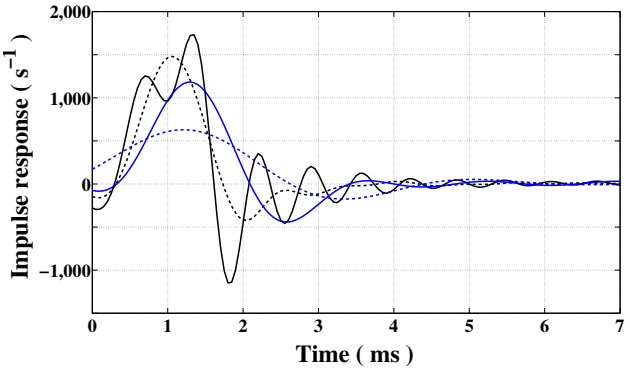

Figure B.7: *Impulse response of a collection of small premixed laminar conical flames. These data are determined from FDF measurements where $v_1^{\mathrm{rms}}/U_b = 0.06$ (black solid line), 0.26 (black dashed line), 0.46 (blue solid line) and 0.66 (blue dashed line).*

also plotted for reference. In the case of positive growth rates, the analytical model is well retrieved. For small negative values of the growth rates, the results collapse as well. Some differences appear in the FTF gain, but only at very large negative growth rates. The order of magnitude is well retrieved but no exact match is reached.

B.3.3 Results of the method on a measured FDF

The method is further applied to an experimental FDF that was measured during the Ph.D. thesis of Boudy (2012) (see Fig. B.8 (circles)). This set of flame frequency response was measured for a collection of small premixed laminar conical flames with a mass flow rate $\dot{m} = 4.71$ g.s^{-1} and an equivalence ratio $\phi = 1.03$. The flames were anchored on a perforated plate of thickness $l = 3$ mm, hole radius $r_p = 1$ mm and hole pitch $d = 3$ mm. This FDF was determined by perturbing the flow with constant-amplitude harmonic signals. It was measured between 0 and 1600 Hz with a constant frequency resolution $\Delta f = 20$ Hz. First, these data are linearly interpolated to reduce the frequency resolution to $\Delta f = 2$ Hz and are padded with zeros up to 10 kHz in order to increase the sampling frequency f_s without modifying the frequency content of the measurements. This last operation enables to calculate the impulse response from Eq. (B.6) with a much better time resolution.
The time domain response derived from the FTF (i.e. the frequency response determined at low perturbation level $v_1^{\mathrm{rms}}/U_b = 0.06$ where v_1 is the velocity perturbation and U_b stands for the bulk velocity) is plotted as a black solid line in Fig. B.7. This response is called the impulse response in the following even though, strictly speaking, it is important to notice that this is not exactly the impulse response. As no frequency content above 1600 Hz is taken into account (the FTF gain differs from zero above $f = 1600$ Hz), it thus represents

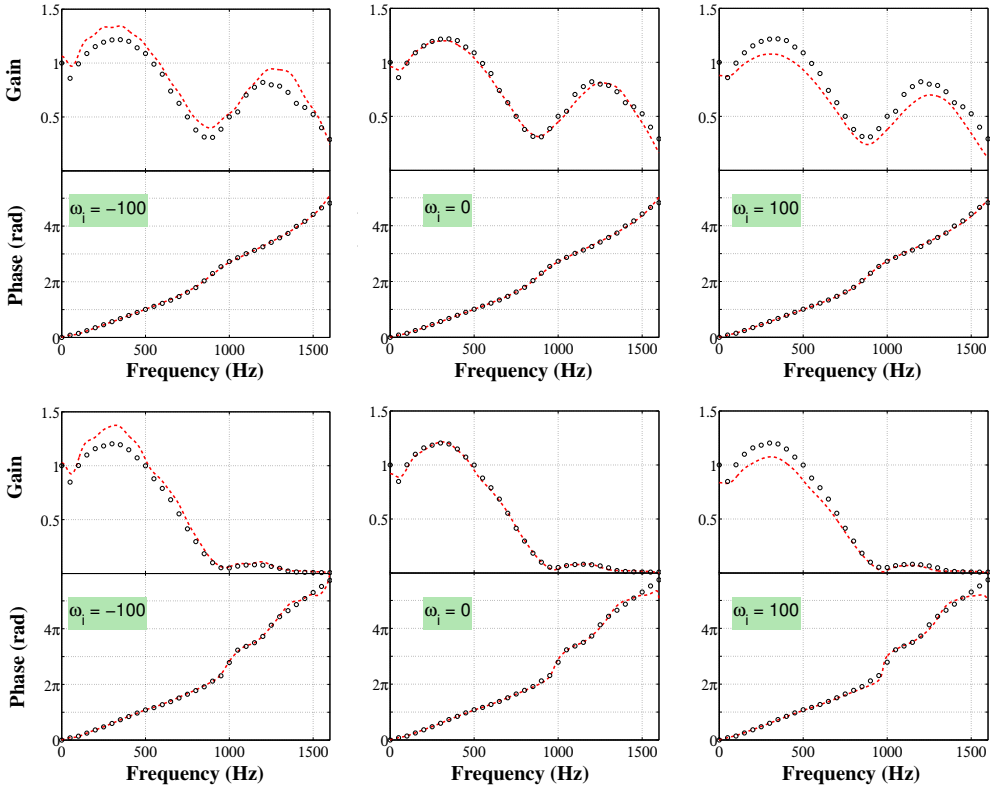

Figure B.8: *FTF as a function of the frequency. (black ∘) Experimental FTF measured with constant amplitude harmonic signals for* $v_1^{\mathrm{rms}}/U_b = 0.06$ *(top row) and* $v_1^{\mathrm{rms}}/U_b = 0.26$ *(bottom row). (red line) FTF for different growth rates* $\omega_i = -100$ *(left),* 0 *(center) and* 100 *rad.s*$^{-1}$ *(right), determined with the reconstruction based on the experimental data measured for* $\omega_i = 0$.

the result of a filtering operation of the impulse response with a low-pass filter which cut-off frequency is 1600 Hz. This filtered impulse response has an oscillatory behavior between 0 and 5 ms before vanishing. The initial value of the impulse response is not zero at initial times, because some frequency content was removed. The same operation is performed for other flame frequency response taken from the same FDF, for other perturbation levels $v_1^{\mathrm{rms}}/U_b = 0.26$, 0.46 and 0.66. As a general trend, one can observe in Fig. B.7 that the time response decreases in amplitude with the perturbation level used to determine the FTF, but the time duration of the IR does not change much and remains about 5 ms. However, these observations must be interpreted carefully. The time response is here derived from a FDF which is only an approximation of the nonlinear flame frequency response to harmonic flow perturbations. The flame is perturbed with a harmonic signal at a single frequency. Only the principal spectral component of the response is kept and all the harmonics are discarded. This time response is thus not related to the impulse response, but it still can

be used to extend the FDF concept to the complex angular frequency plane.

This is done by using Eq. (B.8). The results are plotted in Fig. B.8 for two different perturbation levels $v_1^{\text{rms}}/U_b = 0.06$ (top) and 0.26 (bottom), and three values of the growth rate $\omega_i = -100$, 0 and 100. It is shown that the method yields a good estimate of the FTF for $\omega_i = 0$ (central column) and gives similar results than with an analytical FTF for other values of the growth rate. The FTF gain values decrease for positive growth rates and increases for negative growth rates. The FTF phase is barely modified in these figures. For larger growth rates (not shown here), the phase lag can be modified.

A method to extend the FTF from the real angular frequency axis to the complex angular frequency plane was presented in this section. It was validated by comparing predictions with an analytical expression for the FTF of a single premixed laminar conical flame and applied to the FDF of a collection of a small premixed laminar conical flames. This last result enables now to perform a full nonlinear stability analysis where the flame frequency response is allowed to also depend on the growth rate ω_i. This is performed in the next section.

B.4 Nonlinear stability analysis performed with F($\omega_r + i\omega_i$)

B.4.1 Results from the nonlinear stability analysis

The method derived in the previous section is used to perform a nonlinear stability analysis based on the FDF methodology (see Chapter 7). This method is here extended by considering flame frequency responses that also depend on the imaginary part of the angular frequency $\omega = \omega_r + i\omega_i$ (see Eq. (B.2)). The system considered here is briefly described in Chapter 8 and was more thoroughly investigated by Boudy (2012). A low-order acoustic network solver is used to perform the nonlinear stability analysis (see [Boudy *et al.* (2011); Boudy *et al.* (2011); Boudy (2012); Boudy *et al.* (2013)] for more details). Only one geometrical configuration is analyzed here. It features a feeding manifold length $L_1 = 0.54$ m, a flame tube length $L_2 = 0.087$ m and a perforated plate of thickness $l = 3$ mm. This last value corresponds to the FDF presented in the previous section (Section B.3.3). The same boundary conditions that were used in Chapter 8 are used here. The inlet reflection coefficient was measured and the outlet reflection coefficient is modeled with the radiation impedance of an unflanged open pipe [Levine and Schwinger (1948); Rienstra and Hirschberg (2012)]

Calculations are first performed without taking the growth rate into account in the FDF formulation. Then, a calculation is carried by allowing the FDF

to depend on the growth rate ω_i. Finally, a last calculation is performed by also considering that the boundary conditions depend on a complex angular frequency. For the outlet boundary condition, the reflection coefficient is determined with the value of an analytical model for an unflanged open pipe (see Eq. (8.1) in Chapter 8) taken at $\omega = \omega_r + i\omega_i$. For the inlet boundary condition, the reflection coefficient was measured for $\omega_i = 0$ and the method described in the previous section is applied to extend these measurements to complex angular frequencies.

Results from that nonlinear stability analysis are shown in Fig. B.9 for the three first eigenmodes of the combustor. The first combustor mode lies between 130 Hz and 150 Hz. Its growth rate is always negative and thus features a stable mode. No changes are observed when the growth rate ω_i is taken into account in the FDF and the boundary conditions. The third mode is presented in Fig. B.9-bottom. It represents the most unstable mode in the linear regime (i.e. for small perturbation levels) and features large growth rates in this regime. However, the value of this growth rate is modified if one takes into account the growth rate (blue and green lines) or not (red line) in the description of the flame response to acoustic perturbations. The growth rates are significantly reduced if one allows the FDF or the boundary conditions to depend on ω_i. However, the predicted limit cycle oscillation amplitude is not modified because when $\omega_i = 0$, the FDF $\mathrm{F}(\omega_r + i\omega_i)$ and the boundary conditions $R(\omega_r + i\omega_i)$ reduce then to the analytical or experimental functions $\mathrm{F}(\omega_r)$ and $R(\omega_r)$. The prediction is thus only modified when the growth rate takes large values. This observation is emphasized by the frequency prediction that shows slight differences but only in regions corresponding to large growth rates. Finally, results for the second mode are presented in Fig. B.9-center. One identifies the mode switching phenomenon described in Chapter 8. The third mode reaches stability for perturbation levels larger than $v_1^{\mathrm{rms}}/v_0 = 0.35$ while the second mode takes over and reach a limit cycle at a perturbation level $v_1^{\mathrm{rms}}/v_0 = 0.6$. The prediction of the limit cycle amplitude is not modified and the three methods yield the same value $v_1^{\mathrm{rms}}/v_0 = 0.6$ for the limit cycle amplitude. However, for intermediate perturbation levels, when the growth rate takes large positive values, a large difference is observed between predictions obtained with (blue and green lines) and without (red line) taking into account the growth rate in the FDF and the boundary condition expressions in the simulations.

Results presented here show that no modification of the predicted limit cycle amplitude are observed in this case. However, simulations show that the predicted growth rate differs, altering in turn the time that the instability takes to reach limit cycle. This problem is studied in the next subsection.

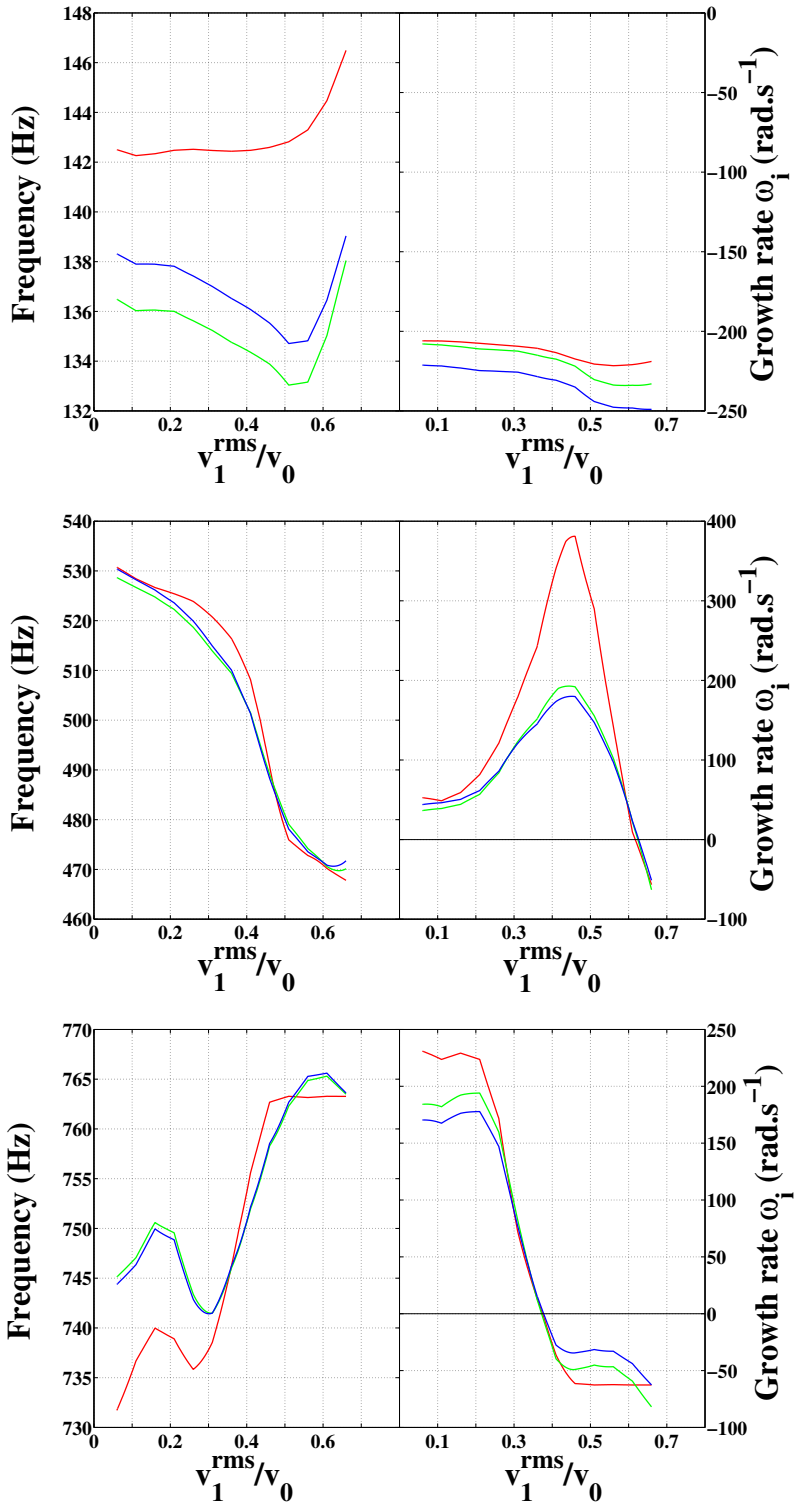

Figure B.9: *Results from a nonlinear stability analysis combining a low-order acoustic network solver and the FDF methodology, for the first (top), second (center) and third (bottom) eigenmode. (red line) The flame frequency response and the inlet and outlet reflection coefficients are taken as* $\mathrm{F}(\omega_r)$ *and* $R(\omega_r)$*. (green line)* $\mathrm{F}(\omega)$ *and* $R(\omega_r)$*. (blue line)* $\mathrm{F}(\omega)$ *and* $R(\omega)$*.*

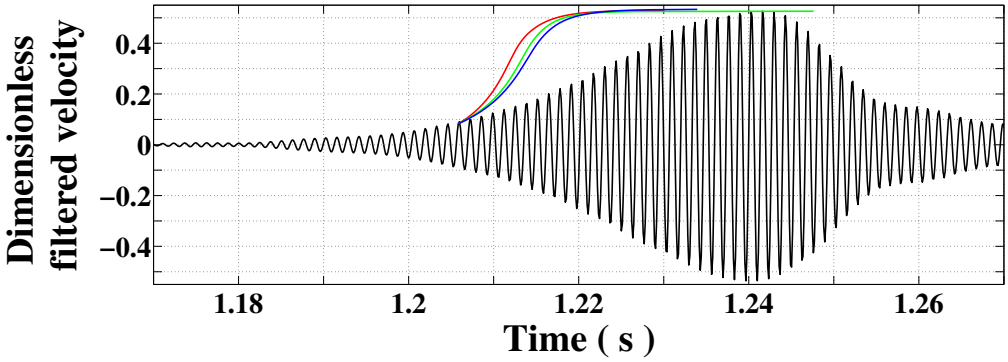

Figure B.10: *Filtered dimensionless velocity measurements as a function of time. Colored lines represents the instability amplitude time evolution determined from the results of the nonlinear stability analysis: (red line) The flame frequency response and the inlet and outlet reflection coefficients are taken as* $\mathrm{F}(\omega_r)$ *and* $R(\omega_r)$*. (green line)* $\mathrm{F}(\omega)$ *and* $R(\omega_r)$*. (blue line)* $\mathrm{F}(\omega)$ *and* $R(\omega)$*.*

B.4.2 Time evolution of the instability amplitude

Measurements of the velocity signal shown in Fig.8.11 from Chapter 8 indicate that a mode switching occurs when the plenum length is set to $L_1 = 0.54$ m. This signal is here filtered around the third mode frequency to extract the time evolution of that mode. The results are plotted in Fig. B.10. The amplitude of the third mode first increases before reaching a maximum corresponding to the condition $\omega_i = 0$ and then decreases before almost vanishing.

In the following, the dimensionless rms amplitude of a mode is defined as $a_1 = v_1^{\mathrm{rms}}/U_b$. The time evolution of the instability amplitude is determined by the following differential equation:

$$\frac{da_1}{dt} = \omega_i(a_1)a_1 \tag{B.9}$$

A comparison between results from simulations with the FDF and the velocity time signal is conducted by determining the time evolution of the instability amplitude $a_1(t)$. It relies on the integration of Eq. (B.9) performed from the lowest perturbation level investigated $a_{11} = 0.06$ to a perturbation level a_{1k}, where $k \in [1 : N]$ and N is the number of amplitudes investigated in the nonlinear stability analysis:

$$t_k = \int_{a_{11}=0.06}^{a_{1k}} \frac{da_1}{\omega_i(a_1)a_1} \tag{B.10}$$

Results for the discrete time evolution of the instability amplitude $a_{1k}(t_k)$ are plotted along with the instability velocity filtered signal in Fig. B.10. Results

show that simulation with the FDF with or without including the growth rate ω_i in the calculations does not reproduce the exact time evolution of the third mode amplitude. However, differences appear in the slope of the time evolution of this amplitude. Due to smaller growth rates, the new method exhibits a slower increase towards its maximum amplitude (blue line in Fig. B.10) compared to the previous method (red line in Fig. B.10). Although the result is still far from measurements, the new method still represents an improvement compared to the classical FDF method.

B.5 Synthesis

A study conducted with analytical FTF expressions showed that including the growth rate ω_i in the FTF expression can change drastically the predicted flame response to incoming perturbations. A theoretical study showed that, if the growth rate is taken into account in the FTF used for a linear stability analysis, the prediction of the stability of a combustor can be significantly modified. A reconstruction technique was proposed to extend FTF measured for real angular frequencies to build a frequency response representation of the FTF over the whole complex angular frequency plane. Analytical expressions and results from this technique were shown to match well as long as the growth rate does not take large negative values. Finally, this technique was coupled to a nonlinear stability analysis that showed that limit cycle predictions are not modified in the configuration investigated in this work. In that case, only the time evolution of the instability amplitude is modified due to smaller growth rates, but the system reaches the same oscillation state at limit cycle.

These problems were used to emphasize that more work is necessary on the way FTF and FDF may be coupled to acoustics to conduct stability analyses. This point needs to be addressed in more details, especially in configurations with larger damping rates, in order to fully assess the impact of the growth rate ω_i on thermo-acoustic instability prediction methods.

Appendix C

Validation of the Melling model for perforates in AVSP

The Helmholtz solver AVSP allows to take into account perforated plate models as a jump condition between two coupled boundaries (see [Gullaud *et al.* (2009); Gullaud (2010); Gullaud and Nicoud (2012)]. The model developed by Howe (1979) was included in AVSP to model the response of small perforations traversed by a bias flow to sound waves without describing all flow and geometrical details within these perforations in combustion chambers. It is well known that in these situations, sound waves may interact with vortices shed from the perforates resulting in sound absorption. The Howe model reproduces quite well this dissipation of acoustic energy that needs to be taken into account to determine limit cycles of thermo-acoustic instabilities in combustion chambers equipped with perforates [Tran *et al.* (2009)]. In the case considered in this study where a collection of conical flames are anchored on a perforated plate, there are no vortices shed from the plate holes [Noiray *et al.* (2006b); Noiray *et al.* (2007)]. For low frequency sound waves, the motion within the perforations may be considered in bulk oscillation mode. The model proposed by Melling (1973) reproduces well this behavior [Noiray (2007); Boudy (2012)]. An implementation of this model in the AVSP Helmholtz solver is here validated by different simulations.

C.1 Low-order model (LOM)

A low-order acoustic network model is used to obtain a reference solution to validate simulations with AVSP and the Melling model. A generic configuration is considered with two cylindrical cavities (of length L_1 and L_2) that are separated by a perforated plate of thickness h (see Fig. C.1). In each cavities, longitudinal acoustic waves are propagating:

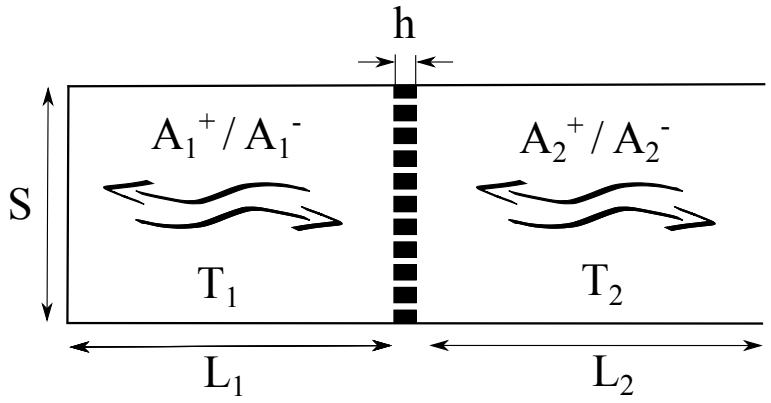

Figure C.1: *Scheme of the theoretical validation case investigated. It comprise two cavities separated by a perforated plate of thickness h. The first (resp. the second) cavity is of temperature T_1 (resp. T_2) and of length L_1 (resp. L_2). Both cavities are of cross-section area S.*

$$p_{1,n}(z_n) = A_n^+ e^{ik_n z_n} + A_n^- e^{-ik_n z_n} \tag{C.1}$$

$$\rho_n c_n u_{1,n}(z_n) = A_n^+ e^{ik_n z_n} - A_n^- e^{-ik_n z_n} \tag{C.2}$$

where $n = 1$ or 2 in the first and the second cavity, c_n, $k_n = \omega/c_n$ and ρ_n are the speed of sound, the acoustic wavelength and the density in the n^{th} cavity. A velocity node is fixed at the inlet and a pressure node is used at the outlet:

$$u_{1,1}(z_1 = 0) = 0 \tag{C.3}$$

$$p_{1,2}(z_2 = L_2) = 0 \tag{C.4}$$

The model proposed by Melling (1973) is used to model the response of a perforated plate linking the two cavities. In this model, the acoustic pressure difference between the two extremities of the perforated plate is linked to the acoustic velocity on the upstream side of the perforated plate and the acoustic volume flowrate remains constant:

$$p_{1,2}(z_2 = 0) - p_{1,1}(z_1 = L_1) = \frac{i\omega\rho_1 h}{\sigma}\left(1 + \frac{l_\nu}{a}(1+i)\right) u_{1,1}(z_1 = L_1) \tag{C.5}$$

$$S_2 u_{1,2}(z_2 = 0) - S_1 u_{1,1}(z_1 = L_1) = 0 \tag{C.6}$$

where h is the perforated plate thickness, $l_\nu = (2\nu/\omega)^{1/2}$ is the viscous acoustic boundary layer thickness in the perforations, ν is the kinematic viscosity, a is the perforated plate hole radius, σ is the perforated plate porosity and $S_1 = S_2 = S$ is the cross section area of the cavities. By combining these different expressions Eq. (C.1) to Eq. (C.6), one finds the following dispersion relation:

$$\frac{S_1\rho_2 c_2}{S_2\rho_1 c_1}\sin(\omega L_1/c_1)\sin(\omega L_2/c_2) - \cos(\omega L_1/c_1)\cos(\omega L_2/c_2) + \frac{\omega h}{c_1\sigma}\left(1+\frac{l_\nu}{a}(1+i)\right)\cos(\omega L_2/c_2)\sin(\omega L_1/c_1) = 0 \tag{C.7}$$

This equation is solved by an iterative method in Matlab for the following parameters: $h = 0.003$ or 0.015 m, $T_1 = 300$ K, $T_2 = 300$ or 900 K, $L_1 = L_2 = 0.5$ m, $S = S_1 = S_2 = 0.031$ m^2 (corresponding to a radius of 0.1 m), $a = 0.001$ m, $d = 0.003$ m, $\sigma = 0.34$, $\nu = 15.6 \cdot 10^{-6}$ m^{2}s^{-1}. The ratio ρ_2/ρ_1 is given by T_1/T_2 and the speed of sound is determined in each cavity with the following relation: $c_n = (\gamma r T_n)^{\frac{1}{2}}$ where $\gamma = 1.4$ and $r = 287$ J.kg^{-1}.K^{-1}.

C.2 AVSP model validation

The same system is simulated using AVSP. A mesh is generated for two geometrical configurations with two different perforated plate thicknesses $h = 0.003$ or 0.015 m (see Fig. C.2). For each geometrical configuration, simulations are carried out with two different temperature fields. Simulations are first carried out with a uniform speed of sound field corresponding to air at $T_u = 300$ K. Simulations are then conducted with the first cavity filled with air at $T_u = 300$ K and the second cavity filled with air at $T_b = 900$ K. These two configurations are shown in Fig. C.3 for the thicker perforated plate $h = 15$ mm. Then, the

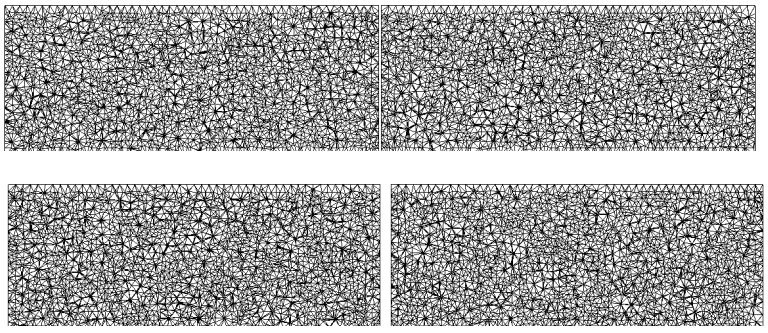

Figure C.2: *2D slices of the meshes used for the calculations. Top figure: thin plate $h = 3$ mm. Bottom figure: thick plate $h = 15$ mm.*

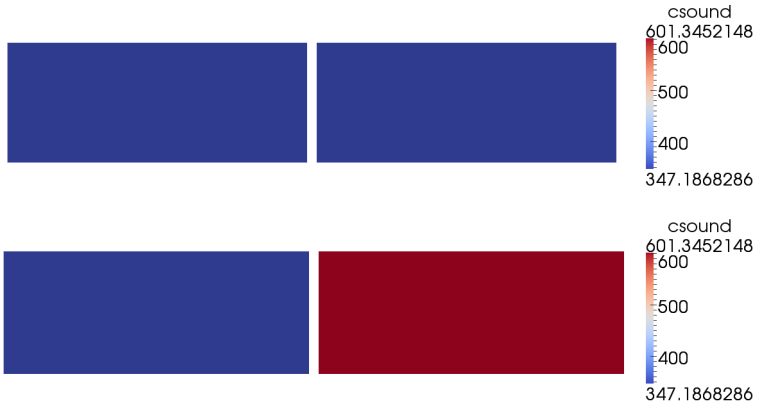

Figure C.3: *Distribution of the speed of sound used for the calculations. Top figure:* $c_0 = 347 m.s^{-1}$. *Bottom figure:* $c_0 = 347 m.s^{-1}$ *in the upstream cavity corresponding to* $T_1 = 300$ *K and* $c_0 = 601 m.s^{-1}$ *in the downstream cavity, corresponding to* $T_2 = 900$ *K.*

acoustic eigenmodes are determined in terms of real frequencies and growth rates of the modes. These simulations also give the corresponding structure of the modes in terms of the pressure fluctuation modulus spatial distribution. Typical results are shown in Figs. C.4 and C.5 for the first and the second acoustic eigenmodes when the whole setup is filled with air at a constant temperature $T_1 = T_2 = 300$ K and for the two different perforated plates investigated. These figures show that the pressure distributions correspond to a 1/4-wave mode and a 3/4-wave mode that are distributed over the whole length of the combustor $L_1 + L_2 + h$. One can also observe that the perforated plate has only a very weak effect on the modal structure. Simulations performed with different temperatures in the cavities, $T_1 = 300$ K and $T_2 = 900$ K, are not shown here. The resulting pressure distributions still feature a 1/4-wave and a 3/4-wave modal distribution.

C.3 Comparison between AVSP and LOM simulations

Results from simulations with AVSP and the LOM are presented in Table C.1, for different plate thicknesses, temperature differences between cavities 1 and 2, and different modes. Results appear to match extremely well in terms of real frequency f and growth rates $\omega_i/(2\pi)$. One can also observe that an increase in the plate thickness leads to a significant increase in the damping of the system while the frequency does not change much. A change of temperature in the second cavity results in a strong modification of the acoustic eigenfrequency due to the modification of the speed of sound.

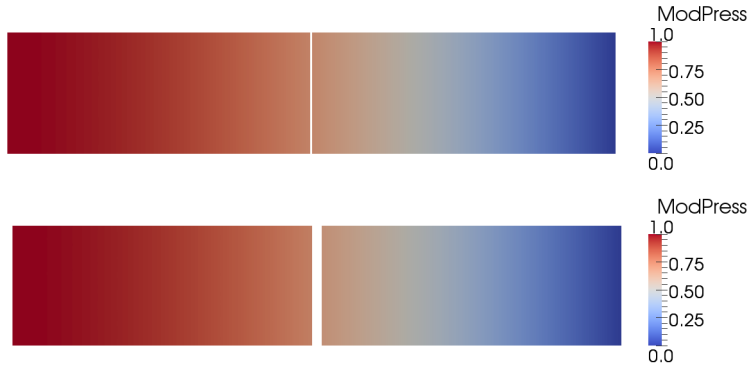

Figure C.4: *Pressure modulus distribution of the first acoustic eigenmode of the system. Top figure: $h = 3$ mm. Bottom figure: $h = 15$ mm.*

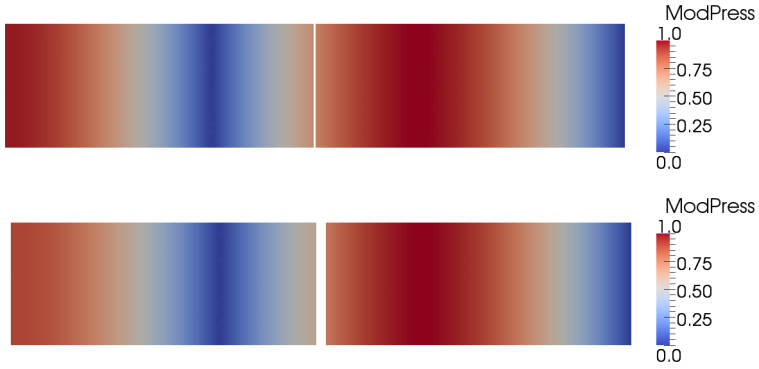

Figure C.5: *Pressure modulus distribution of the second acoustic eigenmode of the system. Top figure: $h = 3$ mm. Bottom figure: $h = 15$ mm.*

These simulations show that the model of Melling can now be used with confidence in AVSP to represent the acoustic response of perforated plate (without flow separation and acoustic dissipation taking place at the perforation outlet). This model is used in the generic combustor configuration investigated in Chapters. 8.

Plate thickness h (mm)	$\Delta_1^2 T$ (K)	Mode number	AVSP	LOM
3	0	1	86.3236 -0.090872i	86.3245 -0.090886i
3	600	1	125.2989 -0.24892i	125.3002 -0.24908i
3	0	2	259.0709 -0.15736i	259.089 -0.15741i
3	600	2	323.8776 -0.015498i	323.9026 -0.015512i
15	0	1	84.4787 -0.43916i	84.4814 -0.44016i
15	600	1	119.5956 -1.1348i	119.604 -1.1399i
15	0	2	254.0098 -0.75442i	254.0289 -0.75557i
15	600	2	323.3162 -0.077135i	323.3407 -0.077218i

Table C.1: *Acoustic eigenmodes and growth rates of the combustor determined with AVSP and with the LOM.*

References

Altay, H., S. Park, D. Wu, D. Wee, A. Annaswamy, and A. Ghoniem (2009). Modeling the dynamic response of a laminar perforated-plate stabilized flame. *Proceedings of the Combustion Institute 32*(1), 1359–1366. *(p. 26, 39, 40, 41, 45, 104, 107, 109, 149)*

Altay, H. M., K. S. Kedia, R. L. Speth, and A. F. Ghoniem (2010). Two-dimensional simulations of steady perforated-plate stabilized premixed flames. *Combustion Theory and Modelling 14*(1), 125–154. *(p. 40, 115)*

Armitage, C., R. Balachandran, E. Mastorakos, and R. Cant (2006). Investigation of the nonlinear response of turbulent premixed flames to imposed inlet velocity oscillations. *Combustion and Flame 146*(3), 419–436. *(p. 10)*

Baade, P. K. (1978). Design criteria and models for preventing combustion oscillations. *ASHRAE Transactions*. *(p. 13)*

Baillot, F. and A. Bourehla (1997). Burning velocity of pockets from a vibrating flame experiment. *Combustion Science and Technology 126*(1-6), 201–224. *(p. 82)*

Baillot, F., A. Bourehla, and D. Durox (1996). The Characteristics Method and Cusped Flame Fronts. *Combustion Science and Technology 112*(1), 327–350. *(p. 10, 24, 26, 27, 30, 44, 78, 136)*

Baillot, F., D. Durox, and R. Prud'homme (1992). Experimental and theoretical study of a premixed vibrating flame. *Combustion and Flame 88*(2), 149–168. *(p. 10, 24, 26, 27, 29, 30, 72, 78, 88, 101, 136, 144)*

Balachandran, R., B. Ayoola, C. Kaminski, A. Dowling, and E. Mastorakos (2005). Experimental investigation of the nonlinear response of turbulent premixed flames to imposed inlet velocity oscillations. *Combustion and Flame 143*(1-2), 37–55. *(p. 11, 43, 57, 158)*

Bédat, B. and R. K. Cheng (1996). Effects of buoyancy on premixed flame stabilization. *Combustion and Flame 107*(1-2), 13 – 26. *(p. 51)*

Bellows, B. D., M. K. Bobba, A. Forte, J. M. Seitzman, and T. Lieuwen (2007). Flame transfer function saturation mechanisms in a swirl-stabilized combustor. *Proceedings of the Combustion Institute 31*(2), 3181–3188. *(p. 10, 11, 12, 43, 158)*

Beltagui, S. and N. Maccallum (1976). Aerodynamics of vane-swirled flames in furnaces. *Journal Of The Institute Of Fuel 49*(401), 183–193. *(p. 122)*

Benoit, L. (2005). *Prédiction des Instabilités Thermoacoustiques dans les turbines à gaz*. Ph. D. thesis, Université Montpellier II. *(p. 164)*

Birbaud, A., S. Ducruix, D. Durox, and S. Candel (2008). The nonlinear response of inverted "V" flames to equivalence ratio nonuniformities. *Combustion and Flame 154*(3), 356–367. *(p. 6, 10)*

Birbaud, A., D. Durox, and S. Candel (2006). Upstream flow dynamics of a laminar premixed conical flame submitted to acoustic modulations. *Combustion and Flame 146*(3), 541–552. *(p. 10, 26, 28, 29, 78, 88, 136, 193)*

Birbaud, A., D. Durox, S. Ducruix, and S. Candel (2007a). Dynamics of confined premixed flames submitted to upstream acoustic modulations. *Proceedings of the Combustion Institute 31*(1), 1257–1265. *(p. 26, 31, 122)*

Birbaud, A. L. (2006). *Dynamique d'interactions - Sources des instabilités de combustion*. Ph. D. thesis, Ecole Centrale Paris. *(p. 3, 191)*

Birbaud, A. L., D. Durox, S. Ducruix, and S. Candel (2007b). Dynamics of free jets submitted to upstream acoustic modulations. *Physics of Fluids 19*(1), 013602. *(p. 12)*

Blackshear, P. L. J. (1953). Driving standing waves by heat addition. *Symposium (International) on Combustion 4*(1), 553–566. *(p. 19, 21)*

Blumenthal, R. S., P. Subramanian, R. Sujith, and W. Polifke (2013). Novel perspectives on the dynamics of premixed flames. *Combustion and Flame 160*(7), 1215–1224. *(p. 26, 37, 38, 72, 79, 94, 96, 144)*

Borghesi, G., F. Biagioli, and B. Schuermans (2009). Dynamic response of turbulent swirling flames to acoustic perturbations. *Combustion Theory and Modelling 13*(3), 487–512. *(p. 194)*

Boudy, F. (2012). *Analyse de la dynamique non-linéaire et du contrôle des instabilités de combustion fondée sur la "Flame Describing Function" (FDF)*. Ph. D. thesis, Ecole Centrale Paris. *(p. 4, 16, 41, 148, 149, 159, 171, 172, 173, 175, 177, 191, 212, 214, 219)*

Boudy, F., D. Durox, T. Schuller, and S. Candel (2011). Nonlinear mode triggering in a multiple flame combustor. *Proceedings of the Combustion Institute 33*(1), 1121–1128. *(p. 11, 12, 39, 42, 43, 118, 119, 148, 159, 160, 163, 171, 184, 185, 188, 214)*

Boudy, F., D. Durox, T. Schuller, and S. Candel (2012). Nonlinear flame describing function analysis of galloping limit cycles featuring chaotic states in premixed combustors. *ASME Conference Proceedings*. *(p. 160)*

Boudy, F., D. Durox, T. Schuller, and S. Candel (2013). Analysis of limit cycles sustained by two modes in the flame describing function framework. *Comptes Rendus Mécanique 341*(1-2), 181–190. Combustion, spray and flow dynamics for aerospace propulsion. *(p. 148, 160, 195, 214)*

Boudy, F., D. Durox, T. Schuller, G. Jomaas, and S. Candel (2011). Describing function analysis of limit cycles in a multiple flame combustor. *Journal of Engineering for Gas Turbines and Power 133*(6), 061502. *(p. 122, 148, 159, 163, 171, 183, 186, 187, 214)*

Bourehla, A. and F. Baillot (1998). Appearance and Stability of a Laminar Conical Premixed Flame Subjected to an Acoustic Perturbation. *Combustion and Flame 114*(3-4), 303–318. *(p. 11, 82)*

Boyer, L. and J. Quinard (1990). On the dynamics of anchored flames. *Combustion and Flame 82*(1), 51–65. *(p. 23, 24, 30, 32)*

Camporeale, S. M., B. Fortunato, and G. Campa (2011). A finite element method for three-dimensional analysis of thermo-acoustic combustion instability. *Journal of Engineering for Gas Turbines and Power 133*(1), 011506. *(p. 9, 160)*

Candel, S. (2002). Combustion dynamics and control: Progress and challenges. *Proceedings of the Combustion Institute 29*(1), 1–28. *(p. 4, 6)*

Candel, S. M. (1992). Combustion instabilities coupled by pressure waves and their active control. *Symposium (International) on Combustion 24*(1), 1277–1296. Twenty-Fourth Symposium on Combustion. *(p. 4, 5)*

Cho, J. H. and T. Lieuwen (2005). Laminar premixed flame response to equivalence ratio oscillations. *Combustion and Flame 140*(1-2), 116–129. *(p. 10)*

Chung, S. and C. Law (1984). An invariant derivation of flame stretch. *Combustion and Flame 55*(1), 123–125. *(p. 36)*

Chung, S. and C. Law (1988). An integral analysis of the structure and propagation of stretched premixed flames. *Combustion and Flame 72*(3), 325–336. *(p. 36)*

Coats, C., Z. Chang, and P. Williams (2010). Excitation of thermoacoustic oscillations by small premixed flames. *Combustion and Flame 157*(6), 1037–1051. *(p. 39)*

Coats, C., Z. Chang, and P. Williams (2011). Thermoacoustic oscillations in ducted domestic heating systems. *Applied Acoustics 72*(5), 268–277. *(p. 39)*

Correa, S. M. (1998). Power generation and aeropropulsion gas turbines: From combustion science to combustion technology. *Symposium (International) on Combustion 27*(2), 1793–1807. *(p. 2)*

Crighton, D., A. Dowling, J. Ffowcs Williams, M. Heckl, and F. Leppington (1992). *Modern Methods in Analytical Acoustics - Lecture Notes*. Spinger-Verlag, New York. *(p. 7)*

Crocco, L. (1951). Aspects of combustion instability in liquid propellant rocket motors. part 1. *Journal of the American Rocket Society 21*. *(p. 4, 20)*

Crocco, L. and S. Cheng (1956). Theory of combustion instability in liquid propellant rocket motors. In *AGARDO-GRAPH number 8*. Butterworths Science Publication. *(p. 4, 7, 20)*

Culick, F. (1994). Some recent results for nonlinear acoustic in combustion chambers. *AIAA Journal 32*(1), 146–169. *(p. 158)*

Culick, F. (2006). *Unsteady motions in combustion chambers for propulsion systems*. AGARDograph, NATO/RTO-AG-AVT-039. *(p. 4, 7)*

Cuquel, A., D. Durox, and T. Schuller (2011a). Experimental Determination of Flame Transfer Function Using Random Velocity Perturbations. *ASME Conference Proceedings 2011*(54624), 793–802. *(p. 90)*

Cuquel, A., D. Durox, and T. Schuller (2011b). Theoretical and experimental determination of the flame transfer function of confined premixed conical flames. *7th Mediterranean Combustion Symposium*. *(p. 123, 144)*

Cuquel, A., D. Durox, and T. Schuller (2013a). Impact of flame base dynamics on the nonlinear frequency response of conical flames. *Comptes Rendus Mécanique 341*(1-2), 171–180. Combustion, spray and flow dynamics for aerospace propulsion. *(p. 109)*

Cuquel, A., D. Durox, and T. Schuller (2013b). Scaling the flame transfer function of confined premixed conical flames. *Proceedings of the Combustion Institute 34*(1), 1007 – 1014. *(p. 93, 177)*

de Goey, L., J. van Oijen, V. Kornilov, and J. t. T. Boonkkamp (2011). Propagation, dynamics and control of laminar premixed flames. *Proceedings of the Combustion Institute 33*(1), 863–886. *(p. 4, 12, 33, 34)*

Docquier, N. and S. Candel (2002). Combustion control and sensors: a review. *Progress in Energy and Combustion Science 28*(2), 107–150. *(p. 6)*

Dowling, A. P. (1997). Nonlinear self-excited oscillations of a ducted flame. *Journal of Fluid Mechanics 346*, 271–290. *(p. 11, 20, 43, 53, 71)*

Dowling, A. P. (1999). A kinematic model of a ducted flame. *Journal of Fluid Mechanics 394*, 51–72. *(p. 53, 104, 120, 158)*

Dowling, A. P. and A. S. Morgans (2005). Feedback control of combustion oscillations. *Annual Review of Fluid Mechanics 37*(1), 151–182. *(p. 6)*

Duchaine, F., F. Boudy, D. Durox, and T. Poinsot (2011). Sensitivity analysis of transfer functions of laminar flames. *Combustion and Flame 158*(12), 2384–2394. *(p. 6, 20, 26, 39, 42, 118, 122)*

Ducruix, S. (1999). *Dynamique des Interactions Acoustique-Combustion*. Ph. D. thesis, Ecole Centrale Paris. *(p. 3, 191)*

Ducruix, S., D. Durox, and S. Candel (2000). Theoretical and experimental determinations of the transfer function of a laminar premixed flame. *Proceedings of the Combustion Institute 28*(1), 765–773. *(p. 10, 20, 21, 27, 28, 29, 32, 37, 57, 79, 80, 81, 82, 84, 85, 87, 94, 104, 118, 123, 144, 177)*

Ducruix, S., T. Schuller, D. Durox, and M. Candel, Sébastien (2003). Combustion Dynamics and Instabilities: Elementary Coupling and Driving Mechanisms. *Journal of Propulsion and Power 19*(5), 722–734. *(p. 5, 19)*

Durox, D., F. Baillot, P. Scouflaire, and R. Prud'homme (1990). Some effects of gravity on the behaviour of premixed flames. *Combustion and Flame 82*(1), 66 – 74. *(p. 51, 101)*

Durox, D., A. L. Birbaud, and S. Candel (2004). Dynamique de l'écoulement dans les flammes oscillantes prémélangées. *Congrès Francophone de Vélocimétrie Laser*. *(p. 3, 88)*

Durox, D., S. Ducruix, and F. Lacas (1999). Flow seeding with an air nebulizer. *Experiments in Fluids 27*, 408–413. *(p. 50)*

Durox, D., T. Schuller, and S. Candel (2005). Combustion dynamics of inverted conical flames. *Proceedings of the Combustion Institute 30*(2), 1717–1724. *(p. 10, 12)*

Durox, D., T. Schuller, N. Noiray, A. Birbaud, and S. Candel (2009). Rayleigh criterion and acoustic energy balance in unconfined self-sustained oscillating flames. *Combustion and Flame 156*(1), 106–119. *(p. 180)*

Durox, D., T. Schuller, N. Noiray, and S. Candel (2009). Experimental analysis of nonlinear flame transfer functions for different flame geometries. *Proceedings of the Combustion Institute 32*(1), 1391–1398. *(p. 11, 20, 29, 39, 43, 45, 46, 57, 58, 67, 68, 87, 94, 117, 118, 119, 122, 136, 142, 158)*

Fanaca, D., P. R. Alemela, C. Hirsch, and T. Sattelmayer (2010). Comparison of the flow field of a swirl stabilized premixed burner in an annular and a single burner combustion chamber. *Journal of Engineering for Gas Turbines and Power 132*(7), 071502. *(p. 122)*

Fleifil, M., A. M. Annaswamy, Z. A. Ghoneim, and A. F. Ghoniem (1996). Response of a laminar premixed flame to flow oscillations: A kinematic model and thermoacoustic instability results. *Combustion and Flame 106*(4), 487–510. *(p. 27, 104, 123)*

Giauque, A., L. Selle, L. Gicquel, T. Poinsot, H. Buechner, P. Kaufmann, and W. Krebs (2005). System identification of a large-scale swirled partially premixed combustor using LES and measurements. *Journal of Turbulence 6*. *(p. 6, 10)*

Gicquel, L., G. Staffelbach, and T. Poinsot (2012). Large Eddy Simulations of gaseous flames in gas turbine combustion chambers. *Progress in Energy and Combustion Science 38*(6), 782–817. *(p. 6)*

Gikadi, J., W. Ullrich, T. Sattelmayer, and F. Turrini (2013). Prediction of the acoustic losses of a swirl atomizer nozzle under non-reactive conditions. *ASME Conference Proceedings*. *(p. 195)*

Goy, C. J., S. R. James, and S. Rea (2006). *Monitoring Combustion Instabilities: E.ON UK's Experience*. American Institute of Aeronautics and Astronautics. *(p. 2)*

Graham, O. S. and A. P. Dowling (2011). A low-order modelling of ducted flames with temporally varying equivalence ratio in realistic geometries. *ASME Conference Proceedings 2011*(54624), 277–288. *(p. 10)*

Gu, X., M. Haq, M. Lawes, and R. Woolley (2000). Laminar burning velocity and Markstein lengths of methane/air mixtures. *Combustion and Flame 121*(1-2), 41–58. *(p. 110, 116)*

Gullaud, E. (2010). *Impact des plaques multiperforées sur l'acoustique des chambres de combustion aéronautiques*. Ph. D. thesis, Université Montpellier II. *(p. 164, 166, 169, 219)*

Gullaud, E., S. Mendez, C. Sensiau, F. Nicoud, and T. Poinsot (2009). Effect

of multiperforated plates on the acoustic modes in combustors. *Comptes Rendus Mécanique 337*(6-7), 406–414. Combustion for aerospace propulsion. *(p. 166, 219)*

Gullaud, E. and F. Nicoud (2012). Effect of perforated plates on the acoustics of annular combustors. *AIAA journal 50*(12), 2629–2642. *(p. 9, 166, 219)*

Hauser, M., C. Hirsch, and T. Sattelmayer (2011). Influence of the confinement on the flame transfer function. *18th International Congress on Sound and Vibration*. *(p. 122, 194)*

Hemchandra, S. (2012). Premixed flame response to equivalence ratio fluctuations: Comparison between reduced order modeling and detailed computations. *Combustion and Flame 159*(12), 3530 – 3543. *(p. 10, 45, 193)*

Hemchandra, S. and T. Lieuwen (2010). Local consumption speed of turbulent premixed flames - an analysis of memory effects. *Combustion and Flame 157*(5), 955 – 965. *(p. 45)*

Hemchandra, S., N. Peters, and T. Lieuwen (2011). Heat release response of acoustically forced turbulent premixed flames - role of kinematic restoration. *Proceedings of the Combustion Institute 33*(1), 1609 – 1617. *(p. 44)*

Hermeth, S., G. Staffelbach, L. Gicquel, and T. Poinsot (2013). LES evaluation of the effects of equivalence ratio fluctuations on the dynamic flame response in a real gas turbine combustion chamber. *Proceedings of the Combustion Institute 34*(2), 3165 – 3173. *(p. 10)*

Higuera, F. (2009). Aerodynamics of a slender axisymmetric Bunsen flame with large gas expansion. *Combustion and Flame 156*(5), 1063–1067. *(p. 124)*

Hirsch, C., D. Fanaca, P. Reddy, W. Polifke, and T. Sattelmayer (2005). Influence of the swirler design on the flame transfer function of premixed flames. *ASME Conference Proceedings 2005*(4725X), 151–160. *(p. 10, 12)*

Howe, M. (1979). On the theory of unsteady high reynolds number flow through a circular aperture. *Proceedings of the royal society A 366*, 205–223. *(p. 166, 219)*

Hubbard, S. and A. Dowling (1998). Acoustic instabilities in premix burners. *AIAA Aerospace Sciences Meeting*. *(p. 9)*

Hubbard, S. and A. P. Dowling (2001). Acoustic Resonances of an Industrial Gas Turbine Combustion System. *Journal of Engineering for Gas Turbines and Power 123*(4), 766–773. *(p. 10, 13)*

Huber, A. and W. Polifke (2009a, 06). Dynamics of practical premixed flames, part I: model structure and identification. *International Journal of Spray and Combustion Dynamics 1*(2), 199–228. *(p. 59)*

Huber, A. and W. Polifke (2009b, 06). Dynamics of practical premixed flames, part II: identification and interpretation of CFD data. *International Journal of Spray and Combustion Dynamics 1*(2), 229–249. *(p. 59, 62)*

Hurle, I. R., R. B. Price, T. M. Sugden, and A. Thomas (1968). Sound

Emission from Open Turbulent Premixed Flames. *Proceedings of the Royal Society of London. Series A. Mathematical and Physical Sciences 303*(1475), 409–427. *(p. 10, 25, 51, 57, 126)*

Jegadeesan, V. and R. Sujith (2013). Experimental investigation of noise induced triggering in thermoacoustic systems. *Proceedings of the Combustion Institute 34*(2), 3175–3183. *(p. 163)*

Joulin, G. (1982). Flame oscillations induced by conductive losses to a flat burner. *Combustion and Flame 46*(0), 271–281. *(p. 12, 33, 107)*

Joulin, G. and G. Sivashinsky (1991). Pockets in premixed flames and combustion rate. *Combustion Science and Technology 77*(4-6), 329–335. *(p. 82)*

Kabiraj, L. and R. I. Sujith (2012). Nonlinear self-excited thermoacoustic oscillations: intermittency and flame blowout. *Journal of Fluid Mechanics*, 1–22. *(p. 195)*

Karimi, N., M. J. Brear, S.-H. Jin, and J. P. Monty (2009). Linear and non-linear forced response of a conical, ducted, laminar premixed flame. *Combustion and Flame 156*(11), 2201–2212. *(p. 26, 29, 33, 67, 68, 82, 104, 114, 116, 118, 119)*

Kashinath, K., S. Hemchandra, and M. P. Juniper (2012). Nonlinear phenomena in thermoacoustic systems with premixed flames. *ASME Conference Proceedings 2012*. *(p. 7)*

Kedia, K., H. Altay, and A. Ghoniem (2011). Impact of flame-wall interaction on premixed flame dynamics and transfer function characteristics. *Proceedings of the Combustion Institute 33*(1), 1113–1120. *(p. 26, 39, 40, 109, 115)*

Kedia, K. S. and A. F. Ghoniem (2012). Mechanisms of stabilization and blowoff of a premixed flame downstream of a heat-conducting perforated plate. *Combustion and Flame 159*(3), 1055–1069. *(p. 40)*

Kedia, K. S. and A. F. Ghoniem (2013). An analytical model for the prediction of the dynamic response of premixed flames stabilized on a heat-conducting perforated plate. *Proceedings of the Combustion Institute 34*(1), 921 – 928. *(p. 39, 40, 115)*

Keller, J. J. (1995). Thermoacoustic oscillations in combustion chambers of gas turbines. *AIAA Journal 33*(12), 2280–2287. *(p. 9, 13)*

Kim, K. and S. Hochgreb (2011). The nonlinear heat release response of stratified lean-premixed flames to acoustic velocity oscillations. *Combustion and Flame 158*(12), 2482 – 2499. *(p. 43)*

Kim, K. T., J. G. Lee, H. J. Lee, B. D. Quay, and D. A. Santavicca (2010). Characterization of forced flame response of swirl-stabilized turbulent lean-premixed flames in a gas turbine combustor. *Journal of Engineering for Gas Turbines and Power 132*(4), 041502. *(p. 10, 57)*

Kim, K. T., J. G. Lee, B. D. Quay, and D. Santavicca (2011). Experimental investigation of the nonlinear response of swirl-stabilized flames to equivalence ratio oscillations. *Journal of Engineering for Gas Turbines*

and Power 133(2), 021502. *(p. 10)*

Kim, K. T., J. G. Lee, B. D. Quay, and D. A. Santavicca (2010). Spatially distributed flame transfer functions for predicting combustion dynamics in lean premixed gas turbine combustors. *Combustion and Flame 157*(9), 1718 – 1730. *(p. 11, 160)*

Komarek, T. and W. Polifke (2010). Impact of swirl fluctuations on the flame response of a perfectly premixed swirl burner. *Journal of Engineering for Gas Turbines and Power 132*(6), 061503. *(p. 12)*

Kornilov, V. (2006). *Experimental research of acoustically perturbed bunsen flames*. Ph. D. thesis, Technische Universiteit Eindhoven. *(p. 104, 114)*

Kornilov, V., M. Manohar, and L. de Goey (2009). Thermo-acoustic behaviour of multiple flame burner decks: Transfer Function (de)composition. *Proceedings of the Combustion Institute 32*(1), 1383–1390. *(p. 39, 41, 42, 177)*

Kornilov, V., R. Rook, J. t. T. Boonkkamp, and L. de Goey (2009). Experimental and numerical investigation of the acoustic response of multi-slit Bunsen burners. *Combustion and Flame 156*(10), 1957–1970. *(p. 26, 29, 39, 41, 42, 118, 119, 177)*

Kornilov, V., K. Schreel, and L. de Goey (2007). Experimental assessment of the acoustic response of laminar premixed Bunsen flames. *Proceedings of the Combustion Institute 31*(1), 1239–1246. *(p. 26, 29, 30, 32, 33, 45, 67, 104, 118, 177, 193, 197)*

Kostiuk, L. and R. Cheng (1994). Imaging of premixed flames in microgravity. *Experiments in Fluids 18*, 59–68. *(p. 51)*

Krebs, W., P. Flohr, B. Prade, and S. Hoffmann (2002). Thermoacoustic stability chart for high-intensity gas turbine combustion systems. *Combustion Science and Technology 174*(7), 99–128. *(p. 10, 157)*

Krediet, H., C. Beck, W. Krebs, and J. Kok (2013). Saturation mechanism of the heat release response of a premixed swirl flame using LES. *Proceedings of the Combustion Institute 34*(1), 1223 – 1230. *(p. 158)*

Krediet, H. J., C. H. Beck, W. Krebs, S. Schimek, C. O. Paschereit, and J. B. W. Kok (2012). Identification of the Flame Describing Function of a Premixed Swirl Flame from LES. *Combustion Science and Technology 184*(7-8), 888–900. *(p. 158)*

Kulsheimer, C. and H. Buchner (2002). Combustion dynamics of turbulent swirling flames. *Combustion and Flame 131*(1-2), 70 – 84. *(p. 10)*

Lamarque, N. and T. Poinsot (2008). Boundary conditions for acoustic eigenmode computations in gas turbine combustion chambers. *AIAA journal 46*(9), 2282. *(p. 8)*

Law, C. and C. Sung (2000). Structure, aerodynamics, and geometry of premixed flamelets. *Progress in Energy and Combustion Science 26*(4-6), 459–505. *(p. 36)*

Lawn, C. J., S. Evesque, and W. Polifke (2004). A model for the thermoacoustic response of a premixed swirl burner, Part I: Acoustic aspects.

Combustion Science and Technology 176(8), 1331–1358. *(p. 9)*

Lee, D.-H. and T. C. Lieuwen (2003). Premixed flame kinetics in a longitudinal acoustic field. *Journal of Propulsion and Power 19*(5), 837–846. *(p. 32, 33, 79, 80, 104)*

Lefebvre, A. H. and D. R. Ballal (2010). *Gas Turbine Combustion, 3rd edition*. Taylor and Francis Group. *(p. 1, 2)*

LeHelley, P. (1994). *Etude théorique et expérimentale des instabiltés de combustion et de leur contrôle dans un brûleur prémélangé.* Ph. D. thesis, Ecole Centrale Paris. *(p. 4, 9, 36, 37, 191)*

Levine, H. and J. Schwinger (1948, Feb). On the Radiation of Sound from an Unflanged Circular Pipe. *Phys. Rev. 73*, 383–406. *(p. 177, 214)*

Li, J., F. Richecoeur, and T. Schuller (2012). Determination of heat release rate disturbances in unconfined flames based on fluctuations in the travel time of ultrasonic waves. *Combustion Science and Technology 184*(4), 533–555. *(p. 101)*

Lieuwen, T. (2005). Nonlinear kinematic response of premixed flames to harmonic velocity disturbances. *Proceedings of the Combustion Institute 30*(2), 1725–1732. *(p. 26, 43, 44)*

Lieuwen, T. and Y. Neumeier (2002). Nonlinear pressure-heat release transfer function measurements in a premixed combustor. *Proceedings of the Combustion Institute 29*(1), 99–105. Proceedings of the Combustion Institute. *(p. 11, 43)*

Lieuwen, T. and V. Yang (Eds.) (2005). *Combustion instabilities in gas turbine engines: operational experience, fundamental mechanisms, and modeling*. American Institute of Aeronautics and Astronautics, Reston, VA, USA. *(p. 2, 4, 5)*

Lieuwen, T. and B. T. Zinn (1998). The role of equivalence ratio oscillations in driving combustion instabilities in low NOx gas turbines. *Symposium (International) on Combustion 27*(2), 1809–1816. *(p. 13)*

Lieuwen, T. C. (2003). Modeling premixed combustion-acoustic wave interactions: a review. *Journal of Propulsion and Power 19*(5), 765–781. *(p. 79, 80)*

Ljung, L. (1999). *System Identification : Theory for the user* (2nd edition ed.). Prentice Hall, Englewood Cliffs, NJ. *(p. 58)*

Margolis, S. B. (1980). Bifurcation phenomena in burner-stabilized premixed flames. *Combustion Science and Technology 22*(3-4), 143–169. *(p. 33)*

Markstein, G. *et al.* (1964). *Nonsteady flame propagation*. Pergamon. *(p. 23, 36)*

Martin, C. E., L. Benoit, Y. Sommerer, F. Nicoud, and T. Poinsot (2006). Large-eddy simulation and acoustic analysis of a swirled staged turbulent combusstor. *AIAA Journal 44*(4), 741–750. *(p. 9)*

Matalon, M. and B. J. Matkowsky (1982, 10). Flames as gasdynamic discontinuities. *Journal of Fluid Mechanics 124*, 239–259. *(p. 36)*

Matsui, Y. (1981). An experimental study on pyro-acoustic amplification of

premixed laminar flames. *Combustion and Flame 3*(0), 199 – 209. *(p. 19, 22)*

McIntosh, A. C. and J. F. Clarke (1984). Second order theory of unsteady burner-anchored flames with arbitrary lewis number. *Combustion Science and Technology 38*(3-4), 161–196. *(p. 12, 33, 107)*

Mclntosh, A. C. (1990). On flame resonance in tubes. *Combustion Science and Technology 69*(4-6), 147–152. *(p. 33, 107)*

Mehta, P., M. Soteriou, and A. Banaszuk (2005). Impact of exothermicity on steady and linearized response of a premixed ducted flame. *Combustion and Flame 141*(4), 392–405. *(p. 20, 26, 31, 122, 124)*

Melling, T. (1973). The acoustic impedance of perforates at medium and high sound pressure levels. *Journal of Sound and Vibration 29*(1), 1–65. *(p. 167, 219, 220)*

Merk, H. (1957). An analysis of unstable combustion of premixed gases. *Symposium (International) on Combustion 6*(1), 500–512. *(p. 19, 21, 144)*

Moeck, J. P. and C. O. Paschereit (2012). Nonlinear interactions of multiple linearly unstable thermoacoustic modes. *International Journal of Spray and Combustion Dynamics 4*(1), 1–28. *(p. 72, 192)*

Nicoud, F., L. Benoit, C. Sensiau, and T. Poinsot (2007). Acoustic modes in combustors with complex impedances and multidimensional active flames. *AIAA Journal 45*(2), 426–441. *(p. 9, 157, 160, 165, 169)*

Noiray, N. (2007). *Analyse linéaire et non-linéaire des instabilités de combustion, application aux systèmes à injection multipoints et stratégies de contrôle*. Ph. D. thesis, Ecole Centrale Paris. *(p. 4, 159, 191, 219)*

Noiray, N., D. Durox, T. Schuller, and S. Candel (2006a). Dynamique de flames laminaires et couplage acoustique-combustion. *Congrès Francophone de Techniques Laser 2006*. *(p. 29, 42)*

Noiray, N., D. Durox, T. Schuller, and S. Candel (2006b). Self-induced instabilities of premixed flames in a multiple injection configuration. *Combustion and Flame 145*(3), 435–446. *(p. 39, 42, 87, 157, 177, 219)*

Noiray, N., D. Durox, T. Schuller, and S. Candel (2007). Passive control of combustion instabilities involving premixed flames anchored on perforated plates. *Proceedings of the Combustion Institute 31*(1), 1283–1290. *(p. 219)*

Noiray, N., D. Durox, T. Schuller, and S. Candel (2008). A unified framework for nonlinear combustion instability analysis based on the flame describing function. *Journal of Fluid Mechanics 615*, 139–167. *(p. 11, 12, 20, 43, 58, 118, 158, 159, 160, 161, 163, 177)*

Noiray, N. and B. Schuermans (2012). Theoretical and experimental investigations on damper performance for suppression of thermoacoustic oscillations. *Journal of Sound and Vibration 331*(12), 2753–2763. *(p. 7)*

Oppenheim, A. V., R. W. Schafer, and J. R. Buck (1998). *Discrete-Time Signal Processing* (2nd edition ed.). Prentice Hall. *(p. 65)*

Palies, P. (2010). *Dynamique et instabilités de combustion de flammes swirlées*. Ph. D. thesis, Ecole Centrale Paris. *(p. 180)*

Palies, P., D. Durox, T. Schuller, and S. Candel (2010). The combined dynamics of swirler and turbulent premixed swirling flames. *Combustion and Flame 157*(9), 1698–1717. *(p. 10, 12, 57, 58)*

Palies, P., D. Durox, T. Schuller, and S. Candel (2011). Nonlinear combustion instability analysis based on the flame describing function applied to turbulent premixed swirling flames. *Combustion and Flame 158*(10), 1980–1991. *(p. 11, 12, 158, 160, 161, 163, 180, 195)*

Palies, P., T. Schuller, D. Durox, and S. Candel (2011). Modeling of premixed swirling flames transfer functions. *Proceedings of the Combustion Institute 33*(2), 2967–2974. *(p. 12)*

Paschereit, C. O., B. Schuermans, W. Polifke, and O. Mattson (2002). Measurement of transfer matrices and source terms of premixed flames. *Journal of Engineering for Gas Turbines and Power 124*(2), 239–247. *(p. 11, 57)*

Petersen, R. E. and H. W. Emmons (1961). Stability of Laminar Flames. *Physics of Fluids 4*(4), 456–464. *(p. 32)*

Poinsot, T. and S. M. Candel (1988). A nonlinear model for ducted flame combustion instabilities. *Combustion Science and Technology 61*(4-6), 121–153. *(p. 31)*

Poinsot, T., T. Echekki, and M. Mungal (1992). A study of the laminar flame tip and implications for premixed turbulent combustion. *Combustion science and technology 81*(1-3), 45–73. *(p. 92, 136)*

Poinsot, T. and D. Veynante (2012). *Theoretical and Numerical Combustion, 3rd edition*. *(p. 4, 5, 6, 7, 9, 159, 206)*

Poinsot, T. J., A. C. Trouve, D. P. Veynante, S. M. Candel, and E. J. Esposito (1987). Vortex-driven acoustically coupled combustion instabilities. *Journal of Fluid Mechanics 177*, 265–292. *(p. 12)*

Polifke, W., A. Poncet, C. Paschereit, and K. Dobbeling (2001). Reconstruction of acoustic transfer matrices by instationary computational fluid dynamics. *Journal of Sound and Vibration 245*(3), 483–510. *(p. 11, 58)*

Preetham, S. Hemchandra, and T. Lieuwen (2008). Dynamics of Laminar Premixed Flames Forced by Harmonic Velocity Disturbances. *Journal of Propulsion and Power 24*(6), 1390–1402. *(p. 26, 30, 44, 79, 80, 119, 123)*

Preetham and T. Lieuwen (2004). Nonlinear flame-flow transfer function calculations: flow disturbances celerity effects. *40th AIAA/ASME/SAE/ASEE Joint Propulsion Conference and Exhibit Proceedings AIAA 2004-4035*. *(p. 24, 26, 44, 104)*

Preetham, H. Santosh, and T. C. Lieuwen (2007). Response of turbulent premixed flames to harmonic acoustic forcing. *Proceedings of the Combustion Institute 31*(1), 1427–1434. *(p. 10, 45)*

Preetham, S. K. Thumuluru, H. Santosh, and T. Lieuwen (2010). Linear

response of laminar premixed flames to flow oscillations: unsteady stretch effects. *Journal of Propulsion and Power 26*(3), 524–532. *(p. 26, 36, 37, 88)*

Putnam, A. (1970). *Combustion driven oscillations in industry*. Elsevier. *(p. 4, 5)*

Rao, A., V. Ganesan, K. Gopalakrishnan, and R. Natarajan (1983). Experimental and theoretical investigations of vane-generated swirling flows in a circular chamber. *Journal of the Institute of Energy 41*(428), 137–144. *(p. 122)*

Rayleigh, L. (1878). The explanation of certain acoustic phenomena. *Nature 18*, 319–321. *(p. 4, 5)*

Remie, M., M. Cremers, K. Schreel, and L. de Goey (2006). Flame jet properties of Bunsen-type flames. *Combustion and Flame 147*(3), 163–170. *(p. 123)*

Richards, G. A., D. L. Straub, and E. H. Robey (2003, 2013/03/22). Passive control of combustion dynamics in stationary gas turbines. *Journal of Propulsion and Power 19*(5), 795–810. *(p. 6)*

Richecoeur, F., T. Schuller, A. Lamraoui, and S. Ducruix (2013). Analytical and experimental investigations of gas turbine model combustor acoustics operated at atmospheric pressure. *Comptes Rendus Mécanique 341*(1-2), 141–151. Combustion, spray and flow dynamics for aerospace propulsion. *(p. 8, 9)*

Rienstra, S. and A. Hirschberg (2012). *An Introduction to Acoustics*. *(p. 177, 214)*

Rook, R. and L. de Goey (2003). The acoustic response of burner-stabilized flat flames: a two-dimensional numerical analysis. *Combustion and Flame 133*(1-2), 119–132. *(p. 20, 26, 33, 34, 40, 104, 107, 109)*

Rook, R., L. P. H. de Goey, L. M. T. Somers, K. R. A. M. Schreel, and R. Parchen (2002). Response of burner-stabilized flat flames to acoustic perturbations. *Combustion Theory and Modelling 6*(2), 223–242. *(p. 12, 26, 33, 34, 35, 39, 40, 104, 107)*

Roux, S., G. Lartigue, T. Poinsot, U. Meier, and C. Bérat (2005). Studies of mean and unsteady flow in a swirled combustor using experiments, acoustic analysis, and large eddy simulations. *Combustion and Flame 141*(1-2), 40–54. *(p. 6, 9)*

Sattelmayer, T. and W. Polifke (2003). Assessment of methods for the computation of the linear stability of combustors. *Combustion Science and Technology 175*(3), 453–476. *(p. 7)*

Schimek, S., J. P. Moeck, and C. O. Paschereit (2011). An experimental investigation of the nonlinear response of an atmospheric swirl-stabilized premixed flame. *Journal of Engineering for Gas Turbines and Power 133*(10), 101502. *(p. 11, 43, 58, 158)*

Schreel, K., R. Rook, and L. D. Goey (2002). The acoustic response of burner-stabilized premixed flat flames. *Proceedings of the Combustion In-*

stitute 29(1), 115–122. *(p. 11, 26, 33, 34, 35, 40, 109)*

Schreel, K., E. van den Tillaart, and L. de Goey (2005). The influence of burner material properties on the acoustical transfer function of radiant surface burners. *Proceedings of the Combustion Institute 30*(2), 1741–1748. *(p. 33, 35, 109)*

Schuermans, B., F. Guethe, D. Pennell, D. Guyot, and C. O. Paschereit (2010). Thermoacoustic modeling of a gas turbine using transfer functions measured under full engine pressure. *Journal of Engineering for Gas Turbines and Power 132*(11), 111503. *(p. 10, 157)*

Schuller, T. (2003). *Mécanismes de couplage dans les interactions acoustique-combustion*. Ph. D. thesis, Ecole Centrale Paris. *(p. 3, 4, 12, 51, 191, 194)*

Schuller, T., S. Ducruix, D. Durox, and S. Candel (2002). Modeling tools for the prediction of premixed flame transfer functions. *Proceedings of the Combustion Institute 29*(1), 107–113. *(p. 10, 26, 29, 30, 44, 78, 82, 88, 90, 93, 124, 177)*

Schuller, T., D. Durox, and S. Candel (2003a). A unified model for the prediction of laminar flame transfer functions: comparisons between conical and V-flame dynamics. *Combustion and Flame 134*(1-2), 21–34. *(p. 23, 24, 26, 27, 28, 32, 37, 44, 67, 79, 80, 81, 82, 84, 85, 87, 94, 104, 123, 144, 177, 204)*

Schuller, T., D. Durox, and S. Candel (2003b). Self-induced combustion oscillations of laminar premixed flames stabilized on annular burners. *Combustion and Flame 135*(4), 525–537. *(p. 60, 87, 157)*

Schuller, T., N. Tran, N. Noiray, D. Durox, S. Ducruix, and S. Candel (2009). The role of nonlinear acoustic boundary conditions in combustion/acoustic coupled instabilities. ASME. *(p. 195)*

Schwarz, H., L. Zimmer, D. Durox, and S. Candel (2010). Detailed measurements of equivalence ratio modulations in premixed flames using laser rayleigh scattering and absorption spectroscopy. *Experiments in Fluids 49*, 809–821. *(p. 10)*

Selimefendigil, F., S. Föller, and W. Polifke (2012). Nonlinear identification of unsteady heat transfer of a cylinder in pulsating cross flow. *Computers & Fluids 53*(0), 1–14. *(p. 193)*

Selle, L., L. Benoit, T. Poinsot, F. Nicoud, and W. Krebs (2006). Joint use of compressible large-eddy simulation and Helmholtz solvers for the analysis of rotating modes in an industrial swirled burner. *Combustion and Flame 145*(1-2), 194–205. *(p. 6, 9)*

Selle, L., T. Poinsot, and B. Ferret (2011). Experimental and numerical study of the accuracy of flame-speed measurements for methane/air combustion in a slot burner. *Combustion and Flame 158*(1), 146–154. *(p. 3)*

Sensiau, C. (2008). *Simulations numériques des instabilités thermoacoustiques dans les chambres de combustion annulaires*. Ph. D. thesis, Université Montpellier II. *(p. 8, 164, 169)*

Sewell, J. B. and P. A. Sobieski (2006). *Monitoring of Combustion Instabilities: Calpine's Experience*. American Institute of Aeronautics and Astronautics. *(p. 2)*

Shin, D.-H. and T. Lieuwen (2012). Flame wrinkle destruction processes in harmonically forced, laminar premixed flames. *Combustion and Flame 159*(11), 3312–3322. *(p. 26, 33)*

Shreekrishna, S. Hemchandra, and T. Lieuwen (2010). Premixed flame response to equivalence ratio perturbations. *Combustion Theory and Modelling 14*(5), 681–714. *(p. 10)*

Silva, C., F. Nicoud, T. Schuller, D. Durox, and S. Candel (2013). Using a Helmholtz solver to assess combustion instabilities amplitudes in a premixed swirled combustor. *Submitted to Combustion and Flame*. *(p. 9, 12, 160, 170, 195)*

Stohr, M., I. Boxx, C. Carter, and W. Meier (2011). Dynamics of lean blowout of a swirl-stabilized flame in a gas turbine model combustor. *Proceedings of the Combustion Institute 33*(2), 2953–2960. *(p. 194)*

Stow, S. R. and A. P. Dowling (2009). A time-domain network model for nonlinear thermoacoustic oscillations. *Journal of Engineering for Gas Turbines and Power 131*(3), 031502. *(p. 7)*

Sugimoto, T. and Y. Matsui (1982). An experimental study on the dynamic behavior of premixed laminar flames. *Symposium (International) on Combustion 19*(1), 245–250. *(p. 21, 22, 27, 28, 78, 136, 142)*

Tay-Wo-Chong, L., S. Bomberg, A. Ulhaq, T. Komarek, and W. Polifke (2012). Comparative Validation Study on Identification of Premixed Flame Transfer Function. *Journal of Engineering for Gas Turbines and Power 134*(2), 021502. *(p. 6, 10, 59)*

Tay-Wo-Chong, L., T. Komarek, R. Kaess, S. Foller, and W. Polifke (2010). Identification of flame transfer functions from les of a premixed swirl burner. *ASME Conference Proceedings 2010*(43970), 623–635. *(p. 59)*

Tay-Wo-Chong, L. and W. Polifke (2012). LES-based study of the influence of thermal boundary condition and combustor confinement on premix flame transfer function. *ASME Conference Proceedings 2012*(68796). *(p. 20, 59, 122, 194)*

Tran, N., S. Ducruix, and T. Schuller (2009). Damping combustion instabilities with perforates at the premixer inlet of a swirled burner. *Proceedings of the Combustion Institute 32*(2), 2917–2924. *(p. 8, 195, 219)*

Truffin, K. and T. Poinsot (2005). Comparison and extension of methods for acoustic identification of burners. *Combustion and Flame 142*(4), 388–400. *(p. 11, 19)*

Tsien, H. (1952). Servo-stabilization of combustion in rocket motors. *Journal of the American Rocket Society 22*, 256–263. *(p. 4, 20)*

Vagelopoulos, C. M. and F. N. Egolfopoulos (1998). Direct experimental determination of laminar flame speeds. *Symposium (International) on Combustion 27*(1), 513–519. *(p. 93)*

Wang, H., C. Law, and T. Lieuwen (2009). Linear response of stretch-affected premixed flames to flow oscillations. *Combustion and Flame 156*(4), 889–895. *(p. 26, 36, 37, 88)*

Wee, D., S. Park, and A. Ghoniem (2012). Impact of curvature on the kinematic response of small flames. *Journal of Engineering Mathematics 74*(1), 37–52. *(p. 36)*

Williams, G. (1985). Combustion theory. *(p. 4, 23)*

Wolf, P., G. Staffelbach, L. Y. Gicquel, J.-D. Müller, and T. Poinsot (2012). Acoustic and Large Eddy Simulation studies of azimuthal modes in annular combustion chambers. *Combustion and Flame 159*(11), 3398–3413. *(p. 6, 9, 87)*

Worth, N. A. and J. R. Dawson (2012). Cinematographic OH-PLIF measurements of two interacting turbulent premixed flames with and without acoustic forcing. *Combustion and Flame 159*(3), 1109–1126. *(p. 46)*

Yuan, T., D. Durox, and E. Villermaux (1994). An analogue study for flame flickering. *Experiments in Fluids 17*, 337–349. *(p. 51)*

Zhu, M., A. P. Dowling, and K. N. C. Bray (2005). Transfer Function Calculations for Aeroengine Combustion Oscillations. *Journal of Engineering for Gas Turbines and Power 127*(1), 18–26. *(p. 59)*

Zimmer, L. and S. Tachibana (2007). Laser induced plasma spectroscopy for local equivalence ratio measurements in an oscillating combustion environment. *Proceedings of the Combustion Institute 31*(1), 737–745. *(p. 10)*